Self-pulsations of a dichloromethane drop on a surfactant solution

Florian Wodlei

THÈSE

En vue de l'obtention du

DOCTORAT DE L'UNIVERSITÉ DE TOULOUSE

Délivré par : *l'Université Toulouse 3 Paul Sabatier (UT3 Paul Sabatier)*

Présentée et soutenue le *29/09/2017* **par :**

Florian WODLEI

Self-Pulsations of a Dichloromethane Drop on a Surfactant Solution

---

JURY

FABIAN BRAU	Chargé de Recherche
PIERRE-ANTOINE BONNEFONT	Maitre de Conférences
MARTINE MEIRELES	Directeur de Recherche
THIERRY ONDARÇUHU	Directeur de Recherche
ANTONIO STOCCO	Maitre de Conférences
VÉRONIQUE PIMIENTA	Professeur d'Université

École doctorale et spécialité
SDM : Chimie macromoléculaire et supramoléculaire - CO044
Unité de Recherche
Laboratoire des Interactions Moléculaires et Réactivité Chimique et Photochimique (UMR 5623)
Rapporteurs
Fabien BRAU et *Pierre-Antoine BONNEFONT*
Directeur de Thèse
Véronique PIMIENTA

Es ist doch nicht genug, eine Sache zu beweisen, man muß die Menschen zu ihr auch noch verführen.
[It is still not enough to prove something, one also has to seduce the people to it]

Friedrich Nietzsche

dedicated to Helfried Biernat
Professor in theoretical Plasmaphysics
(1947-2016)

Acknowledgement

Before everyone else I have to thank my supervisior Véronique PIMIENTA, who not only helped me in scientific respects during these three years but also taught me what it means to be "pragmatic" in doing research, which is something that will help me with my future research projects. I also appreciated a lot the collegial atmosphere we had in carrying out the research.
The theoretical part of my research was developed together with Charles ANTOINE, to whom I'm very thankful for his help and also the collegial atmosphere in which we were working together.
I thank also Jacques MAGNAUDET and Julien SEBILLEAU from the institute of fluid mechanics (IMFT) with whom we were collaborating.

I also want to thank my teachers at high school, Jan Albert RISPENS, who was my chemistry and biology teacher and Mihnea HRISTEA, who was my physics and maths teacher who prepared my path in science, which was continued by Helfried BIERNAT and Hans-Hennig von GRÜNBERG at the university.

A very big thanks goes to Marcello BUDRONI and Federico ROSSI who made the connection to the scientific community in which I am working now which eventually led me to my supervisor and the research topic which is the subject of this work.

In regards to the PhD defence I thank all the members of my jury, especially my two reporters Fabian BRAU and Pierre-Antoine BONNEFONT for their detailed comments on my work.

I also thank all my friends who supported and helped me during these last three years, especially Giuseppe ALBERTI, Andreas GAVRIELIDES and Suhail USMANI.

At the end I also want to thank all the members of the laboratory, the new laboratory director Christophe MINGOTAUD as well as the old one, Monique MAUZAC for their support. In this context I want to mention also Charles-Louis SERPENTINI who helped me with the technical part of my work, as well as Sebastian CAZIN from the Institute of fluid mechanics (IMFT), who advised me with the high speed camera.

Last but not least I thank my family, my parents, grandparents and my brother for their support as well as my girlfriend Jessica FRANCO, who supported me especially in the last months.

Florian WODLEI
November 2017

Contents

General Introduction

General Introduction

In the last 15 years there has been a growing interest in synthetic, chemical systems capable of undergoing autonomous shape changes and self-motion. This is also related to new kinds of possible applications in miniaturization techniques. In microfluidics for example such phenomena appear as a possible answer to problems related to fluid circulation and homogenization of microreactors. The induced motility of these systems is also a key motivation in the domain of artifical cell design. Motility is one of the vital functions of microorganisms in search of new resources. The aim here is to reproduce different propulsion modes observed in biological systems in order to identify the possible energy source and observe the shape and trajectories spontaneously chosen to adapt to motility.

Far-from-equilibrium chemical systems seem to be able to answer these demands. These systems exhibit a wide variety of spatial and temporal patterns known as dissipative structures. The interplay between physico-chemical processes and mass or heat transfer may give rise to spatio-temporal structures induced by convective flows. The conversion from chemical to mechanical energy is at the origin of a wide variety of dissipative structures such as regular convective cells, interfacial deformation, eruptions, interfacial turbulence or emulsification. These flows, triggered by density or surface tension gradients are crucial to many natural and man-made situations as for instance, extraction processes, spreading of spills in aquifers, oil recovery, ocean and atmospheric flows and of course chemical reactors at all scales.
When the phases in contact exhibit very different sizes, this energy conversion may set the smaller phase into spontaneous motion. This is the case with liquid drops on solid or liquid substrates . With drops, the scale of the object and those of the convective cells interfere, leading to strong deformation and sometimes directional motion. Drops are perfect models for laboratory experiments and theoretical development.

In this work we will explore a drop of dichloromethane that undergoes remarkable shape transformations when put on a aqueous solution of different concentrations of cetyl trimethylammonium bromide (CTAB). Among these shape transformations there is one with a striking periodicity: a pulsating drop. The main focus of this work will be on this regime, which appears for a surfactant concentration below the critical micellar concentration (cmc).

The first chapter is a bibliographic approach to the subject describing several systems designed for motion or pulsations on liquid surfaces. It serves as well as an introduction to the theoretical concepts used throughout this work.
The system is introduced in chapter 2 from a historical point of view and by describing the successive regimes observed by varying the CTAB concentration. In chapter 3, we focus on the induction pe-

riod observed for specific experimental conditions that exists before the instability starts. The shape evolution showed an unexpected behavior for a drop deposited on a liquid surface. Based on particle image velocimetry (PIV) measurements we propose an interpretation, which is confirmed by a simple analytical model. Chapter 4 and 5 are devoted to the pulsating regime. In chapter 4, we study the case where the surfactant is only in the aqueous phase. Starting from analyzing the periodicity of the pulsations, we focus on the rim that forms at the end of each pulsation and breaks-up into many small droplets, which are ejected radially. The manner in which this rim breaks up resembles to an instability known as the Rayleigh-Plateau instability. Nevertheless the rim break-up in this system here has its origin in more than one instability, involving also thermal convection induced by a Benard-Marangoni effect. An analytical model has been developed in order to check our hypothesis.

The addition of surfactant to the organic phase, discussed in chapter 5, reveals a new flower pattern, that occurs during the dewetting stage of the pulsating drop. This dewetting also involves very ordered droplet ejection from the "flower petals". We propose a qualitative explanation of the global behavior of the drop and compare these results to the regime observed in the absence of surfactants. At the end of the main chapters (3,4 and 5) a summary of the chapter is given in French.

Introduction générale

Introduction générale

Au cours des 15 dernières années, un intérêt croissant est apparu pour des systèmes chimiques synthétiques donnant lieu spontanément à des modifications de forme ou capables de motilité. Ces travaux sont en relation avec des applications dans les techniques de miniaturisation. En microfluidique, par exemple, de tels phénomènes pourraient apporter des réponses à des problèmes liés à la circulation des fluides ou l'homogénéisation de microréacteurs. The motilité induite dans de tels systèmes est également à l'origine de leur intérêt dans le domaine du design de cellules artificielles. Se déplacer est l'une des fonctions vitales des microorganismes à la recherche de nouvelles ressources. Le but est dans ce cas de reproduire différents modes de propulsion observés dans ls systèmes biologiques dans le but d'identifier les sources possibles d'énergie et d'observer la forme et les trajectoires choisies spontanément pour s'adapter au mouvement.

Les systèmes hors équilibre sont susceptibles de répondre à de telles motivations. Ces systèmes montrent une grande variété de structures spatiales ou temporelles connues sous le nom de structures dissipatives. Le couplage entre processus physico-chimiques et le transfert de matière ou de chaleur peuvent donner lieu à la formation de structures spatio-temporelles induites par des flux convectifs. La conversion d'énergie chimique en énergie mécanique est à l'origine de grande variété de structures dissipatives telles que des cellules de convection, des déformations interfaciales, des éruptions, de la turbulence interfaciale ou des phénomènes d'émulsification. Ces flux, induits par des gradients de densité ou de tension superficielle sont cruciaux dans différentes situations naturelles ou industrielles comme par exemple pour les processus d'extraction, la récupération du pétrole, les flux océaniques ou atmosphériques et dans les réacteurs à toutes les échelles.

Quand ls phases en contacts sont de taille très différente, cette conversion d'énergie peut mettre la phase de plus petite taille en mouvement. Ceci est le cas pour des gouttes sur surfaces solides ou liquides. Pour les gouttes, la taille du système et des cellules de convection interfèrent menant à de fortes déformations ou à la motilité. Les gouttes apparaissent comme des modèles parfaits pour des expériences en laboratoire et le développement de théories. Dans ce travail, nous allons explorer le comportement d'une goutte de dichlorométhane qui donne lieu à des transformations remarquables de sa forme lorsqu'elle est déposée sur des solutions de bromure de cétyltriméthylammonium de concentration différente. Parmi ces transformations, il y en a une montrant une périodicité surprenante : la goutte pulse de façon régulière. Le sujet principal de cette thèse porte sur ce régime qui apparait pour une concentration en tensioactif inférieur à la concentration micellaire critique (cmc).

Le premier chapitre est une approche bibliographique du sujet décrivant plusieurs systèmes capables de se déplacer ou montrant des pulsations sur surfaces liquides. Il constitue également une introduction aux concepts théoriques utiles tout au long de ce travail.

Le système est ensuite introduit dans le chapitre 2 d'un point de vue historique et par la description des régimes successifs observés en faisant varier la concentration de CTAB. Au chapitre 3, nous nous intéressons plus particulièrement sur la période d'induction observée avant le début de l'instabilité. L'évolution de la forme de la goutte montre un comportement inattendu sur surface liquide. Des mesures de vélocimétrie par imagerie de particules (PIV) nous a permis de proposer une interprétation du phénomène et de proposer un modèle analytique simple rendant compte de nos observations. Les chapitres 4 et 5 sont dédiés au régime de pulsation. Au chapitre 4, nous avons étudié le cas où le tensioactif se trouve uniquement dans la phase aqueuse. Nous nous sommes en particulier intéressés au bourrelet qui se forme à l'extrémité du film en expansion et donne lieu après rupture à l'éjection de gouttelettes en direction radiale. L'instabilité est similaire à une instabilité de Rayleigh-Plateau mais elle présente ici des propriétés particulières liées à des phénomènes thermiques. Un modèle analytique a été développé dans le but de vérifier nos hypothèses. L'addition de tensioactifs à la phase organique, discuté au chapitre 5, révèle une nouvelle structure hautement ordonnée qui apparait lors de la phase de démouillage du régime de pulsation. Nous proposons une interprétation qualitative du comportement de la goutte et une comparaison des systèmes en présence et en l'absence de CTAB dans la goutte.

À la fin des chapitres principaux (3,4 et 5) un résumé du chapitre est donné en français.

1

Surface-Tension induced Motion and Deformation on Solid and Liquid Surfaces

Erst wenn du die Stadt verlassen hast, siehst du, wie hoch sich ihre Türme über die Häuser erheben.

[*Only after you leave the city you see how high its towers rise above the houses.*]

Friedrich Nietzsche

In this Chapter we will introduce the theoretical background needed to understand the basics of surface tension induced motion and deformation of drops on solid and liquid surfaces. This will be followed by a literature study on the existing systems, that move, spread and transform themselves on liquid (and solid) surfaces.

1.1. Introduction to Capillarity

In this section we will introduce the theoretical concepts to understand surface-tension induced motion and deformation of objects on liquid and solid surfaces. This section is based on the books of de Gennes [1], Adamson [2] and on the articles by Brochard-Wyart [3], Sebilleau [4] and Bonn et al. [5] for the topic of "pseudo-partial" wetting.
Etymologically speaking, capillarity (also known as capillary action) is the phenomenon that pulls a liquid in a narrow tube upwards against the gravity force[1]. The word capillarity is also used in a more general way to cover interfacial phenomena between immiscible liquids or liquids and gases. The research field investigating these phenomena was founded by Pierre S. de Laplace [6] and Thomas Young [7] in the beginning of the 19th century and has grown nowadays to a huge field of scientific research with applications in the fields of physical chemistry (e.g. microdroplets in microfluidics [8]), biology (e.g. lipid droplet formation in the biological cell [9]) and industry (e.g. inkjet printing or coating of surfaces [10]).

1.1.1. Cohesive and Adhesive Forces

The forces that hold any body together are the so called cohesive[2] forces which are weaker in a liquid than in a solid and therefore allow the liquid to be more flexible and adaptable than a solid. This is the reason why a liquid can flow but still doesn't change significantly its volume.
When a liquid gets in contact with another liquid, gas or solid, there are new forces acting: the adhesive[3] forces, which are the forces between the different substances that hold them together.
By looking at the microscopic picture of matter, these forces have their origin in the interactions between the molecules from which they are build up. A molecule inside the bulk is submitted to all the forces of the other molecules surrounding it in such a way that the net force equals zero in average (these forces are the cohesive forces). In contrast, at the interface with another liquid, solid or gas a molecule is submitted to forces from the molecules of its kind and also to the forces of the molecules or atoms of the other substance. If these forces are different from the one of its own kind the molecule will feel a non-zero net force.
If the other substance is in the gaseous state, the cohesive forces are much bigger than the adhesive ones and the molecules at the interface will feel a net force that is directed inside the bulk of the liquid. Therefore a molecule at the interface is immediately pulled back into the bulk. As a result other molecules from the bulk are now exposed to the interface which again will be pulled back into the bulk (see Fig. 1.1).

[1] the word capillary comes from the latin word *capillus* which stands for a a long narrow diameter tube
[2] from Latin *cohaerere* which stands for stick or stay together
[3] from Latin *adhaerere* which stands for stick or being attached to something

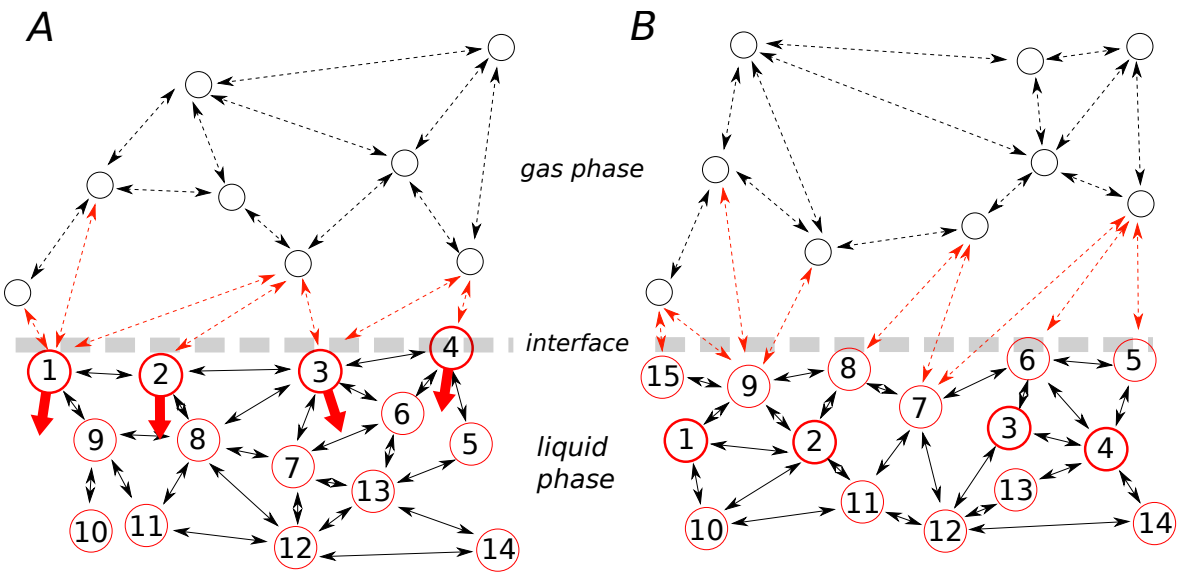

Figure 1.1: *Simplified schematic microscopic pictures of the molecular interactions at a gas/liquid interface. Cohesive forces between the molecules are shown in black, adhesive forces in red dashed; the molecules of the liquid phase are numbered to show their change in position after an instant due the fact that they experience a non-zero net force (big red arrows). B shows the situation of A at a later instant.*

1.1.2. Surface Tension as an Energy

This dynamic process at a microscopic level, that results in the exposure of the smallest possible amount of molecules to the interface, leads at a macroscopic picture to the fact that the surface area of the interface will tend to be minimal for a given volume.
For example the equilibrium state of a liquid drop in a gas phase is therefore the state of a perfect sphere (neglecting gravity), since this is the state with the minimal surface area for a given volume of liquid. Any other state with a surface different from a sphere is a non-equilibrium state and is accompanied by a higher free energy. The increase in the free energy is directly proportional to the increase in the surface area while the proportionality factor is the *surface tension* denoted γ:

$$dG_{surface} = \gamma \cdot dA. \tag{1.1}$$

Its value is directly linked to the cohesive energy per molecule, U, which is the energy that holds a molecule inside the bulk. The energy needed to increase the surface area by an amount of dA is therefore equal to the energy for maintaining the number of molecules N at the interface. This area dA is $N \cdot a$, where a is the surface area of one molecule and the energy is N times the energy needed to keep one molecule at the surface.
For a liquid in contact with gas the adhesive forces can be neglected and the energy needed to keep

one molecule at the surface is around $\frac{U}{2}$. So the energy needed to increase the area by an amount of dA is therefore $\frac{N \cdot U}{2}$. Rewriting and comparing it with Eqn. (1.1) leads to

$$dG_{surface} = \frac{N \cdot U}{2} = \frac{U}{2 \cdot a} dA, \tag{1.2}$$

where the surface tension is given by

$$\gamma = \frac{U}{2 \cdot a}. \tag{1.3}$$

For water which has a quite strong cohesive energy around 18 kT ($\approx 7 \cdot 10^{-20} J$ at 25^o C) due to hydrogen bonds, this leads to a surface tension of around 72 mN/m. For most oils it is around kT ($\approx 4 \cdot 10^{-21} J$ at 25^o C) which leads to surface tensions around 30 mN/m.

1.1.3. Spreading and Wetting

When a liquid is spreading on a solid or liquid surface, it is said that the liquid is wetting the surface. Depending on the cohesive forces and the adhesive forces between the liquid and the solid two scenarios are possible: (i) the total wetting case, where the drop spreads to cover the surface (Fig. 1.2 (A)) and (ii) the partial wetting case, where the drop reaches an equilibrium shape with a given contact angle (see Fig. 1.2 (B)). The non-wetting case can be seen as a special case of the partial wetting case with a contact angle bigger than 90^o (see Fig. 1.2 (C,D)).

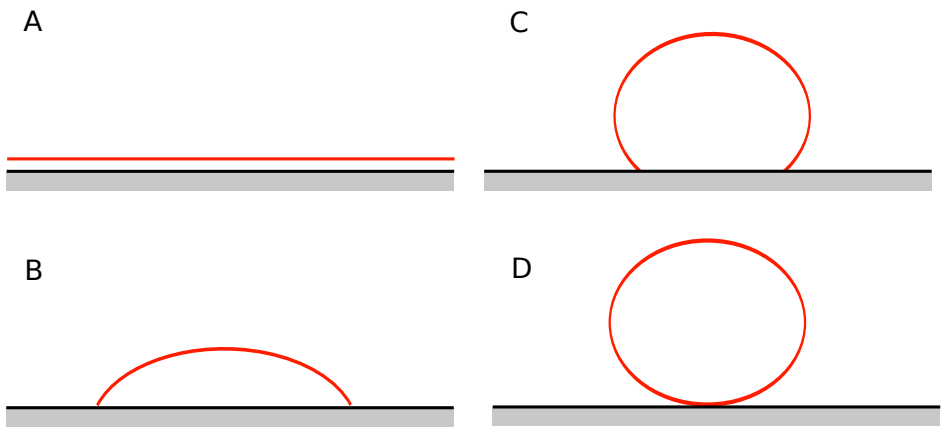

Figure 1.2: *Spreading of liquids on solid surfaces. A: Total wetting. B: Partial wetting. C: Non-wetting. D: Perfect non-wetting.*

The equilibrium state of a liquid drop on a solid surface in the partial wetting case is given by the Young equation, which will be derived here from a thermodynamical point of view. Fig. 1.3 shows

an equilibrium state of a drop on a solid surface showing the contact angle θ and the connected surface areas.
The system has three surfaces and a contact line, where these three interfaces meet called the *triple contact line*.

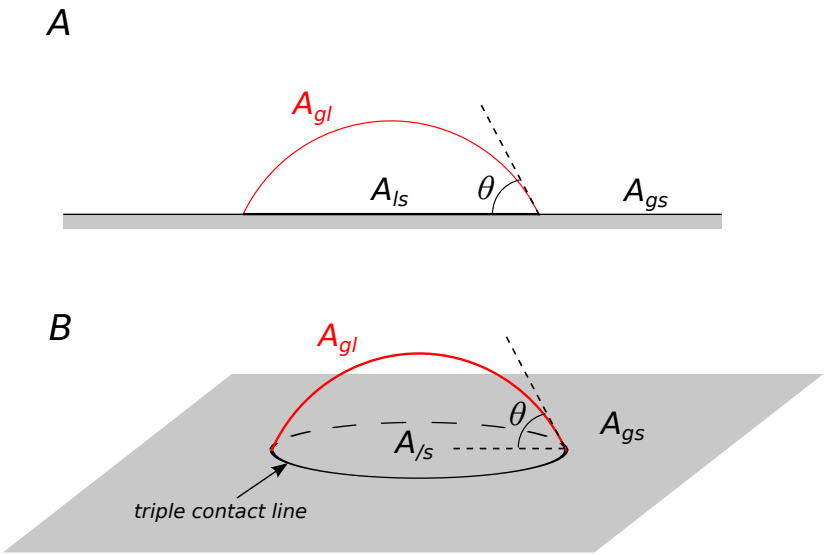

Figure 1.3: *A liquid drop on a solid surface. A: side view showing the contact angle, θ. B: A 3-dimensional view showing the corresponding surface areas and the triple contact line.*

By calculating the change in the free energy of the system, the equilibrium state of the droplet is obtained. An infinitesimal change in the free energy is accompanied by an infinitesimal small change in the spreading of the drop (see Fig. 1.4). This change of energy is given by

$$dG = \frac{\partial G}{\partial A_{\mathrm{gs}}}\, dA_{\mathrm{gs}} + \frac{\partial G}{\partial A_{\mathrm{gl}}}\, dA_{\mathrm{gl}} + \frac{\partial G}{\partial A_{\mathrm{ls}}}\, dA_{\mathrm{ls}} = \gamma_{\mathrm{gs}}\, dA_{\mathrm{gs}} + \gamma_{\mathrm{gl}}\, dA_{\mathrm{gl}} + \gamma_{\mathrm{ls}}\, dA_{\mathrm{ls}}, \tag{1.4}$$

where the subscripts of the surface areas, gs, gl and ls are denoting the interfaces gas/solid, gas/liquid and liquid/solid respectively. In terms of the increase in the surface area dA_{ls}, the change of the energy is given by

$$dG = \left(-\gamma_{\mathrm{gs}} + \gamma_{\mathrm{gl}} \cos\theta' + \gamma_{\mathrm{ls}}\right)\, dA_{\mathrm{ls}}, \tag{1.5}$$

where $dA_{\mathrm{gs}} = -dA_{\mathrm{ls}}$ and $dA_{\mathrm{gl}} = dA_{\mathrm{ls}} \cos\theta'$ allows to express the other areas in terms of the area dA_{ls} (see inset of Fig. 1.4). At equilibrium the change in energy is zero, which is equivalent to the bracket being zero in Eqn. (1.4), or in other words:

$$\boxed{\gamma_{\mathrm{gs}} = \gamma_{\mathrm{gl}} \cos\theta + \gamma_{\mathrm{ls}}}. \tag{1.6}$$

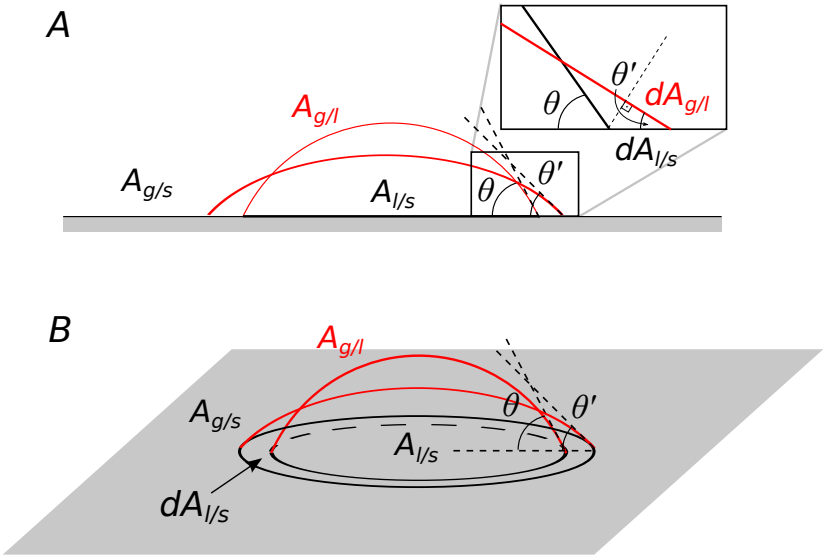

Figure 1.4: *Spreading of liquid drop on a solid surface. A: side view showing the change in surfaces and contact angle (inset showing the relation between the surfaces at the triple contact lines). B: Corresponding 3-dimensional side view of the spreading.*

This equation is known as the ***Young*** equation.

1.1.3.1. Contact Angle Hysteresis

If the drop is volatile and losing volume due to evaporation or if volume is sucked away by a syringe, the contact line will not move but stay pinned and the contact angle will decrease[4]. This contact angle which will be smaller than the equilibrium contact angle is called *receding contact angle*, θ_R. On the other hand if the volume of the drop is increased with a syringe, the contact line again will not move but the contact angle will increase. This contact angle, bigger than the equilibrium contact angle, is called the *advancing contact angle*, θ_A. Pinned evaporating drops have been extensively studied in the framework of the so-called "Coffee ring" effect [12].

[4]This depends on the hydrophobic and hydrophilic interactions between the drop and the surface. A water droplet for example can be pinned on a hydrophilic surface while it will not pin on a hydrophobic one, where it will shrink due to evaporation by maintaining the equilibrium contact angle [11].

1.1.3.2. The Spreading Parameter

The initial wetting state can be predicted by the spreading parameter S, which is defined as the difference between the free energy per surface area of the dry surface and the free energy per surface area of the wetted surface, i.e.

$$\boxed{S = \gamma_{\text{gs}} - (\gamma_{\text{gl}} + \gamma_{\text{ls}})} \tag{1.7}$$

where γ_{gs}, γ_{gl} and γ_{ls} are the surface tensions at the gas/solid, gas/liquid and liquid/solid interfaces, respectively.

If the parameter S is positive, i.e. $\gamma_{\text{gs}} > (\gamma_{\text{gl}} + \gamma_{\text{ls}})$, a liquid spreads and wets the surface completely (total wetting case), while in the case of S negative, i.e. $\gamma_{\text{gs}} < (\gamma_{\text{gl}} + \gamma_{\text{ls}})$, a drop spreads until it reaches the equilibrium contact angle calculated above (partial wetting case).
The spreading parameter is commonly used to predict the spreading behavior of a drop on a solid and liquid surface. Due to the possible evolution of the surface tensions the spreading parameter can become also time dependent.
In general it is not possible to determine the equilibrium spreading coefficient S from the pure interfacial tensions since as in the example illustrated above the surfaces can be modified by the formation of films or/and the modification of its composition due to evaporation and/or the adsorption of surfactants. A benzene droplet placed on a water surface for example spreads out shortly after its deposition and then retracts to form a droplet [5]. This means that the initial spreading parameter $S_i > 0$, while the equilibrium spreading parameter $S < 0$. Since the interfacial tension between water and benzene is low, complete wetting is initially favored. This effect becomes overpowered by the modification of the water/air interface by the formation of a microscopic benzene film that lowers the corresponding interfacial tension.

In general, in such systems the spreading behavior can be understood by the evolution of the spreading parameter $S(t)$, rather than by its equilibrium value.

1.1.4. Surface Tension as a Force

The surface tension can also be interpreted as a force that acts tangentially to the surface and perpendicular to the contact line and in the direction that minimizes the surface (see Fig. 1.5). The free energy can be written as:

$$dG = \gamma \, dA = \gamma \, \ell \, dx = \ell \, \vec{\gamma} \cdot d\vec{x}, \tag{1.8}$$

where ℓ is the circumference of the surface A, $d\vec{x}$ is a vector in the direction of the increase of A and

$$\vec{\gamma} = \gamma \cdot \vec{e}_{||} \tag{1.9}$$

is the interfacial tension, where $\vec{e}_{||}$ is the tangent unit vector to the surface perpendicular to the circumference.

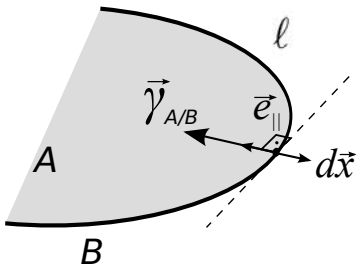

Figure 1.5: *Interpretation of the surface tension as a force acting at the contact line ℓ between phases A and B.*

This point of view is commonly used to derive the Young equation by writing down the equilibrium of forces at a point of the triple contact line[5] (see Fig. 1.6).

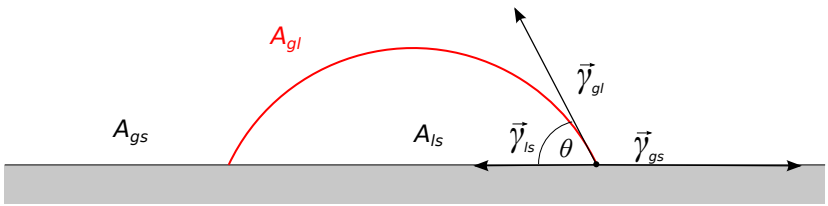

Figure 1.6: *Interfacial forces acting on the triple contact line for a liquid droplet on a solid surface.*

Everything derived so far is also applicable to a liquid drop on a liquid interface. The only difference is that the supporting interface is not rigid anymore and is deforming itself according to the forces acting on it (see Fig. 1.7).

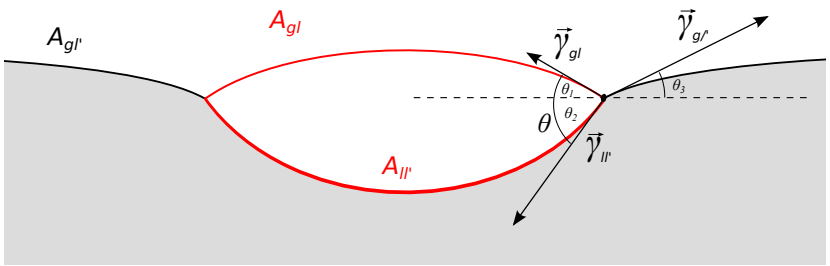

Figure 1.7: *Interfacial forces acting on the triple contact line for a liquid droplet on a liquid surface.*

[5] due to the fact that the solid substrate does not deform, only the horizontal projections of the force $\vec{\gamma}_{g/l}$ enters the equation while the vertical projection counterbalances the force with which the substrate is acting on the contact line

A relation between the parameters can be obtained again by writing down the equilibrium of forces at a point at the triple contact line i.e.

$$\begin{aligned} \gamma_{\mathrm{gl'}} \cos\theta_3 &= \gamma_{\mathrm{gl}} \cos\theta_1 + \gamma_{\mathrm{ll'}} \cos\theta_2 \\ \gamma_{\mathrm{ll'}} \sin\theta_2 &= \gamma_{\mathrm{gl}} \sin\theta_1 + \gamma_{\mathrm{gl'}} \sin\theta_3 \end{aligned} \tag{1.10}$$

where γ_{gl}, $\gamma_{\mathrm{ll'}}$ and $\gamma_{\mathrm{gl'}}$ are the surface tensions at the gas/liquid, liquid/liquid and gas/liquid(bulk) interfaces, respectively. On the other hand at equilibrium the forces also have to fulfill the vector equation

$$\vec{\gamma_{\mathrm{ls}}} + \vec{\gamma}_{\mathrm{gl}} + \vec{\gamma}_{\mathrm{ll'}} = \vec{0} \tag{1.11}$$

which can be graphically represented by a triangle, the so called Neumann triangle (see Fig. 1.8). In this way the following equation for the contact angle θ can be obtained by using the law of cosines:

$$\boxed{\cos\theta = \frac{\gamma_{\mathrm{gl'}}^2 - \gamma_{\mathrm{gl}}^2 - \gamma_{\mathrm{ll'}}^2}{2\gamma_{\mathrm{gl}}\gamma_{\mathrm{ll'}}}.} \tag{1.12}$$

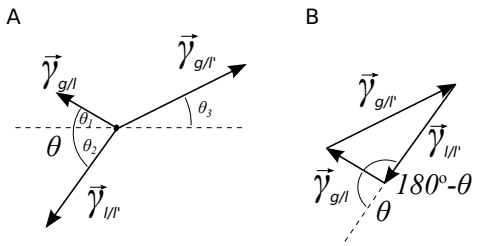

Figure 1.8: *A: Neumann construction of the forces at the triple contact line. B: Neumann triangle.*

1.1.5. Pseudo-Partial Wetting and Thin Films

The case where a liquid lens, that is formed at a water gas interface, is in equilibrium with a surrounding thin film is called pseudo-partial wetting (see Fig. 1.9).

To find the equilibrium state of such a system the free energy density of the film is investigated, which reads

$$g(h) = \gamma_{\mathrm{gl}} + \gamma_{\mathrm{ll'}} + \tilde{\gamma}(h). \tag{1.13}$$

Here $\tilde{\gamma}(h)$ is the contribution of long range forces across the film of thickness h. In the limit $h \to 0$, i.e. when the film reduces to the gas/liquid(bulk) interface, $\tilde{\gamma}(h) = S_i$ to retrieve the gas/liquid(bulk) interfacial tension. The limit $h \to \infty$ leads to $\tilde{\gamma}(h) = 0$ since for larger distances the effect of the

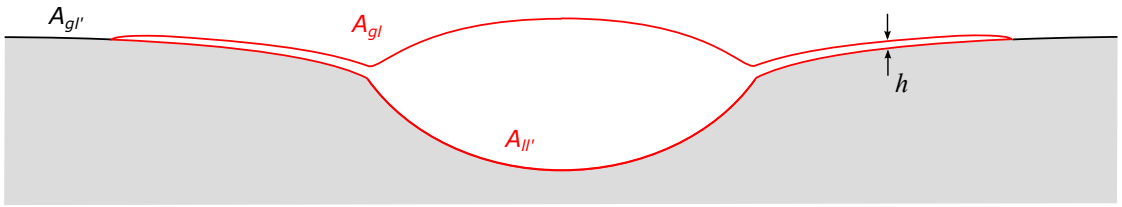

Figure 1.9: *Pseudo-partial wetting. A drop in equilibrium with a surrounding thin film of thickness h.*

molecular forces vanishes. To find an expression for $\tilde{\gamma}(h)$ the change in free energy of the system that is generated by the presence of the liquid film is calculated. The free energy of the system reads

$$G(h) = (\gamma_{\mathrm{gl}} + \gamma_{\mathrm{ll'}} + P(h))A, \tag{1.14}$$

where $P(h)$ is the free energy per area that arises from the interaction of the underlying liquid with the gas phase through the thin film of liquid of thickness h. A is the surface area of the film. By keeping the volume of the film constant, the change in free energy that is accompanied by the increase of the film area A is obtained:

$$dG = \gamma_{\mathrm{gl}}\, dA + \gamma_{\mathrm{ll'}}\, dA + d(P(h)\cdot A) = \left(\gamma_{\mathrm{gl}} + \gamma_{\mathrm{ll'}} + P(h) - h\frac{dP(h)}{dh}\right) dA. \tag{1.15}$$

Comparing with Eqn. (1.13) we get the expression for $\tilde{\gamma}(h)$, i.e.

$$\tilde{\gamma}(h) = P(h) - h\frac{dP(h)}{dh}. \tag{1.16}$$

The spreading dynamics in the pseudo-partial wetting regime is therefore determined by $P(h)$. Regarding the limit $h \to 0$ of $\tilde{\gamma}(h)$ the expression of $P(h)$ for this case can be already determined:

$$\lim_{h\to 0}\tilde{\gamma}(h) = \lim_{h\to 0}\left(P(h) - h\frac{dP(h)}{dh}\right) = \underbrace{\lim_{h\to 0} P(h)}_{:=P(0)} \stackrel{!}{=} S_i \qquad \Rightarrow \qquad \boxed{P(0) = S_i} \tag{1.17}$$

From theoretical considerations[6]:

$$P(h) = \frac{A_H}{12\pi h^2} \qquad \text{for} \qquad d_o < h < \infty \tag{1.18}$$

is obtained, where d_o is the molecular distance and A_H is the effective Hamaker constant, which is a measure for the strengths of the London-van der Waals interaction energy[7].

[6] assuming London–van der Waals interactions between the liquid and the gas phase through the liquid film of thickness h [13]

[7] the effective Hamaker constant is a sum of all contributions, i.e. $A_H = A_{l'g} - A_{gg} + A_{ll'} - A_{ll}$ with A_{ij} the corresponding Hamaker constants for the interface ij. The van der Waals interaction of the gas phase for non-volatile is neglectable, leading to $A_H \approx A_{ll'} - A_{ll}$

Knowing this, the four simplest cases of the possible dependency of P on the thickness h will be discussed here (see Fig. 1.10). For a positive Hamaker constant (orange curves) the case of total wetting is obtained. Partial wetting and pseudo-partial wetting are obtained for a negative Hamaker constant. The pseudo-partial wetting is obtained when the curve of $P(h)$ shows a minimum. This minimum corresponds to the equilibrium film thickness h_{min} of the film that is surrounding the drop. In general the situation is not as simple as shown in Fig. 1.10 since the dependency of $P(h)$ can be quite complex for small h.

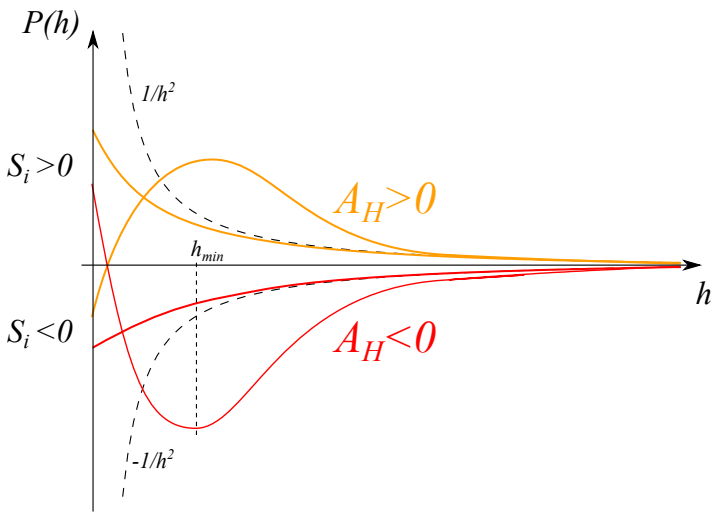

Figure 1.10: *Dependency of the $P(h)$ on the film thickness that determines the wetting behavior (the four simplest cases); dashed lines are the curves $\pm 1/h^2$, that serve as asymptotes. Orange curves ($A_H > 0$): Total ($S_i > 0$) and partial ($S_i < 0$) wetting. Red curves $A_H < 0$: Partial ($S_i < 0$) and pseudo-partial ($S_i > 0$) wetting.*

In general, the possibility of a lens having a thin film of thickness h surrounding it, is determined by the initial spreading parameter and the value of the effective Hamaker constant.

1.2. Spreading of Drops on Liquid Surfaces

Spreading of one liquid on the surface of another is studied since the early 70s in regard to oil slicks and the spreading of crude oil on sea water [14, 15, 16, 17, 18].

A volume of a less denser liquid spreads out on a denser one due to gravity and surface-tension forces, which are counterbalanced by viscous forces. The rate of spreading is following a power law, i.e.

$$r(t) = k \cdot t^n, \tag{1.19}$$

where $r(t)$ is the radius of the oil slick at the time t and k is a factor depending on the volume, the spreading parameter, the density, the gravitational acceleration and the viscosity of the bulk. The exponent n can range from $1/10$ to close to 1 depending on the systems and the processes involved.

Classically three regimes are observed for these kind of systems, which are governed by the relative importance of different forces. As spreading initiates, it starts with a regime where inertia and gravity are important. k is only depending on the relative densities and the volume and n is 0.25. As the volume of oil gets thinner viscous forces get more important and k now also depends of the viscosity of the bulk phase and the power exponent n increases to 0.5. In the last regime, gravity effects decrease and only surface tension and viscous forces determine the spreading. In this case k only depends on the spreading parameter and the viscosity of the bulk phase. In summary:

$$\begin{aligned}
r(t) &= (\Delta\rho V)^{1/4}\ t^{1/4} && \text{gravitiy-inertia regime} \\
r(t) &= \left(\frac{\Delta\rho V^2}{\nu^{1/2}}\right)^{1/6} t^{1/2} && \text{gravitiy-viscous regime} \\
r(t) &= \left(\frac{S^2}{\rho^2\nu}\right)^{1/6} t^{3/4} && \text{Surface tension-viscous regime}
\end{aligned}$$

Here $\Delta\rho$ is the difference between the densities of the liquids, ρ is the density of the bulk phase, V is the volume, ν is the viscosity of the bulk phase and S is the spreading parameter. The spreading of a volume of oil on a water surface is therefore passing subsequently from a gravity-inertia regime over a gravity viscous regime to finally reach a surface tension-viscous regime when it is already very flat. Spreading in the surface tension-viscous regime is called ***Marangoni-driven spreading***.

The spreading of flat oil lenses is therefore expected to follow a Marangoni-driven spreading and a power law with n =0.75, but there are also other parameters that can influence the spreading dynamics as the height of the bulk fluid layer, the presence or creation of surfactants, the fact that the two liquids are partially miscible or the evaporation of the liquid lens.

Dussaud and Troian [19] found for spreading with evaporation on a deep fluid layer a reduced spreading exponent of n = 0.5. They attribute this to a visible convective roll right beneath the leading edge of the expanding drop, which was caused by evaporation and subsequent surface cooling of the rapidly spreading film according to a Benard-Marangoni instability.
Santiago-Rosanne et al. [20] showed that the spreading follows also a power law in the case of partially miscible liquids. The value of the spreading parameter S, the power and the pre-factor k are

largely influenced by dissolution and the thereby induced convections and the height of the fluid layer. They found a spreading exponent around n = 0.5 for fluid layers thicker than 3.5 mm and a reduction of the spreading exponent down to $n \sim 0.1$ for smaller fluid layer heights.
Van Nierop et al. [21] investigated the spreading behavior of a reactive oil drop. They observed that the initial spreading was followed by the retraction of the drop with a spreading exponent between 0.64 and 0.89.

Generally speaking, spreading of liquid lenses on liquid surfaces follow a power law with exponents ranging between 0.1 and 0.9 depending on the particularity of the system. The more complex the systems the more difficult it is to theoretically predict their spreading dynamics.

1.3. The Marangoni Effect and Related Instabilities

The movement, that is induced on the surface due to surface tension inhomogeneities is known as the ***Marangoni effect*** (see Fig. 1.11) and the induced flows are sometimes referred to as ***Marangoni flows*** [22].

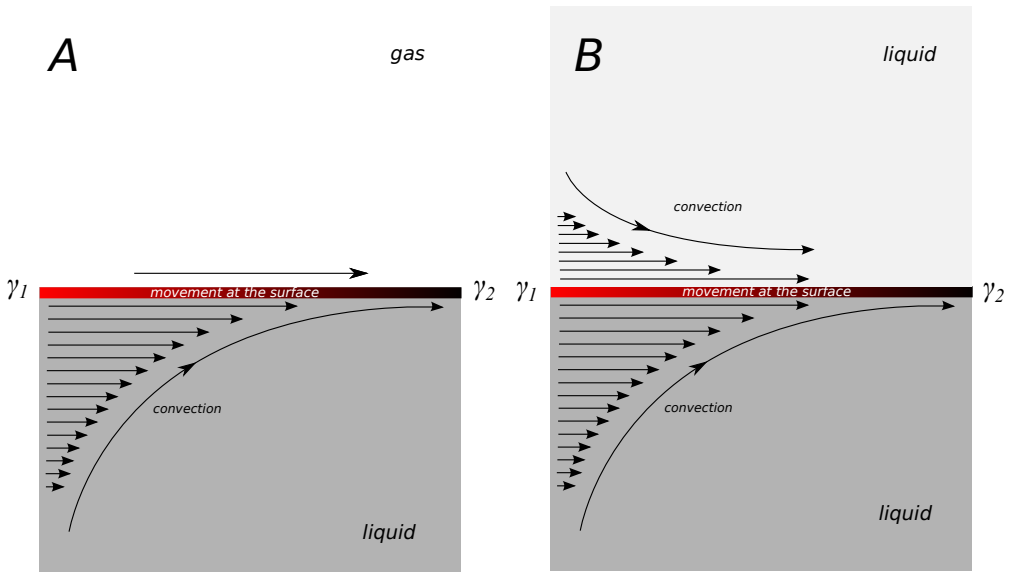

Figure 1.11: *The Marangoni effect. Movements at the interface that are induced by a difference in surface tension ($\gamma_2 > \gamma_1$), which induce convective motions in the bulk phase. A: Gas/liquid interface. B: Liquid/liquid interface; convections induced in both phases, while their amplitude depends on the respective viscosities.*

These flows can also induce motion in the bulk phase by transfer of momentum and depending on the viscosities of the two phases the induced convective motion can be different in the two phases.
There are two main reasons for the creation of surface tension inhomogeneities at the surface. One is due to the temperature dependency of the surface tension and the other one is due to the dependency of the surface tension on the chemical composition of the interface.

A change in the surface tension can be induced by temperature changes of the surface or by the presence of other substances on the surface. A Marangoni effect that is induced by temperature gradients is referred to as ***thermo-capillary Marangoni effect***, while a Marangoni effect that is induced by the non-homogeneous chemical composition of the surface is referred to as ***soluto-capillary Marangoni effect***.

1.3.1. Tears of Wine and Rayleigh-Plateau Instability

The tears of wine is a well known phenomenon which is the continuous formation of liquid droplets, that fall along the wall of a wine glass.The phenomenon is known since ancient times and is mentioned even in the bible[8]. J. Thomson [23] identified the driving force for the upward flow necessary for the formation of the liquid droplets as a gradient in surface tension. Later it was described by Marangoni [22].

The phenomenon is a consequence of the evaporation of alcohol, which has a lower surface tension and a lower boiling point than water which leads to Marangoni flows and a Rayleigh-Plateau-like instability [24] that leads to the formation of the droplets, which are sliding down the wall.
In the following we shall look in detail at the related mechanism.

At the wall of a glass filled with wine, adhesive forces induce the liquid to climb slightly on the glass wall of the glass to form a meniscus. Alcohol and water evaporate from the surface (Fig. 1.12, (A)), but due to its lower boiling point alcohol evaporates faster, changing the water/ethanol composition at the surface. This and also the decrease in surface temperature due to evaporation [25] result in an increase of the surface tension which induces Marangoni flows and more liquid is drawn up the wall from the bulk of the wine (Fig. 1.12, (B)).
At a certain point the accumulated liquid forms a rim (Fig. 1.12, (C)) which gets unstable and undulates and under the influence of gravity droplets are formed which are sliding down the wall of the glass (see Fig. 1.12 (D) and (E)). The formation of the droplets is assumed to follow a Rayleigh-Plateau like instability, which will be discussed in detail in chapter 4.

[8] "*Do not gaze at wine when it is red, when it sparkles in the cup, when it goes down smoothly*" (Proverbs 23:31)

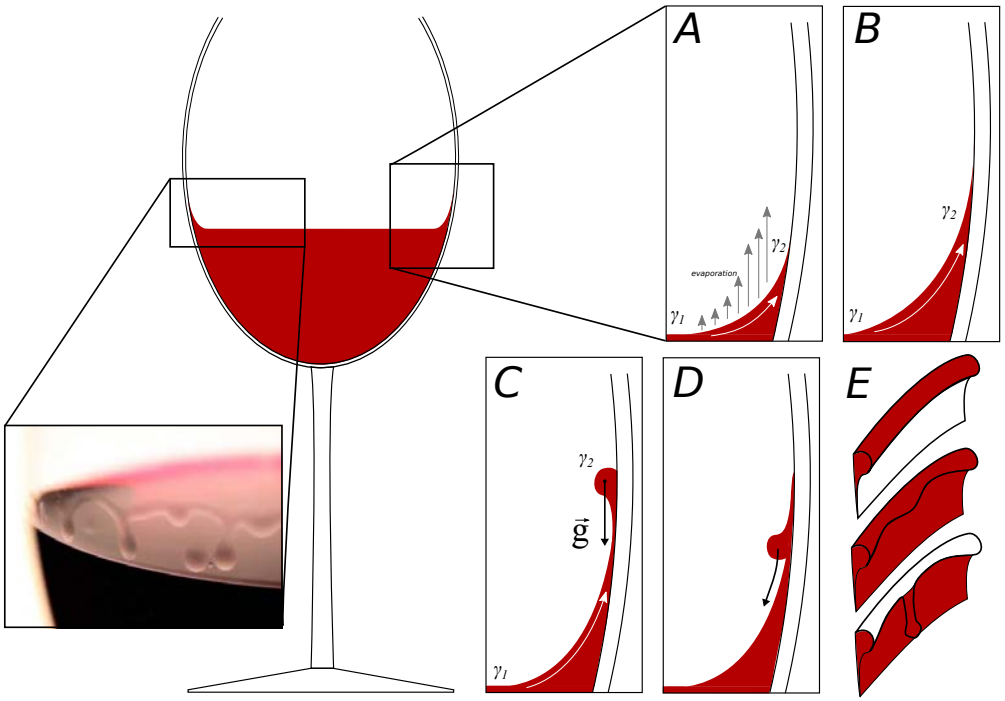

Figure 1.12: *The tears of wine. A/B: Marangoni-induced flow which leads to a rise along the glass wall. C: At a certain point at the top a rim is formed, which gets unstable. D: From the rim droplets are created which are gliding down the glass wall. E: Three-dimensional illustration of the formation of the "tears" of wine from the formed rim.*

1.4. Motion of Objects on Solid and Liquid Surfaces

There are many systems in the literature in which a drop or a solid moves on a solid or a liquid surface. The motivation of doing research on these systems are diverse: From mimicking the behavior of biological systems to systems which are manufactured in order to achieve a special task as transport, surface cleaning or energy transduction.
In general two main types of motions can be differentiated:

- Motion that is driven by the asymmetry of the interfacial tension surrounding an object on a solid surface or a liquid surface, where there is none or only little Marangoni-induced convection, which we call in the following ***capillary-driven motion*** and
- motion that is mainly driven by Marangoni-induced convections, which we call in the following ***convection-driven motion***.

There are many different ways to create a surface tension gradient on solid or liquid subphases. We will discuss here motion of drops on pre-prepared solid surfaces, that move due to the induced

surface tension gradient or that move autonomously by modifying the surface itself. On liquid subphases, we will discuss the motion of solids, gels and drops.

1.4.1. Capillary-Driven Motion

The motion of solid or liquid objects like solid scraps, specially manufactured boats or drops on surfaces can be achieved by surface tension differences between the back and the front of the object. Due to this difference a driving force proportional to the difference in surface tension, i.e. $F_{drive} \sim \gamma_2 - \gamma_1$, will lead to the motion of the object in the direction of higher surface tension[9].
Since the surface tension is depending on temperature and chemical composition of the substrate this difference in surface tension can be achieved by creating gradients of temperature or chemical composition on solid or liquid surfaces (schematically illustrated in Fig. 1.13).

1.4.1.1. Motion on a Solid Subphase

The motion of drops on solids under a horizontal temperature gradient is known for a long time [26]. One of the first who theoretically investigated this phenomenon was Brochard, who also considered the motion induced by pre-treated surfaces to obtain a chemical gradient [27]. Brzoska et al. [28] experimentally investigated the motion induced by a temperature gradient on hydrophobic surfaces. Chaudhury and Whitesides [29] were able to make microliter drops of water run uphill an inclined plane of 15°. To obtain this behavior a gradient of hydrophobicity was created by diffusing a vapor of decyltrichlorosilane on a silicon wafer.

There is also the possibility that the motion itself modifies the surface and creates a self-induced autonomous motion of the drop.

[9] Assuming a surface tension variation along the triple contact line a driving force in direction of the higher surface tension is obtained . The total force is given by

$$\vec{F} = \int_0^{2\pi} \vec{\gamma}(\theta) d\theta, \tag{1.20}$$

where we will assume a symmetric distribution of surface tension between the two sides of the circular object and therefore $\vec{\gamma}(\theta)$ shall be

$$\vec{\gamma}(\theta) = \gamma_1 + (\gamma_2 - \gamma_1)\cos\theta \ \vec{e}_r, \tag{1.21}$$

with $\vec{e}_r = (\cos\theta, \sin\theta)$ (see Fig. 1.13 (A)).
Calculating the forces in x- and y-direction, leads to

$$F_x = \int_0^{2\pi} [\gamma_1 + (\gamma_2 - \gamma_1)\cos\theta]\cos\theta d\theta = \pi(\gamma_2 - \gamma_1) \tag{1.22}$$

$$F_y = \int_0^{2\pi} [\gamma_1 + (\gamma_2 - \gamma_1)\cos\theta]\sin\theta d\theta = 0 \tag{1.23}$$

so there is an effective driving force of magnitude $\pi(\gamma_2 - \gamma_1)$ in the positive x-direction.

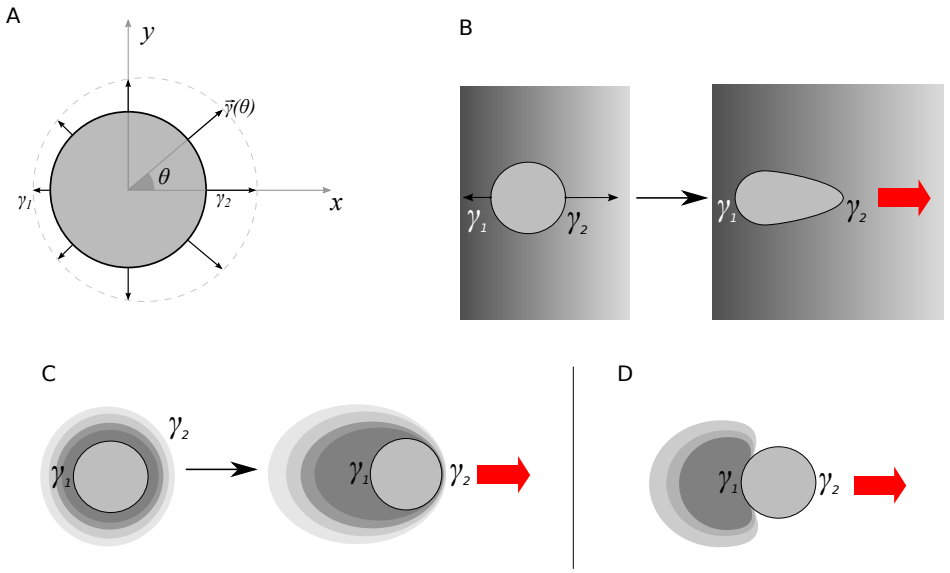

Figure 1.13: *Schemes of capillary-induced motion of objects on solid and liquid surfaces ($\gamma_2 > \gamma_1$). A: Surface tension gradient along the triple contact line. B: Motion of a drop on a solid surface presenting a surface tension gradient. C: Motion of a drop on a liquid surface induced by a low surface tension film that is formed around by its dissolution. Motion is spontaneously obtained if symmetry is broken. D: Motion of an object on a liquid surface that is induced by the deposition of a low surface tension substance on the surface.*

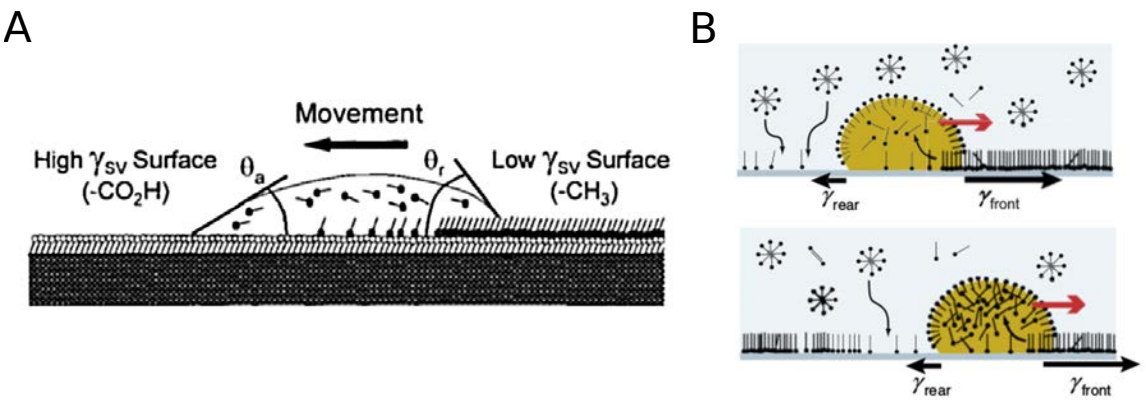

Figure 1.14: *Drops on solid surfaces. A: Schematic cross section of a decahydronaphthalene drop on a pre-prepared solid surface (Figure taken from [30]). B: Schematic cross section of an organic drop which moves by dissolving STA+ ions adsorbed to the glass surface (Figure taken from [31]).*

An autonomously moving droplet was created by Domingues Dos Santos and Ondarçuhu [32] by putting a hydrophobic agent (1H,1H,2H,2H-perfluorodecyltriethoxysilane) inside n-alcane droplets

that left a dense grafted monolayer on a glass surface as it moved. The motion was initiated by gently pushing the drop. The movement continued autonomously due to the creation of a hydrophobic monolayer at the backside of the drop that led to the surface tension difference. The drop was moving autonomously as long as there was glass surface available. Lee and Laibinis [30] are following a similar idea. They prepared a surface of low surface tension (-CHO_3) in which they engraved a track of high surface tension (-CO_2H) in which a solvent drop (decahydronaphthalene (DHN)) containing alkylamine was deposited. The drop started spontaneously to move by creating a layer of alkylamine behind it, which has a lower surface tension and which led to the surface tension difference necessary to its motion (see scheme (A) in Fig. 1.14).

Another moving drop was investigated by Sumino et al. [31]. There, a glass slide was put in an aqueous phase of stearyl trimethyl ammonium chloride (STAC) on which STA+ ions got adsorbed. An organic drop containing an iodine solution of nitrobenzene saturated with potassium iodide was placed on the glass surface. The STA+ ions adsorbed to the glass surface were reacting in the oil drop to form STA-I, with the iodide ions created from the iodine present in the drop. This hydrophobic compound was dissolving in the oil drop, which left a clean surface with a lower surface tension behind it that maintained the difference in surface tension between the head and the tail necessary for its motion (see scheme (B) in Fig. 1.14).

Motion of drops on solid surfaces can also be induced by external stimulus. Ichimura et al. [33] investigated a drop of olive oil that was moving on a solid surface covered by a photoisomerizable monolayer due to irradiation. Irradiating the surface with UV light started the isomerization process and made the surface hydrophilic while irradiating the surface with blue light had the opposite effect. The light-guided movement of the drop was realized by a spatially controlled irradiation to generate a gradient in the level of photoisomerization on the surface, which created the surface tension gradient necessary for the motion of the drop. By moving the light-beam the drop could be moved along the surface.
A similar approach with a low-volatile drop (like diiodomethane) on a photo-modifiable surface was investigated by Berna et al. [34]. A glass or mica surface was covered with gold on which rotaxane molecules were physisorbed, which turned the surface hydrophobic. Irradiation with UV light changed the configuration of the rotaxane molecules and turned the surface more hydrophobic. Asymmetric irradiation of the drop on the surface led to its motion in direction of the irradiation. The drop could also run uphill an inclined surface of 12° in this way.

1.4.1.2. Motion on a Liquid Subphase

On liquid surfaces one of the most studied autonomously moving object is the famous "camphor disk" (or camphor scrapping). The first explanation of its movements dates back to 1890 and was

given by Van de Mensbrugghe [35]. Lord Rayleigh [36] studied the effect of grease on the water surface on the self motion of the camphor scrapping.

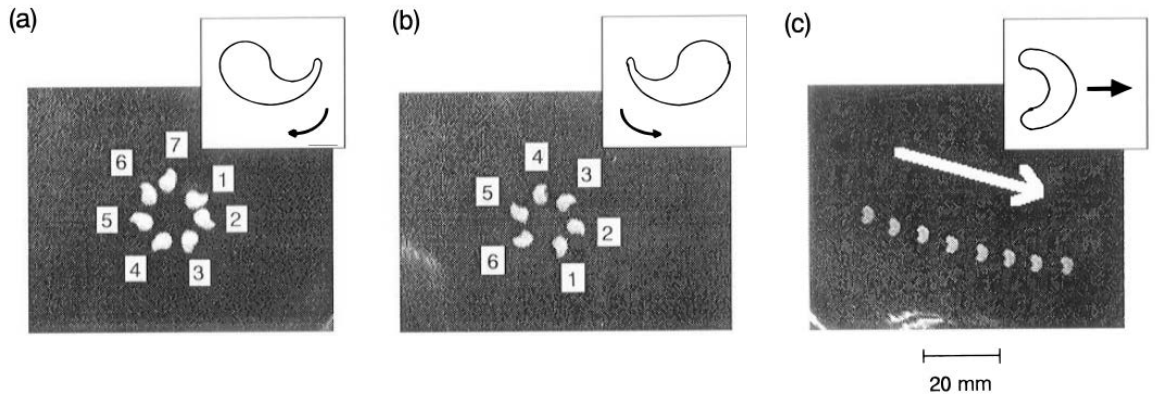

Figure 1.15: *Camphor systems on liquid surfaces. A: Motion of camphor scrappings with different geometries that lead to different kind of motions (Figure taken from [37]).*

The group of Nakata is investigating this system since the 90s exploring many different aspects of its motion [37, 38, 39, 40, 41, 42, 43, 44].

The motion of camphor arises from the film of dissolved camphor that decreases the surface tension around the disk. If the symmetry is broken, motion is induced towards the "clean" surface (like schematically illustrated in Fig. 1.13 (C)). Motion is maintained by the sublimation of the camphor, that restores the surface. By choosing special shapes of the camphor scrapping the random motion can be transformed into directional-controlled motion like rotation or translation. U-like shaped scraps lead to translational motion, while comma-like scraps lead to rotation (see Fig. 1.15). This is due to the fact that in concave regions of the scrap dissolving camphor will accumulate more than in convex regions. The concentration of camphor will be higher in concave regions lowering the surface tension more there than in convex regions. The corresponding difference in surface tension is again at the origin of motion.
Recently, the competition between convection and capillary induced motion was also investigated [38]. The system consisted of two geometries: a camphor disk and a camphor boat, i.e. a plastic plate on which on one side a piece of camphor was attached. The convections induced by the Marangoni flows had an inhibiting effect on the motion for the camphor boat (see Fig. 1.15 (B) (b), left column) while an inverse picture was found for the camphor disk where the convections induced by the Marangoni flows were amplifying the effect of capillarity and therefore the motion (see Fig. 1.15 (B) (b), right column). In both cases the depths of the container increased the magnitude of the con-

vection and therefore the importance of the convection induced part of the motion.
Another similar system is the movement of aspirin crystals studied by Bansagi et al. [45]. Aspirin crystals of around 1 mm are placed on the water surface and start to move in regular circular and circular ellipsoidal motion. As the crystals slowly dissolve and hydrolyze the surface tension is lowered locally. Additionally due to the difference in hydrophilicity of the facets of the crystal the surface surrounding the crystals is deformed asymmetrically. These two effects collaborate to the observed motion.

In the same category falls the autonomous motion of solid objects which release substances that decrease the surface-tension. Nakata et al. [42] has investigated the motion of a sodium oleate (soap) disk at an oil-water interface which was maintained by the release of oleate molecules. The motion of a capsule motor (polysulfone(PSf)-N,N'-dimethylformamide(DMF)) at the surface of an oil film on water was investigated by Zhao and Pumera [46], where the motion was induced due to the release of DMF from the very small pores of the solidified Psf capsule. Recently, Liu et al. [47] investigated a spindle-like "micro-motor" of around 10 μm of polycaprolactone containing an anionic surfactant (sodium 1-dodecanesulfonate) that was released to the water surface to obtain motion .

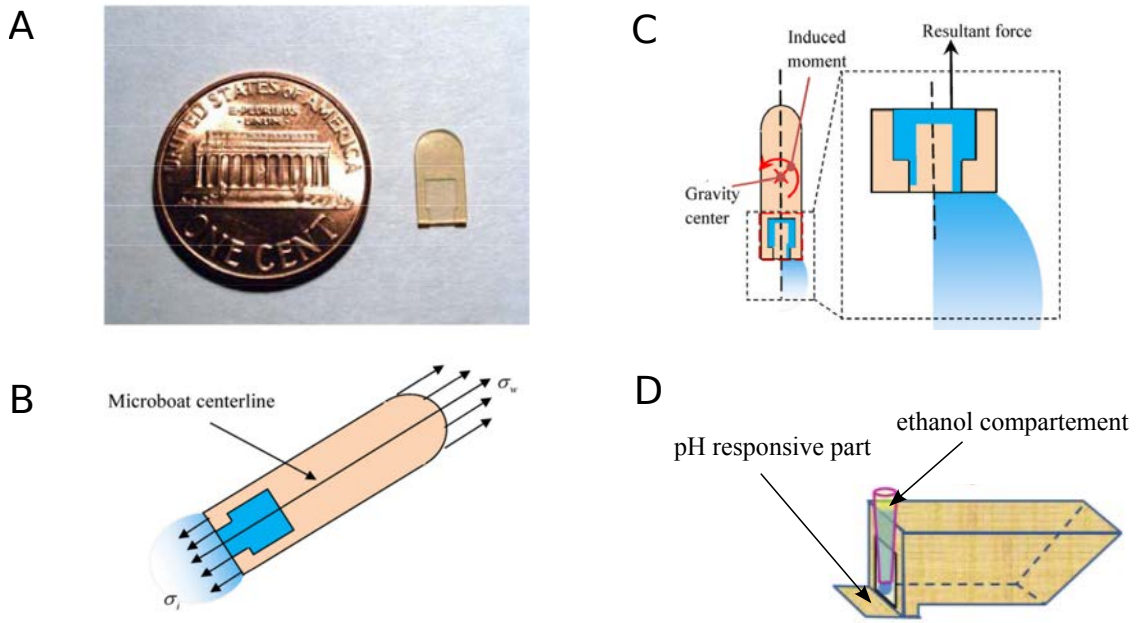

Figure 1.16: *Milli- to centimeter-sized boats that move on liquid surfaces by expelling different solvents. A: Image of the SU-8 boat. B: Scheme of a SU-8 microboat showing the fuel compartment (Figure taken from [48]) and a modified SU-8 microboat to allow rotational motion (Figure taken from [49]). C: Boat that mimics the locomotion of the beetle of genus stenus (Figure taken from [50]).*

There exists also the category of millimeter- to centimeter-sized manufactured boats that move autonomously on liquid surfaces and can also act as transport vehicles. Here the difference in surface tension surrounding the boat is obtained by the expulsion of a solvent having a lower surface tension than the surrounding liquid (see scheme (B) in Fig. 1.16) .
Qiao et al. [49] investigated the motion of an SU-8 microboat[10] that uses isopropyl alcohol (IPA) for propulsion (see Fig. 1.16 (A) to (C)).
Jin et al. [51] also use a centimeter-sized boat but the "fuel" is now provided by the vapor of volatile liquids like ethanol that is released to the surface where it reduces the surface tension.
Xiao et al. [50] investigated a similar system where they used ethanol as propellant. The originality of the system lays in the fact that their boat is mimicking the locomotion of the beetle of genus stenus. This beetle moves on the surface of water by emitting pygidial gland secretions that reduce surface tension in response to exteral stimuli [52]. To mimic the response to external stimuli they added a pH responsive part that controlled the release of ethanol. This part was a specially prepared surface that changed from superhydrophobicity to superhydrophilicity depending on the pH (see Fig. 1.16 (D)).

Solids or amorphous solids are not the only one to move autonomously on liquid surfaces, there are also the category of gels that release a propellant that can move autonomously: A gel that released an organic solvent (alcohol or tetrahydrofuran) was investigated by Mitsumata et al. [53], [54], a PNIPAm gel soaked in ethanol on water was investigated by Bassik et al. [55] or the movement of a gel-based particle (ethanol-infused polyacrylamide hydrogel incorporated in a plastic tubing with one end closed) was investigated by Sharma et al. [56].
The last and most important category for us concerns drops that move and deform autonomously on liquid surfaces.

Nagai et al. [57] investigated the spontaneous motion of an alcohol droplet (pentanol) where the motion is attributed to the asymmetry that arises due to the deformation of the droplet. The dissolution of the pentanol lowers the surface tension around the droplet and give rise to a surface tension gradient. When the droplet volume was small (0.017 µL) the droplet was moving in an irregular manner, while for bigger drops (10 µL) a directed translational motion was observed. On such a drop a shape deformation is induced, which leads to a U-shaped drop (Fig. 1.17 (B)), similar to the shape of the U-shaped camphor scrap of Nakata [37] . The induced broken symmetry leads to the motion of the drop, like in the case of the camphor scrap. For large enough droplets the forces exerting on the droplet can also lead to its fission into many smaller droplets. The motion of the drop is attributed to an instability of the triple contact line that arises due to a solutal Marangoni effect. The dissolution and evaporation rate of the pentanol are important parameters for the transition from irregular to regular translational motion.

[10]SU-8 is a commonly used epoxy-based negative photo-resist

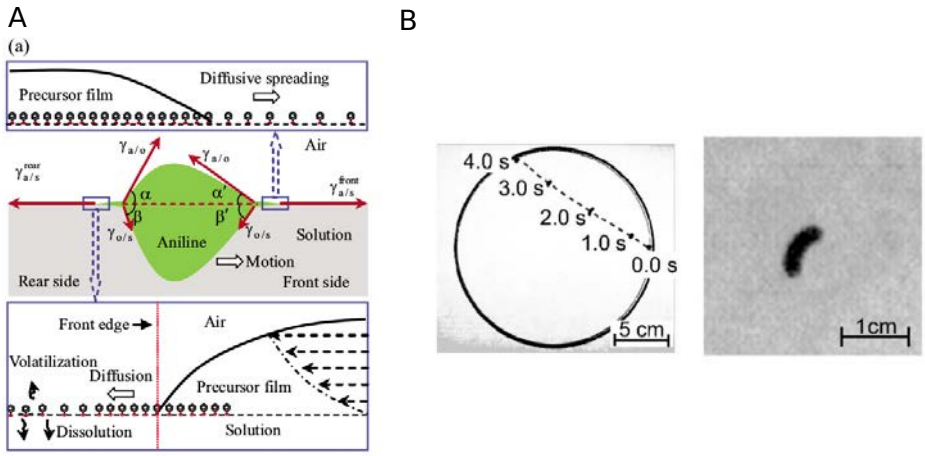

Figure 1.17: *Drops on liquid surfaces. A: Autonomous motion of an aniline drop. a) Schematic side view with details on the mechanism of motion. B: pentanol droplet moving autonomously on an aqueous solution; left: directed translational motion for a drop of 10 µL, right: top view of the U-shaped pentanol drop (Figure taken from [57]).*

Another very interesting system is an aniline drop on an aqueous aniline solution which was investigated by Chen et al. [58]. The drop shows two kinds of motion: beeline motion and circular motion. The first one is obtained for a drop deposited at the center of the subphase. However, this linear motion finally switches to circular motion to avoid repeated collision with the wall. In that regime motion has been maintained for hours. Evaporation and solubilization are relatively slow and the drop appears as a macroscopic drop coexisting with a surrounding precursor film. Motility was again ascribed to a surface tension imbalance at the front and rear of the drop. This difference, revealed by a difference in contact angle, was attributed to the precursor film and more precisely to the effect of fluid flow of the solution passing the drop. Driven by a Marangoni flow, the film may lose its initial symmetry. The initiated translation is then sustained by the distortion of the surface active film pointing to the rear of the drop. For small enough concentrations of aniline in the aqueous solution irregular motion is observed that can be attributed to the instability of the contact line, like it is the case in the pentanol drop discussed above.

1.4.2. Convection-Driven Motion

As described above the Marangoni effect can also induce convective flows in the bulk phase. For a drop this can induce convective motion inside the drop and in the surroundings of the drop. Depending on the viscosities and the importance of the convective motion this can lead to the motion of the object itself. In contrast to the capillary-driven motion where the objects are moving always in direction of higher surface tension here the induced convections can lead also to a motion in the direction of lower surface tension (see schemes in Fig. 1.18).

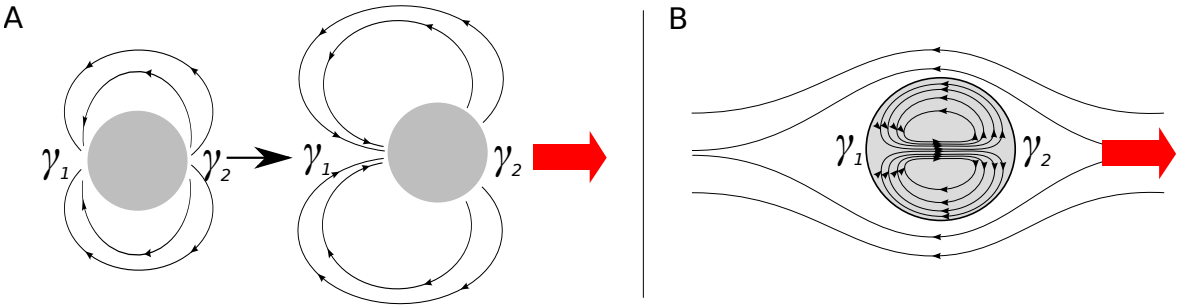

Figure 1.18: *Convection induced motion ($\gamma_1 > \gamma_2$). A: Convection induced motion around a solid object. B: Convections induced inside and surrounding a drop that induces its motion.*

Takabatak et al. [59] investigated a composite solid/liquid system, where an oleic acid drop was attached to a solid sodium oleate piece and placed on a water phase (see scheme in Fig. 1.19 (A)). The solid piece acted as a surfactant-supply that decreased locally the surface tension surrounding it, which induced Marangoni flows at the interface. As a result convective flows were induced around and inside the drop, which led to the motion of the drop. Self-motion in this system was obtained for minutes while motion also occurred in the non-composite system (i.e. the drop of oleic acid alone) for some seconds. Observed motions are translational motion and circular motion. The type of motion was controlled by the size of the solid column, while translational motion was obtained for bigger sizes of the soap piece. These observations were also confirmed theoretically by Nagai et al. [60] where they showed that the two different types of motion occur due to a competition between convection flows and diffusion of the surfactant.

1.4.2.1. Motion Induced by an External Energy Source

Motion can also be induced by irradiation with light, as it is the case for drops on solid surfaces. An otherwise not moving drop can be brought into motion by irradiation with laser light which was investigated by Ichikawa et al. [61]. The irradiation with a a green laser light source (532 nm), that acts here as a local heat source can induce attractive and repulsive motion of a droplet of fluid paraffin on a sodium dodecyl sulfate (SDS) solution (see Fig. 1.19 (B)). The scrolling flows inside the droplet were induced by the direct irradiation and lead to a photophilic motion (i.e. a motion towards the irradiation zone) on a SDS solution while the same irradiation lead to a photophobic motion (i.e. a motion away from the irradiation zone) on pure water. This is is the result of the competition of the flows induced around the drop and inside the drop. Heating a spot on the surface of the drop induces a temperature gradient in the surrounding liquid and induced convective flows inside and outside the drop. Since the surface tension dependency on the temperature of an SDS solution is decreasing with increasing concentration of SDS the flows induced in the surrounding are getting

less and less important with the increase of the concentration of SDS, which explains why only the internal convective motions determine its motion.

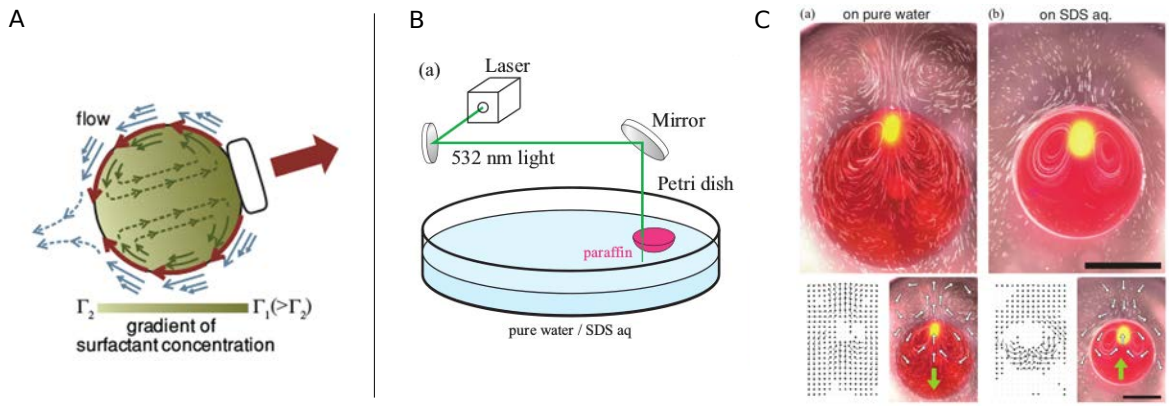

Figure 1.19: *Drops on liquid sufaces. A: Self-Motion of a liquid/solid composite system. Scheme of the induced flows that lead to its motion (Figure taken from [59]). B/C: Laser induced motion of a drop of fluid paraffin on a sodium dodecyl sulfate (SDS) solution (Figure taken from [61]). B: Scheme of the setup. C: Top and side view of the colored paraffin drop on water and SDS. B: Flow field inside and outside the drop visualized with tracer particles. a) Droplet on pure water. b) Droplet on SDS solution.*

Motion of droplets can also be induced by irradiating photoactive sub-millimeter sized droplets in an oleic acid solution with UV light [62]. The movement is now induced by a photoreaction which creates surfactants at the irradiated side of the drop and therefore lowers the surface tension there. This then induces Marangoni flows at the surface of the droplet which leads to its movement towards the light source. This kind of photo-manipulation was also used in Diguet et al. to move millimeter-sized oil droplets containing AzoTAB, a photoactive surfactant [63]. Irradiated with UV light, the photoactive surfactant transforms into its cis form (cis-AzoTAB) which has lower surface activity than the trans form. Irradiating one side of the drop with UV light leads to a motion away form the irradiation source while irradiating with visible light leads to the contrary. In both systems described here induced internal convective flows lead to the movement of the droplets.

1.4.2.2. Motion induced by an External Chemical Source

Drops can also move on liquid surfaces if they are placed on a non-homogeneous liquid bulk phase. Creating a pH gradient or any gradient of chemical species in a solution can induce such a non-homogeneous liquid bulk phase. This method is used for example to move polymer hydrogels (Wang et al. [64]) or drops (Lagzi et al. [65]) across mazes. As in the other systems discussed above motion is created by convective flows which are induced due to interfacial tension gradients.

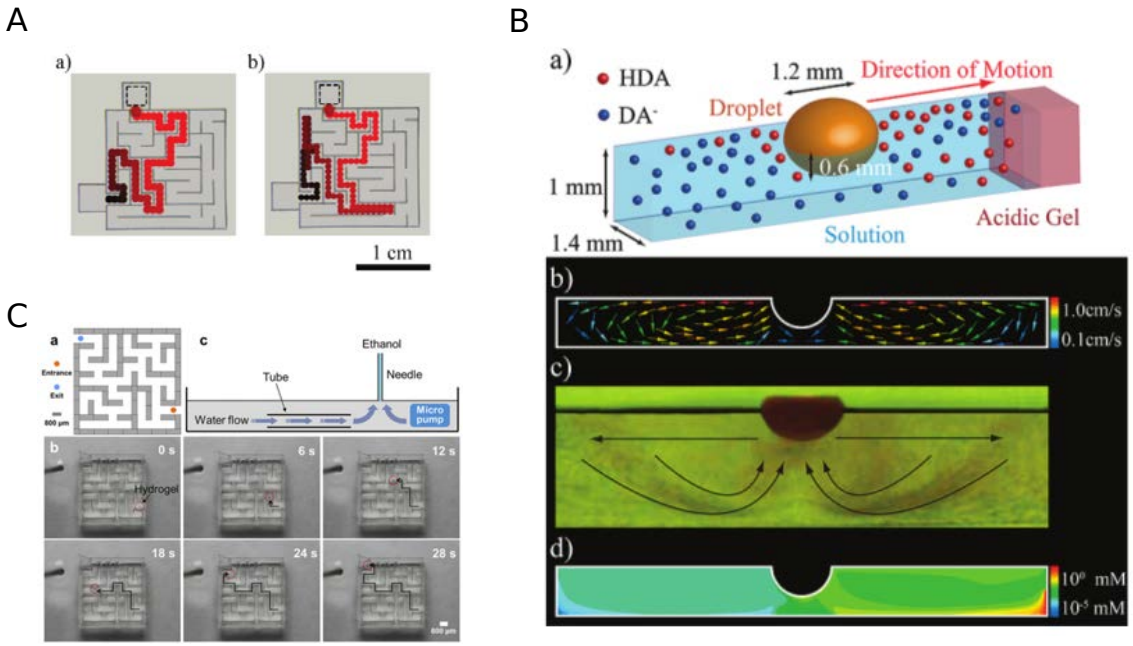

Figure 1.20: *A: Maze solving by chemotactic droplets (two different outcomes of the same experiment; Figure taken from [65]). B: Scheme and sideview showing the convective flows of the maze solving chemotactic droplet (Figure taken from [65]). C: Polymer hydrogel solving a microfluidic maze (Figure taken from [64]).*

In the first example by Wang et al. [64], motion is induced by Marangoni driven spreading, where the source is far away from the spherical alginate hydrogel which is submerged in the water layer. When ethanol is dropped on water at some distance from the gel, ethanol spreads on the surface in an outward radial direction, the vacancy created at the injection point induces an upward flow and both result in the formation of a toroidal convective cell. The submerged hydrogel is dragged along by the flow on its way back in direction of the source. Moving the position of the injection point is an easy way to control the trajectory of the gel. The gel can also find the path to walk through a microfluidic maze when a fixed source is placed at the exit. Maze solving was also achieved, this time for floating drops, by Lagzi et al. [65]. A drop of a non-water soluble oil containing a weak acid was placed away from a fixed source of a strong acid (HCl). The weak acid which is surface active spreads around the drop where it gets partially deprotonated to a less surface active form. However, on the side of the HCl source, deprotonation is limited, giving rise to a steeper surface tension gradient. Convective rolls have been observed on each side of the drop but the spatial surface tension asymmetry results in a higher velocity of the roll facing the HCl source and so to the displacement of the drop in the same direction.

1.5. Pulsating Drops on Liquid Surfaces

Pulsating drops are very rare in the literature. One of the few examples known is the oscillating mineral oil drop containing a non-ionic, non-water soluble surfactant placed on water by Stocker and Bush [66]. The pulsations last for minutes but are not very regular (see Fig. 1.21). They are generated by the decrease of the oil/water surface tension due to adsorption of surfactants and an increase of the air/water surface tension due to evaporation of surfactants. This leads to a positive spreading parameter that induces an expansion of the drop (Fig. 1.21 II(a)). Subsequent partial emulsification at the lens edge due to surfactant accumulation lead to an decrease of the air/water interfacial tension which causes the lens to retract (Fig. 1.21 II(b)). This behavior was sustained by the continuous evaporation and adsorption of the surfactants which led to the periodic change in the radius of the drop (see Fig. 1.22(a)).

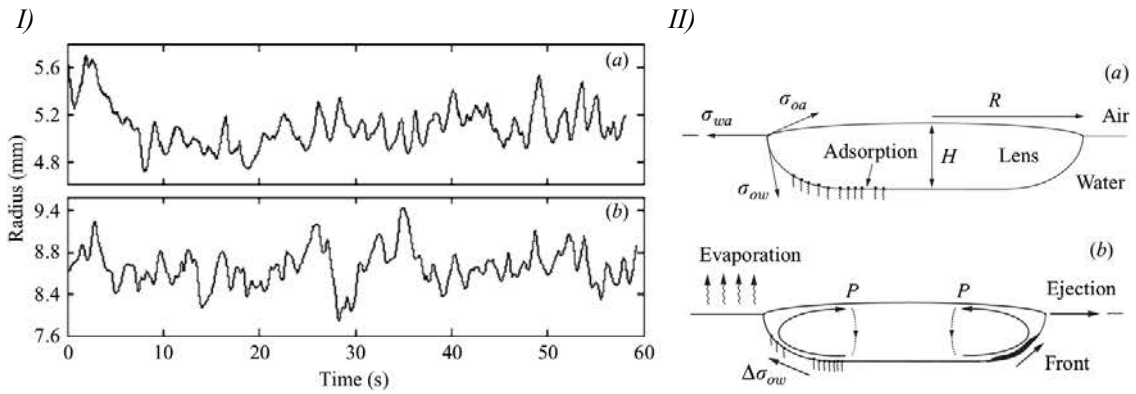

Figure 1.21: *A pulsating drop mineral oil containing a non-ionic, non-water soluble surfactant (taken from [66]). I: (a) Pulsations of a 25 µm drop. (b) Pulsations of a 100 µL drop. II: Supposed mechanisms. a: Adsorption at the oil/water interface. b: Partial emulsification at the lens edge due to surfactant accumulation and surfactant evapororation.*

The pulsations were modeled by Karapetsas et al. [67], where the theoretical results suggest a spreading exponent close to one. Another example of a pulsating drop was investigated by Bates et al. [68]. A pulsating regime of a very short life time that gave rise to the ejection of a ring of droplets for a 1-butanol drop cooled to 1 °C deposited on a 40 °C water phase was observed (Fig. 1.22 (b)).

The last system to our knowledge that performs periodic pulsations is an immiscible, surface-active liquid droplet on thin liquid films of higher surface tension investigated by Sinz et al. [69]. Periodic pulsations of a surfactant drop are observed on a 780 µm thick glycerol film. Nevertheless the amplitude of these pulsations are very small (in the range of 20 um, i.e. 3% of the radius of the droplet).

There is also a system with only one pulsation that was investigated by van Nierop et al. [21]. A heavy mineral oil drop of 0.1 µL containing oleic acid was placed on a sodium hydroxide solution.

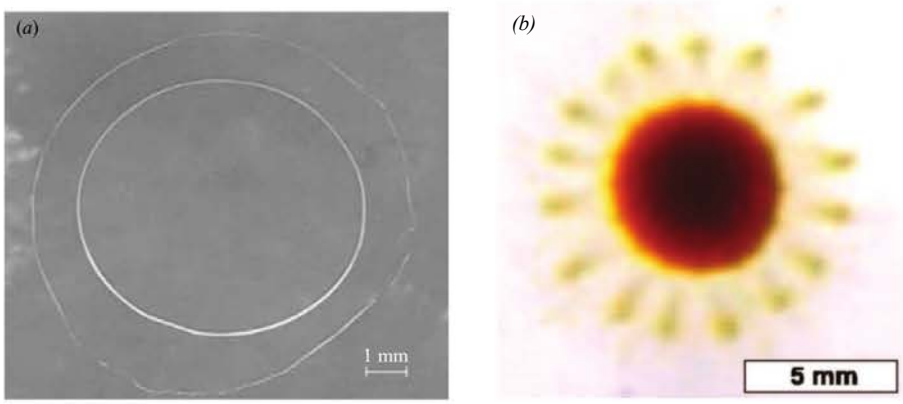

Figure 1.22: *Pulsating drops. a: A pulsating drop mineral oil containing a non-ionic, non-water soluble surfactant (taken from [66]). b: A 1-butanol drop cooled to 1 °C deposited on a 40 °C water phase (taken from [68]).*

In this system expansion with rim formation and subsequent retraction was observed. The expansion is due to the decrease of the oil/water interfacial tension as a result of a saponification reaction (sodium oleate is produced), while the recoil of the drop is due to the fact that diffusion overcomes the rate of surfactant production.

These systems show one or more aspects we also observe in the pulsating regime in the system under investigation in this work, which will be discussed in chapter 4 and 5 in detail.

1.6. Conclusion

In this chapter we have focused on the basics of capillarity including the Young and Neumann equations for the equilibria of liquid drops on solid and liquid surfaces, the concept of the spreading parameter and the pseudo-partial wetting case, where a drop is in equilibrium with a thin film surrounding it.
The Marangoni effect, which is at the origin of motion of liquid or solid objects on liquid surfaces, was another topic deepened in this chapter. As illustrative example we discussed the phenomenon of "tears of wine", which is the result of the Marangoni effect combined with a Rayleigh-Plateau instability.
The second part of the chapter was devoted to the different systems that move on solid and liquid surfaces with the focus on drops on liquid surfaces. We distinguished two types of motion, the capillary driven motion, that arises due to surface tension differences at the two sides of the object and the convection driven motion.
The interests in such systems have different origins. They range from mimicking the behavior of bi-

ological systems to systems, which are manufactured in order to achieve a special task as transport, surface cleaning or energy transduction.

Bibliography

1. P.-G. de Gennes, F. Brochard-Wyart, and D. Quéré, *Capillarity and Wetting Phenomena: Drops, Bubbles, Pearls, Waves*. Springer New York, 2004.

2. A. W. Adamson and A. P. Gast, *Physical Chemistry of Surfaces*. John Wiley & Sons, Inc., 1997.

3. F. Brochard-Wyart, J. Di Meglio, D. Quéré, and P. de Gennes, "Spreading of nonvolatile liquids in a continuum picture," *Langmuir*, vol. 7, no. 2, pp. 335–338, 1991.

4. J. Sebilleau, "Equilibrium thickness of large liquid lenses spreading over another liquid surface," *Langmuir*, vol. 29, no. 39, pp. 12118–12128, 2013.

5. D. Bonn, J. Eggers, J. Indekeu, J. Meunier, and E. Rolley, "Wetting and spreading," *Rev. Mod. Phys.*, vol. 81, pp. 739–805, May 2009.

6. P.-S. de Laplace, *Traité de Mécanique Céleste. Supplément au dixième livre du Traité de Mécanique Céleste*, vol. volume 4. Paris, France: Courcier, 1805.

7. T. Young, "An essay on the cohesion of fluids," *Philosophical Transactions of the Royal Society of London*, vol. 95, pp. 65–87., 1805.

8. A. Theberge, F. Courtois, Y. Schaerli, M. Fischlechner, C. Abell, F. Hollfelder, and W. Huck, "Microdroplets in microfluidics: An evolving platform for discoveries in chemistry and biology," *Angewandte Chemie International Edition*, vol. 49, no. 34, pp. 5846–5868, 2010.

9. J. Zanghellini, F. Wodlei, and H. von Grünberg, "Phospholipid demixing and the birth of a lipid droplet," *Journal of Theoretical Biology*, vol. 264, no. 3, pp. 952 – 961, 2010.

10. S. D. Hoath, ed., *Fundamentals of Inkjet Printing: The Science of Inkjet and Droplets*. Wiley-VCH, 2016.

11. K. Uno, K. Hayashi, T. Hayashi, K. Ito, and H. Kitano, "Particle adsorption in evaporating droplets of polymer latex dispersions on hydrophilic and hydrophobic surfaces," *Colloid and Polymer Science*, vol. 276, no. 9, pp. 810–815, 1998.

12. K. Sefiane, "Patterns from drying drops," *Advances in Colloid and Interface Science*, vol. 206, pp. 372 – 381, 2014.

13. J. N. Israelachvili, *Intermolecular and Surface Forces*. Academic Press, 2011.

14. Fay, *Oil on the sea*, ch. The Spread of Oil Slicks on a Calm Sea, p. 53. Department of Naval Architecture and Marine Engineering Massachusetts Institute of Technology, 1969.

15. D. P. Hoult and W. Suchon, *The spread of oil in a channel*. Massachusetts Institute of Technology, Dept. of Mechanical Engineering, 1970.

16. J. A. Fay, "Physical processes in the spread of oil on a water surface," *International Oil Spill Conference Proceedings*, vol. 1971, no. 1, pp. 463–467, 1971.

17. D. P. Hoult, "Oil spreading on the sea," *Annual Review of Fluid Mechanics*, vol. 4, no. 1, pp. 341–368, 1972.

18. N. D. Dipietro, C. Huh, and R. G. Cox, "The hydrodynamics of the spreading of one liquid on the surface of another," *Journal of Fluid Mechanics*, vol. 84, no. 3, pp. 529–549, 1978.

19. A. D. Dussaud and S. M. Troian, "Dynamics of spontaneous spreading with evaporation on a deep fluid layer," *Physics of Fluids*, vol. 10, no. 1, pp. 23–38, 1998.

20. M. Santiago-Rosanne, M. Vignes-Adler, and M. G. Velarde, "On the spreading of partially miscible liquids," *Journal of Colloid and Interface Science*, vol. 234, no. 2, pp. 375 – 383, 2001.

21. E. A. van Nierop, A. Ajdari, and H. A. Stone, "Reactive spreading and recoil of oil on water," *Physics of Fluids*, vol. 18, no. 3, p. 038105, 2006.

22. C. Marangoni, "Ueber die ausbreitung der tropfen einer flüssigkeit auf der oberfläche einer anderen," *Annalen der Physik*, vol. 219, no. 7, pp. 337–354, 1871.

23. J. Thomson, "On certain curious motions observable at the surfaces of wine and other alcoholic liquors," *Philosophical Magazine Series 4*, vol. Volume 10, Issue 67, 1855.

24. J. W. Strutt (Lord Rayleigh), "On the instability of jets," *Proceedings of the London mathematical society*, vol. 10, pp. 4–13, 1878.

25. D. C. Venerus and D. Nieto Simavilla, "Tears of wine: new insights on an old phenomenon," *Scientific Reports*, vol. 5, pp. 16162 EP –, Nov 2015. Article.

26. H. Bouasse, *Capillarite, phenomenes superficiels*. Delagrave, Paris, 1924.

27. F. Brochard, "Motions of droplets on solid surfaces induced by chemical or thermal gradients," *Langmuir*, vol. 5, no. 2, pp. 432–438, 1989.

28. J. B. Brzoska, F. Brochard-Wyart, and F. Rondelez, "Motions of droplets on hydrophobic model surfaces induced by thermal gradients," *Langmuir*, vol. 9, no. 8, pp. 2220–2224, 1993.

29. M. K. Chaudhury and G. M. Whitesides, "How to make water run uphill," *Science*, vol. 256, no. 5063, pp. 1539–1541, 1992.

30. S.-W. Lee and P. E. Laibinis, "Directed movement of liquids on patterned surfaces using noncovalent molecular adsorption," *Journal of the American Chemical Society*, vol. 122, no. 22, pp. 5395–5396, 2000.

31. Y. Sumino, H. Kitahata, K. Yoshikawa, M. Nagayama, S.-i. M. Nomura, N. Magome, and Y. Mori, "Chemosensitive running droplet," *Phys. Rev. E*, vol. 72, p. 041603, Oct 2005.

32. F. Domingues Dos Santos and T. Ondarçuhu, "Free-running droplets," *Phys. Rev. Lett.*, vol. 75, pp. 2972–2975, Oct 1995.

33. K. Ichimura, S.-K. Oh, and M. Nakagawa, "Light-driven motion of liquids on a photoresponsive surface," *Science*, vol. 288, no. 5471, pp. 1624–1626, 2000.

34. J. Berna, D. A. Leigh, M. Lubomska, S. M. Mendoza, E. M. Perez, P. Rudolf, G. Teobaldi, and F. Zerbetto, "Macroscopic transport by synthetic molecular machines," *Nat Mater*, vol. 4, pp. 704–710, Sep 2005.

35. V. der Mensbrugghe *Memoires Couronnes (4to) of the Belgian Academy*, 1869.

36. Rayleigh, "Measurements of the amount of oil necessary in order to check the motions of camphor upon water," *Proc. R. Soc. Lond.*, vol. 47, pp. 364–367, 1890.

37. S. Nakata, Y. Iguchi, S. Ose, M. Kuboyama, T. Ishii, and K. Yoshikawa, "Self-rotation of a camphor scraping on water: New insight into the old problem," *Langmuir*, vol. 13, no. 16, pp. 4454–4458, 1997.

38. Y. Matsuda, N. J. Suematsu, H. Kitahata, Y. S. Ikura, and S. Nakata, "Acceleration or deceleration of self-motion by the marangoni effect," *Chemical Physics Letters*, vol. 654, pp. 92 – 96, 2016.

39. S. Nakata and Y. Hayashima, "Spontaneous dancing of a camphor scraping," *J. Chem. Soc., Faraday Trans.*, vol. 94, pp. 3655–3658, 1998.

40. M. I. Kohira, Y. Hayashima, M. Nagayama, and S. Nakata, "Synchronized self-motion of two camphor boats," *Langmuir*, vol. 17, no. 22, pp. 7124–7129, 2001.

41. H. Kitahata, S.-i. Hiromatsu, Y. Doi, S. Nakata, and M. Rafiqul Islam, "Self-motion of a camphor disk coupled with convection," *Phys. Chem. Chem. Phys.*, vol. 6, pp. 2409–2414, 2004.

42. S. Nakata and K. Matsuo, "Characteristic self-motion of a camphor boat sensitive to ester vapor," *Langmuir*, vol. 21, no. 3, pp. 982–984, 2005.

43. N. J. Suematsu, Y. Ikura, M. Nagayama, H. Kitahata, N. Kawagishi, M. Murakami, and S. Nakata, "Mode-switching of the self-motion of a camphor boat depending on the diffusion distance of camphor molecules," *The Journal of Physical Chemistry C*, vol. 114, no. 21, pp. 9876–9882, 2010.

44. S. Nakata, R. Tenno, and Y. S. Ikura, "Mode-selection and mode-switching of an autonomous motor composed of a camphor rotor and a mobile loop," *Chemical Physics Letters*, vol. 514, no. 1-3, pp. 159 – 163, 2011.

45. T. Bansagi, M. M. Wrobel, S. K. Scott, and A. F. Taylor, "Motion and interaction of aspirin crystals at aqueous-air interfaces," *The Journal of Physical Chemistry B*, vol. 117, no. 43, pp. 13572–13577, 2013.

46. G. Zhao and M. Pumera, "Liquid-liquid interface motion of a capsule motor powered by the interlayer marangoni effect," *The Journal of Physical Chemistry B*, vol. 116, no. 35, pp. 10960–10963, 2012.

47. L. Liu, Y. Dong, Y. Sun, M. Liu, Y. Su, H. Zhang, and B. Dong, "Motion-based ph sensing using spindle-like micromotors," *Nano Research*, vol. 9, no. 5, pp. 1310–1318, 2016.

48. C. Luo, H. Li, and X. Liu, "Propulsion of microboats using isopropyl alcohol as a propellant," *Journal of Micromechanics and Microengineering*, vol. 18, no. 6, p. 067002, 2008.

49. L. Qiao, D. Xiao, F. K. Lu, and C. Luo, "Control of the radial motion of a self-propelled microboat through a side rudder," *Sensors and Actuators A: Physical*, vol. 188, pp. 359 – 366, 2012. Selected papers from The 16th International Conference on Solid-State Sensors, Actuators and Microsystems.

50. M. Xiao, M. Cheng, Y. Zhang, and F. Shi, "Combining the Marangoni Effect and the pH-Responsive Superhydrophobicity-Superhydrophilicity Transition to Biomimic the Locomotion Process of the Beetles of Genus Stenus," *Small*, vol. 9, no. 15, pp. 2509–2514, 2013.

51. H. Jin, A. Marmur, O. Ikkala, and R. H. A. Ras, "Vapour-driven marangoni propulsion: continuous, prolonged and tunable motion," *Chem. Sci.*, vol. 3, pp. 2526–2529, 2012.

52. G. Billard and C. Bruylant, "Sur un mode particulier de locomotion de certains stenus," *C. R. Soc. Biol.*, vol. 59, pp. 102–103, 1905.

53. T. Mitsumata, K. Ikeda, J. P. Gong, and Y. Osada, "Controlled motion of solvent-driven gel motor and its application as a generator," *Langmuir*, vol. 16, no. 2, pp. 307–312, 2000.

54. T. Mitsumata, J. P. Gong, and Y. Osada, "Shape memory functions and motility of amphiphilic polymer gels," *Polymers for Advanced Technologies*, vol. 12, no. 1-2, pp. 136–150, 2001.

55. N. Bassik, B. T. Abebe, and D. H. Gracias, "Solvent driven motion of lithographically fabricated gels," *Langmuir*, vol. 24, no. 21, pp. 12158–12163, 2008.

56. R. Sharma, S. T. Chang, and O. D. Velev, "Gel-based self-propelling particles get programmed to dance," *Langmuir*, vol. 28, no. 26, pp. 10128–10135, 2012.

57. K. Nagai, Y. Sumino, H. Kitahata, and K. Yoshikawa, "Mode selection in the spontaneous motion of an alcohol droplet," *Phys. Rev. E*, vol. 71, p. 065301, Jun 2005.

58. Y.-J. Chen, Y. Nagamine, and K. Yoshikawa, "Self-propelled motion of a droplet induced by marangoni-driven spreading," *Phys. Rev. E*, vol. 80, p. 016303, Jul 2009.

59. F. Takabatake, N. Magome, M. Ichikawa, and K. Yoshikawa, "Spontaneous mode-selection in the self-propelled motion of a solid/liquid composite driven by interfacial instability," *The Journal of Chemical Physics*, vol. 134, no. 11, p. 114704, 2011.

60. K. H. Nagai, F. Takabatake, Y. Sumino, H. Kitahata, M. Ichikawa, and N. Yoshinaga, "Rotational motion of a droplet induced by interfacial tension," *Phys. Rev. E*, vol. 87, p. 013009, Jan 2013.

61. M. Ichikawa, F. Takabatake, K. Miura, T. Iwaki, N. Magome, and K. Yoshikawa, "Controlling negative and positive photothermal migration of centimeter-sized droplets," *Phys. Rev. E*, vol. 88, p. 012403, Jul 2013.

62. K. Suzuki and T. Sugawara, "Phototaxis of oil droplets comprising a caged fatty acid tightly linked to internal convection," *ChemPhysChem*, vol. 17, no. 15, pp. 2300–2303, 2016.

63. A. Diguet, R.-M. Guillermic, N. Magome, A. Saint-Jalmes, Y. Chen, K. Yoshikawa, and D. Baigl, "Photomanipulation of a droplet by the chromocapillary effect," *Angewandte Chemie International Edition*, vol. 48, no. 49, pp. 9281–9284, 2009.

64. Y. Wang, X. Liu, X. Li, J. Wu, Y. Long, N. Zhao, and J. Xu, "Directional and path-finding motion of polymer hydrogels driven by liquid mixing," *Langmuir*, vol. 28, no. 31, pp. 11276–11280, 2012.

65. I. Lagzi, S. Soh, P. J. Wesson, K. P. Browne, and B. A. Grzybowski, "Maze solving by chemotactic droplets," *Journal of the American Chemical Society*, vol. 132, no. 4, pp. 1198–1199, 2010.

66. R. Stocker and J. W. M. Bush, "Spontaneous oscillations of a sessile lens," *Journal of Fluid Mechanics*, vol. 583, pp. 465–475, 2007.

67. G. Karapetsas, R. V. Craster, and O. K. Matar, "Surfactant-driven dynamics of liquid lenses," *Physics of Fluids*, vol. 23, no. 12, p. 122106, 2011.

68. C. M. Bates, F. Stevens, S. C. Langford, and J. T. Dickinson, "Motion and dissolution of drops of sparingly soluble alcohols on water," *Langmuir*, vol. 24, no. 14, pp. 7193–7199, 2008.

69. D. K. Sinz, M. Hanyak, and A. A. Darhuber, "Immiscible surfactant droplets on thin liquid films: Spreading dynamics, subphase expulsion and oscillatory instabilities," *Journal of Colloid and Interface Science*, vol. 364, no. 2, pp. 519 – 529, 2011.

2

The Dichloromethane Drop on a Surfactant Solution: General Introduction

知之为知之，不知为不知，是知也。

[*When you know a thing, to hold that you know it and when you do not know a thing, to allow that you do not know it - this is knowledge.*]

Confucius

In this chapter we will introduce our system: its historical origin, the processes at play, an overview of the regimes observed for different concentrations of the surfactants in the aqueous phase, followed by a short description of each regime.

2.1. Historical Origin of the System

The system under investigation in this work originated from an oscillatory system, which is part of oscillatory interfacial phenomena observed in biphasic systems in the presence of surfactants far from the partition equilibrium. This biphasic system consisting of an oil-water system containing CTAB in the aqueous phase shows oscillations of the interfacial tension that can be related to a Marangoni effect at the interface between the two phases.

The first theoretical study aimed to establish criteria predicting Marangoni instability onset during solute mass transfer in biphasic systems was performed by Sternling and Scriven [1] in 1959. They applied a linear stability analysis to systems where a solute is transferred through a non-deformable interface between two semi-infinite liquid layers. The instability can develop in systems far from partition equilibrium and its appearance depends mainly on the solvent properties, the surface activity of the solute and on the formation of critical solute concentration gradients in the normal to the interface direction (Kovalchuk et al. [2]). Unstable transfer is expected when the solute diffuses out of the phase in which its diffusivity is lower and kinematic viscosity is higher.

Dupeyrat and Nakache [3] discovered such solutal Marangoni effect at the interphase of a biphasic system composed of a nitrobenzene layer containing picric acid (PH) on which a cetyl trimethylammonium bromide (CTAB) solution was placed. The two solutes, out of partition equilibrium, travel toward the interface where they meet and react to form a highly hydrophobic ion pair (CTA^+P^-) that dissolves in the organic phase. In their interpretation they already identified the part of the Marangoni effect but also attributed a major contribution to the interfacial reaction.
The study performed in our group confirmed the correlation between the oscillations and the movements arising in the bulk phases close to the interface. A second important result was that the interfacial reaction was not mandatory to observe the oscillations as they were observed in an simpler ternary system composed of dichloromethane (DCM), CTAB and water [4]. CTAB mass transfer and a related hydrodynamic effect was then identified as the key process for these systems [5].
The occurrence of the oscillations can be understood in the following way: under mass transfer, concentration gradients build up in the diffusion layer at the interface [6]. The surfactant concentration in contact with the interface (that determines the corresponding adsorption level) decreases. At the interface, concentration heterogeneities are likely to occur, leading to tangential concentration gradients that induce stretching of the interface due to the Marangoni effect. This radial flow creates in turn a vertical flow that brings aqueous solution from the bulk, richer in surfactants, to the interface and will amplify the initial surface heterogeneities to give rise to convective flows in both phases. The related intense mixing of the aqueous layer near the interface destroys the normal gradients, the instability vanishes, and the system switches to a slower, diffusive process. During this phase, normal gradients, induced by CTAB mass transfer, built up again and the cycle starts anew.

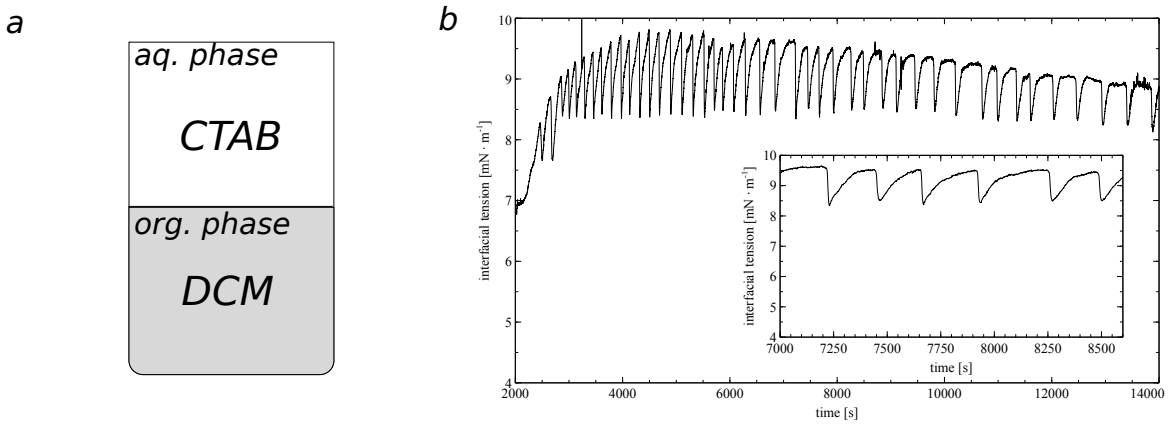

Figure 2.1: *a: Scheme of the biphasic system in a beaker. b: Oscillations of the interfacial tension between DCM and an aqueous solution containing 5 mM CTAB. Inset shows the oscillations between 6850 - 7800 sec in detail.*

DCM/CTAB/water is the system under study in the present work but the geometry has been now modified (details on the chemicals are given in appendix A).

2.2. A drop of DCM on a CTAB solution

The system consists now of a 25 µL drop of pure DCM which is placed on the surface of the CTAB solution. The experiment is generally carried out in a Petri dish, that is covered after the deposition of the drop on the surface. The coverage is not hermetic but increases the lifetime of the drop (by limiting evaporation) and, so, of the related instabilities.
The drop is visualized with the help of an optical setup using the Schlieren technique (for details see appendix A).

2.2.1. Processes at Play

In the biphasic configuration the DCM was the lower phase and the aqueous phase was placed on top of it since the density of DCM is about 33% higher than the density of the water (see Fig. 2.2). In this new configuration where the organic phase is a drop on top of the aqueous phase there are new effects that arise due to the physico-chemical properties of DCM (see Fig. 2.2).
Additionally to the CTAB mass transfer from the aqueous to the organic phase and the related adsorption/desorption dynamics at the interface, the drop also undergo evaporation of the very volatile DCM (boiling point is at 39°C) and the dissolution of DCM in the aqueous phase. The solubility of DCM in pure water is rather low (0.15 M). It is however highly increased in the presence of CTAB

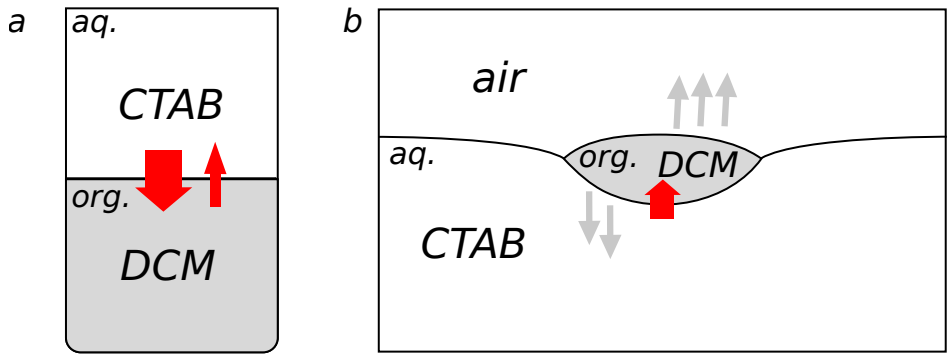

Figure 2.2: *Different configurations of the CTAB/DCM system. a: Biphasic configuration where the CTAB solution is placed on the pure DCM phase. b: Drop configuration where one drop of DCM is placed on the surface*

due to the formation of an oil in water microemulsion (CTAB aggregates containing DCM) [7]. In the presence of DCM the critical micellar concentration (cmc) is decreasing from 0.9 mM to 0.12 mM and the corresponding minimum in the water/air surface tension increases from 42 mN/m to 62 mN/m (see chapter 5). Another important property of DCM is its capacity to decrease the water/air surface tension by forming a film on its surface.

It is the interplay between these processes, i.e. the adsorption/desorption dynamics of CTAB at the oil/water interface, solubilization and evaporation of DCM and its surface activity at the water/air interface that creates the unique behavior of the drop at the water/air interface.
To understand the importance of the different processes at play we tried to suppress one of the effects at a time to simplify the system. The result was either that the drop did not even stay on the surface or that the system became even more complex.
Suppressing the evaporation by saturating the gas phase with DCM or suppressing the dissolution by saturating the water phase with DCM, both resulted in the falling down of the drop. The addition of CTAB in the organic phase at its partition equilibrium also resulted in the same behavior. However for lower CTAB concentrations, its addition resulted in an increased organization (see chapter 5).

On one hand this makes the system very difficult to investigate but on the other hand it shows that the processes at play are strongly coupled.

2.2.2. *Different Regimes Controlled by the CTAB Concentration*

The lifetime of the drop is limited due to evaporation and solubilization. It can vary from 5 to 500 seconds depending on the initial conditions including the size of the container. By varying the CTAB concentration from 0.25 mM to 30 mM a sucession of different regimes are obtained: spreading

and translation at 0.25 mM, very regular pulsations at 0.5 mM, rotations at 10 mM and a regime of polygonal-shaped drops at 30 mM (a overview is given in Fig. 2.9). In the following we will describe the different regimes.

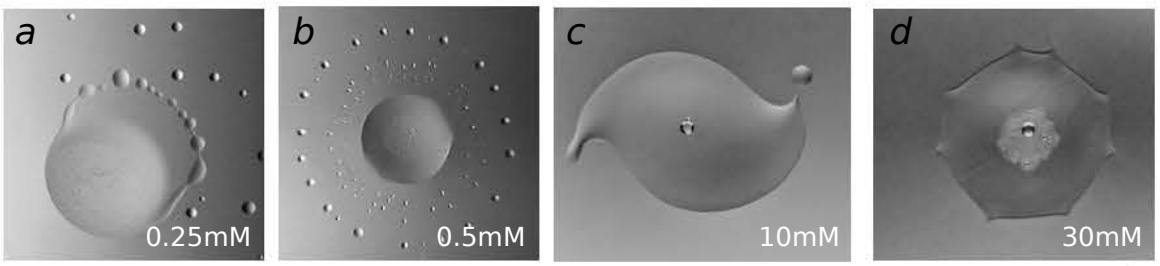

Figure 2.3: *Overview of the instabilities of the drop in the different regimes. a: Spreading and translation. b: Pulsation. c: Rotation. d: Polygonal-shaped drop.*

2.2.3. Spreading and Translation Regime

For the lower CTAB concentration the drop appears as a central reservoir surrounded by a thin film. The edge of the film is unstable and produces droplets which are randomly ejected. The deformation arising at the edge of the film are some kind of fingering. The fingers detach and form ejected droplets. For some reason at one point the film symmetry can break and the droplet undergoes a translational motion.

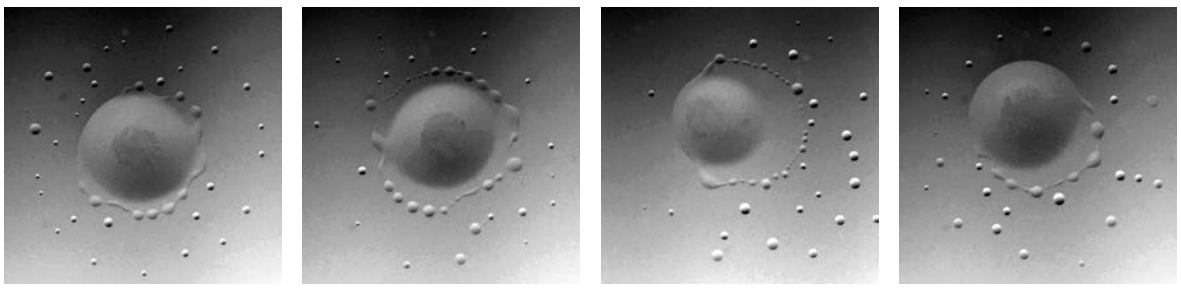

Figure 2.4: *Series of a DCM drop on a 0.25 mM CTAB solution. As it evolves it undergoes translational motion (last two images).*

The mechanism at play is the same as for the camphor boat or the aniline droplet (see chapter 1 (1.4.1.2)): the surface active DCM released at the back of the drop induces a surface tension difference and drives the motility.

2.2.4. Pulsating Regime

For a CTAB concentration of 0.5 mM, pulsations that last between 5 and 20 s with a mean frequency of about 1 Hz are obtained quasi systematically. Each pulsation consists of a rapid spreading of the drop. At maximum expansion the rim formed at the edge of the expanding film undergoes a Rayleigh-Plateau-like instability and breaks up into small droplets that move radially away from the drop (over a distance of 5 to 6 mm) and rapidly disappear by evaporation and dissolution. After detachment of the rim the remaining film recedes to form a compact drop again (Fig. 2.5). This pulsating regime is at the center of the present work. It will be analyzed in detail in the chapter 4.

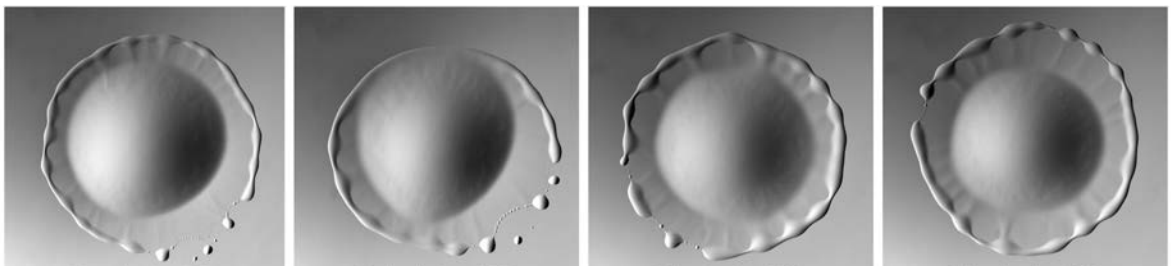

Figure 2.5: *Sequence of subsequent pulsations of a DCM drop on a 0.5 mM CTAB solution.*

2.2.5. Rotating Regime

For a CTAB concentration of 10 mM, the drop undergoes a major shape deformation after the induction period, leading to an elongated structure with two sharp tips (Fig. 2.6). This structure then rotates in an arbitrary (clock-wise and counterclock-wise rotations are equally observed), but constant, direction. The rotating two-armed drop is the most frequently encountered structure, but also rotating drops with three or sometimes four tips are observed.

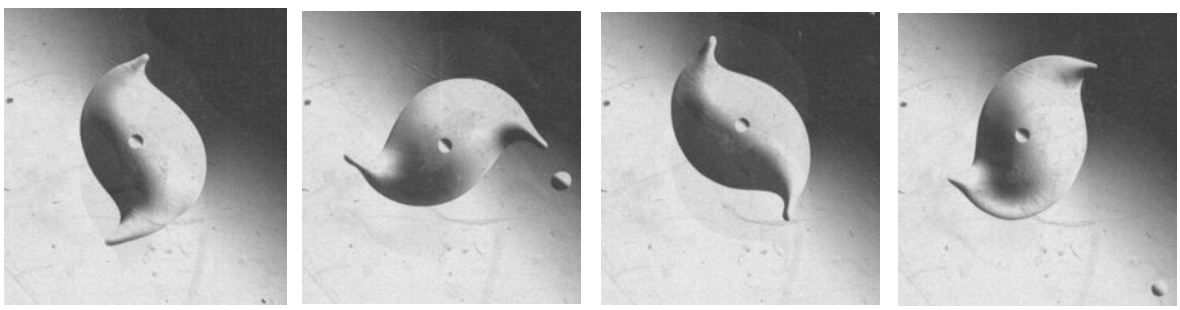

Figure 2.6: *Rotation of a DCM drop on a 10 mM CTAB solution (time increases from left to right). Approx. 1 rotation is shown (with 200 ms between each image).*

Typically a drop can perform between 10 and 30 rotations with a steady rotation frequency of around 1.9 Hz, which is independent of the drop volume and time. During this stable rotation, the drop ejects smaller droplets from its tips. Each daughter droplet moves approximately 4 mm, flattens slightly, and then decays into several smaller droplets, that finally disappear.

Although there are no examples of rotating drops in literature, there are rotating solids and gels on liquid phases (e.g. Nakata et al. [8]; Sharma et al. [9]).
In the article by Nakata et al. [8] a solid camphor fragment with a comma-shaped form is rotating. The authors explain the rotation in the same way as the pure translation regime discussed above. The dissolving camphor forms a thin layer at the interface, which locally reduces the interfacial tension. In the concave region of the "rotor", due to the curvature, there is an accumulation of dissolved camphor in contrast to the convex region. Therefore a gradient in the surface tension is created and the rotor moves with the convex region ahead and the fragment starts to rotate.

For the DCM drop the same mechanism might be at play. Moreover the constant rotation frequency could be explained by the fact that the concentration in the concave regions of the rotors of the drop are continuously renewed from the bulk solution of the droplet, which is pure DCM.

2.2.6. *Polygonal-like Regime*

For higher CTAB concentrations, a polygonal-like shape is observed (Fig. 2.7). After the induction period, small tips form along the edge of the drop, which confers the drop the shape of a polygon. This tips move and when two of them collide they can give rise to the ejection of a smaller droplet. During shrinkage of the drop the number of tips is reduced until the final disappearance of the drop. At the moment, we have no insight on this behavior, which, to our knowledge, has never been described in the literature.

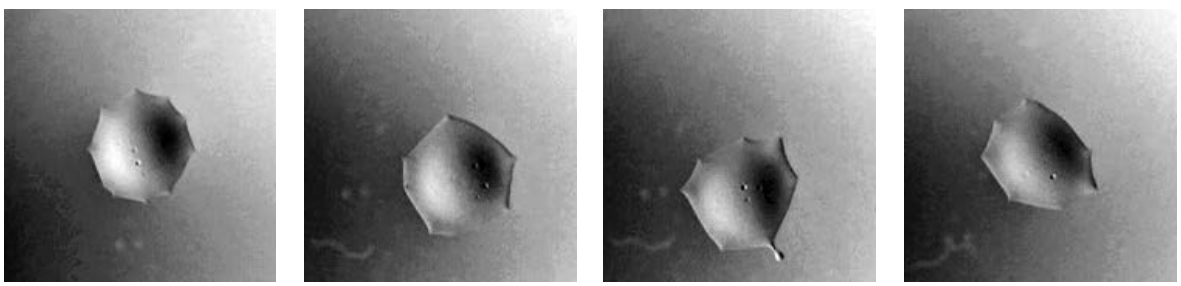

Figure 2.7: *Series of a DCM drop on a 30 mM CTAB solution. As it evolves it starts ejecting smaller droplets (visible in the last two images).*

In this chapter we discussed the historical origin of the system as well as the observed regimes controlled by the CTAB concentration. In the following the main focus is on the pulsating regime observed for a 0.5mM CTAB solution. Chapter 4 will be concerned with the pulsations observed in this regime and will discuss in detail the rim break-up we observe at the end of each pulsations. The change in the behavior, specially the complex dewetting pattern observed, when adding CTAB also to the organic phase will be the subject of the chapter 5. Before that, chapter 3 concerns the behavior of the drop during the induction phase (for specific experimental conditions) that proceeds the more complex behavior described above. We will first precise the main parameters affecting the duration of the induction period and then we will focus on the complex interplay between evaporation and dissolution leading to an unexpected evolution of the drop shape. The drop diameter showed "pinning" although such a behavior was only reported for drop evaporation on solid surfaces.

Bibliography

1. C. V. Sternling and L. E. Scriven, "Interfacial turbulence: Hydrodynamic instability and the marangoni effect," *AIChE Journal*, vol. 5, no. 4, pp. 514–523, 1959.

2. N. M. Kovalchuk, V. Pimienta, R. Tadmouri, R. Miller, and D. Vollhardt, "Ionic strength and ph as control parameters for spontaneous surface oscillations," *Langmuir*, vol. 28, no. 17, pp. 6893–6901, 2012.

3. M. Dupeyrat and E. Nakache, "205 - direct conversion of chemical energy into mechanical energy at an oil water interface," *Bioelectrochemistry and Bioenergetics*, vol. 5, no. 1, pp. 134 – 141, 1978.

4. V. Pimienta, D. Lavabre, T. Buhse, and J.-C. Micheau, "Correlation between electric potential and interfacial tension oscillations in a water-oil-water system," *The Journal of Physical Chemistry B*, vol. 108, no. 22, pp. 7331–7336, 2004.

5. D. Lavabre, V. Pradines, J.-C. Micheau, and V. Pimienta, "Periodic marangoni instability in surfactant (ctab) liquid/liquid mass transfer," *The Journal of Physical Chemistry B*, vol. 109, no. 15, pp. 7582–7586, 2005.

6. V. Pradines, R. Tadmouri, D. Lavabre, J.-C. Micheau, and V. Pimienta, "Association, partition, and surface activity in biphasic systems displaying relaxation oscillations," *Langmuir*, vol. 23, no. 23, pp. 11664–11672, 2007.

7. R. Tadmouri, C. Zedde, C. Routaboul, J.-C. Micheau, and V. Pimienta, "Partition and water/oil adsorption of some surfactants," *The Journal of Physical Chemistry B*, vol. 112, no. 39, pp. 12318–12325, 2008.

8. S. Nakata, Y. Iguchi, S. Ose, M. Kuboyama, T. Ishii, and K. Yoshikawa, "Self-rotation of a camphor scraping on water: New insight into the old problem," *Langmuir*, vol. 13, no. 16, pp. 4454–4458, 1997.

9. R. Sharma, S. T. Chang, and O. D. Velev, "Gel-based self-propelling particles get programmed to dance," *Langmuir*, vol. 28, no. 26, pp. 10128–10135, 2012.

RESUMÉE EN FRANÇAIS

L'effet accélérant d'instabilités hydrodynamiques sur les processus d'extraction a en premier lieu éveillé l'intérêt des ingénieurs du genre chimique. Parmi les différents régimes décrits, un comportement particulier est observé pour des systèmes impliquant des molécules tensioactives. L'instabilité n'apparaît alors que transitoirement, le système bascule de façon périodique entre un régime diffusif et un régime convectif. Ce comportement a été observé pour la premier fois pour des systèmes pour lesquels le transfert de tensioactif est couplé à une réaction chimique: la formation d'une paire d'ion hydrophobe. Dans ce domaine, le système CTAB/acide picrique initialement décrit par Nakache et Dupeyrat est à l'origine de nombreuses études. Au cours du transfert, des oscillations de la tension interfaciale sont observées. L'interprétation détaillée de ces signaux corrélés à l'observation de mouvements de grande amplitude en phase aqueuse nous a permis de confirmer l'origine hydrodynamique de l'instabilité. Nous avons également montré que le CTAB seul peut induire l'instabilité en l'absence d'acide picrique.
Lors du transfert diffusif la formation de gradients normaux induisent à proximité de l'interface une concentration plus faible et donc une faible adsorption du tensioactif. Les molécules adsorbées sont mobiles et une inhomogénéité peut alors apparaître localement. Un excès local de tensioactif induit un gradient de tension interfaciale et le déplacement du fluide dans la direction radiale. Ceci induit un flux vertical descendant qui apporte à l'interface une solution plus concentrée de tensioactif. La perturbation initiale est alors amplifiée. Sous l'effet de l'agitation et des effets de bords l'instabilité est ensuite annihilée, le régime diffusif est restauré jusqu'à ce que des gradients critiques apparaissent à nouveau.

La géométrie du système a par la suite été modifiée, il est maintenant constitué d'une goutte de dichlorométhane (25 uL) déposé sur une solution aqueuse (25 mL) de CTAB. Le dichlorométhane est un solvant organique très volatil, partiellement soluble en phase aqueuse et de masse volumique supérieure à l'eau. La goutte de phase organique est donc soumise à différents processus. Au transfert de matière viennent se rajouter maintenant : évaporation, solubilisation et effets dus à la gravité.

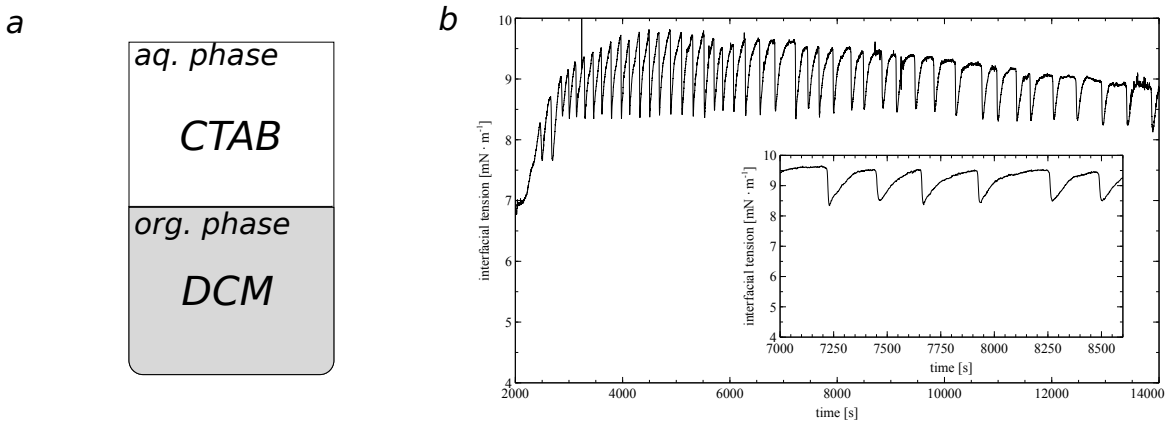

Figure 2.8: *a: Schema du system biphasique dans une becher. Oscillations de la tension interfaciale entre le DCM et une solution aqueuse de CTAB à 0.5 mM.*

En faisant varier la concentration du tensioactif présent en phase aqueuse nous avons mis en évidence une succession de régimes dynamiques couplés à des variations importantes de la forme de la goutte. Ces structures caractéristiques induisent différents régimes.

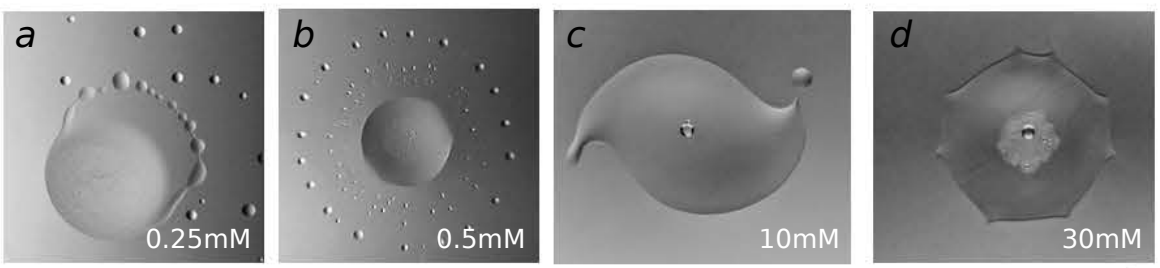

Figure 2.9: *Différents régimes controlés par la concentration de CTAB. a: Etalement. b: Pulsation. c: Rotation. d: goutte en forme polygonale*

Pour la concentration la plus faible (0.25 mM), la goutte apparait comme un réservoir central entouré d'un film dont les bords sont instables et donnent lieu à l'éjection de gouttelettes. Si la symétrie du système est brisée on peut alors observer le déplacement de la goutte sur une trajectoire circulaire. Le film est alors formé sur un seul côté de la goutte entrainant une différence de tension superficielle entre l'avant et l'arrière de la goutte donnant lieu à son déplacement. Lorsque la concentration atteint 0.5 mM, on observe un régime de pulsation qui consiste en un étalement rapide de la goutte, un bourrelet apparait au bord du film en expansion, il se détache de la goutte et donne lieu à la forma-

tion d'un anneau de gouttelettes qui s'éloignent avant de disparaitre sous l'effet de l'évaporation et de la dissolution. Ce régime est au centre des études effectuées au cours de cette thèse.

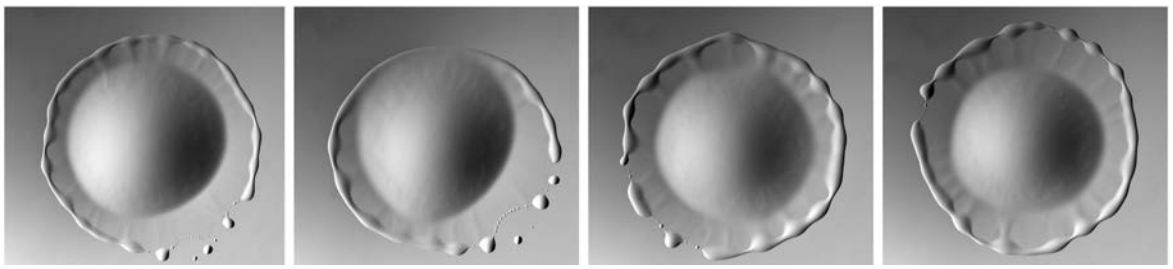

Figure 2.10: *Pulsations subséquentes d'une goutte de DCM sur une solution à 0.5 mM CTAB*

Lorsque la concentration atteint 10 mM (c'est-à-dire au-delà de la concentration micellaire critique) la goutte entre en rotation donnant lieu à des formes très caractéristiques, elle s'allonge et fait apparaître 2 pointes qui se recourbent selon le sens de rotation. La goutte peut typiquement effectuer entre 30 et 60 rotations en fonction de son volume initial. La fréquence de rotation est parfaitement constante (1.9 Hz) et indépendante du volume de la goutte. Des gouttelettes sont éjectées en direction radiale par les pointes mais aucune corrélation n'est observée concernant la fréquence d'éjection et la fréquence de rotation de la goutte ce qui indique que l'éjection n'est pas à l'origine de la rotation.

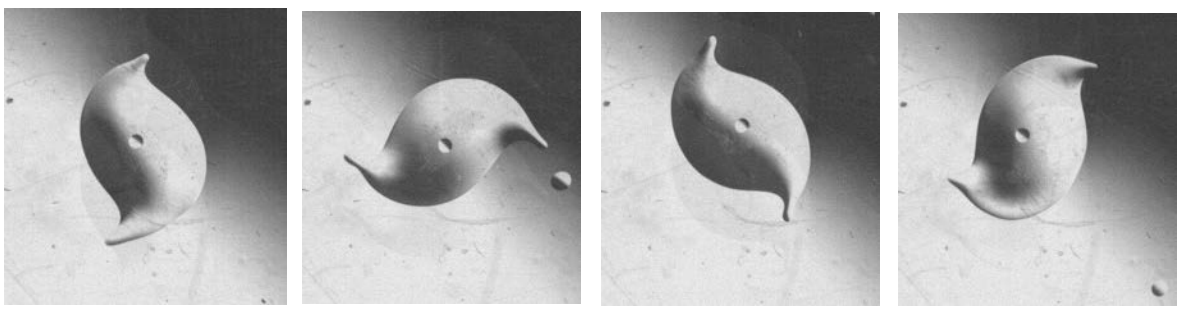

Figure 2.11: *Rotation d'une goutte de DCM sur une solution à 10 mM CTAB.*

Bien qu'il n'existe pas d'exemple de goutte donnant lieu à un mouvement de rotation dans la littérature, on trouve des solides ou des gels qui sont capables d'un tel effet mais seulement si la forme de l'objet a été dessinée spécialement dans ce but. Des travaux effectués dans l'équipe de S. Nakata on montré qu'un morceau de camphre de la forme d'une virgule donne lieu à un mouvement de rotation. La rotation est alors induite par l'accumulation de camphre dans la partie concave de la goutte induisant la mise en rotation du système. Dans le cas de la goutte, un mécanisme similaire est

peut être à l'œuvre, cette fois la forme ressemble à deux virgules accolées donnant lieu à la rotation de la goutte. Le fait que la vitesse de rotation soit constante pourrait alors être du au fait que le dichlorométhane utilisé pur a une concentration qui ne varie pas au cours du temps.

Le dernier régime observé lorsque la concentration atteint 30 mM est un régime polygonal (Figure 2.12). La succession de forme conduit à l'observation de pentagones, d'hexagones et même de carrés. Après la période d'induction on voit apparaitre sur les bords de la goutte des petites pointes qui se déplacent le long de la ligne de contact dans des directions aléatoires. Lorsque deux pointes se rencontrent elles donnent lieu à l'éjection de gouttelettes. Nous n'avons pas pour l'instant d'interprétation de ce phénomène qui n'a, à notre connaissance, jamais été décrit dans la littérature.

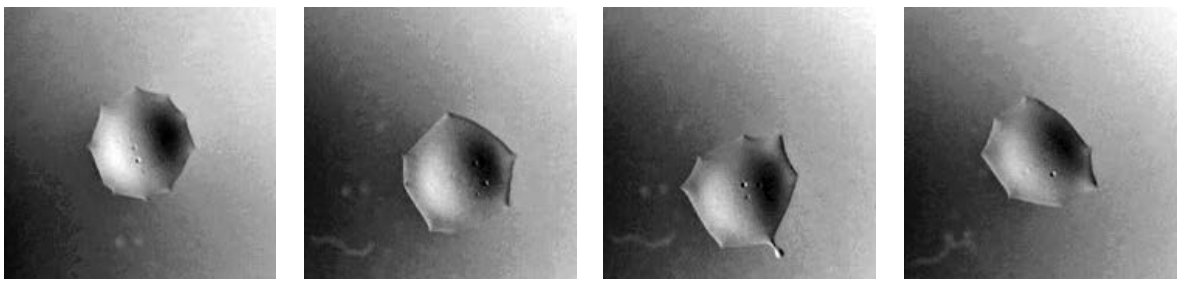

Figure 2.12: *Series d'une goutte de DCM sur une 30 mM CTAB solution.*

3

The Evolution during the Induction Period

Φύσις κρύπτεσθαι φιλεῖ.

[*The real nature remains a mystery*]

attributed to Heraclitus

The induction period of the drop is the period in which the drops triple contact line stays stable while it is shrinking due to evaporation and dissolution. The behavior of the drop during this period shows an interesting and complex behavior so far not seen for liquid lenses on liquid surfaces: drop-pinning. It resembles to what is known for drops on solid surfaces but its mechanism, which in our case is the result of an interplay between DCM dissolution and CTAB adsorption at the oil/water interface, is very different.

3.1. Appearance of an Induction Period

DCM is about 33% heavier than water and that is why the drop is deformed in such a way that most of its volume is emerged in the aqueous phase. The occurrence of an induction period can be understood in this context as a competition between surface tension and gravity effects. If gravity effects are dominant a more compact drop (smaller initial diameter) is observed and in this case mass loss is observed before the surface tension effects overcome the gravity effects and induce the deformation of the drop. A higher contribution of gravity effect compared to surface tension is therefore expected to lead to the existence of an induction period while their relative importance seems to be responsible for its duration.

3.1.1. Initial Diameter as a Function of the CTAB Concentration

The initial diameter of the drop right after its deposition was measured as a function of the CTAB concentration. A decrease is observed until the cmc after which it stayed quasi-constant for higher concentrations. This behavior of the initial diameter can be understood by looking at the dependency of the air/water interfacial tension as a function of the CTAB concentration (Fig. 3.1 (b)).

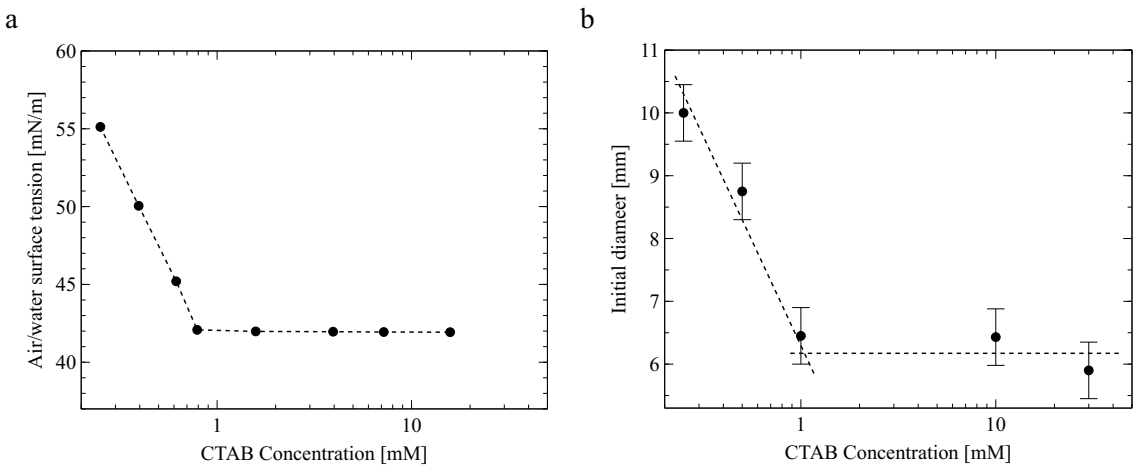

Figure 3.1: *Water/air interfacial tension (a) and initial diameter (b) for a 25µL drop in a Petri dish as a function of the CTAB concentration.*

The initial diameter actually follows exactly the same trend as the water/air interfacial tension (Fig. 3.1 (a)). The fact that the initial diameter follows the same trend as the interfacial tension can be understood as follows. As illustrated schematically in Fig. 3.2 the reduction of the air/water inter-

facial tension leads to an increase of the contact angle according to the Young-Neumann relations discussed in chapter 2. In consequence this leads to an increase in the height of the drop, which, since the volume of the drop is the same, leads to a smaller initial diameter. In other words the initial diameter just reflects the relative importance of the air/water interfacial tension with increasing CTAB concentration[1].

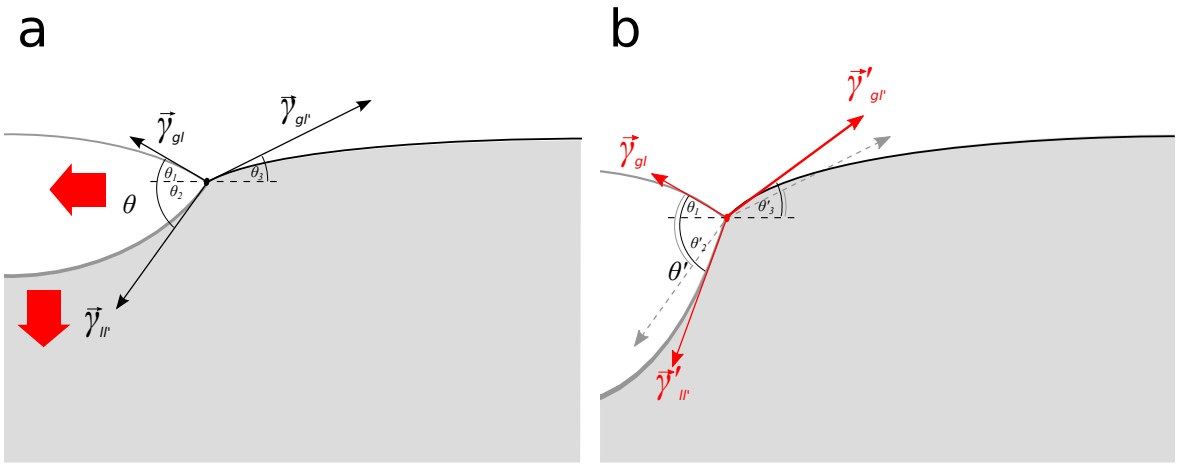

Figure 3.2: *Forces acting on a liquid droplet. The decrease in the air/water interfacial tension $\gamma_{gl'}$ leads also to an increase in the contact angle ($\theta \mapsto \theta' > \theta$), when the other forces stay constant (b). This leads to an increase in the height of the drop (compared to (a)).*

3.1.2. Induction Time as a Function of the CTAB Concentration

The appearance of an induction period is seen by increasing the CTAB concentration in the aqueous phase. While for low concentration, below the cmc, no or only a very short induction time[2] exists, for higher concentration, above the cmc, induction periods of several tens of seconds are observed. The longest induction period is observed at 1 mM, while its duration decreases again with increasing CTAB concentration (Fig. 3.3 (a)).

The evaporation rates were measured as a function of the CTAB concentration. An inverse correlation with the induction time as a function of the CTAB concentration is observed. Before the cmc

[1] if the air/water interfacial tension is too low the drop is dropping down (a stability analysis is carried out in the appendix B).

[2] the induction time is the time until the instability starts, which corrsponds to what is denoted as t_{inst} in the following

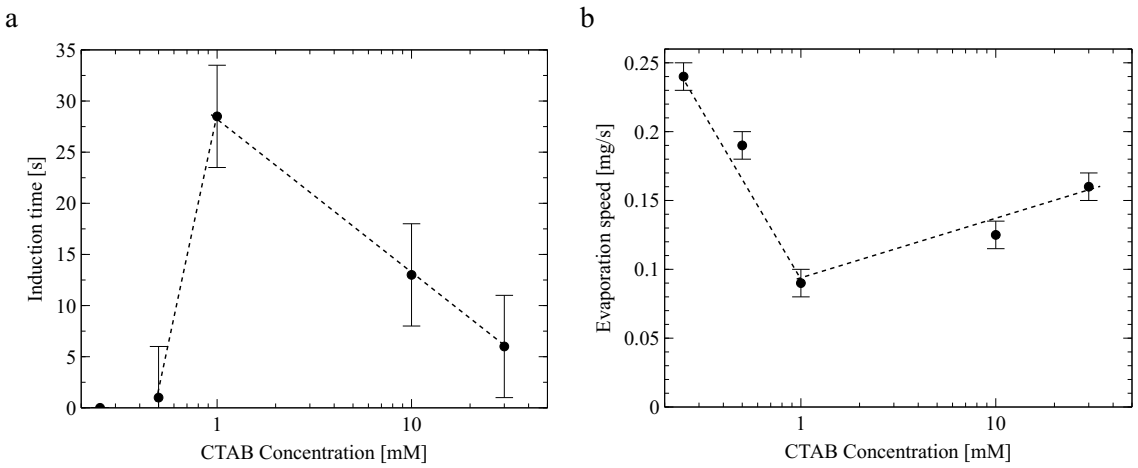

Figure 3.3: *Induction time (a) and evaporation rate (b) for a 25 µL DCM drop as a function of the CTAB concentration.*

the evaporation rate decreases and after it increases again. The decrease can be correlated to the decrease in the initial diameter of the drop mentioned above due to the fact that the evaporation is proportional to the surface area of the drop which is smaller for smaller diameters. The increase after the cmc concentration, where the diameter does not change anymore, was no expected. The only interpretation we have at this moment is that this is related to an increase in evaporation due to the fact that the drop is moving around on the surface. The evaporation has a cooling effect on the surrounding of the drop and therefore a negative feedback effect on the evaporation rate. The movement of the drop, which is not observed for lower concentrations, leads to the fact that the drop is always surrounded by new liquid hence avoiding the cooling effect.

There are other effects too, that can lead to an increase of the induction time for a given CTAB concentration. The increase in the volume of the drop, as we will see in section 4.3. and the size of the reactor, which leads to confinement. The latter one will be discussed in the next section.

3.1.3. Film Formation and Confinement

During the dissolution process a thin film, which diameter is roughly 4 times the drop diameter, arises around the drop. Not visible at the beginning, it appears as a quasi-perfect circle in the Petri-dish geometry. We have varied the surface area between 9 and 25 cm^2 in rectangular cuvettes, which are the experimental geometries used in the following and found that for areas larger than 16 cm^2 the film is a quasi-perfect circle as in the Petri-dish geometry. The appearance of the film reveals the formation of a dissolution downstream flow due to the accumulation of dichloromethane at the edge

of the film. The corresponding buoyant plumes can be visualized on a side view by the addition of methylene blue, which also reveals the dissolution downflow directly under the drop, which will be of importance to explain the behavior reported in the next section (Fig. 3.4).

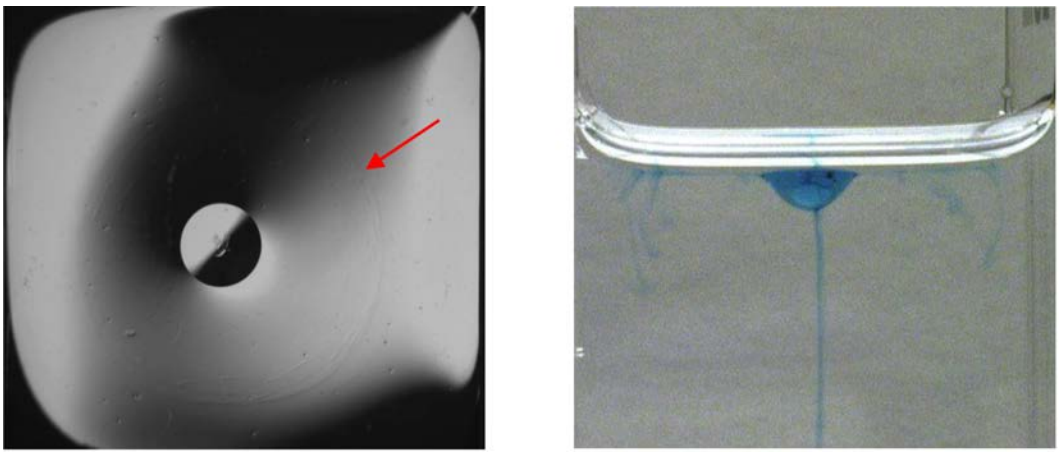

Figure 3.4: *a) Top view: film formation (indicated by an arrow) around a 25* µ*L drop on a 0.5 mM CTAB solution in a 5 cm squared cuvette. b) Side view: main downflow below the drop and buoyant plumes observed at the edge of the film by adding methylene blue in the drop.*

When the size of the cuvette is decreased the edge of the film interacts with the side-walls and the perturbed dissolution driven flow appears as stripes that marbles the aqueous surface (see Fig. 3.5).
Confinement does not affect the diameter evolution of the drop, which shows an interesting effect as discussed in the next section, but affects the development of the instability during the second stage of the process.
Every time the film showed a well-defined round shape around the drop, a pulsating regime gives rise to the periodical expansion of the drop coupled to the ejection in the radial direction of smaller droplet that form a perfect expanding ring (as shown for example in Fig. 2.5. When film confinement is effective, the instability gives rise to very fast deformation of the drop contour with random ejection of droplets. We call this regime "effervescence" (see Fig. 3.5).
The effect of the change in the reactor free air/water interfacial area on the induction time and the initial diameter was measured. It was found that the decrease of this area led to an increase of the induction time and an decrease of the initial diameter (see Fig. 3.6). The confinement of the film leads to an increased thickness of the film, which itself leads to a decrease of the air/water interfacial tension. And that a decrease in the air/water interfacial tension leads to a decrease of the initial diameter was already discussed above, which explains the dependency of the initial diameter on the free air/water interfacial area. Also the increase in the induction time with decreasing free air/water

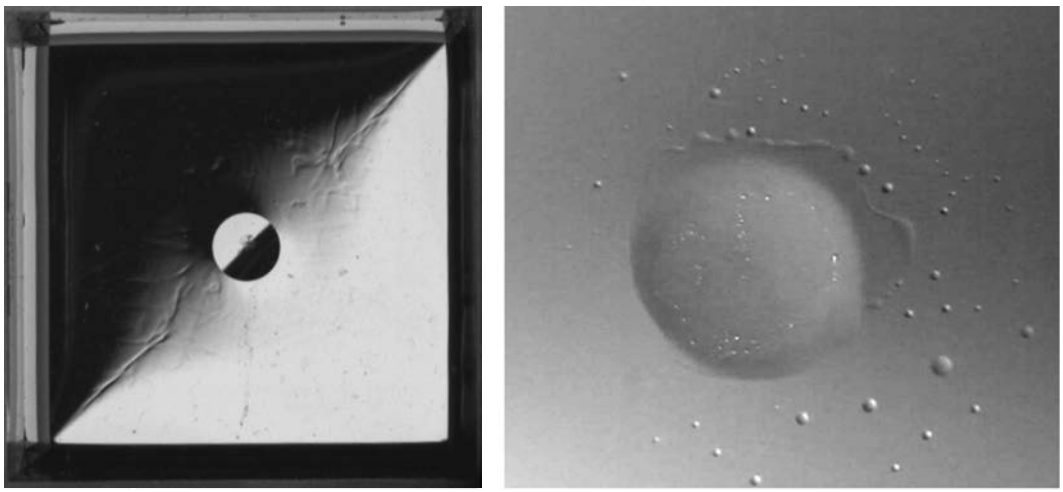

Figure 3.5: *Left: Film confinement for a 25 µL drop on a 0.5 mM CTAB solution in a 3 cm squared cuvette. Right: "Effervescent" instability observed when confinement effects are important for a 25 µL drop deposited on a 0.5 mM CTAB solution.*

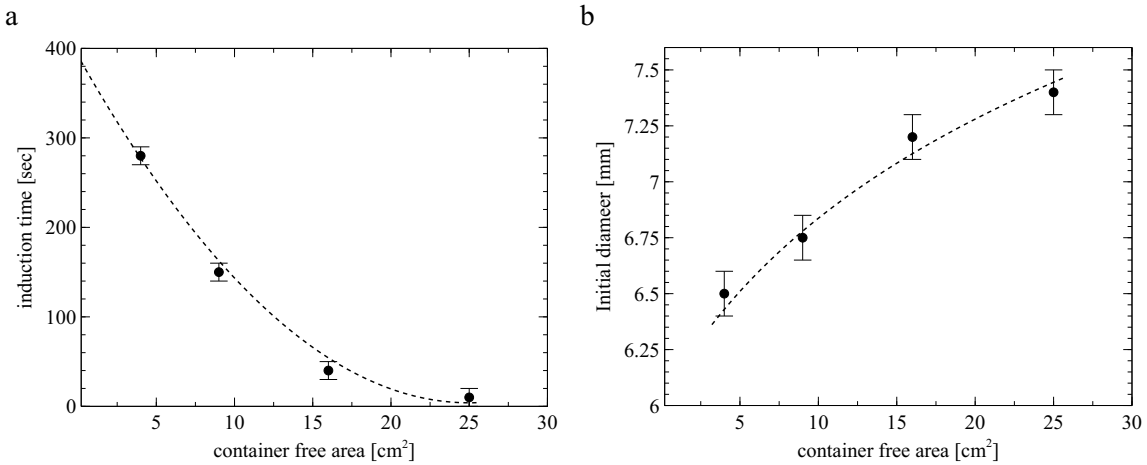

Figure 3.6: *Dependency of the induction time and initial diameter for a 25µL drop on a 0.5 CTAB solution in squared cuvettes. Initial diameter (A), water/air interfacial tension (B) and induction time (C) as a function of the CTAB concentration.*

interfacial area can be understood in this way. A small initial diameter shows the relative importance of the gravity effects which is the supposed reason for the induction period. In such a case mass loss occurs before the surface tension effects overcome the gravity effects and induce the deformation of

the drop.

After this first study of the induction period, were the dependency of its duration on the CTAB concentration and the confinement of the reactor has been studied we now restrict the following studies about the dynamics of the drop during this induction period to a concentration of 0.5 mM CTAB in the aqueous phase.

3.2. Self-Pinning of the Drop

A side view of the drop allows to measure the diameter, height and contact angle evolution with time. The dynamics of the disolving /evaporating stable drop revealed an unexpected transition from a drop initially shrinking without deformation to a drop maintaining a constant diameter while height and contact angle are decreasing. Such a behavior is similar to the one called drop pinning observed on solid surfaces [1, 2, 3], as in the coffee ring effect [3, 4, 5, 6, 7] but not known on liquid surfaces [8, 9, 10]. However the reasons for the "pinning" are completely different here. In the following we will discuss this behavior in detail and also give an explanation, that is supported by an analytical model.

The contact angle, height and diameter were measured as a function of time in a cuvette with 2.5x2.5cm free surface area. A computer program (see appendix C.1) was used to extract this parameters from the recorded images. The drop volume was varied from 5 to 30 µL (the latter being the maximum volume for the drop to float on the aqueous surface).
The results obtained for the contact angle, height and diameter are shown in Fig. 3.7 (upper parts). The evolution of these parameters is qualitatively similar for all the initial volumes.
The initial values of these parameters vary with increasing initial volume of the drop. The initial contact angle varies from 22 to 35 degrees, the initial height varies from 0.5 to 1.3 mm and the initial diameter varies from 4.0 to 6.8 mm.
Until a certain time, which we denote with t_1, the evolution of the parameters is monotonous and linear. At t_1 there is a change in the slope for all parameters. The contact angle, which stayed constant until this point starts to decrease linearly, the height starts to decrease linearly too but with an increased slope while the diameter becomes constant. This is the beginning of the pinned stage. The diameter values corresponding to the pinned stage are almost independent from the initial volume with the exception of 5µL. At the end of the pinned phase the diameter starts to increase again just shortly before the instability starts at t_{inst} (this is observed for drop volumes between 5 and 20 µL). The peak is followed by a fast and strong decrease of the mean diameter during the instability (see peaks in diameter in Fig. 3.7).

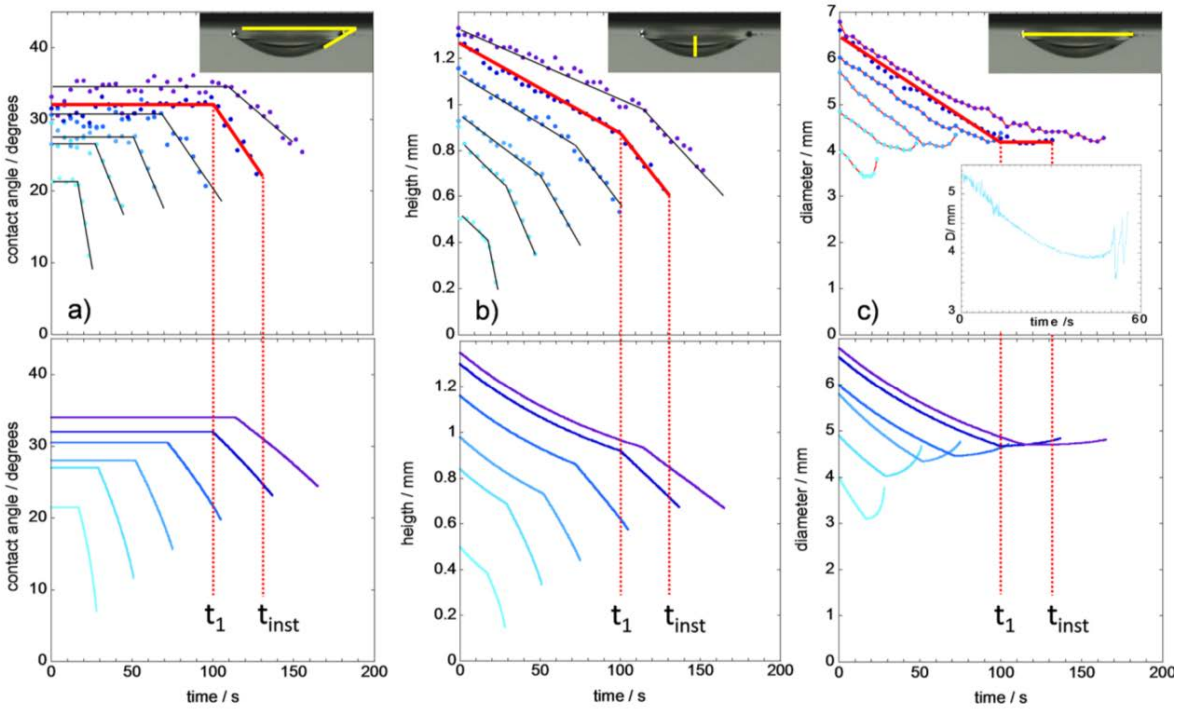

Figure 3.7: *Results obtained from experiments in a 2.5x2.5x7cm cuvette (25mL of a 0.5mM CTAB solution, 18.5mL air above) for different initial volumes (ranging from 5µL to 30µL); red fit lines corresponding to the parameters of the 25µL drop. Panels show the contact angle, the height and the diameter as a function of time. The pinned phase appears between t_1 and t_{inst} (lower panels show the corresponding theoretical results obtained with the model described in the text).*

An increase in the induction time, i.e. t_{inst}, with increasing initial volume is also observed. This increase in the induction time can be understood due to an increase in the importance of gravity effects due to an accompanied increase in the height of the drop as discussed in the preceding chapter.

To sum up, the evolution of the drop shows 3 stages:

- The *shape preserving stage*, where the height and diameter decrease while the contact angle remains constant and the shape of the drop is preserved ($t \leq t_1$)
- The *pinned stage*, where the drop diameter is almost constant while the contact angle and height decrease ($t_1 < t < t_{inst}$)
- The *instability*, which follows the sudden increase of the diameter (clearly observable on smaller drops) at the end of the pinned phase ($t > t_{inst}$), during which the drop shape becomes unstable.

To better understand this behavior we also tried to get information about the flows induced in the aqueous phase. A first attempt was to color the DCM with a blue dye that helped to visualize the DCM dissolution flows. Just after the deposition of the drop, a vertical down-flow appears at the bottom of the drop as well as the formation of plumes at the extremity of the film which forms around the drop (see Fig. 3.4). Similar vertical down-flow are generally observed for dissolving pendant drops as for example a drop of aniline [11]. This flow corresponds to a stable solubilization regime.

With the help of Particle Image Velocimetry (PIV), we could obtain more quantitative information about the convective flows in the vicinity of the drop during the drop evolution. The velocity fields (Fig. 3.8 (a)) obtained from these measurements show three different stages, represented by the x-component of the velocity (Fig. 3.8 (b)). We have measured the characteristic geometric parameters (contact angle, height and diameter) and observed exactly the same qualitative behavior as in the slightly bigger cuvette used to obtain the results shown in Fig. 3.7 . However, in the 2 cm squared-cuvette used for PIV, the initial diameter of the drop is observed to be smaller and the induction period longer ($t_{inst} = 185$s; Fig. 3.8 (b)) in agreement with the results reported in section 3.1.3.

The PIV measurements showed convective counterclockwise motion induced in the bulk by the DCM dissolution flow below the drop. By continuity, the buoyant stream of dichloromethane-rich fluid gives rise to a large-scale toroidal flow around the drop (Fig. 3.9 (b)). Its radial inflow is visualized by the x-component of the velocity, determined at a distance of 0.5 mm from the initial position of the triple line (circles in Fig. 3.8 (a)). The corresponding negative values of the x-component of the velocity in Fig. 3.8 (b) are maintained during the whole induction period (i.e. the flow stays counterclockwise during the whole induction period). However, we see two sub-stages appearing. The velocity magnitude, fluctuating strongly in the beginning, decreases to a quieter period afterwards. If we correlate these data to the diameter evolution (Figure 3.8 (b), blue dots, red lines are a guide to the eye), it turns out that the decreased activity corresponds to the pinned phase. At the time the instability starts the direction of the subsurface flow is suddenly reversed and the x-component becomes positive. On the velocity field plot, this corresponds to the formation of a clockwise toroidal flow around the drop (Fig. 3.8 (a), last images).

In order to check that the confinement was not modifying the shape evolution of the drop we have performed experiments in larger containers, like Petri dishes. The drop evolution becomes quantitatively independent of the available aqueous surface (Fig. 3.10), which shows that the confinement is not at the origin of the shape evolution described here.

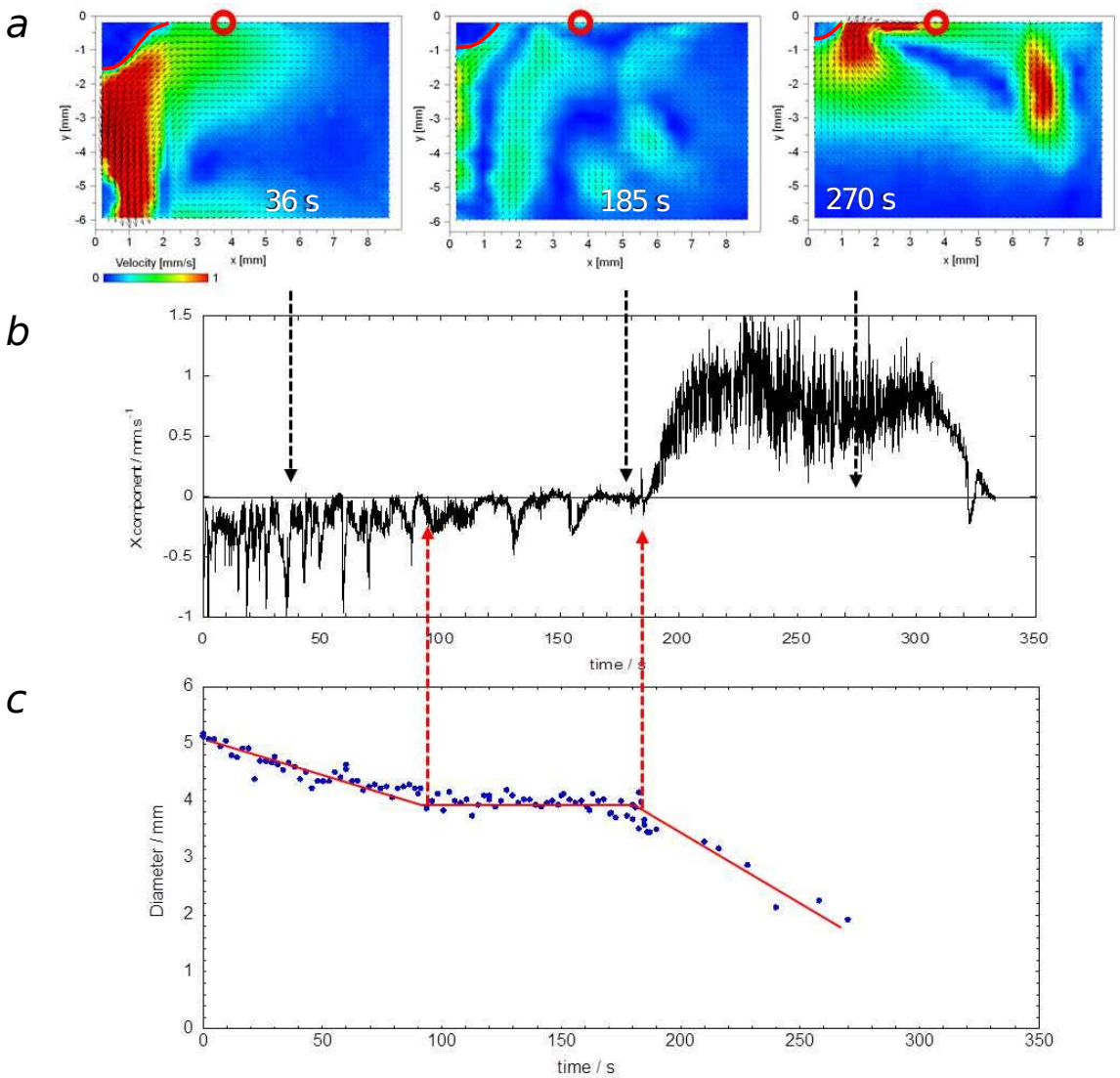

Figure 3.8: *a: Velocity field obtained by PIV; b: related x-component of the velocity obtained by PIV at the position of the red circle in (a) and c: diameter evolution of a 25 mL drop on a 0.5 mM CTAB solution in a 2 cm squared-cuvette.*

3.2.1. Interpretation

As mentioned above the evolution of the drop shape during the induction period and the occurrence of a pinned phase is unexpected for a drop deposited on a liquid surface [8, 9, 10]. Pinning occurs on solid surface but it is observed at the very beginning of the evaporative process and is related to microscopic heterogeneity of the solid. In this case, the contact angle decreases until the receding

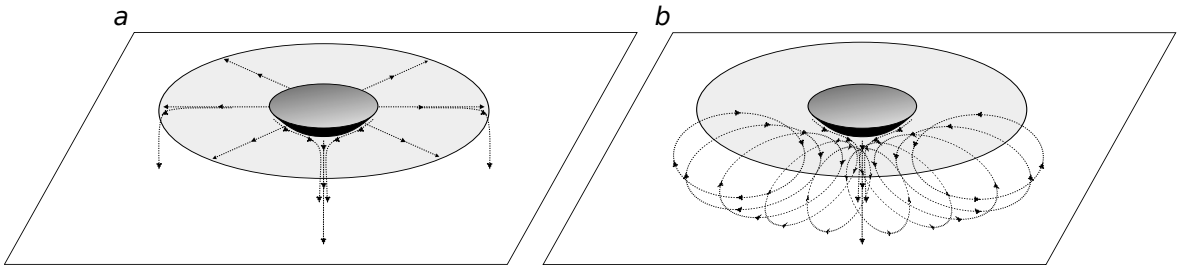

Figure 3.9: *Flows induced on the surface and in the bulk. a: radial DCM flows on the surface form a thin film surrounding the droplet, while at its extremities dissolution down flows occur as well as directly below the drop. b: Toroidal flows around the drop which are induced by the down flow of DCM.*

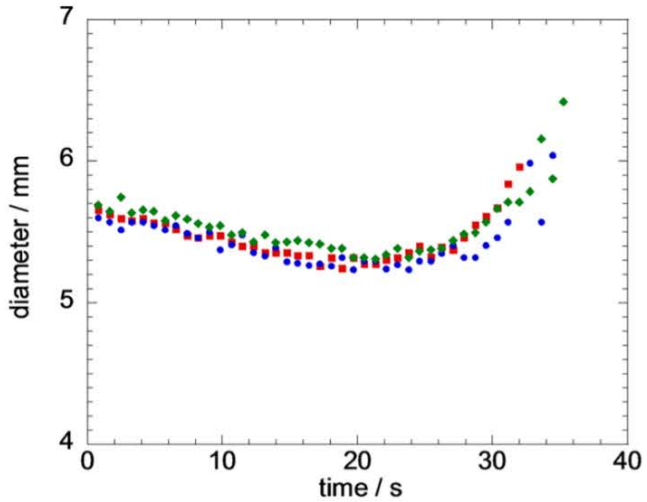

Figure 3.10: *Diameter evolution of a 25 µL drop on a 1 mM solution in Petri dishes of increasing diameter: 11 (red squares), 14.6 (blue circles), and 18.5 cm (green diamonds) diameter, with the liquid height being 5mm in all cases.*

contact angle is reached, then the diameter of the drop decreases maintaining a constant contact angle [1, 2, 3]. If particles are added in the drop, their deposition is induced by the evaporation driven flow which drives the fluid toward the edge of the drop in order to replace the loss of liquid due to higher evaporation in that place [4, 7].

In the literature, data reported for evaporating lenses of pure liquids on water show a continuous decrease of the diameter (that can be almost linear for smaller drops and shows a progressive acceleration for bigger ones) followed, at the very end of the process, by an accelerated shrinkage [8, 9, 10]. In the system described here, a much more complex behavior is obtained since evaporation is coupled to solubilization, surfactant mass transfer and adsorption at the water/oil interface.

During the first stage, despite the high-intensity gravity-driven flow, the drop evolution is similar to the one described for evaporating lenses on pure water. The volume decreases without affecting the shape of the drop (constant contact angle). This suggests that the capillary forces exerted at the contact line remain unchanged. Due to the gravity-driven dissolution flow going down along the water/oil interface the adsorption of CTAB at the water/oil interface is hindered.
In the second stage the dissolution flow is highly reduced due to the partial DCM saturation of the aqueous phase in the immediate surrounding of the drop. This effect now favors adsorption of CTAB at the water/oil interface, decreasing the water/oil interfacial tension and hence the contact angle.
During its evolution the drop is in fact submitted to two antagonistic effects leading to a constant diameter in the pinned phase. The mass loss due to evaporation and solubilization tends to decrease the diameter while the reduction of the water/oil interfacial tension induced by the CTAB adsorption tends to increase the diameter. The non-trivial dynamics of the diameter results from these two opposite effects: The first one is progressively diminished because of the saturation of the adjoining aqueous phase, allowing the second effect to take place and to rule the drop evolution.
From this point of view, the "pinned" stage we observe before the instability arises correspond to a minimum in the diameter evolution and is a result of these two antagonistic effects.

3.2.2. Modeling

To better understand the underlying dynamics we have developed a simple analytical model (Antoine et. al. [12]). For simplicity, the drop was modeled as a spherical cap (see Fig. 3.11) with homogeneous surface tension. The oil and water phase are considered homogeneous.

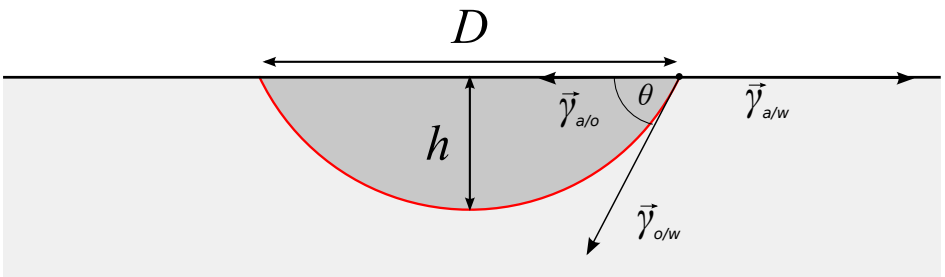

Figure 3.11: *Parameters of the spherical cap approximation. Scheme shows the contact angle φ, the diameter D and the height h of the drop as well as the involved surface tensions at the water/oil, water/air and oil/water interface.*

The dissolution process of DCM is described by the volume change rate (Peña et al. [13])

$$\frac{1}{A(t)}\frac{dV(t)}{dt} = -\frac{V_m(C_{sat} - C(t))}{\mathcal{R}_D}, \tag{3.1}$$

where $A(t)$ is the oil/water interfacial area and $C_{sat} - C(t)$ is the driving concentration difference between the saturation concentration of DCM in the aqueous phase C_{sat} and the concentration of DCM at the time t, $C(t)$ and V_m is the molar volume of DCM. $\mathcal{R}_D$ is called the mass transfer resistance and is related to diffusion of DCM. It is reduced by natural convection and is in our case only depending on the contact angle, which can be expressed by the height and the diameter of the drop (Cussler [14]). For the DCM concentration in the aqueous phase a simple saturation dynamics is assumed, i.e. $C(t) = C_{sat}(1 - e^{-t/\tau})$, where τ can be estimated by using the initial values.[3]
By using the formula for the volume and the surface area of a spherical cap, i.e.

$$V(t) = \frac{\pi h}{24}\left(3D(t)^2 + 4h(t)^2\right) \qquad \text{and} \qquad A(t) = \pi\left(h(t)^2 + \frac{D(t)^2}{4}\right) \tag{3.2}$$

the equation (3.1) can be evaluated to obtain the final mass transfer equation, which writes

$$\frac{dD}{dt} + \left(\frac{D}{2h} + \frac{2h}{D}\right)\cdot\frac{dh}{dt} = -\left(\frac{4h}{D} + \frac{D}{h}\right)\frac{V_m}{\mathcal{R}_D(h,D)}C_{sat}\cdot e^{-t/\tau}. \tag{3.3}$$

Another equation is necessary to find h and D, which is provided by the Young equation of the system,

$$\gamma_{\mathrm{o/w}}\cdot\cos\varphi = \gamma_{\mathrm{a/w}} - \gamma_{\mathrm{a/o}}, \tag{3.4}$$

where φ is the contact angle and $\gamma_{\mathrm{o/w}}, \gamma_{\mathrm{a/w}}$ and $\gamma_{\mathrm{o/w}}$ are the oil/water, air/water and air/oil interfacial tensions respectively. Assuming that the air/water and oil/air interfacial tension are not changing significantly during the induction period the right hand side remains constant.
In the spherical cap approximation the contact angle φ can be expressed in terms of h and D, i.e.

$$\cos\varphi(h,D) = \frac{D^2 - 4h^2}{D^2 + 4h^2}. \tag{3.5}$$

For the adsorption dynamics of the surfactants at the oil/water interface the Langmuir adsorption isotherm [15, 16] and the Szyszkowsik equation [17] in considering local equilibrium at the oil/water interface are assumed. This gives us the time dependency of the oil/water interfacial tension, which writes

$$\gamma_{\mathrm{o/w}} = \gamma^o_{\mathrm{o/w}} - \underbrace{2RT\Gamma_m\cdot\ln(1 + K_L C_S(t))}_{\Delta\gamma_{\mathrm{o/w(t)}}}, \tag{3.6}$$

where $\gamma^o_{\mathrm{o/w}}$ is the surfactant-free surface tension, Γ_m is the maximum surface concentration of the surfactants, K_L is an adsorption parameter and $C_S(t)$ is the CTAB concentration in water. Difficult

[3] taking the initial values in equation (3.1), i.e. $\frac{1}{A_o}\frac{V_o}{\tau} \approx \frac{V_m C_{sat}}{\mathcal{R}^0_D}$ we obtain $\tau \approx \frac{V_o}{A_o}\frac{\mathcal{R}^0_D}{V_m C_{sat}} \approx 100$ s

to grasp is the surfactant dragging induced by oil dissolution, which counterbalances the diffusion-controlled adsorption [18] and delays it by a time t_1. Rather than solving the fully coupled transport and transfer equations, we assume here for simplicity a simple first order process [19, 20, 21], i.e.

$$C_S(t) = C_{S0} + (C_{CAC} - C_{S0})(1 - e^{(t-t_1)/\tau_S}), \tag{3.7}$$

where C_{CAC} is the surfactant aggregation concentration in the presence of DCM [22] (C_{CAC}= 0.1 mM) and C_{S0} is the initial CTAB concentration. The parameter τ_S can be related to the effective finite boundary layer l_B and the diffusion coefficient of CTAB in water D_S, i.e. $\tau_S \approx l_B/D_S$ [20, 23]. The only free parameter of the model is l_B, which we will assume to be close to the characteristic adsorption lengths $\Gamma_m K_L$, i.e. $l_B \approx \Gamma_m K_L$ [21, 24, 25].
Adding all together equation (3.4) takes its final form, which reads

$$\left(\gamma^o_{\mathrm{o/w}} - \Delta\gamma_{\mathrm{o/w}}\right) \cdot \frac{D^2 - 4h^2}{D^2 + 4h^2} = \gamma_{\mathrm{a/w}} - \gamma_{\mathrm{a/o}}. \tag{3.8}$$

Together with Eqn. (3.3) we can now calculate $D(t)$ and $h(t)$. In the first shape-preserving stage, i.e. for $t < t_1$, we obtain

$$D(t) = D_o + b_o\tau(e^{-t/\tau} - 1), \tag{3.9}$$

which follows a linear decrease for $t \ll \tau \approx 100$ s, since then $D(t)$ can be written as

$$D(t) = D_o + b_o\tau(e^{-t/\tau} - 1) \approx D_o - b_o t. \tag{3.10}$$

The term b_o is given by

$$b_o = \frac{4cotan(\varphi_o/2)}{2 + cos\varphi_o}\frac{V_m C_{sat}}{\mathcal{R}_D(\varphi_o)}, \tag{3.11}$$

where φ_o is the constant initial contact angle. Since b_o scales as $1/sin^2(\varphi_o/2)$, flatter and smaller drops shrink faster which is in accordance with the experimental results.
In the pinned stage the presence of the second term on the left hand side of equation (3.3) counterbalances the shrinkage due to the right hand side of the same equation and makes the drop expand after a minimum has been reached. This expansion is faster and more intense for smaller drops due to the inverse proportionality of the second term on the left hand side of equation (3.3) to h, which is again in accordance with the experimental results. The solutions of the model for different initial volumes are shown in Fig. 3.7 (lower panels). Table 3.1 gives an overview of the parameters used in the model.

The only input parameters which are taken from the experiment are the initial height, h_o and the initial diameter, D_o. From here the contact angle is calculated aswell as the initial oil/water interfacial tension.

parameter	value
$\gamma^o_{a/w}$	47 mN/m
$\gamma^o_{a/o}$	26.5 mN/m
Γ_m	$2.1 \cdot 10^{-6}$ mol/m^2
K_L	110 m^3/mol
V_m	64.1 mL/mol
C_{sat}	0.15 mol/L
C_{CAC}	0.1 mmol/L
C_{S0}	0.5 mmol/L
$\mathcal{R}^o_D$	$\sim$ 250 s/m
D_S	$2 \cdot 10^{-10}$ m^2/s

Table 3.1: *Parameters of the model*

3.3. Discussion

Despite its simplicity the model quantitatively accounts for all experimental features (compare the model (b) with the experimental results (a) in Fig. 3.7). The pinned stage of the drop is precisely captured as well as the faster shrinkage of smaller drops that also show a steeper rise in the drop diameter before the instability sets in. The dynamics of the system in the induction period is highly non-trivial and the simple model discussed here proves what was expected already, the importance of the interplay between dissolution and adsorption dynamics. Nevertheless the fact that the model describes the dynamics fairly well without taking evaporation of DCM into account shows that evaporation seems not to be a key ingredient for the dynamics during the induction period.

The model allows the evaluation of the water/oil interfacial tension if the oil/air and water/air contributions are known. We have shown that the main process taking place during the induction period is the progressive adsorption of CTAB at the water/oil interface. An evaluation of the spreading coefficient (S) is hence possible during the evolution of the drop in the induction period. These calculations were performed and plotted in Fig. 3.12 for the six experiments of increasing volume modeled in Fig. 3.7.

The spreading coefficient is constant during the shape preserving stage (until t_1) as adsorption is considered to not occur during this stage. The corresponding values are negative which is coherent with the lens shape of the drop, but the calculated values are only slightly negative (between -2.5 and -3.9) At t_1, water/oil adsorption becomes effective and the spreading parameter starts to increase rapidly. At the end of the induction period, indicated by the vertical dotted lines, the spreading

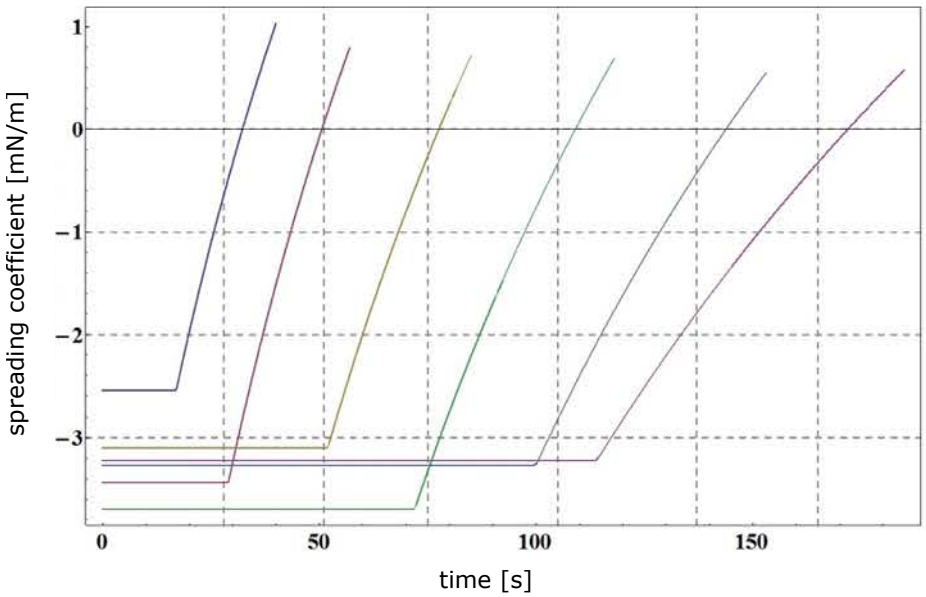

Figure 3.12: *Evolution of the spreading coefficient simulated for drops of increasing volume from 5 to 30* µL *corresponding to the experiments presented in Fig. 3.7. The vertical dotted lines correspond to the time* t_{inst} *at which the instability starts.*

coefficient gets very close to 0. The global evolution of the spreading parameter is certainly caught by the simulation. However the results obtained are not very precise because of several approximations: simple spherical cap geometry is considered, evaporation is neglected and the evaluation of the fixed water/air surface tension does not take into account the contribution of DCM which certainly modifies the implemented value. The evolution of the drop during the induction period and the subsequent expansion of the drop entering the pulsating regime are in any way in agreement with a transition between an initial negative spreading coefficient that switches to a positive value when the instability starts.

3.4. Conclusion

In this chapter we described how the drop behaves during the induction period, which is in fact more complex than it was expected. The dynamical change of the shape of the drop, which was followed in terms of the diameter, height and contact angle, showed different stages among one of them was specifically interesting. The behavior during this stage resembled to what is known for drop pinning of evaporating drops on solid surfaces. It is manifested by the constancy of the diameter while the height and contact angle decrease constantly.

This behavior, which we called "self-pinning" has never been observed on liquid surfaces to our knowledge. With the help of particle image velocimetry (PIV) we discovered that this self-pinning is the result of two antagonistic effects that lead to the observed constancy of the diameter. The mass loss due to evaporation and solubilization of the DCM tends to decrease the diameter while the reduction of the water/oil interfacial tension which is induced by the CTAB adsorption tends to increase the diameter.
So, finally, the dissolution flow that prevents surfactant adsorption at the water/oil interface induces a delay in this adsorption process which has to reach a given value in order for the instability to be triggered.

The effect of confinement on the induction time and the observed instability was also examined. It was observed that confinement increases the induction time due to the fact that when the drop is confined, the film, which forms around it, gets thicker and therefore the water/air interfacial tension is decreasing. This led to a relative increase in the importance of gravity effects which explains the increase of the induction time. Also the observed instability was affected, which did not anymore show the nice pulsations observed in bigger reactors. The behavior of the instability was less ordered and looked more like an effervescent motion, with chaotic ejection of small droplets.

Bibliography

1. A.-M. Cazabat and G. Guena, "Evaporation of macroscopic sessile droplets," *Soft Matter*, vol. 6, pp. 2591–2612, 2010.

2. B. Sobac and D. Brutin, "Triple-line behavior and wettability controlled by nanocoated substrates: Influence on sessile drop evaporation," *Langmuir*, vol. 27, no. 24, pp. 14999–15007, 2011.

3. B. M. Weon and J. H. Je, "Self-pinning by colloids confined at a contact line," *Phys. Rev. Lett.*, vol. 110, p. 028303, Jan 2013.

4. R. G. Larson, "Transport and deposition patterns in drying sessile droplets," *AIChE Journal*, vol. 60, no. 5, pp. 1538–1571, 2014.

5. M. C. Lopes and E. Bonaccurso, "Influence of substrate elasticity on particle deposition patterns from evaporating water-silica suspension droplets," *Soft Matter*, vol. 9, pp. 7942–7950, 2013.

6. R. D. Deegan, O. Bakajin, T. F. Dupont, G. Huber, S. R. Nagel, and T. A. Witten, "Capillary flow as the cause of ring stains from dried liquid drops," *Nature*, vol. 389, pp. 827–829, Oct 1997.

7. K. Sefiane, "Patterns from drying drops," *Advances in Colloid and Interface Science*, vol. 206, pp. 372 – 381, 2014.

8. M. Bentwich, U. Landau, and S. Sideman, "Direct contact heat transfer with change of phase," *International Journal of Heat and Mass Transfer*, vol. 13, no. 6, pp. 945 – 956, 1970.

9. M. Kaneko and Y. H. Mori, "Evaporation of a volatile-liquid lens floating on the surface of a stagnant immiscible liquid," *International Communications in Heat and Mass Transfer*, vol. 11, no. 3, pp. 209 – 218, 1984.

10. T. Nosoko, T. Ohyama, and Y. H. Mori, "Evaporation of volatile-liquid lenses floating on an immiscible-liquid surface: effects of the surface age and fluid purities in n-pentane/water system," *Journal of Fluid Mechanics*, vol. 161, pp. 329–346, 1985.

11. D. Agble and M. Mendes-Tatsis, "The effect of surfactants on interfacial mass transfer in binary liquid-liquid systems," *International Journal of Heat and Mass Transfer*, vol. 43, no. 6, pp. 1025 – 1034, 2000.

12. C. Antoine, J. Irvoas, K. Schwarzenberger, K. Eckert, F. Wodlei, and V. Pimienta, "Self-pinning on a liquid surface," *The Journal of Physical Chemistry Letters*, vol. 7, no. 3, pp. 520–524, 2016.

13. A. A. Pena and C. A. Miller, "Solubilization rates of oils in surfactant solutions and their relationship to mass transport in emulsions," *Advances in Colloid and Interface Science*, vol. 123, pp. 241 – 257, 2006. Special Issue in Honor of Dr. K. L. Mittal.

14. E. L. Cussler, *Diffusion: Mass Transfer in Fluid Systems*. Cambridge University Press, 2009.

15. I. Langmuir, "The condensation and evaporation of gas molecules," *Proc Natl Acad Sci U S A*, vol. 3, pp. 141–147, Mar 1917.

16. I. Langmuir, "The adsorption of gases on plane surfaces of glass, mica and platinum.," *Journal of the American Chemical Society*, vol. 40, no. 9, pp. 1361–1403, 1918.

17. B. von Szyszkowski, "Experimentelle studien ueber kapillare eigenschaften der waesserigen loesungen von fettsaeuren," *Zeitschrift für Physikalische Chemie*, vol. 64, pp. 385–414, 1908.

18. N. Mucic, N. Kovalchuk, V. Pradines, A. Javadi, E. Aksenenko, J. Krägel, and R. Miller, "Dynamic properties of cntab adsorption layers at the water/oil interface," *Colloids and Surfaces A: Physicochemical and Engineering Aspects*, vol. 441, pp. 825 – 830, 2014.

19. E. Johannsen, J. Chung, C. Chang, and E. Franses, "Lipid transport to air/water interfaces," *Colloids and Surfaces*, vol. 53, no. 1, pp. 117 – 134, 1991.

20. C.-H. Chang and E. I. Franses, "Adsorption dynamics of surfactants at the air/water interface: a critical review of mathematical models, data, and mechanisms," *Colloids and Surfaces A: Physicochemical and Engineering Aspects*, vol. 100, pp. 1 – 45, 1995.

21. S. N. Moorkanikkara and D. Blankschtein, "Possible existence of convective currents in surfactant bulk solution in experimental pendant-bubble dynamic surface tension measurements," *Langmuir*, vol. 25, no. 3, pp. 1434–1444, 2009. PMID: 19128044.

22. R. Tadmouri, C. Zedde, C. Routaboul, J.-C. Micheau, and V. Pimienta, "Partition and water/oil adsorption of some surfactants," *The Journal of Physical Chemistry B*, vol. 112, no. 39, pp. 12318–12325, 2008.

23. N. J. Alvarez, D. R. Vogus, L. M. Walker, and S. L. Anna, "Using bulk convection in a microtensiometer to approach kinetic-limited surfactant dynamics at fluid–fluid interfaces," *Journal of Colloid and Interface Science*, vol. 372, no. 1, pp. 183 – 191, 2012.

24. C. Chang, N.-H. Wang, and E. Franses, "Adsorption dynamics of single and binary surfactants at the air/water interface," *Colloids and Surfaces*, vol. 62, no. 4, pp. 321 – 332, 1992.

25. L.-H. Chen and Y.-L. Lee, "Adsorption behavior of surfactants and mass transfer in single-drop extraction," *AIChE Journal*, vol. 46, no. 1, pp. 160–168, 2000.

RESUMÉE EN FRANÇAIS

Dans ce chapitre, nous nous sommes intéressés à la phase d'induction observée avant que l'instabilité ne démarre. Pendant cette phase la goutte garde une forme circulaire et son volume diminue graduellement sous les effets conjugués de l'évaporation et de la solubilisation.
Le diamètre initial de la goutte est parfaitement corrélé aux valeurs de tension superficielle en fonction de la concentration en CTAB en phase aqueuse. Le diamètre initial varie entre 6.5 mm et 10 mm pour des concentrations entre 0.25 mM et 1 mM. Il reste constant et egal à 6.5 mm au-delà de la cmc. Ceci montre que les forces en jeu sont principalement les tensions superficielles s'exerçant sur la ligne triple. Le temps d'induction dépend de différents paramètres : de la concentration en CTAB, du volume de la goutte et de la taille du réacteur. Nous avons effectué une étude systématique de l'évolution de la forme de la goutte (vue de côté) par la mesure du diamètre, de la hauteur et de l'angle de contact dans un réacteur carré pour une concentration de CTAB dans l'eau de 0.5 mM.
Nous avons également effectué des mesure de PIV afin de corréler l'évolution de la forme de la goutte avec les flux convectifs créés autour de la goutte. Ces mesures ont été effectuées dans un réacteur carré de 2 cm de côté.
La phase initiale montre un écoulement dirigé de la surface vers la goutte et qui se prolonge sous celle-ci par un écoulement vertical. Cette phase correspond à la phase d'induction observée avant le début de l'instabilité. Le mouvement du fluide s'inverse lorsque l'instabilité démarre et s'intensifie ensuite pendant cette phase jusqu'à disparition de la goutte (Figure 3.13).

Nous avons effectué ces mesures pour des gouttes entre 5 uL et 30 uL, l'évolution observée reste identique quelque-soit le volume de la goutte. L'évolution de la forme de la goutte avant l'instabilité est la suivante. Lors d'une première phase le diamètre diminue régulièrement, l'angle de contact restant inchangé (comportement attendu). Celle-ci est suivie d'une deuxième phase au cours de laquelle le diamètre reste pratiquement constant alors que l'angle de contact diminue, l'instabilité apparaît ensuite après une brusque augmentation du diamètre. L'évolution observée pendant la deuxième phase est tout à fait inattendue pour une goutte déposée sur surface liquide. Le phénomène

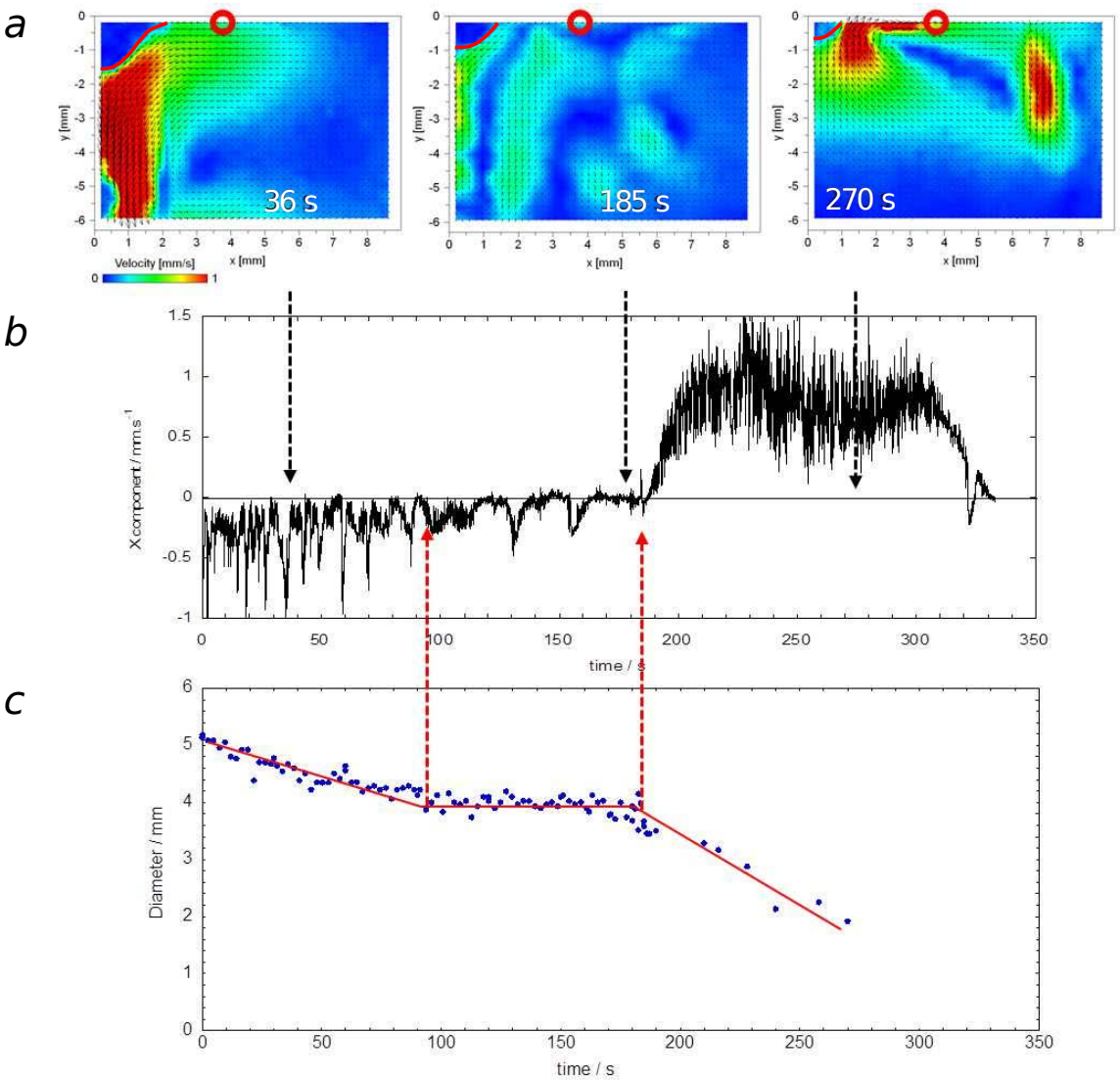

Figure 3.13: *a) Champs de vitesse observés par PIV pour une goutte de 25 uL sur une solution de CTAB à 0.5 mol.L-1. b) Composante en x de la vitesse de flux au point signalé par un cercle rouge. c) Evolution du diamètre au cours de l'évolution du système.*

d'ancrage (diamètre inchangé au cours du transfert de matière) observé n'avait jamais était décrit jusque-là sur surface liquide. Ce phénomène est bien connu dans le cas de gouttes déposées sur substrat solide. Lors de l'évaporation, le volume de la goutte diminue sans variation du diamètre.

Ce phénomène dû aux micro-hétérogénéités de surface est à l'origine du « coffee ring effect » observé en présence de particules. Les surfaces liquides ne présentant pas d'hétérogénéités, l'observation de

cette phase doit trouver une explication différente dans le cas présent. L'intérêt de ce travail est de caractériser la goutte au moment ou l'instabilité démarre. Il apparait que l'instabilité ne démarre que lorsque les effets de tension superficielle dominent les effets dus à la gravité.

L'évolution non conventionnelle du diamètre de la goutte (plateau observé avant la phase d'induction) correspond en fait à une phase au cours de laquelle les mouvements convectifs sont les plus faibles. L'interprétation proposée est la suivante : pendant la première phase, les flux convectifs importants et le renouvellement de l'interface du à la solubilisation limite l'adsorption du CTAB. Celle-ci devient possible dans un deuxième temps. La goutte est alors soumise à deux effets contradictoires, le premier, la solubilisation, a pour effet de diminuer le diamètre de la goutte alors que le deuxième, l'adsorption induirait une augmentation du diamètre. La résultante de ces deux effets pourrait être à l'origine du plateau observé.

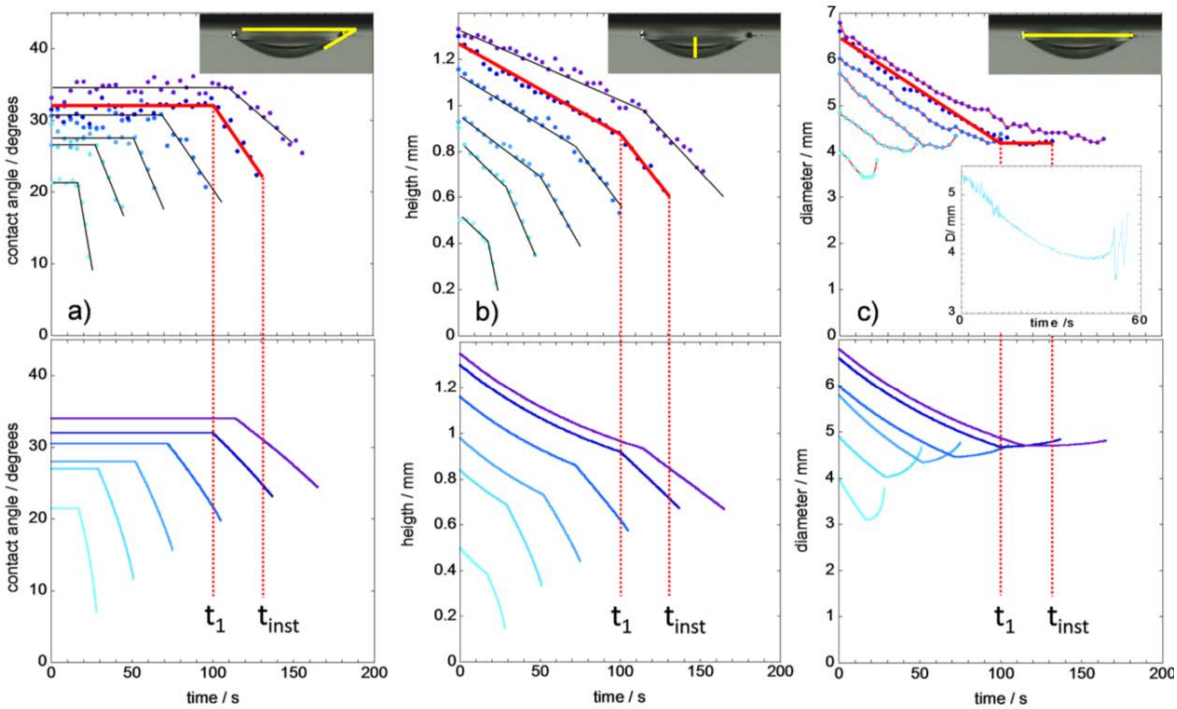

Figure 3.14: *Angle de contact, hauteur et diamètre mesurés au cours de la phase d'induction pour des gouttes entre 5 et 30 uL. Première ligne : expériences ; deuxième ligne : simulation.*

Notre collaboration avec Charles Antoine a permis d'effectuer la modélisation de ce scénario et de reproduire de façon tout à fait remarquable les propriétés des courbes obtenues aux différents vol-

umes (Figure 3.14). Le modèle reproduit l'évolution plus rapide pour les gouttes plus petites ainsi qu'une augmentation plus marquée du diamètre juste avant la période d'induction.

4

The Pulsating Regime and the Rayleigh-Plateau-like Rim Break-Up

"Die Möglichkeit einer mechanischen Erklärung der ganzen Natur ist nicht bewiesen, ja, dass wir dieses Ziel vollkommen erreichen werden, kaum denkbar."

[*The possibility of a mechanistic explanation of the whole nature is not proven, that we will reach this goal hardly imaginable*]

Ludwig Boltzmann

4.1. Introduction

The focus of this chapter is on the toroidal rim, which is formed in the pulsating regime during the last phase of the expansion of the drop and further expands until it eventually breaks-up into smaller droplets. This break-up is strongly reminiscent of what is known as the Rayleigh-Plateau (RP) instability [1].

Before focusing on the rim break-up we will describe and characterize in detail the pulsations the drop is performing in a very regular way. The pulsations of the drop can be visualized through the oscillations of the drop radius. These oscillations are so regular that a simple mechanical mass-spring model is able to reproduce them almost perfectly by considering only an elastic-like force, friction and buoyancy.
Then we will analyze the expanding part of the drop, during which the rim is formed. The expansion of the drop is linear only in the beginning, which is observed for spreading drops on liquids (see discussion in section 2.2 and 2.5), while during the formation of the rim the expansion is accelerated. An accelerated expanding drop has not been observed so far to our knowledge. This last step in the expansion of the drop is one of the key processes to understand the rim break-up in our system.

The following part of the chapter is dedicated to the RP instability and the rim-break up dynamics in our system. Even though the rim break-up resembles quite well the RP instability the characteristic reduced wavelength, $\bar{\lambda}$, observed in our case is a factor of 2 too small. We found a value of 5.91, while a theoretical value of 10.7 in a classic RP instability (considering our viscosities) is expected. One could imagine that this factor of 2 arises due to the special geometry (liquid torus instead of a cylindrical column) and dynamics of our system (accelerated expanding torus instead of a column at rest as well as the connection of the torus to an oil film).
The fact that the experiments for static (i.e. a torus at rest) liquid-liquid toroidal systems[1] (Pairam and Fernández-Nieves [2]) and also for static liquid-solid toroidal systems[2] (McGraw et al. [3]) are in agreement with the standard RP instability indicates that it is not the toroidal structure that gives rise to this difference in $\bar{\lambda}$.
Zhang et. al [4], who studied crown splashes, found that the toroidal rim formed at the edge of a liquid sheet, which is expanding in a decelerated way, also follows the standard RP mechanism. Roisman et al. [5], found again a confirmation of the standard RP mechanism for a decelerated or linear expanding toroidal rim connected to a liquid sheet in a spray impact.

Even in our system we can observe a characteristic reduced wavelength close to the one of the standard RP instability but for different initial conditions. A 5.6µL drop of DCM containing 0.5mM CTAB

[1] $\bar{\lambda} = 11.02$ compared to $\bar{\lambda}_T^{\text{theory}} = 11.64$ (for their viscosities)
[2] $\bar{\lambda} = 9.52$ compared to $\bar{\lambda}_{RP}^{\text{theory}} = 9.02$

on a 0.5mM CTAB solution, a system which shows very complex dewetting dynamics and which will be the subject of the chapter 6, shows a first pulsation, which is expanding in a non-accelerated, linear manner[3]. For this pulsation we find a rim break-up with a reduced characteristic wavelength, which is in agreement with the standard RP mechanism[4].
In summary, static, non-accelerated or decelerated rim expansions are expected to follow the standard RP mechanism.

But it is not only the fact that the toroidal rim is accelerating that differentiates our system from the rim break-ups known in the literature. It is also, and maybe most importantly, the fact that the torus in our system is created from an expanding drop which stays always connected to the rim through a film until its final break-up (even when the mother drop is already receding). This film, in which most certainly also a liquid flow is present due to expansion of the system, is very much like the liquid sheet in the system of Roisman et al.
It seems that it is this film between the mother drop and the toroidal rim, that is responsible for the evolution of the rim break-up and the discrepancy between reduced wavelength obtained for the classical RP instability and the one observed. More precisely the induced flows inside the film and the formation of wrinkles observed inside the connecting film reminiscent of a Benard-Marangoni instability which we will discuss in detail in section 5.6.4.

4.2. Phenomenology of the Drop Pulsations

After a short induction period (tens of seconds), while the drop is changing only slightly its form (as described in detail in the last chapter), the drop starts to expand. During this expansion a toroidal rim is formed (see Fig. 4.21, b)).
This toroidal rim accelerates, while along its perimeter it is getting more and more corrugated. During this time the remaining inner drop is receding (see space-time plot in Fig. 4.4 in the accelerated region, black dashed line). This separation of the toroidal rim from the central inner drop leads to the formation of a film between them. The thickness of this film is expected to be several orders of magnitude bigger than the thickness of the precursor film forming around the drop during the induction phase. At a certain point the rim breaks-up into smaller droplets and the film gets disconnected. These droplets move radially away from the drop. While the film recedes to join the central inner drop even smaller droplets are ejected from its extremities (see Fig. 4.21, c)). As the droplets, which are originated from the toroidal rim, move away radially they get smaller and smaller due to evaporation and dissolution of the DCM. If the size of an ejected droplet is still big enough it can undergo a similar torus formation, which breaks up again into even smaller droplets. When the film

[3] $r(t) \sim t^{\alpha}$, with α close to one ($\alpha = 1.16$)

[4] in this case we get $\bar{\lambda}$ = 12.97 $\pm$ 0.86 compared to $\bar{\lambda}_T^{\text{theory}} = 10.7$ (for our viscosities)

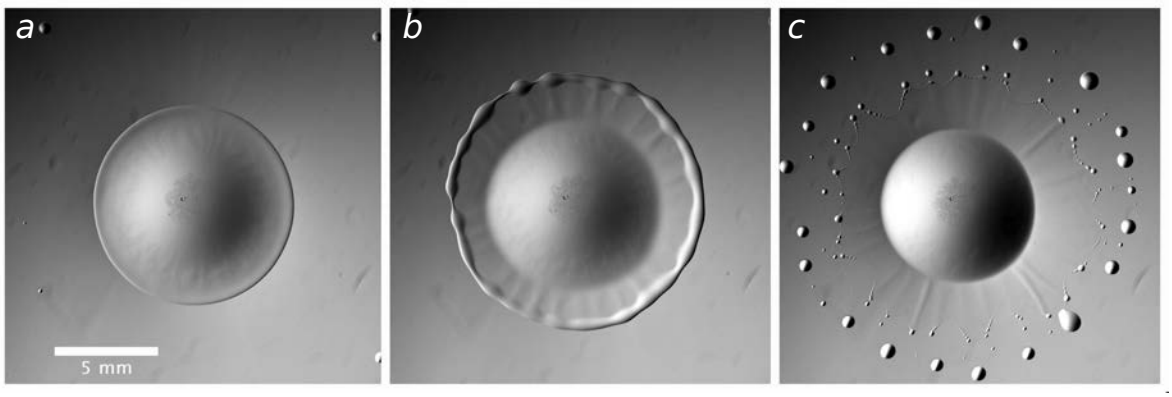

Figure 4.1: *Expansion of the drop and formation of the toroidal rim that breaks-up into smaller droplets. a: First visible appearance of the rim. b: Rim just before the break-up. c: Shortly after rim break-up, when the connecting film is receding, ejecting smaller droplets at its perimeter.*

has completely receded, a new expansion phase arises.

A drop of 25 µL can perform up to 25 pulsations. The regularity of these pulsations is striking and can be visualized by plotting the radius of the drop as a function of time.
Subsequent pulsations get slowly less and less ordered, while there is a trend for larger initial radii of the torus, which leads to the ejection of bigger droplets.
After some time the drop has lost so much volume due to these regular ejections that it cannot form anymore a torus and it gets torn apart in an irregular way. The remaining droplets are dissolving and evaporating quite fast such that finally the whole drop disappears.

The regularity of the pulsations is also reflected in the change in the radius of the drop, which can be nicely modeled with a simple mass-spring model, which is the subject of the following section.

4.3. Periodic Self-Pulsations

The striking regularity of the observed pulsations can be visualized by showing the drop radius as a function of time as shown in Fig. 4.2. In the standard configuration, i.e. for a covered Petri dish, the period increases. The 12th pulsation is already around three times longer than one of the first pulsations (≈ 1.1 s compared to ≈ 3.5 s). This is not the case if the Petri dish is uncovered. In this case the period is quasi-constant and slightly smaller than the initial duration of a pulsation in the closed case (≈ 0.8 s). Fig. 4.2 shows a typical recording of the oscillations of the radius during the pulsating regime.
The recorded oscillations are not time-symmetric: the ascending, spreading parts are slightly longer

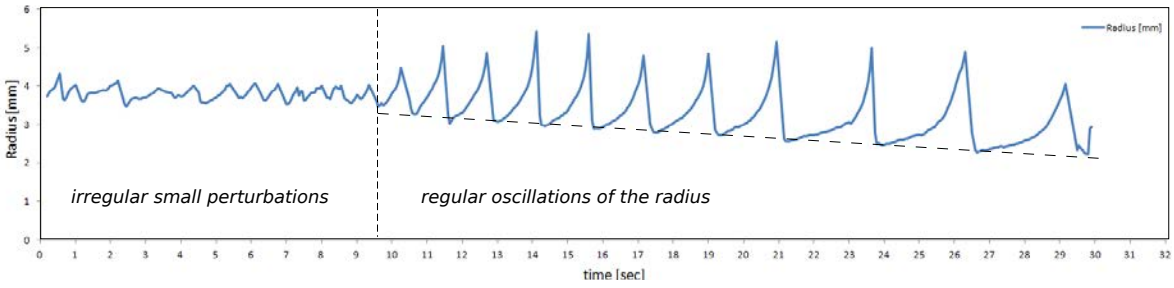

Figure 4.2: *Oscillations of the radius in the pulsating regime. Left side shows transient irregular perturbations of the triple contact line that transform into very regular oscillations. Linear decrease of the minimal drop radius is shown by the dashed line which is due to the mass loss of the drop due to the ejected droplets.*

($\sim$ 60% of the duration) than the descending, receding parts ($\sim$ 40% of the duration). This time-asymmetry increases significantly in the course of time (see the last oscillations compared to first ones in Fig. 4.2).

The radius oscillations of this periodic self-pulsations can be modeled by a very simple mechanical model, which reproduces the observed behavior (Antoine and Pimienta [6]).
The drop rim, that forms during expansion, is described as a toroidal tube of oil, that is located at the drop radius position $R(t)$, having a (time-dependent) mass m. A time-dependent spring parameter $k(t)$, that takes all the springlike forces acting on the rim into account, is used. These forces are surface tensions, Marangoni stress, as well as the drop surface elasticity due to the formation of a surfactant monolayer [7, 8, 9, 10]. The spring parameter can be interpreted as the opposite of an effective spreading coefficient ($S_{\text{eff}}(t) = -k(t)/2\pi$).

The model also takes into account the hydrostatic force acting on the rim and also a kind of damping force, that is caused by the friction of the toroidal rim with the water surface [11, 12, 13]. Finally, by summing up all forces, the dynamics of the rim is given by

$$\frac{d}{dt}\left(m(t)\frac{dR}{dt}\right) = k(t)R + k_0\frac{R_0^4}{R^3} - bR\frac{dR}{dt}, \tag{4.1}$$

where the first term on the right hand side corresponds to the spring-like, the second to the hydrostatic and the third to the frictional forces, where $k_0 = k(t=0)$ and b is the friction coefficient given by

$$b = \frac{8\pi^2\eta}{|\log\left(\frac{1}{Re}\right)|} \tag{4.2}$$

with η and Re being the dynamic viscosity and the Reynolds number respectively. The initial radius, $R(t=0) = R_o$ and the initial expansion velocity $\dot{R}(t=0) = v_o$ where used as initial values to solve

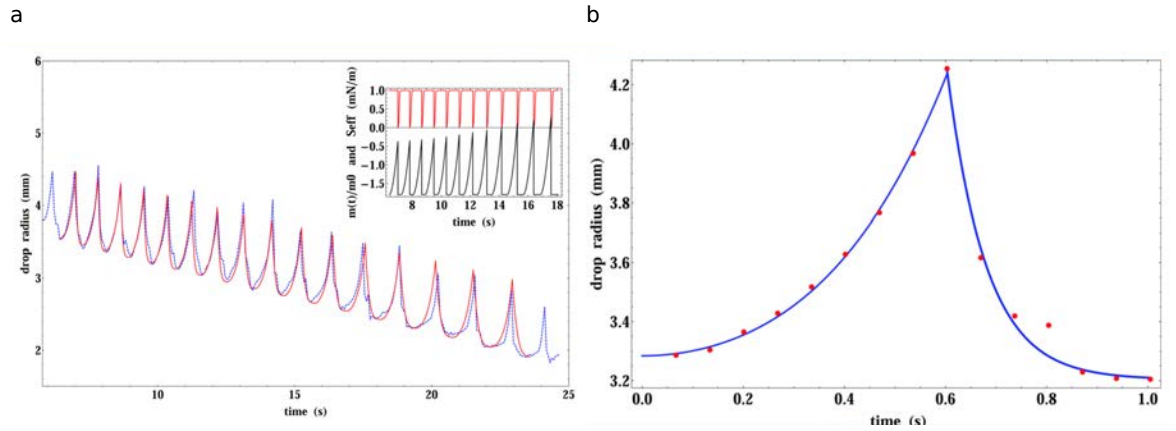

Figure 4.3: *Comparison between model and experimental results. a: Blue: oscillations obtained experimentally; red: theoretical model; inset shows the variation of the mass $m(t)$ and the spreading parameter $S_{\text{eff}}(t)$. b: One oscillation in detail. The asymmetry between spreading and receding part of the oscillation is visible (blue curves are fits of the corresponding parts) (taken from [6]).*

this differential equation. A constant mass m_0 and a decreasing spring parameter $k(t)$ (i.e. an increasing spreading parameter) is considered for the mean ascending part of $R(t)$ and a constant spring parameter k_0 and an increasing mass $m(t)$ for the mean receding part. The whole curve of $R(t)$ can be simulated by choosing a simple rim breakup criterion given by the capillary length. To account for the slight period increase observed, a slight increase of the rim mass over all of the pulsations is included, which actually can be observed experimentally, since the diameter of the rim for subsequent pulsations is increasing. The comparison between model and experimental results is given in Fig. 4.3.

Even thought the theoretical model describes almost perfectly the experimentally obtained oscillations (parameters of the model in 4.1), the physical significance is less clear, specially with the more precise analyses done recently which we will describe in detail later in this chapter starting with the expanding part of the drop where the rim is forming.

parameter	value
mass, m_0	5 mg
spring parameter, k_0	10 mN/m
friction coefficient (spreading), b	0.5 Pa · s
friction coefficient (receding), b	0.73 Pa · s

Table 4.1: *Parameters of the model*

4.4. Drop and Rim Expansion

The expansion of the drop and the formation and further expansion of the rim at the edge of the drop are crucial to understand the rim break-up dynamics. We will look here in detail at the drop expansion and specially at the last stage where the rim is forming.

As seen in Fig. 4.2 and 4.3 the drop is increasing its radius in an accelerated manner while it is spreading. As we will see later, the acceleration part in the increase of the drop starts with the formation of the rim, while during the first (almost linear) part of the acceleration no rim is yet visible. Therefore we distinguish between an elastic deformation of the drop during its expansion and a plastic deformation, which corresponds to the rim formation and which ends up with the rim detachment from the drop.

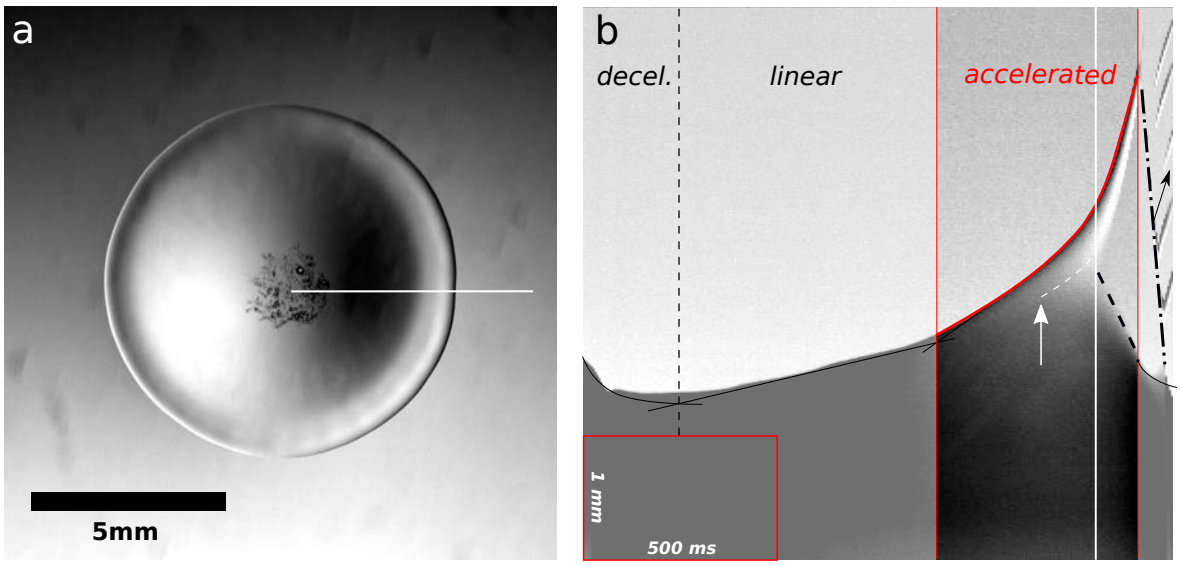

Figure 4.4: *Drop during expansion phase. a: Image of a drop in the expanding phase, where the rim and the connecting film is visible. b: Space-Time plot of the rim expansion (along the white line shown in (a)) showing the different phases of expansion (white line in the accelerated expansion phase corresponds to the time of the image in (a)*

The drop expansion can be visualized by a time-space plot along a ray starting from the center of the drop (see Fig. 4.4). We can distinguish three different phases of expansion. It starts with a linear expansion of velocity $v_1 = 0.8\ mm \cdot s^{-1}$, which changes after some time to an accelerated regime with an initial velocity of v_2 =2.3 $mm \cdot s^{-1}$. During the accelerated phase the rim gets separated from the drop, while still being connected through a film. As the rim advances the edge of the inner drop recedes with a velocity of 6 $mm \cdot s^{-1}$. At the end of the accelerated phase the rim breaks-up and the

resulting droplets get disconnected from the film and escape with a velocity of around 10 $mm \cdot s^{-1}$ (black arrow in Fig. 4.4). In the next phase the film is receding with a speed of 31 $mm \cdot s^{-1}$ (dotted-dashed line), while the retraction of the inner drop is slowing down. All velocity values mentioned here are measured from one single pulsation, which is shown in Fig. 4.4. The relative variance of these velocities for an average over 7 pulsations is of around 20 %.

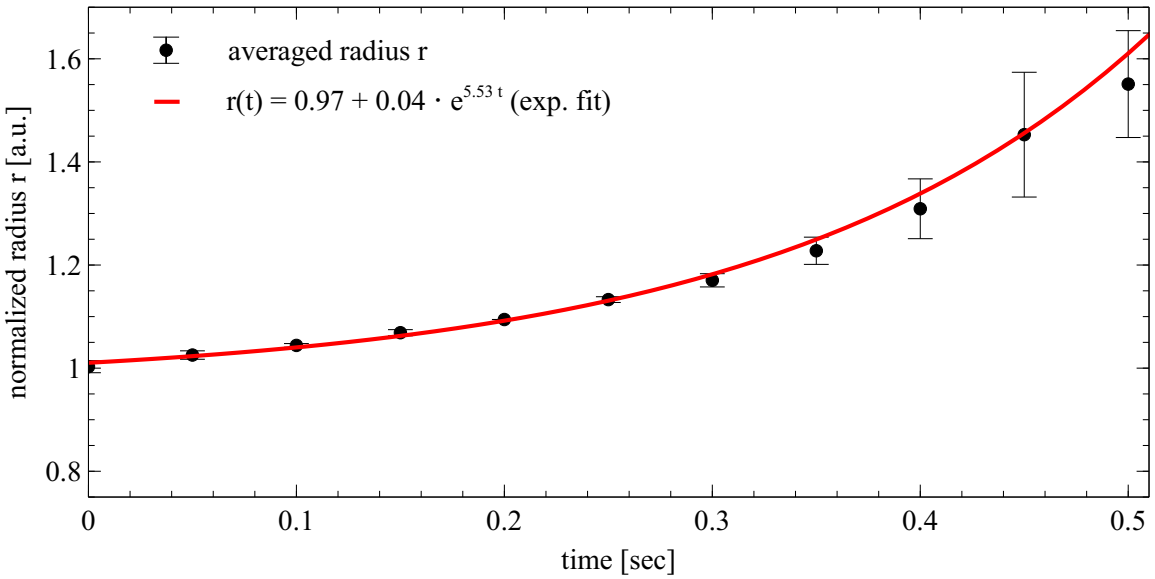

Figure 4.5: *Fit of the normalized radius $r(t)$ averaged over 7 different pulsations.*

In general the rim acceleration is slightly getting smaller for subsequent pulsations (as seen from Fig. 4.2). At the same time also the droplet radius is getting smaller due to the loss of volume due to ejections (mass loss per pulsation is estimated to be around 1-3µL and the measured radius change is of the order of 0.11 mm per pulsation).
The phase, which is of interest for us, is the accelerated one since it is the one in which the toroidal rim is forming and getting detached (first visible appearance of the rim shown by the white arrow in Fig. 4.4). At around 80% of the accelerated phase (white line in Fig. 4.4 (b)) the film between the rim and the central inner drop is getting visible.

We fitted the reduced drop radius, $r(t) := R(t)/R_o$, (where R_o is the radius corresponding to the change between the linear and accelerated regime) with

$$r(t) = \alpha + \beta e^{\sigma t} \qquad \text{with} \quad \alpha = 0.97, \;\; \beta = 0.04, \;\; \sigma = 5.53 s^{-1} \tag{4.3}$$

for the accelerated expansion phase averaged over 7 different pulsations (see Fig. 4.5). The initial

acceleration is given by $a_o = 4.91 \pm 0.03\ mm \cdot s^{-2}$. See Fig. 4.5 for details.

A visible torus is forming at around 50% of the accelerated expansion (white arrow in Fig. 4.4 (b)). At this times the toroidal rim is expanding with an acceleration of $a_o = 19.59 \pm 0.05\ mm \cdot s^{-2}$.

In the following section we will have a closer look to the way the rim is breaking up into smaller droplets and how the number of ejected droplets is related to the dimensions of the rim.

4.5. Rayleigh-Plateau Instability

The rim that is forming at the edge of the drop during its accelerated expansion has a toroidal tube-like geometry. As this rim further expands, while the drop is already receding, it gets more and more corrugated and finally breaks-up into many smaller droplets, which are radially ejected.
This break-up of the rim into smaller droplets, looks very similar to what is happening with a liquid column due to the Rayleigh-Plateau (RP) instability even though here we have a toroidal column rather then a cylindrical one (see Fig. 4.6).

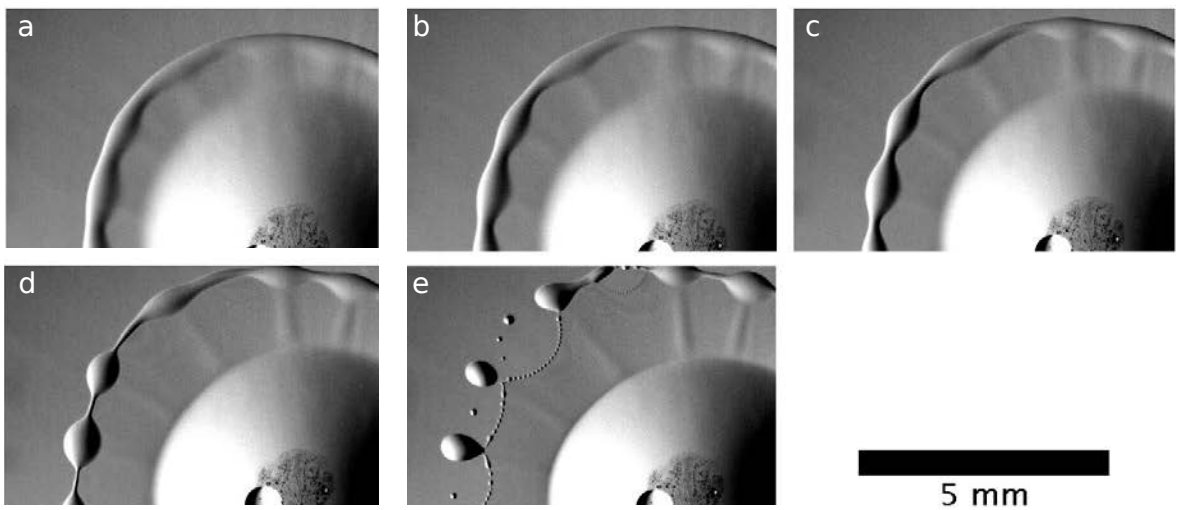

Figure 4.6: *Evolution of the rim until its final break-up.*

In the following we will introduce the RP instability and discuss the differences and common points between the toroidal rim break-up in our system and the RP instability occurring on a cylindrical column.

4.5.1. Standard Rayleigh-Plateau Instability

The RP instabilty was discovered by Plateau [14] and further investigated theoretically by Lord Rayleigh [15]. It is observed for a liquid column, as for example for a liquid jet from a tap. Random initial fluctuations of the surface of the column are more and more amplified, and the column progressively gets modulated and eventually breaks up into droplets (see Fig. 4.7 (A)). The characteristic parameters of this instability are the initial unperturbed radius of the column a and the characteristic (maximum) wavelength of the perturbation λ_{max}. Rayleigh found a relation between the initial unperturbed radius and the characteristic wavelength by using a linear stability analysis of the interface, which reads

$$\lambda_{max} = 9.02\ a. \tag{4.4}$$

This relation was in good agreement with the experimental values. Nevertheless Rayleigh was not taking into account the viscosity of the column and the sourrounding liquid (gas). This was done later by Tomotika in 1935 [16]. Regarding the viscosities in our system Tomotika predicts a slightly bigger value , i.e.

$$\lambda_{max} = 10.7\ a. \tag{4.5}$$

In the following we will call the ratio of the characteristic wavelength and the initial unperturbed radius, λ_{max}/a, the reduced characteristic wavelength, $\bar{\lambda}$, i.e.

$$\bar{\lambda} = \frac{\lambda_{max}}{a}. \tag{4.6}$$

and obtain

$$\lambda_{max} = \bar{\lambda} \cdot a, \tag{4.7}$$

where $\bar{\lambda}$ is a function of the viscosities of the column and the surrounding liquid.

4.5.2. Toroidal Rayleigh-Plateau Instability

The first difference between our system and the classical RP system is that we have a liquid torus instead of a cylindrical column (see Fig. 4.7 (B)). For rim break-ups having a toroidal structure the role of the characteristic wavelength is played by the opening angle, φ (which could be also represented by the number of future droplets, i.e. $n = 2\pi/\varphi$) and the role of the initial unperturbed diameter is played by the aspect ratio, ψ, i.e. the ratio between the initial unperturbed minor radius of the torus, a, and the major radius of the torus, R_a:

$$\psi = \frac{a}{R_a} \tag{4.8}$$

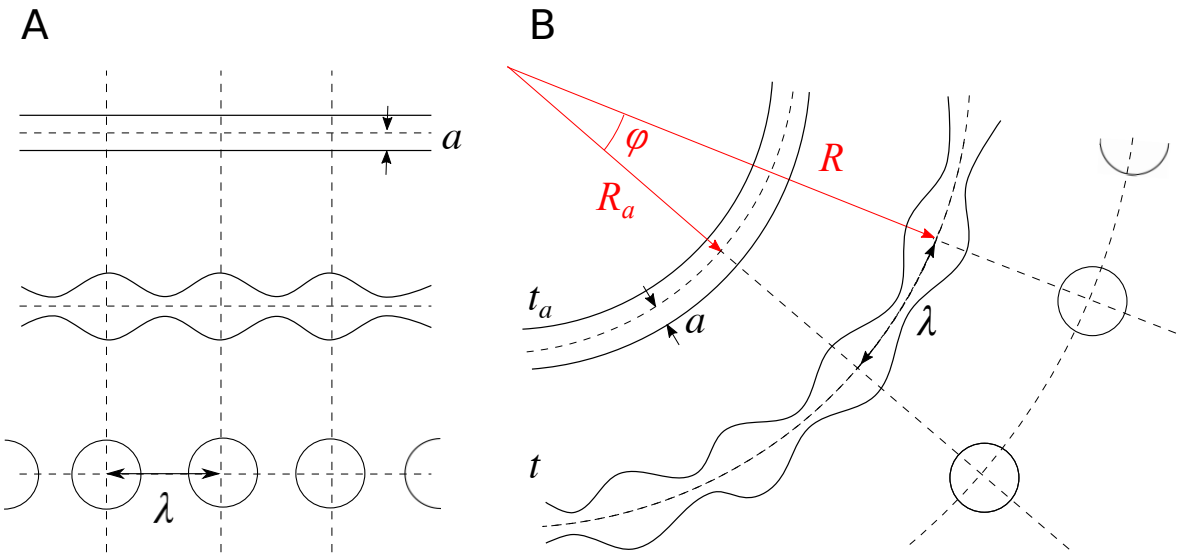

Figure 4.7: *Rim Break-up instabilities. a: Standard RP instability; a is the initial unperturbed radius and λ is the characteristic wavelength of the perturbation. b: Expanding toroidal rim break-up instability; a is the initial unperturbed radius and λ is the characteristic wavelength of the perturbation measured at the time $t' > t_a$. R and R_a are the major radii of the torus at the times t_a and t.*

Such systems were investigated by Pairam et al. [2] and Gonzalez et al. [17], who used these parameters to characterize their toroidal systems.
Instead of having a direct proportionality between the initial unperturbed radius, a, and the characteristic wavelength, λ, as for a cylindrical column, here we have a direct proportionality of the opening angle, φ, and the aspect ratio, ψ for a toroidal geometry, i.e.

$$\varphi = \bar{\lambda} \cdot \psi. \qquad \leftrightarrow \qquad \varphi \cdot R_a = \bar{\lambda} \cdot a \tag{4.9}$$

But the tori of their systems are static, i.e. they are not expanding with time. Fig. 4.7 (B) shows actually the scheme of an expanding torus as in our system. In such a case the major radius of the torus, R, is increasing while at the same time the modulation and amplification of the perturbation takes place. This parallel evolution leads to interesting and non-trivial results which will be discussed in detail in the next section.

4.6. Expanding Toroidal Rim

Due to its expansion, the torus is stretched, and with it its modulations. That is why in this case the characteristic wavelength λ_{max} is not anymore a constant as in the classical RP instability but is

increasing with time, i.e. $\lambda_{max} = \lambda_{max}(t)$.
To compare it with the characteristic wavelength of the classical RP instability we decided to measure the characteristic wavelength at a certain time during the evolution of the torus. This instant was chosen before the corrugation of the torus became too big so as to be compared with the theoretical results from the linear stability analysis.

4.6.1. Constancy of the Opening Angle during one Pulsation

Before determining the right instant when to measure the characteristic wavelength, we will investigate the time dependency of the characteristic wavelength and its connection to the stretching of the torus.

The drifting apart of the corrugations (i.e. the increase in the wavelength) is due to the (longitudinal) stretching, which is known in the literature for cylindrical columns (e.g. Eggers and Villermaux [18]). In our case the stretching has its origin in the expansion of the torus, which leads to an increase of its circumference.
In other words the characteristic wavelength follows the radius, R, that increases during the expansion. We find experimentally that

$$\lambda(t) = \lambda_o \cdot \Lambda(t) \tag{4.10}$$

where $\Lambda(t)$ increases exponentially. On the other hand the radius of the torus increases as

$$R(t) = R_o \cdot \mathcal{R}(t) \tag{4.11}$$

The circumference, L, is given by $L = 2\pi R$ and $L = n \cdot \lambda$, where n is the number of corrugations (future droplets). That leads to $2\pi R = n \cdot \lambda$ and therefore we get

$$\lambda = \frac{2\pi R}{n} \qquad \text{which leads to} \qquad \lambda(t) = \underbrace{\frac{2\pi R_o}{n}}_{=\lambda_o} \cdot \mathcal{R}(t) = \lambda_o \cdot \mathcal{R}(t).$$

Comparing this with Eqn. (4.10) we see immediately that $\Lambda(t) = \mathcal{R}(t)$, which shows that actually λ is following the time dependency of R.

With the relations we derived above, together with the expression for the opening angle we find

$$\varphi = \frac{\lambda}{R} = \frac{\lambda(t)}{R(t)} = \frac{\lambda_o \cdot \Lambda(t)}{R_o \cdot \mathcal{R}(t)} \overset{\Lambda(t)=\mathcal{R}(t)}{\overset{\downarrow}{=}} \frac{\lambda_o}{R_o} := \varphi_o = \text{constant}. \tag{4.12}$$

The constancy of the opening angle is a direct result of the stretching of the toroidal rim, as well as the time dependency of the characteristic wavelength which follows the radius evolution.

The opening angle, as shown here, is a constant of the pulsation but is not the same for different pulsations. The opening angle is increasing for subsequent pulsations and this seems to be connected to the increase in the initial unperturbed radius. This relation between the opening angle and the initial unperturbed radius will be discussed in a following section. But before we will determine the instant at which the characteristic wavelength has to be measured.

4.6.2. Evolution Parameter

The choice of the instant to measure the characteristic wavelength should be around the time when the undulation of the rim is not yet to pronounced. But this instant is not the same for all the pulsations since the initial unperturbed radius of the rim, a, can be different for different experiments, even if the initial conditions are the same.

The origin of this variance is not clear to us but it might be connected to the deposition of the drop on the surface (see appendix for details). The variation is of the order of 20%. This variance and the fact that the time for one pulsation is increasing for subsequent pulsations makes it difficult to compare different pulsations.

By introducing a non-dimensional evolution parameter τ (rescaling the time by the time the torus needs to break-up, $T_{\text{break-up}}$), this problem could be solved. τ is defined as

$$\tau := \frac{t_R - t_{R_o}}{T_{\text{break-up}}} \qquad \text{(with} \quad t_{R_i} = t(R_i) \quad \text{and} \quad T_{\text{break-up}} = t_{R_{min}} - t_{R_o}) \tag{4.13}$$

where t_{R_o} is the time when the rim is first visible and $t_{R_{min}}$ is the time just before the rim breaks up. The instant t_R, which can be expressed by rewriting (4.13), i.e.

$$t_R(\tau) = \tau \cdot t_{R_{min}} + (1 - \tau) \cdot t_{R_o}, \tag{4.14}$$

is the time which corresponds to the chosen value of the evolution parameter τ and runs between 0 and 1. This time will be different for different pulsations but it will show the same level of evolution of the torus in different pulsations.

With this evolution parameter we are now able to compare different pulsations with each others, as seen in Fig. 4.8, where two very different pulsations were compared. One with a large initial unperturbed radius and the other with a smaller one.

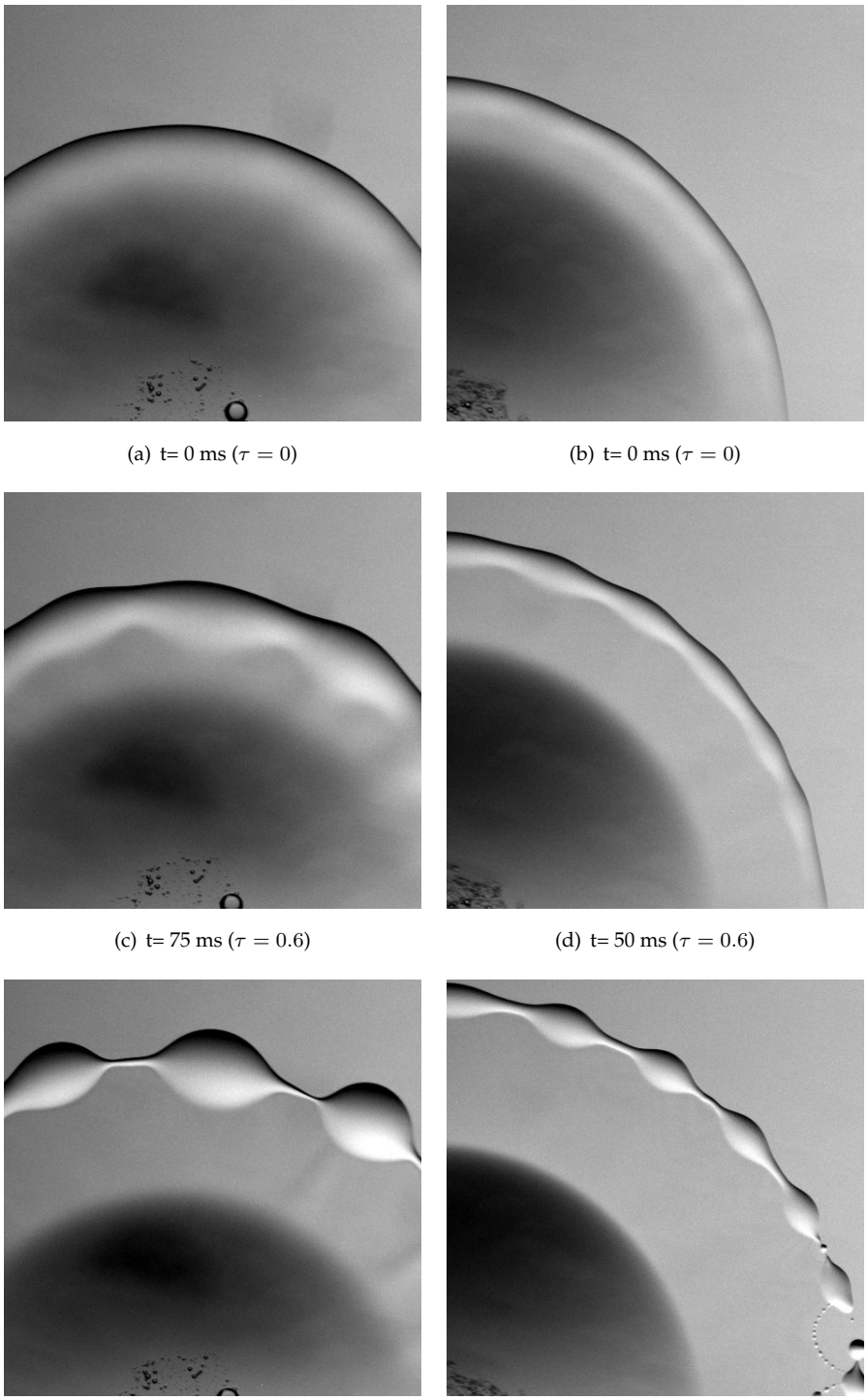

(a) t= 0 ms ($\tau = 0$)

(b) t= 0 ms ($\tau = 0$)

(c) t= 75 ms ($\tau = 0.6$)

(d) t= 50 ms ($\tau = 0.6$)

(e) t= 125 ms ($\tau = 1$)

(f) t= 85 ms ($\tau = 1$)

Figure 4.8: *Comparison of two different pulsations shows that τ represents a good parameter to follow the evolution of the rim instability.*

4.6.3. Reduced Characteristic Wavelength and Invariant Wavenumber

Now that we have found an evolution parameter we are able to compare different pulsations. We have chosen $\tau = 0.6 := \tau^*$) to compare them since for this value the modulations are still not too big and therefore the above mentioned criteria for comparison is fulfilled (Fig. 4.8 (c) and (d)). The increase of the wavelength from this instant on until $\tau = 1$, i.e. until the rim breaks up, is of the order of 30%.
With this method we have determined the characteristic reduced wavelength, $\bar{\lambda}$, for 22 experiments and we obtained an average value of 5.91 ± 0.95 (Fig. 4.9 (a)).

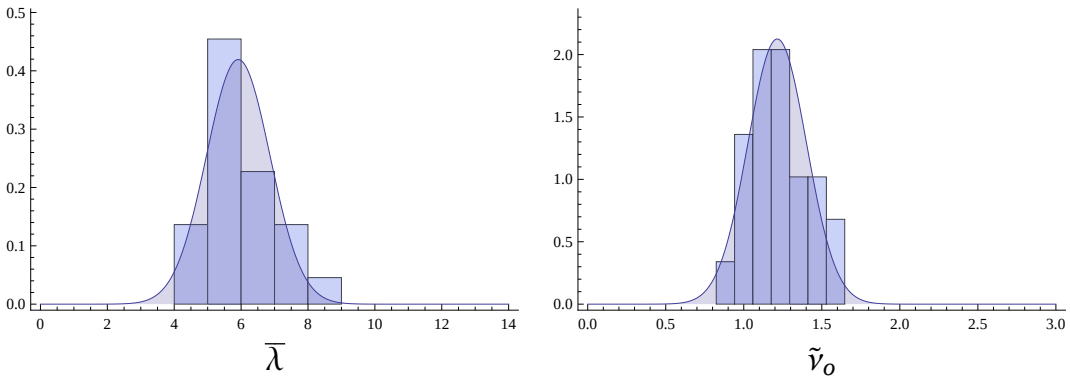

(a) Characteristic reduced wavelength for the toroidal rim break-up ($\langle\bar{\lambda}\rangle = 5.91 \pm 0.95$)

(b) Invariant wavenumber for the toroidal rim break-up ($\langle\tilde{\nu}_o\rangle = 1.21 \pm 0.19\ \mathrm{mm}^{-1}$)

Figure 4.9: *Statistics on the characteristic reduced wavelength and the invariant wavenumber for the toroidal rim break-up.*

This value is around half the value expected by the standard RP instability. We will soon discuss in detail the possibilities to obtain this unexpected small value for the characteristic reduced wavelength.

Before doing that we will discuss another interesting observation. As mentioned above the initial unperturbed radius can vary from experiment to experiment and also within one experiment for subsequent pulsations. Nevertheless it seems to be the case that the opening angle is bigger when the initial unperturbed radius is bigger and vice versa. To verify this qualitative observation we calculated the ratio between the opening angle φ and the initial unperturbed radius a for different pulsations, which we called the invariant wavenumber, $\tilde{\nu}_o$, i.e.

$$\tilde{\nu}_o = \frac{\varphi}{a}. \tag{4.15}$$

We find a value of $\tilde{\nu}_o = 1.21 \pm 0.19\ \mathrm{mm}^{-1}$ averaged again over 22 experiments (Fig. 4.9 (b)).

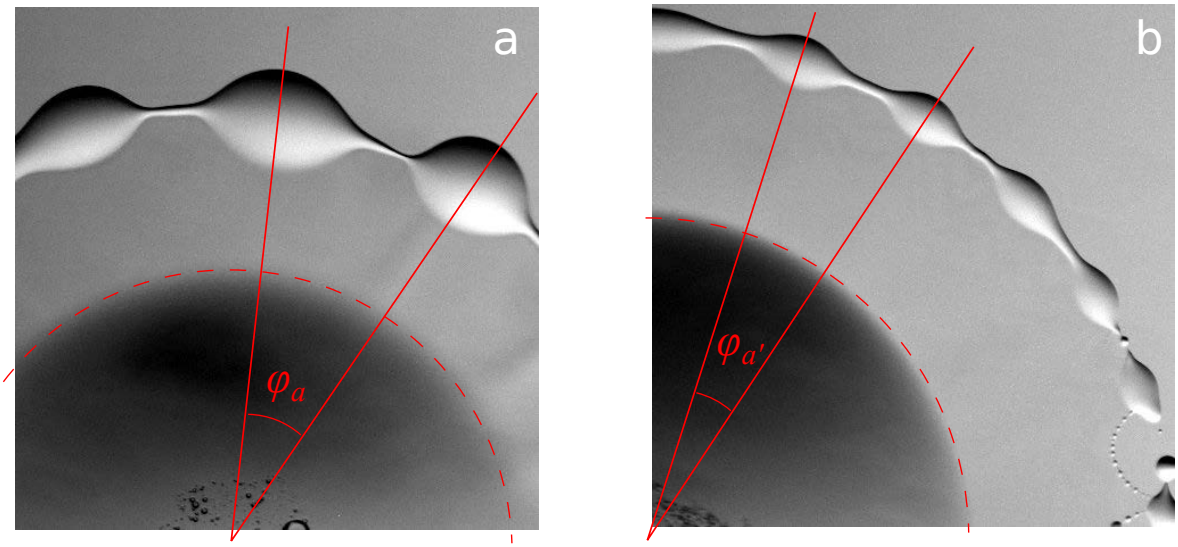

Figure 4.10: *Opening angles φ for tori with a big (a) and a small (b) initial unperturbed radius a.*

The theoretical expression for $\tilde{\nu}_o$ can be derived from the equation (4.7) and it reads

$$\tilde{\nu}_o = \bar{\lambda} \cdot \kappa, \tag{4.16}$$

where $\bar{\lambda}$ is the characteristic reduced wavelength and κ is the major curvature of the torus both for $\tau = \tau^*$, i.e. the inverse of the major radius, $R(\tau^*)$.

The relatively large variance of $\tilde{\nu}_o$ can be attributed to the asymmetry of the rim break-up in most pulsations. By taking the local (curvature) radius for R, as shown in Fig. 4.11, the variance of $\tilde{\nu}_o$ reduces significantly (up to 10 %).
The invariance of $\tilde{\nu}_o$ together with the invariance of the reduced wavelength, $\bar{\lambda}$, leads to the fact that the major radius $R(\tau^*)$ has to be a constant too since they are connected by the Eqn. (4.16). The experimental measured values do actually confirm this ($\bar{R}(\tau^*) = 4.67 \pm 0.61$ mm). Consequently also the major radius for the rim break-up, i.e. $R(\tau = 1) := R_{max}$, has to be invariant.

Most probably the invariance of R_{max} is connected to the break-up time of the rim, $T_{\text{break-up}}$, since it is the time needed to reach R_{max}. In order to justify the latter we examine here qualitatively the dependency of $T_{\text{break-up}}$ on the opening angle and on the initial unperturbed radius by making use of the invariance of $\tilde{\nu}_o$.
Having a bigger initial unperturbed radius leads to an increase in the breakup time (which is also

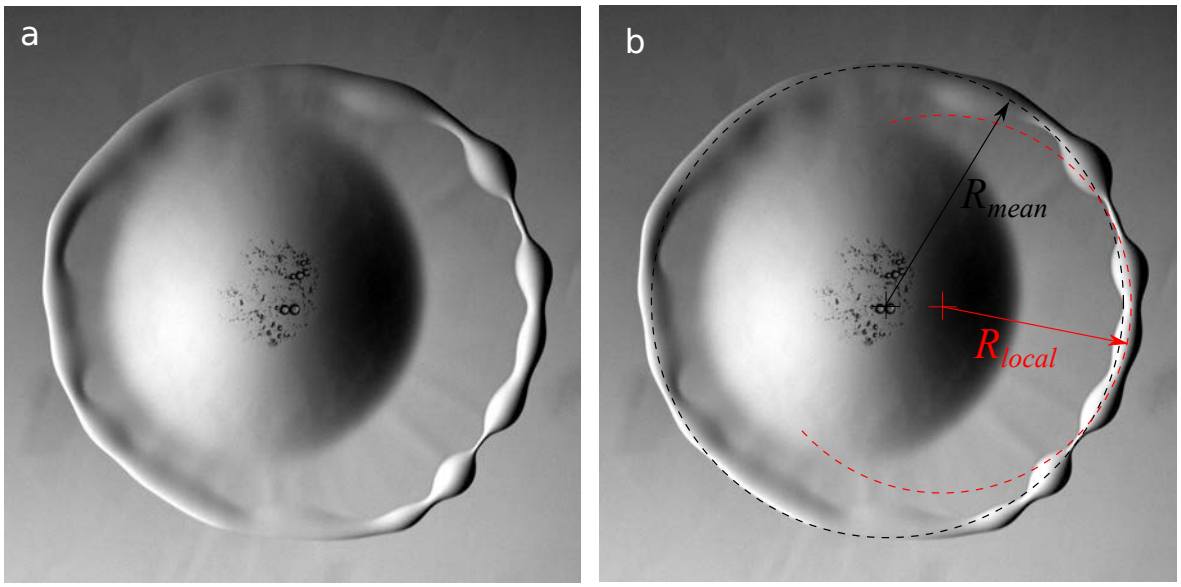

Figure 4.11: *Decrease in the opening angle φ due to an decrease of the initial unperturbed radius a. Left: Bigger a. Right: Smaller a.*

expected by the classical RP instability[5]). On the other hand a bigger opening angle leads to an increase of the drift velocity of the relative movement of the corrugations and so $T_{\text{break-up}}$ is expected to decrease[6]. Hence qualitatively we may say that $T_{\text{break-up}}$ is proportional to the ratio of these parameters, i.e. $T_{\text{break-up}} \sim \frac{a}{\varphi} = \tilde{\nu}_o^{-1}$, so actually proportional to $\tilde{\nu}_o^{-1}$. Since $\tilde{\nu}_o$ itself is invariant, at least in a first order approach, the break-up time can be considered to be also invariant.
In other words the interplay between the opening angle and the initial unperturbed radius for a toroidal structure is in such a way that the break-up time becomes an invariant, explaining the invariance of $\tilde{\nu}_o$.

These more qualitative argumentations can be seen as a first approach in understanding this interesting connection between the opening angle and the initial unperturbed radius of the rim, but it definitely needs further experimental and theoretical investigations to get a better insight in the actual mechanisms at play.

[5]for a linear column this time is given by $T_{break-up} = \frac{1}{\omega_{max}} \log\left(\frac{a^2\omega_{max}}{\tilde{A}}\right)$, where ω_{max} and $\tilde{A}$ are the frequency and the amplitude of the fastest growing mode of disturbance respectively

[6]this makes sense since in the classical RP instability, as mentioned above, $T_{\text{break-up}}$ is depending on the parameter a which role is played by the aspect ratio ψ (which is directly proportional to φ as mentioned above) in the toroidal case.

4.6.3.1. The Existence of Subharmonic Frequencies

Another experimental observation that shows the complexity of the phenomena is the formation of what is known as "secondary swelling" in the literature (Rutland and Jameson [19]), which is the formation of undulations in between two peaks of the characteristic perturbation frequency. This effect was explained theoretically by Yuen in 1968 [20] by using a non-linear theory. He finds that at large times the formation of a peak between two peaks of the characteristic perturbation frequency is possible. He attributes this to the fact that energy is transferred between harmonics such that subharmonic frequencies can arise. In some of our experiments we can clearly see this kind of secondary swelling (Fig. 4.12). It is experimentally not trivial to distinguish between secondary swelling and undulations with the characteristic perturbation frequency. This could be another possible explanation why we observe a too small perturbation wavelength.

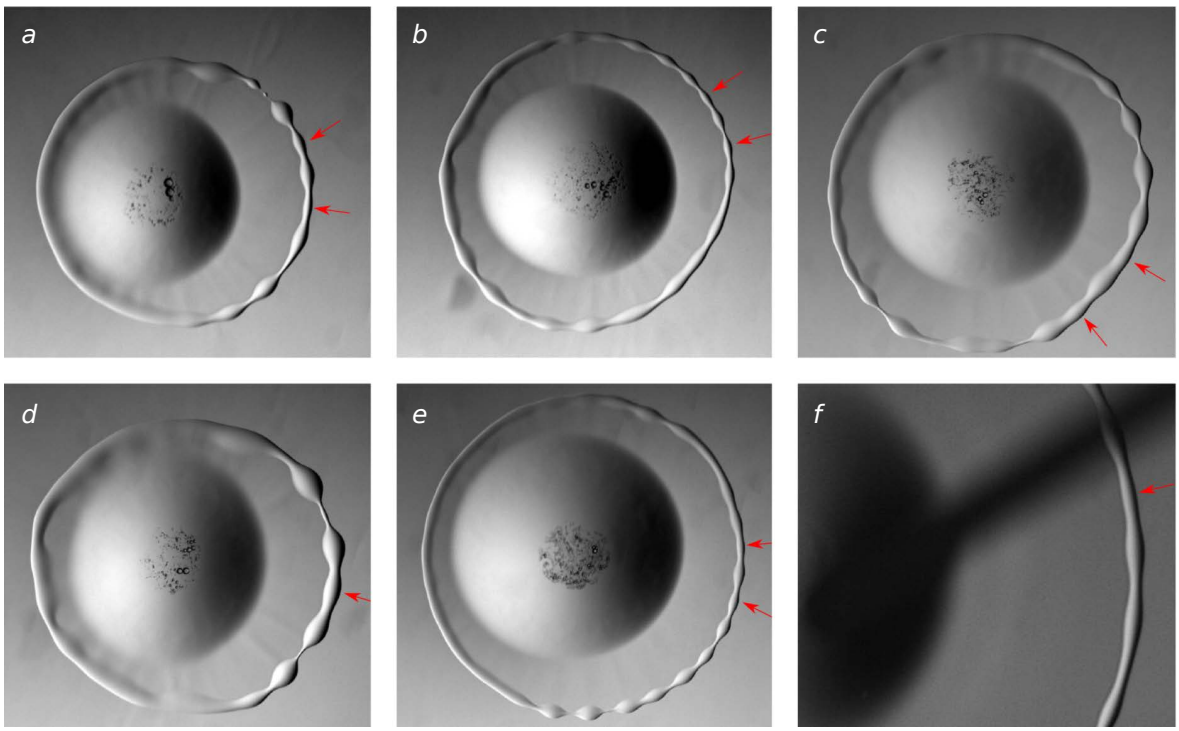

Figure 4.12: *Secondary swelling in our experiments. a-e: 25 µL DCM on a 0.5 mM CTAB solution. f: First pulsation after impact of a 25 µL DCM containing 0.5 mM CTAB on a 0.5 mM CTAB solution.*

4.6.4. Wrinkles in the Film and its Connection to the Characteristic wavelength

Coming back to the characteristic wavelength observed for the toroidal rim break-up, we will now look closer at the processes connected to the formation of the rim.

One major difference between our system and other systems in the literature is that in our case the rim is created from an expanding drop. And additionally that the rim is, from its creation to its break-up, connected to the central drop from which it was generated. The connection is made through a thin film.
The discrepancy between the observed characteristic wavelength and the one predicted by a standard RP instability is expected to come from this particularity of our system.
In the following we will look in detail at what is happening during the formation of the drop until the break-up of the toroidal rim.

During the drop expansion structures are formed inside the droplet close to its boundary. They are observed from the very beginning of the expansion. These structures have a striking periodicity, which can be seen in Fig. 4.13 (a) (black arrows). As the drop expands we see the formation of the toroidal rim, which during expansion gets more and more corrugated until it breaks up. Fig. 4.13 (b) shows the toroidal rim during the breaking up process.
Additionally we see other structures forming, that connect the central inner drop to the highly corrugated regions of the rim. We call these structures wrinkles (they can be very nicely seen in Fig. 4.13 (b)). These two different structures seem to be related to each other and moreover they seem to be the determining reason for the corrugation wavelength.

The first structures have the form of a semi-ellipse and an average width of $d = 0.72 \pm 0.16$ mm (see regions indicated by the black arrows in Fig. 4.13 (a)) which move radially outwards, following the expansion of the drop. Fig. 4.13 d) shows a perimetral projection of the image in 4.13 (a) to better follow the evolution of these structures. The white arrows shown in this figure indicate the semi-elliptic structures, while the red lines separate them. As time evolves these structures move radially outwards. At the moment when the rim gets visible we see also corrugations arising in the film, which connect the inner drop to the toroidal rim. These are the wrinkles mentioned above.

A clear correlation appears between the number of structurations, the wrinkles and the future droplets in the white boxed area in Fig. 5 suggests a direct connection between these structures, i.e. in the sense that one evolves from the other. Nevertheless, outside the box the correlation is not perfect, which can be attributed to secondary effect at play in the complex evolution of the expansion of the drop. For example, the structurations 2 and 3 or 14 and 15 (in a') are reuniting to give rise to only one wrinkle (wrinkle 2 or 11). Also the correlation between wrinkles and future droplets is not perfect

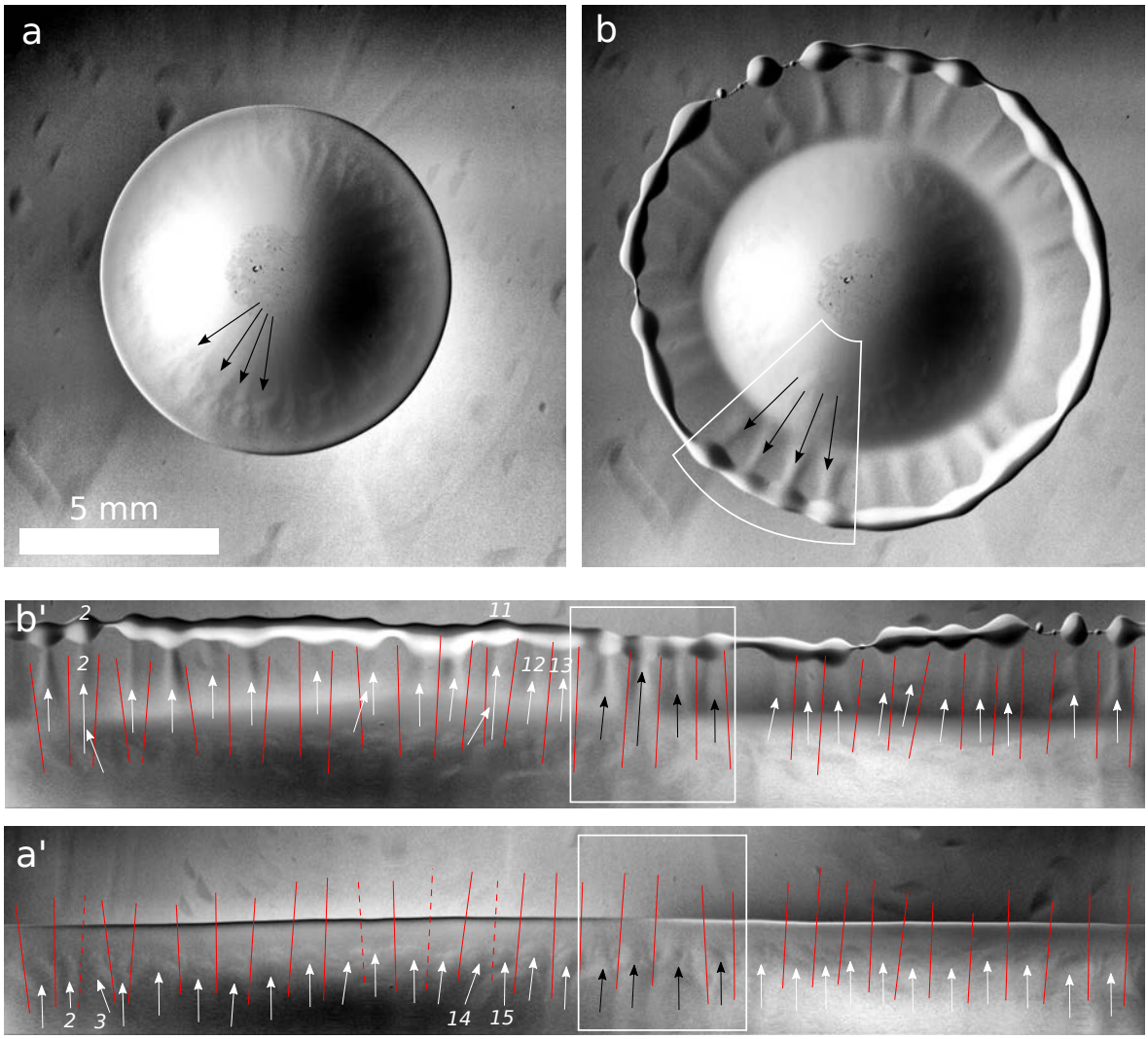

Figure 4.13: *Periodic structuration inside the DCM drop. a: Structuration at the time when the rim is starting to form (a′ is the perimetral projection of a). b: Drop at the time just before the rim starts to break-up (b′ is the perimetral projection of b). Numbers in a′ denote the number of the structure, while the lower numbers in b′ denote the number of wrinkles and the upper number denote the number of future droplets. A strong correlation between the number of structurations, the wrinkles and the future droplets is visible in the white boxed area.*

due to coalescence processes taking place in the rim. An example is given for wrinkles 12 and 13 (in b′) which are giving rise to an elongated undulation on the rim that leads to only one ejected droplet.

The correspondence between these structures supports the idea that the small ejected droplets are

created in a continuous evolution that originates from the mother drop. Moreover the periodicity of the initial semi-elliptic structures seem to be the determining cause for the characteristic wavelength on the torus modulation.

4.6.4.1. Direct Effect of the Wrinkles on the Rim Break-Up

The presence of height inhomogeneities in the film during expansion act as a kind of initial condition for the RP-instability. In contrast to the classical RP instability, which is induced by random fluctuations of the rim the instability in our case might be induced by the already existing thickness inhomogeneities.

An interesting observation shed some light on the possible effect of wrinkles on the rim break-up. In a first pulsation of a drop containing 0.5mM CTAB on a 0.5mM CTAB solution a perfect rim formation takes places with no visible wrinkles formation. Then, at one place of the drop close to the rim (Fig. 4.14, in the middle of the red boxed area) a small air bubble explodes and gives rise to surface waves which induce height modulations, that led to the formation of wrinkles in the film close to it (visible in Fig. 4.14 (a6)). And it was just at this place where the rim broke-up earlier than at the rest of the rim (Fig. 4.14 (d)).
Calculating the corresponding reduced wavelength for this "bubble induced" instability leads to $\bar{\lambda} = 6.42$, which is within the range of the values we get for our pulsations (see Fig. 4.9).
Measuring the wavelength on other parts of the rim we obtain values of 12.36 (lower right part) or 13.58 (upper right part), where no bridges are formed. These values are close to what is expected for a viscous RP instability.

In the following we will look closer at "how" these structures inside the drop could be formed. It seems that these structures are like convective cells which are formed due to flows which might be induced by the expansion of the drop but might also be induced by the evaporation of the DCM from the surface.

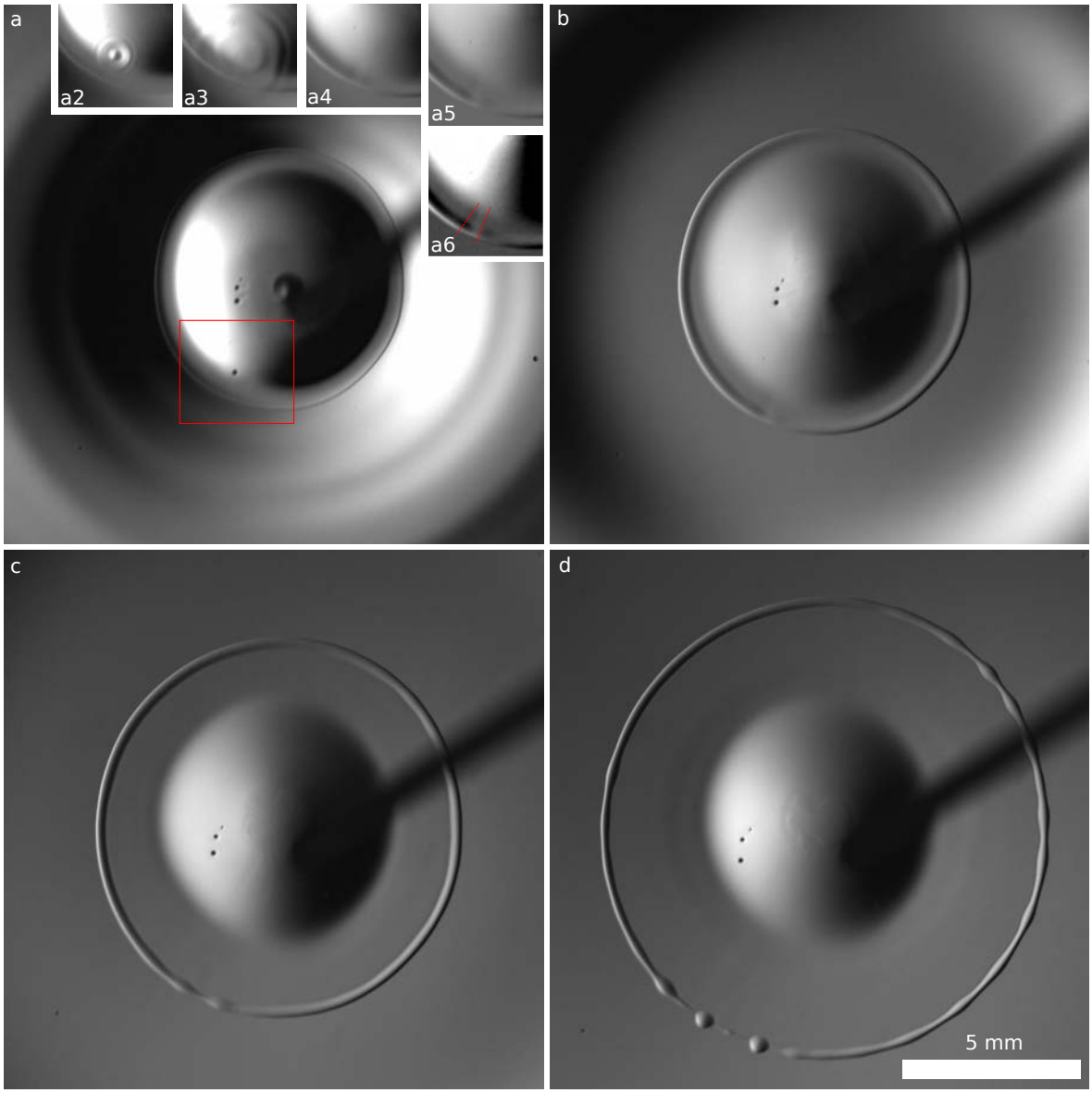

Figure 4.14: Evolution of the first pulsation after the impact of a DCM drop containing 0.5 mM CTAB: Bubble induced bridge formation (red box). (a) first visible appearance of a rim; (a2-a6) Detail of the red box: the formation of two bridges induced by the explosion of a bubble (in the center of the images), subsequent times: (a) 0 ms, (a2) 0.78 ms, (a3) 1.56 ms, (a4) 2.34 ms, (a5) 10.94 ms. (a6) same as (a5) but with enhanced contrast and overlay at the position of the bridges (b) = (a5). (c) 25.79 ms. (d) 40.65 ms.

4.7. Interpretation

We will give here a first interpretation of how the complex dynamics of the pulsating drop is realized. The difficulty of giving a clear and unambiguous interpretation comes from the interconnection of many different processes taking place at the same time:

- The expansion of the drop, which is supposed to happen due to a positive spreading coefficient at the end of the induction period (see chapter 3 (3.3))
- The plastic deformation of the drop at its boundaries which leads to the formation of the rim that breaks-up in a RP like manner;
- The formation of structures inside the drop that most likely leads to the wrinkles formation and the rim pre-modulation.

We will first give an interpretation on the formation of the wrinkles, which seem to be the determining cause for the a factor of half to small measured characteristic wavelength compared to the classic RP instability. In the following we will give an interpretation of the full mechanism from the drop expansion to the rim break-up.

4.7.1. Wrinkles Formation

The formation of the structures inside the drop look like convection rolls, which are induced by flows inside the drop. These flows seem to be induced by the expansion of the drop but they could be also induced by the evaporation of the DCM from the surface as in a Bernard-Marangoni instability. Most probably they are induced by the expansion and amplified by the evaporation to form the visible wrinkles in the connecting film between the rim and the central drop. Such an evaporative instability is also present in the phenomenon of 'tears of wine' described in chapter 2.
What we observe resembles very much what Hosoi and Bush [21] were investigating on film formations of alcohol-water solutions on inclined glass plates (for inclination angles smaller than 3^o) (see Fig. 4.15).
They believe as well that the wrinkles that form in the film are a surface signature of the dynamics in the thin film. Furthermore they connect the formation of wrinkles to the surface tension gradients that arise in vertical direction (y direction in Fig. 4.15 (B)) due to the evaporation of alcohol. This is creating Marangoni convection in the film that amplifies the wrinkles (see scheme in Fig. 4.15 (B)), which they could model accurately with a numerical model. The origin of the wrinkles due to Hosoi and Bush are both thermal and solutal instabilities that are induced by the evaporation of the alcohol.

The role of the alcohol in our case is played by the DCM that creates the thermal gradients by its evaporation. Also in our case the film (which is forming due to the expansion of the drop in our

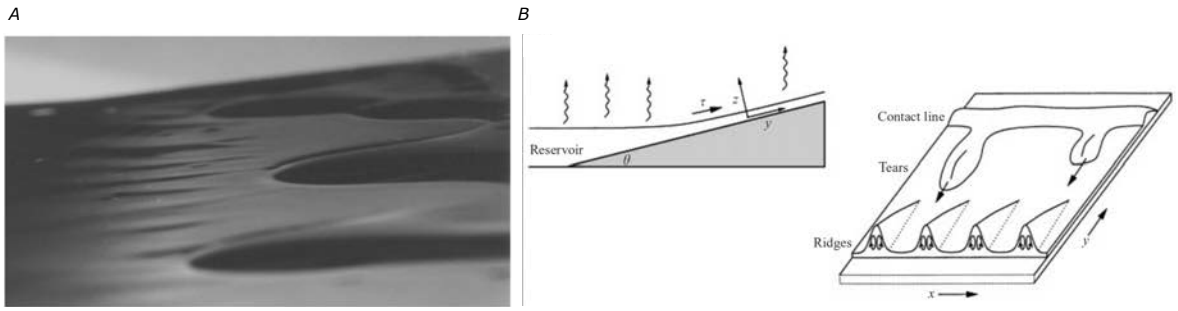

Figure 4.15: *Wrinkles formation in a film climbing an inclined plane. A: Side view picture were wrinkles are visible. B: Scheme of the system (taken from [21])*

experiments) is 'climbing' on the deformation of the surrounding of the free water/air interface, which is induced by the heavy DCM drop, which is of the order of 1-2^o (see Fig. 4.16). The rim that is formed at the upper edge in the scheme in Fig. 4.15) (B) corresponds to our rim, while in our case no tears are formed. The wrinkles (noted as ridges in the Fig. 4.15) are supposed to modulate the rim and subsequent droplets are generated.

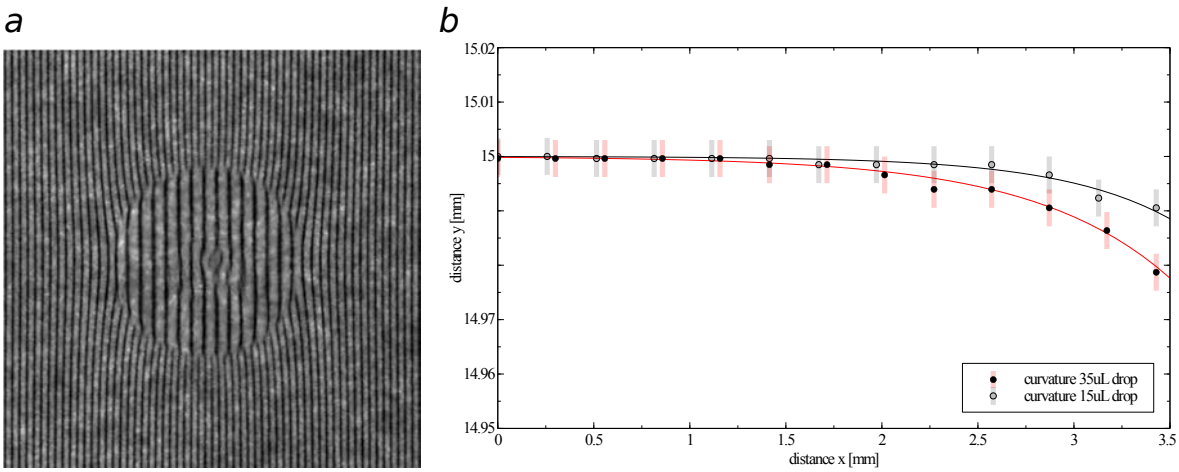

Figure 4.16: *Deformation of the surface surrounding the drop obtained with the Ronchi ruling method* [22]. *a: Optical deformation of a Ronchi ruling due to presence of the drop. b: Calculated deformation of the surface (drop starts at right end); higher volume drops deformed the interface more.*

4.7.2. *Full Mechanism*

With this idea about the wrinkles formation we can now give a full picture of the possible mechanisms at play in our system. At the end of the induction period the drop expands due to the surface

forces that pull on the triple contact line. After the linear expansion of the drop radius, a non-linear expansion starts that corresponds to the formation of the rim. The expansion of the drop leads to a shape transformation, which induces outward directed flows that show a periodic structuration. As the drop expands a more plastic transformation is initiated that leads to the formation of the rim and consequently the formation of the film. As the film gets thinner due to expansion this concentration differences get amplified due to the evaporation of DCM and Marangoni flows are induced which lead to the amplification of the wrinkles. The wrinkles act in such a way on the formation of the rim that they impose an initial undulation on it that evolve and amplify in a Rayleigh Plateau like manner. This evolution and the continuous expansion leads to the disconnection of the toroidal rim from the film and the rim break-up in smaller droplets which move radially away from the drop.

In the next section we will model the rim break-up by including the connecting film and the flows inside it based on a model proposed by Roisman et al., who theoretically discussed the case of an accelerated rim expansion.

4.8. Modeling

The main difference between a standard RP instability and the instability we have in our system is the expansion of the rim and the existence of a film that is connected to the rim. Systems where rims are connected to a 'film' are observed in liquid splashes, when a drop or another object is thrown in another liquid, which sometimes resembles a crown and therefore is called crown-splashing (see e.g. Zhang et al. [4]). The splash is creating a toroidal rim at the end of a liquid sheet that connects to the bulk liquid.

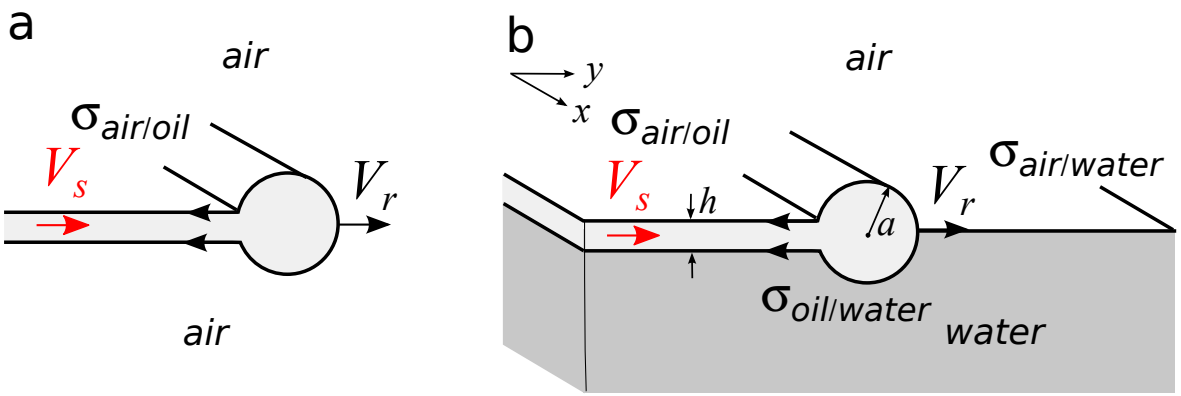

Figure 4.17: *Comparison between our system and the system modeled by Roisman et al. (a) Rim expansion connected to a liquid sheet (Roisman et al.). Rim expansion connected to a liquid film on the surface of another liquid (our system).*

Roisman et al. [5] were investigating a system very similar to ours (at least from a mathematical point of view). In their model an expanding rim is connected to a liquid sheet, that is surrounded by air (see Fig. 4.17 (a)). The rim expansion is the result of the liquid flow in the sheet V_s and the rim speed V_r, which is counterbalanced by the surface tension $\sigma_{\text{air/oil}}$ (see Fig. 4.17 (a)). For constantly and decelerated expansion (i.e. $\dot{V}_r \leq 0$, where V_r is the speed of the rim) a characteristic wavelength in the range of the standard RP instability is obtained. On the other hand, for accelerated expansion (i.e. $\dot{V}_r > 0$), a smaller reduced wavelength of about the half of the classic RP instability is obtained, as we observe it in our case.
We use this model as a starting point, which we adapted to our situation by incorporating also the other surface tensions of our system ($\sigma_{\text{air/water}}$ and $\sigma_{\text{water/oil}}$) (see Fig. 4.17 (b)).

For simplifying the problem, we make several assumptions. First, we neglect the viscosities of oil and water (in any case, they play a minor role and are expected to increase the wavelength of the RP instability of the rim). Second, we neglect the buoyancy effect and assume for simplicity that the cross-section of the rim is circular and only semi-submerged in the water ($\sigma_{air/oil}$ acts on the upper, uncovered half of the rim, and $\sigma_{oil/water}$ acts on the lower, submerged half). Actually, the oil used in the corresponding experiments, DCM, has a higher density than water and the rim is actually more submerged. Third, the film (sheet) is assumed to be non-perturbed by the rim evolution and remains flat and uniform. Fourth, only a simple description of the flow inside the rim is considered here (no vortex for instance), so that only the moment of stress due to the axial rim acceleration is supposed to contribute to the total moment of stress. Finally, as we are interested in the linear stability analysis of the equations, we neglect all the second order terms.

The linearized mass balance, axial and transverse momentum, and momentum of momentum equations of the rim read similarly to the ones by Roisman et al.:

$$\frac{\partial A}{\partial t} + A_0 \frac{\partial u}{\partial x} - h\left(V_s - V_r\right) = 0 \tag{4.17}$$

$$\rho_{oil} A_0 \frac{\partial u}{\partial t} - \frac{\partial P}{\partial x} - f_{sx} = 0 \tag{4.18}$$

$$\rho_{oil} A_0 \frac{\partial V}{\partial t} - P\kappa - \frac{\partial Q}{\partial x} - f_{sy} = 0 \tag{4.19}$$

$$\rho_{oil} \frac{\partial L}{\partial t} - \frac{\partial M}{\partial x} - Q - m_s = 0 \tag{4.20}$$

where h is the thickness of the film, $A = \pi a^2$ is the cross-section area of the rim with a being the radius of the rim, u is the velocity of the fluid in the rim, A_0 is the unperturbed cross-section area of the rim (from now on, the index 0 refers to the unperturbed situation), ρ_{oil} is the density of DCM, κ is the curvature of the center line of the rim, Q is the (unknown) shear force in the y direction applied to the cross section of the rim, $L = I_0 \frac{\partial V}{\partial x}$ is the angular momentum of the rim per unit length

in the plane $\{x, y\}$, $I_0 = \pi a_0^4/4$ is the moment of inertia of the rim cross-section, $M \simeq -\rho_{oil} I_0 \frac{\partial V}{\partial t}$ is the moment of stresses in the cross-section, $m_s \simeq -W_0 a_0 u$ is the distributed moment of the external forces with $W_0 = \rho_{oil} h \left(V_{s0} - V_{r0}\right)$ being the (algebraic) flow from/into the film, f_{sy} and f_{sx} are the external forces applying to the unit lengths along x and y direction and P is the longitudinal force which are given by

$$f_{sy} = \pm\rho_{oil} h \left(V_s - V_r\right)^2 + S \tag{4.21}$$

$$f_{sx} = -Wu - S\frac{\partial Y}{\partial x} \tag{4.22}$$

$$P = \overline{\sigma}\left(\pi a + A\frac{\partial^2 a}{\partial x^2}\right) \qquad with \quad \overline{\sigma} = \frac{\sigma_{air/oil} + \sigma_{oil/water}}{2} \tag{4.23}$$

where S is the spreading parameter, W is the (algebraic) flow from/into the film and Y is the position of the rim.

The four variables of our system are the position of the rim $Y\left(x,t\right)$, the radius of the rim $a\left(x,t\right)$, the transverse liquid velocity $u\left(x,t\right)$ and the shear force distribution $Q\left(x,t\right)$ of the rim.
In line with Roisman et al., small, harmonic disturbances of these variables are considered:

$$Y\left(x,t\right) = Y_0\left(t\right) + \epsilon_1 \mathrm{e}^{\omega t + i\xi x} \tag{4.24}$$

$$a\left(x,t\right) = a_0\left(t\right) + \alpha_1 \mathrm{e}^{\omega t + i\xi x} \tag{4.25}$$

$$u\left(x,t\right) = u_1 \mathrm{e}^{\omega t + i\xi x} \tag{4.26}$$

$$Q\left(x,t\right) = q_1 \mathrm{e}^{\omega t + i\xi x} \tag{4.27}$$

with ω and ξ the growing rate and wave number of the disturbance. The linearized equations (5.16-5.19) become:

$$\begin{pmatrix} 2\pi a_0\omega & A_0 i\xi & h\omega & 0 \\ \pi\overline{\sigma} i\xi - \overline{\sigma} A_0 i\xi^3 & -W_0 - \rho_{oil} A_0\omega & -Si\xi & 0 \\ -2\pi\rho_{oil} a_0 \dot{V_0} & 0 & -\rho_{oil} A_0\omega^2 - \xi^2\pi\overline{\sigma} a_0 \mp 2W_0\omega & i\xi \\ \pi\rho_{oil} a_0^3 \dot{V_0} i\xi/2 & a_0 W_0 & 2\rho_{oil} I_0\omega^2 i\xi + a_0^2 W_0\omega i\xi/2 & -1 \end{pmatrix} \begin{pmatrix} \alpha_1 \\ u_1 \\ \epsilon_1 \\ q_1 \end{pmatrix} = 0 \tag{4.28}$$

where $\dot{V_0}$ is the axial acceleration of the unperturbed rim. The corresponding dispersion equation is given by equating the determinant of the previous 4x4 matrix to 0:

$$\begin{aligned} -2\pi^2\left[\overline{\omega}^2 + \frac{\overline{\xi}^2(\overline{\xi}^2 - 1)}{2}\right]\left[\overline{\omega}^2\left(1 + \frac{\overline{\xi}^2}{2}\right) + \overline{\xi}^2 + \overline{\omega}\,\overline{W_0}\left(\frac{\overline{\xi}^2 \pm 4}{2\pi}\right)\right] & \\ + \overline{\omega}\,\overline{W_0}\overline{\xi}^2\left[2\overline{S} + \overline{h}\left(1 - \overline{\xi}^2\right)\right] & \\ + \overline{\dot{V_0}}\left(2 + \frac{\overline{\xi}^2}{2}\right)\left[\overline{\omega}^2\overline{h}\pi + \overline{\omega}\,\overline{W_0 h} + \pi\overline{S}\overline{\xi}^2\right] &= 0 \end{aligned} \tag{4.29}$$

where we have introduced the following dimensionless parameters

$$\overline{\omega} = \omega\sqrt{\frac{\rho_{oil}a_0^3}{\overline{\sigma}}}, \quad \overline{\xi} = \xi a_0, \quad \overline{W_0} = \frac{W_0}{\sqrt{\rho_{oil}a_0\overline{\sigma}}}, \quad \overline{S} = \frac{S}{\overline{\sigma}}, \quad \overline{h} = \frac{h}{a_0}, \quad \overline{\dot{V}_0} = \dot{V}_0\frac{\rho_{oil}a_0^2}{\overline{\sigma}} \tag{4.30}$$

The dispersion equation being a quartic in $\overline{\omega}$, has four solutions $\overline{\omega}_{1,2,3,4}\left(\overline{\xi}\right)$ which are analytically expressible although very complicated and complex.
When $\dot{V}_{r0} = 0$ (no acceleration) and $W_0 = 0$ (no ingoing/outgoing flow in/from the rim), the second and third lines of Eqn. (4.28) disappear and we naturally recover the usual (approximate) RP result:

$$\overline{\omega} = \sqrt{\frac{\overline{\xi}^2(1-\overline{\xi}^2)}{2}} \tag{4.31}$$

leading to a maximum in $\overline{\omega}$ for $\overline{\xi}_{RP} = 1/\sqrt{2} \simeq 0.7$ for the bell-shaped dispersion curve $\overline{\omega}\left(\overline{\xi}\right)$ (the associated RP wave length λ_{RP} being equal to $\frac{2\pi}{\overline{\xi}_{RP}}a_0 \simeq 8.9a_0$) (see red curve in Fig. 4.18).

The free parameters of the model are the reduced spreading parameter, $\bar{S}$, the reduced rim acceleration, $\overline{\dot{V}_0}$, the reduced (algebraic) flow from/into the film, $\overline{W_0}$ and the reduced thickness of the film, $\bar{h}$. In a first parameter study we investigated the influence of both the rim acceleration and flow towards/from the film. We found that when $\dot{V}_{r0} \neq 0$ and $W_0 \neq 0$ we clearly see that the usual bell-shape RP dispersion curve is modified and that a second maximum appears around $\overline{\xi} \simeq 1.4 \sim 2\overline{\xi}_{RP}$, corresponding almost exactly to half of the usual RP wavelength.

This short-wavelengths rim instability is quite stable. It appears, for example, when the flow is outgoing ($\overline{W_0} < 0$) for thick enough liquid films. And in this case, it almost does not depend on the acceleration of the rim ($\overline{\dot{V}_0}$). A dispersion curve for such a case is shown in Fig. 4.18 (used parameter values are given in table 4.2).

parameter	value
$\bar{S}$	0.12
$\overline{\dot{V}_0}$	0
$\overline{W_0}$	-0.5
$\bar{h}$	2

Table 4.2: *Parameters of the model*

4.8.1. Model Interpretation

The fact that the model leads to the appearance of a second bump in the dispersion relation $\overline{\xi} \simeq 1.4 \sim 2\overline{\xi}_{RP}$ does not yet explain why the corresponding wavelengths is also selected experimentally.

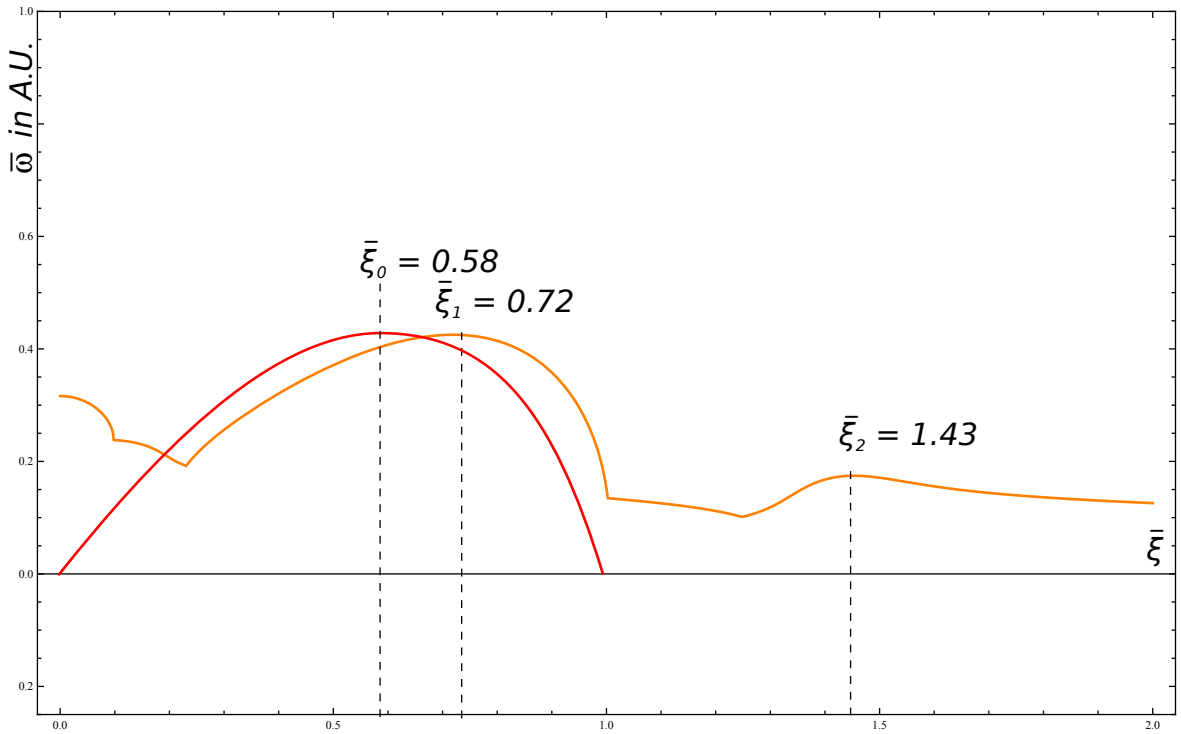

Figure 4.18: *Growth rate as a function of the reduced wavenumber $\bar{\xi}$ of the perturbations. Red curve: Standard RP mechanism. Orange curve: Solution of our model. We obtain two physical solutions, $\bar{\xi} = 0.72$, which corresponds to the standard RP mechanism, and $\bar{\xi}$ =1.43.*

In general the characteristic wavelength of the instability, i.e. the wavelength of perturbation which growths fastest, is the one observed experimentally. It corresponds to the maximum in the growth rate, $\bar{\omega}$ as a function of the reduced wavenumber, $\bar{\xi}$. A standard RP instability, as mentioned above, is obtained for no acceleration and no ingoing/outgoing flow in/from the rim shown in Fig. 4.18, which shows one maxima at $\bar{\xi} = 0.7$, which corresponds to a characteristic reduced wavelength of 8.9.

The model of Roisman et al. [5] and also our adapted model show a more complex growth rate function with several maxima. The existence of several maxima is by itself interesting, while in general only the global maximum is of interest for the characteristic wavelength observed experimentally. In our model we obtain two maxima corresponding to a characteristic reduced wavelength of $\bar{\lambda} = 8.7$ and $\bar{\lambda} = 4.4$ (orange curve in Fig. 4.18). The second value is of interest for us even though it does not correspond to the maximal growth rate.

This is due to the fact, that in contrast to a standard RP instability where the perturbation of the inter-

face of the rim is induced by random fluctuations, the rim is already perturbed when the instability starts to grow. The distance between the wrinkles, and with it the wavelength of the pre-undulated rim corresponds to a wavelength close to the second solution, ka_2 =1.43 (corresponding to a reduced wavelength of 4.4).
As mentioned above in general only the global maximum is of interest for the characteristic wavelength. However this only applies to the cases where the rim was not pre-modulated. In such a case the perturbation with the maximal growth rate will prevail over all the others in a very short time. Since in our case the rim is already pre-corrugated even though the growth rate of the second maxima is lower, it might lead to an amplification of its corresponding wavelength.
In our case we expect that in fact both wavelengths that correspond to the two maxima in the growth rate will be amplified. The wavelength that corresponds to the maximal growth rate is about the half of the second one. But since its growth rate is bigger, the appearance of a secondary periodicity is expected, i.e. that every second undulation is expected to be bigger. This could actually explain the presence of a kind of secondary swelling as the one we observe in some of our pulsations.

In the course of the evolution of the torus the wavelength is going to stretch as described above and the characteristic wavelength is stretched following the radius expansion. This stretching leads to an increase in the characteristic wavelength of around 30% until $\tau = 0.6$. A theoretical characteristic wavelength of 5.72 is obtained in this case compared to the experimentally measured one of 5.91.

The model presented here is able to predict correctly the experimentally obtained characteristic wavelength for the toroidal rim break-up in our system by considering the already pre-undulated rim. Nevertheless it does not give further details in the understanding of the mechanism but it states the theoretical possibility of the experimentally observed characteristic wavelength, which was not supported by a standard RP instability.

4.9. Conclusion

We have discussed in this chapter the behavior of the drop during the pulsating regime. Even though the observed periodic pattern is quite robust, we can observe variations in the appearance of the different pulsations. The variance of the opening angles (or the different initial unperturbed radii of the rim) is of the order of 20%.

By studying in more details the expansion part of the drop we found three distinct stages, while in the last one, the one in which the expansion is accelerated, a rim is forming at the edge, which is breaking-up into smaller droplets. It seems that the acceleration is due to the plastic deformation of the drop that also leads to the rim formation.

The rim break-up was analyzed in terms of the RP instability and we found a factor of 2 of difference between the expected characteristic wavelength.
This discrepancy might be mainly due to the fact that, compared to the standard RP instability where a liquid static column is breaking-up, our system is more complex. First of all it shows a toroidal geometry, and more importantly to its dynamics, it is generated from a drop connected to a thin film throughout its expansion. The liquid flow inside the film seem to be one of the key ingredients to understand how the rim is breaking-up into smaller droplets. The toroidal geometry is not expected to be at the origin of this discrepancy as it was found to be in agreement with the standard RP instability by other researchers. On the other hand, the formation of wrinkles in the film is supposed to be the second key ingredient to understand the rim break-up.
The wrinkles in the film lead to an already pre-corrugated rim when the instability starts. The distance between the wrinkles is exactly of the order of half of the wavelength expected by the RP instability. Roisman et al. proposed a theory in which a rim is connected to a liquid sheet that can break-up with a characteristic wavelength in the range we observe it. Adapting this model to our situation also theoretically predicts a break-up within the range of the values we observe.

Even though this model is able to predict the experimentally observed characteristic wavelength it does not give enough insight into the actual mechanism leading to the rim break-up. In other words further investigation is needed to better understand the wrinkles formation, which are crucial for the break-up of the accelerated expanding rim.

Bibliography

1. J. W. Strutt (Lord Rayleigh), "On the instability of jets," *Proceedings of the London mathematical society*, vol. 10, pp. 4–13, 1878.

2. E. Pairam and A. Fernández-Nieves, "Generation and stability of toroidal droplets in a viscous liquid," *PHYSICAL REVIEW LETTERS*, vol. 102, no. 23, p. 234501(4), 2009.

3. J. D. McGraw, J. Li, D. L. Tran, A.-C. Shi, and K. Dalnoki-Veress, "Plateau-rayleigh instability in a torus: formation and breakup of a polymer ring," *Soft Matter*, vol. 6, pp. 1258–1262, 2010.

4. L. V. Zhang, P. Brunet, J. Eggers, and R. D. Deegan, "Wavelength selection in the crown splash," *Physics of Fluids*, vol. 22, p. 122105(5), 2010.

5. I. V. Roisman, K. Horvat, and C. Tropea, "Spray impact: Rim transverse instability initiating fingering and splash, and description of a secondary spray," *Physics of Fluids*, vol. 18, p. 102104, 2006.

6. C. Antoine and V. Pimienta, "Mass-spring model of a self-pulsating drop," *Langmuir*, vol. 29, pp. 14935–14946, Dec. 2013.

7. E. A. van Nierop, A. Ajdari, and H. A. Stone, "Reactive spreading and recoil of oil on water," *Physics of Fluids*, vol. 18, no. 3, p. 038105, 2006.

8. D. K. Sinz, M. Hanyak, and A. A. Darhuber, "Immiscible surfactant droplets on thin liquid films: Spreading dynamics, subphase expulsion and oscillatory instabilities," *Journal of Colloid and Interface Science*, vol. 364, no. 2, pp. 519 – 529, 2011.

9. G. Karapetsas, R. V. Craster, and O. K. Matar, "Surfactant-driven dynamics of liquid lenses," *Physics of Fluids*, vol. 23, no. 12, p. 122106, 2011.

10. Y. Sumino, H. Kitahata, H. Seto, and K. Yoshikawa, "Dynamical blebbing at a droplet interface driven by instability in elastic stress: a novel self-motile system," *Soft Matter*, vol. 7, pp. 3204–3212, 2011.

11. F. Brochard-Wyart, P. Martin, and C. Redon, "Liquid/liquid dewetting," *Langmuir*, vol. 9, no. 12, pp. 3682–3690, 1993.

12. J. Happel and H. Brenner, *Low Reynolds number hydrodynamics: With Special Applications to Particulate Media*. Kluwer: Dordrecht, The Netherlands, 1983.

13. P. Martin, A. Buguin, and F. Brochard-Wyart, "Bursting of a liquid film on a liquid substrate," *EPL (Europhysics Letters)*, vol. 28, no. 6, p. 421, 1994.

14. J. Plateau, *Statique experimentale et theorique des liliquid soumis aux seules forces moleculaires*. 1873.

15. Rayleigh, "Measurements of the amount of oil necessary in order to check the motions of camphor upon water," *Proc. R. Soc. Lond.*, vol. 47, pp. 364–367, 1890.

16. S. Tomotika, "On the instability of a cylindrical thread of a viscous liquid surrounded by another viscous fluid," *Proceedings of the Royal Society of London. Series A, Mathematical and Physical Sciences*, vol. 150, pp. 322–337, June 1935.

17. A. Gonzalez, J. Diez, and L. Kondic, "Stability of a liquid ring on a substrate," *Journal of Fluid Mechanics*, vol. 718, pp. 246–279, 2013.

18. J. Eggers and E. Villermaux, "Physics of liquid jets," *REPORTS ON PROGRESS IN PHYSICS*, vol. 71, p. 036601, 2008.

19. D. F. Rutland and G. J. Jameson, "A non-linear effect in the capillary instability of liquid jets," *Journal of Fluid Mechanics*, vol. 46, no. 2, pp. 267–271, 1971.

20. M.-C. Yuen, "Non-linear capillary instability of liquid jet," *Journal of Fluid Mechanics*, vol. 33, no. 1, pp. 151–163, 1968.

21. A. E. Hosoi and J. W. M. Bush, "Evaporative instabilities in climbing films," *Journal of Fluid Mechanics*, vol. 442, pp. 217–239, 2001.

22. V. Ronchi, "Le frange di combinazioni nello studio delle superficie e dei sistemi ottici," *Rivista d'Ottica e Meccanica di precisione*, 1923.

RESUMÉE EN FRANÇAIS

Dans ce chapitre, nous nous sommes intéressés au regime de pulsation obtenu pour une concentration de 0.5 mM de CTAB dans la phase aqueuse. Pendant ce regime un bourrelet se forme pendant la phase d'expansion qui ensuite se transforme en petites goutelettes. La transformation du bourrelet en gouttelettes resemble à une instabilité de type Rayleigh Plateau (RP).

L'amplitude des oscillations dépend peu du volume initial de la goutte et vaut toujours autour de 2 mm (Fig. 4.19), l'augmentation du volume entrainant principalement une augmentation de la durée du phénomène.

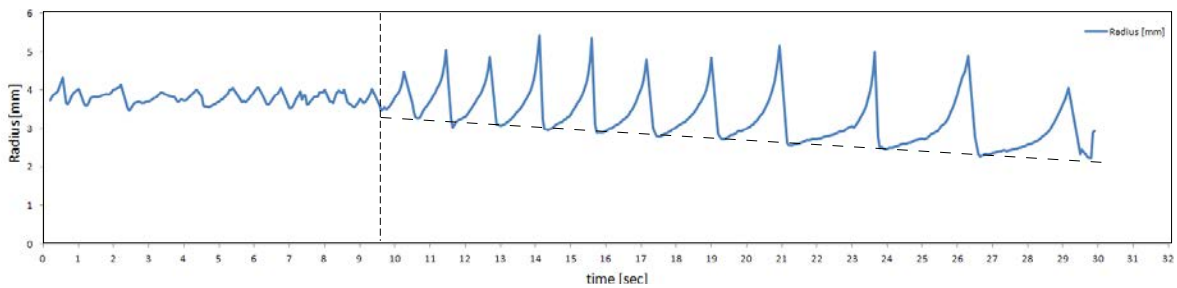

Figure 4.19: *Oscillations du diamètre pour une goutte de 25 uL sur une solution de CTAB à 0.5 mM.*

Les travaux effectués en collaboration avec Charles Antoine ont porté sur le régime de pulsation observé pour une concentration initiale en CTAB de 0.5 mM. Notre étude a montré que la régularité remarquable et la conservation de la symétrie au cours des battements peut être reproduite par un modèle simple de type masse-ressort. Un coefficient d'étalement dépendant du temps regroupant toutes les forces qui poussent ou tirent le bourrelet de la goutte a été introduit. Complétés par des forces hydrostatiques et d'amortissement et en tenant compte d'une augmentation lente de la masse

effective du bourrelet de la goutte, ce modèle mécanique permet de reproduire les pulsations avec une bonne précision (Fig. 4.20).

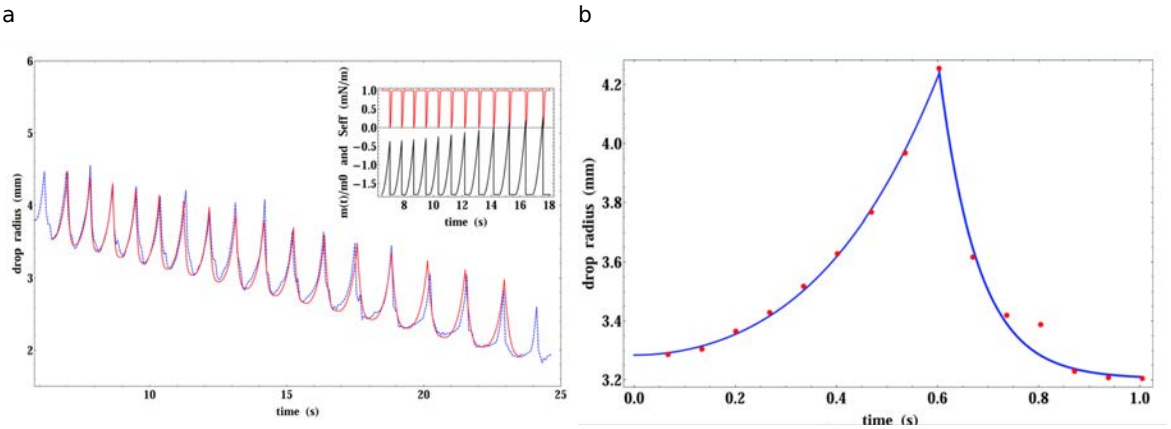

Figure 4.20: *Variation du rayon de la goutte au cours du temps. En pointillé : données expérimentales, en trait plein : modèle.*

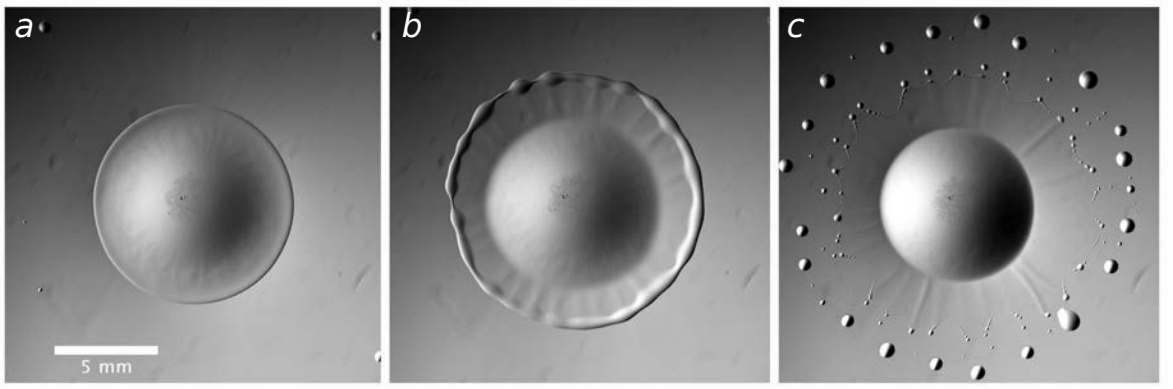

Figure 4.21: *évolution de la goutte (25 uL) au cours d'une pulsation : étalement, apparition du film et du bourrelet autour de la goutte, détachement du bourrelet et éjection de gouttelettes.*

Le fait que l'amplitude est indépendante du volume de la goutte (initial et courant) montre que l'origine du phénomène est principalement due aux effets de tension interfaciale. La diminution de la fréquence de pulsation s'explique par le fait que la surface liquide doit être régénérée entre chaque pulsation par évaporation et dissolution du dichlorométhane. Ces phénomènes sont de plus en lents à cause de l'accumulation de ce composé dans les deux phases aqueuse et gaz.

Des expériences suivies par caméra rapide ont permis une meilleure observation du phénomène de pulsation : étalement, formation d'un bourrelet à l'extrémité du film, détachement du bourrelet et formation de gouttelettes éjectées en direction radiale, démouillage du film et reformation de la goutte.

La longueur d'onde de déformation du bourrelet avant la formation des gouttelettes est analysée afin de déterminer l'origine du phénomène et en particulier d'établir si cette déformation relève de l'instabilité de Rayleigh-Plateau. Pour cela, nous avons determiné la longeur d'onde principale de déformation du bourrelet ainsi que le profil du bourrelet avant sa deformation (Fig. 4.22).

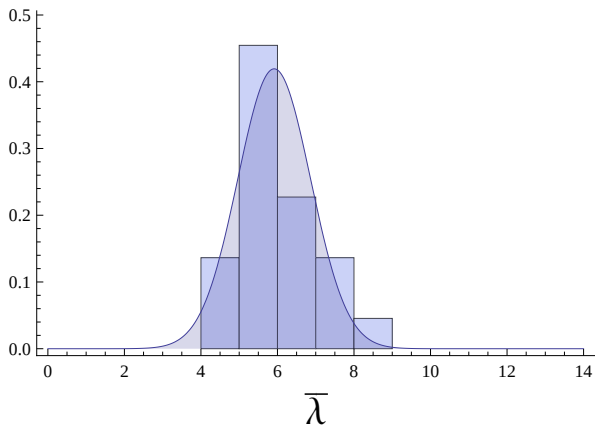

Figure 4.22: *longueur d'onde principale moyenné pour 22 experiences* ($\langle\bar{\lambda}\rangle = 5.91 \pm 0.95$).

Les résultats montrent une longeur d'onde 50% plus petite qu'attendu par l'instabilité RP standard. Une difference majeur entre notre systeme et les autres systemes est que dans notre cas le bourrelet est créé pendant l'expansion de la goutte. Le bourrelet est toujours connecté a la goutte centrale. La connection est fait par un film mince. Ce film mince presente au fait des variations de son epaisseur qui apparaissent comme des ondulation radiales régulieres (Fig. 4.23 (b)). Celles-ci sont clairement correlées aux deformations apparaissant dans le bourrelet avant sa rupture (Fig. 4.23 (a') (b')).

La formation des structures à l'intérieur de la goutte ressemble à des rouleaux de convection, induits par des écoulements dans la goutte. Ces flux semblent être induits par l'expansion de la goutte, mais ils pourraient également être induits par l'évaporation du DCM de la surface comme dans une instabilité Bernard-Marangoni. Très probablement, ils sont induits par l'expansion et amplifié par l'évaporation pour former les wrinkles visibles dans le film de liaison entre le bourrelet et la goutte centrale. Une telle instabilité induite par l''évaporation est également présente dans le phénomène des "larmes du vin" décrit au chapitre 2.

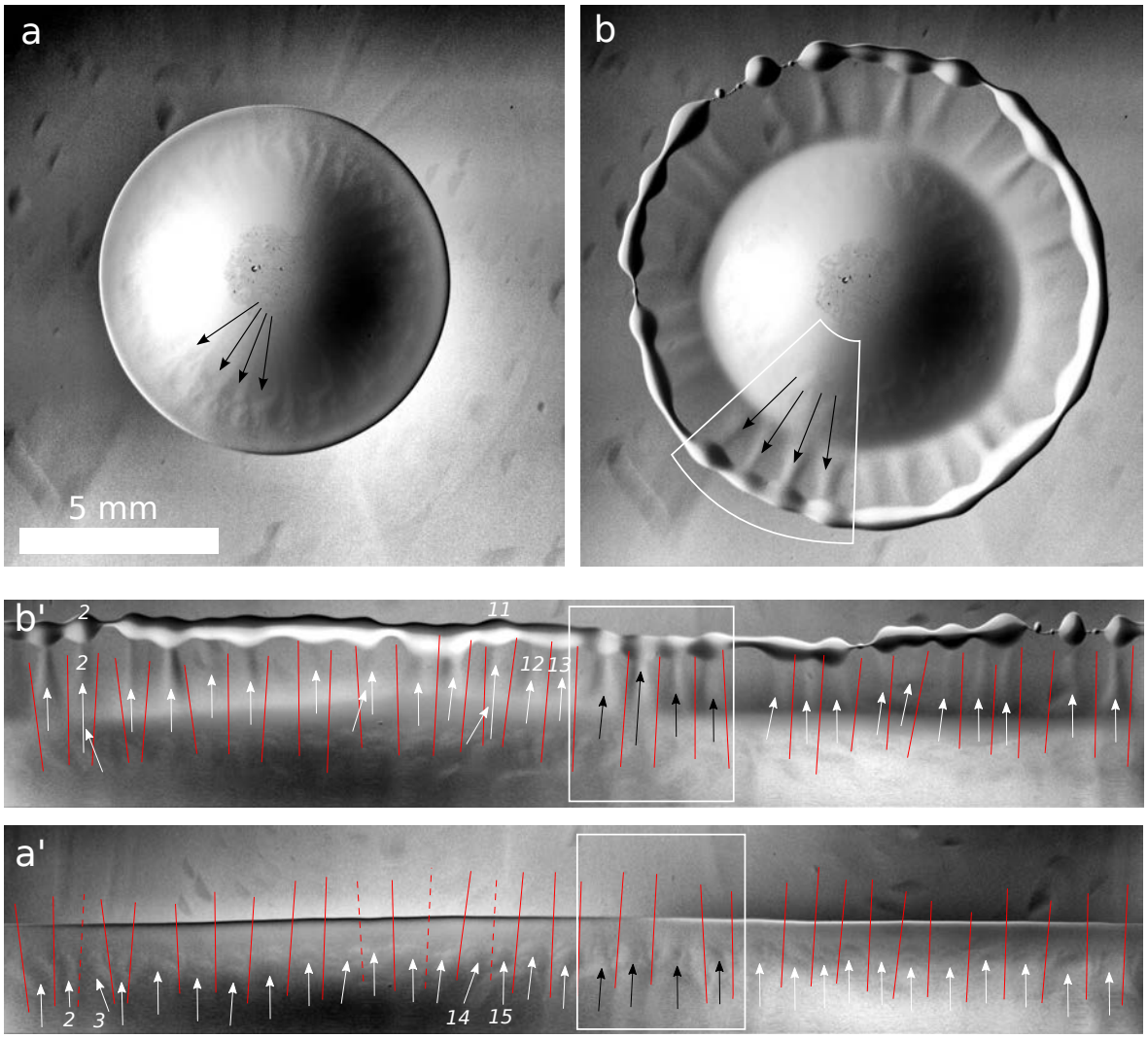

Figure 4.23: *Structure périodique à l'intérieur de la goutte du DCM. a: Structuration au moment où le bourrelet commence à se former (a') est la projection périmétrale de (a). b: Goutte juste avant que le bourrelet commence à se briser, (b') est la projection périmétrique de (b). Les chiffres dans (a') désignent le nombre de structures, tandis que les nombres inférieurs dans (b') désignent le nombre de rides et le nombre supérieur indiquent le nombre de gouttelettes futures. Une forte corrélation entre le nombre de structurations, les rides et les gouttelettes futures est visible dans la zone en caisse blanche.*

Avec cette idée sur la formation des wrinkles, nous pouvons maintenant donner une image complète des mécanismes possibles en jeu dans notre système.

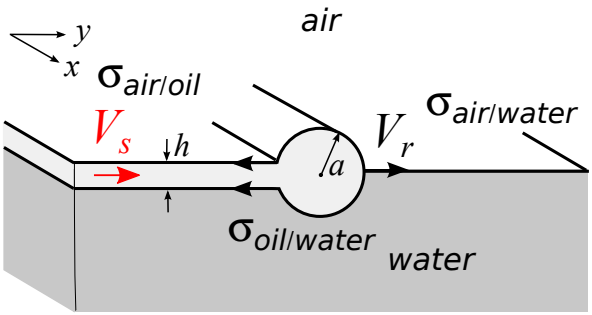

Figure 4.24: *Schema d'expansion du bourrelet connectée à un film liquide à la surface d'un autre liquide utilisé pour le model.*

À la fin de la période d'induction, la goutte s'élargit en raison des forces de surface qui tirent sur la ligne de contact triple. Après l'expansion linéaire du rayon de goutte, une expansion non linéaire commence à correspondre à la formation du bourrelet. L'expansion de la goutte conduit à une transformation de forme, qui induit des flux dirigés vers l'extérieur qui montrent une structuration périodique. À mesure que le film devient plus mince en raison de l'expansion, ces différences de concentration s'amplifient en raison de l'évaporation du DCM et des flux de Marangoni sont induits, ce qui conduit à l'amplification des wrinkles. Les wrinkles agissent de telle manière sur la formation de la jante qu'ils imposent une ondulation initiale qui évolue et amplifie conformement à une instabilité RP. Cette évolution et l'expansion continue conduisent à la déconnexion du bourrelet toroïdal du film et à la rupture du bourrelet en gouttelettes plus petites qui se déplacent radialement à l'écart de la goutte.
Le modèle présenté ici (scheme dans la figure 4.24) est capable de prédire correctement la longueur d'onde caractéristique obtenue expérimentalement pour la rupture du bourrelet toroïdale dans notre système en considérant le bourrelet déjà pré-ondulée. Néanmoins, il ne donne pas d'autres détails dans la compréhension du mécanisme, mais il indique la possibilité théorique de la longueur d'onde caractéristique observée expérimentalement.

5

Addition of Surfactant in the Organic Phase: The Flower-like Dewetting Pattern

Man muss noch Chaos in sich haben, um einen tanzenden Stern gebären zu können.

[*One must still have chaos in oneself to be able to give birth to a dancing star.*]

Friedrich Nietzsche

5.1. Introduction

In this chapter, we will focus on the pulsating regime observed in the presence of CTAB also in the organic (drop) phase. The concentration of the surfactants in the aqueous supporting phase is, as before, 0.5 mM and the same CTAB concentration has been added to the drop phase. The system is still out of partition equilibrium, but the presence of surfactants in the drop gives rise to different dynamics with the most remarkable occurring during the receding (dewetting) phase of the surrounding film. Classically, dewetting of films occurs through the formation of holes that grow, giving rise to the accumulation of the liquid in a rim that forms at the expanding edge of the hole. When all the holes have grown, strings formed in between them transform into droplets according to the Rayleigh-Plateau instability. If we exclude very thin films that give rise to spinodal dewetting through the formation of a multitude of holes and results in the deposition of very small drops on a polygon network [1], the droplets resulting from the dewetting of thicker films do not show organized patterns. However, two recent publications showed that organization of the delivered droplets can also arise for thicker films.
There is the dewetting of a thin film of a liquid fluorocarbon (perfluorooctyl bromide) on water investigated by Yamamoto et al. [2] and the dewetting of a two-component drop of water and volatile alcohol on a bath of sunflower oil investigated by Keiser et al. [3]. In the system investigated by Yamamoto et al. a hole occurs due to the thinning of the film induced by its evaporation. During the thinning process the film becomes unstable when it becomes thinner than a critical thickness, which induces a dewetting transition. A circular water hole is then spontaneously generated within the film. The formation of these humps at the rim is attributable to the bistability of the film height on the water surface. It can be described as a pearling instability (see Fig. 5.1 (a)). The system investigated by Keiser et al. involves the spreading of a millimetric drop of a mixture composed of water and isopropyl alcohol (IPA), which is gently deposited on a centimeter thick layer of sunflower oil. The drop starts to spread shortly and dewets while constantly emitting smaller droplets from its edge in a kind of finger-like instability (see Fig. 5.1 (a)).

5.2. Observations

A 5.6 µL drop containing 0.5 mM CTAB is deposited onto a 25 mL of 0.5 mM CTAB aqueous phase placed in a 7 cm Petri dish. The life time of the drop in this case is about 5 to 6 s and the period of pulsation is around 0.3 s, which is about 3 to 4 times less than in the absence of CTAB in the drop. The drop appears as a reservoir (of radius R_D) surrounded by a film (of radius R_F) (see Fig. 5.2). Both R_D and R_F oscillate with time. The experiment described here showed 12 pulsations.

Nineteen experiments were performed in the same set and the pattern observed for the first four

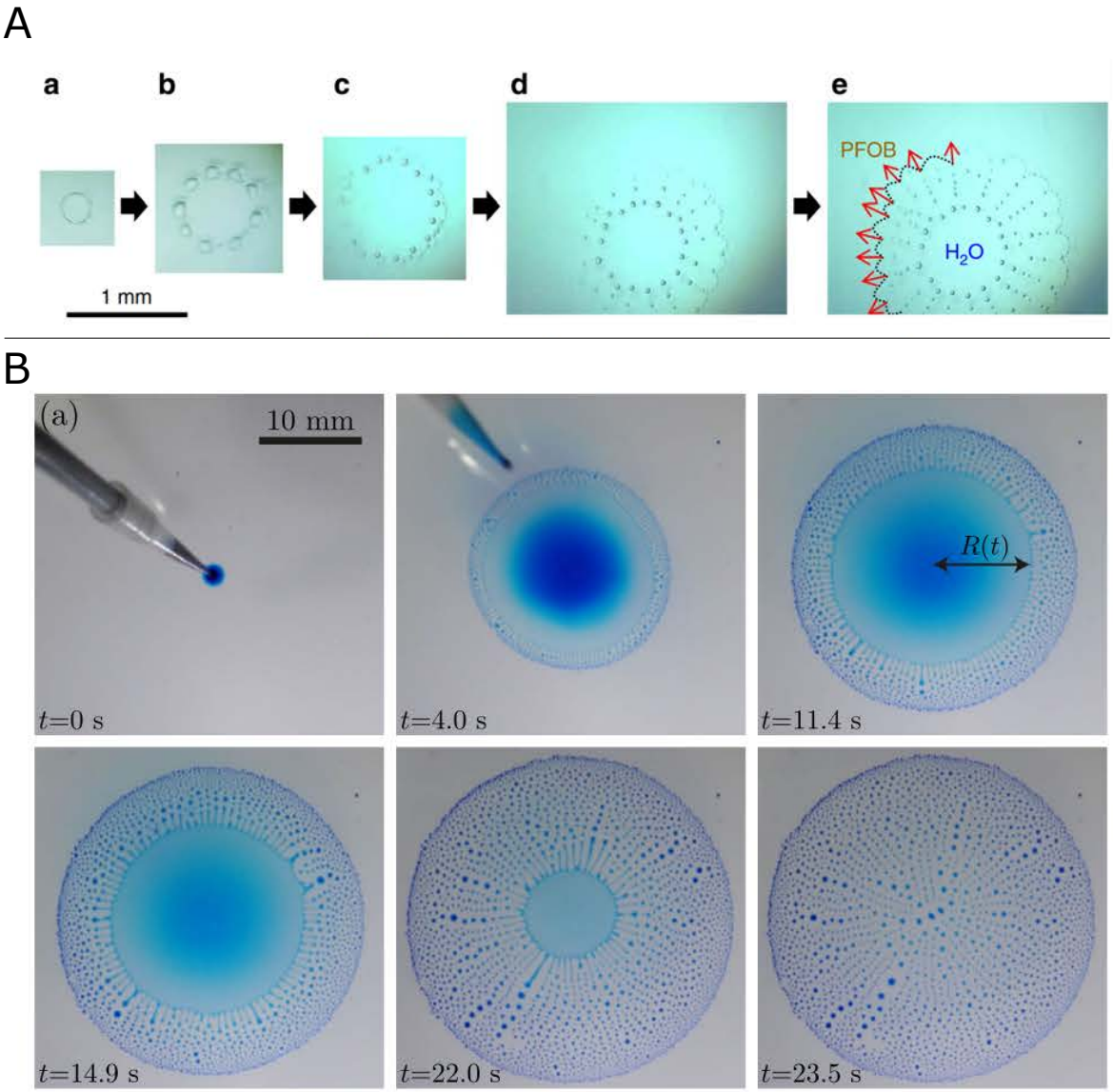

Figure 5.1: *Dewetting patterns. A: Dewetting of a thin film of a liquid fluorocarbon (perfluorooctyl bromide) on water (taken from [2]). B: Dewetting of a two-component drop of water and volatile alcohol on a bath of sunflower oil (taken from [3]).*

pulsations (P1 to P4 in Fig. 5.4) was extremely robust. Obtained eighteen times over nineteen, it resulted in the observation of the highly complex flower-like dewetting structure. Fourteen experiments showed more than four subsequent pulsations where the flower-like dewetting pattern is preserved.

The deposition of the drop induces the deformation of the receiving aqueous surface and subsequent capillary waves [4]. They are immediately followed by a stiff wave (P1) due to drop spreading on the surface. The film arises from the drop as soon as deposition is completed and two contact lines (R_D and R_F) are afterwards discernible (Fig. 5.4). While R_D only slightly varies for P1, it appears for the following pulsations that expansion starts simultaneously at the drop and film edges. However, the drop reaches its maximum expansion before the film, and recoils while the film is still growing. Expansion of the film is visible thanks to the formation of a rim at the leading edge. This one appears as a torus for P1 (Fig. 5.2 (a)), as a ring of closely packed smaller droplets for P2 and P3 (Fig. 5.2 (b)) or as a corrugated torus for P4 (Fig. 5.2 (b)) . Born at the edge of the drop for P1, the rim appears at 3 mm from the edge of the drop reservoir for P2, 1.3 mm for P3 and 0.5 mm for P4. Hence if we consider this property, P1 could be placed after P4.

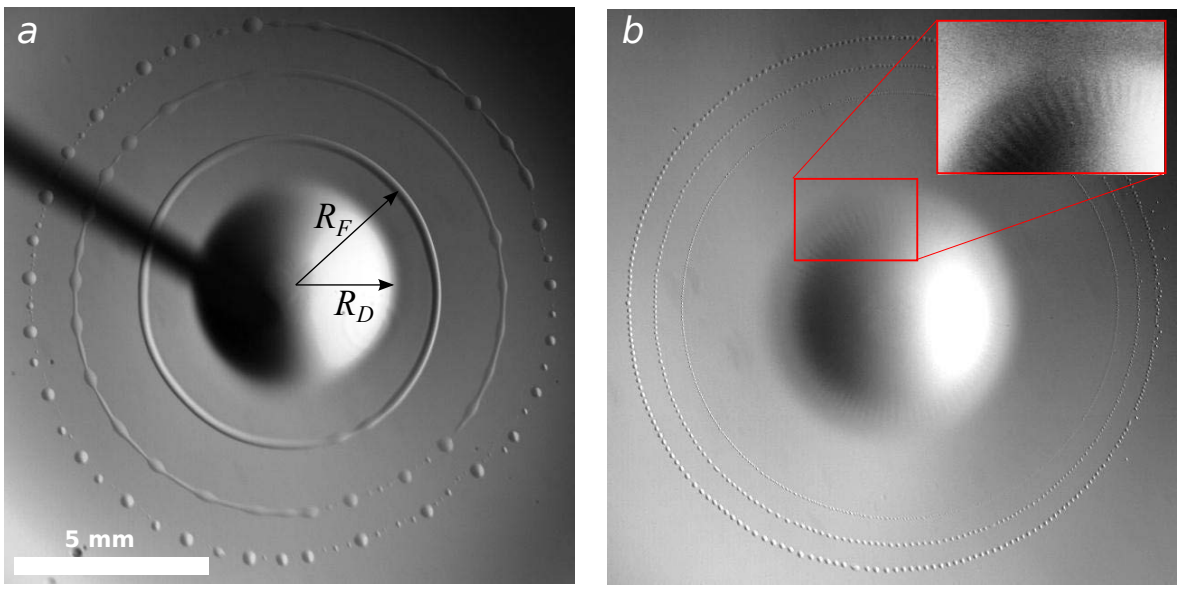

Figure 5.2: *Expanding phase of pulsation. a: P1, 3 images are superimposed Δt = 28.3 ms; arrows indicate the way R_D and R_F are measured in Fig. 5.4. b: P2, 3 images are superimposed Δt = 18.87 ms; insert : zoom on the edge of the drop, where wrinkles are visible.*

This sequence (P2, P3, P4 and P1) is also valid for others properties as the number of ejected droplets which decreases (560, 240, 120 and 30 respectively) while their size increases (75, 100, 240 and 340 um in diameter). The size dispersion of ejected droplets also varies in the same order: perfectly monodisperse for P2, a very small satellite appears in between two droplets for P3 while the number of satellites increases for P4 and P1 (Fig. 5.3). The formation of satellites droplets is favored by a later

transformation into droplets and so related to the thickness of the expanding rim (the thicker the more satellites).

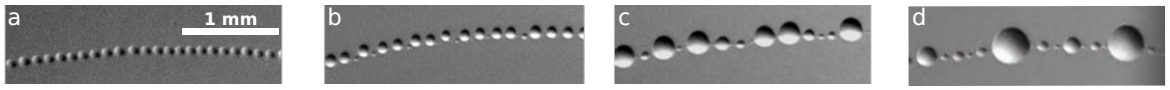

Figure 5.3: *Size dispersion of ejected droplets. a: P2. b: P3. c: P4. d:P1*

The film velocity, faster for P1 (45 mm/s), is similar for the next three pulsations (30 mm/s at the beginning of expansion and quasi constant for quite a long time). The variations of R_D are not measurable for P1, they are very small for P1 and P2, but they increase for P4. The drop grows for a while with an expansion velocity of about 10 mm/s (one third of the film expansion velocity). The decrease is smoother, the recoil velocity being about 3 times slower. The drop shrinks until a minimum radius which remains constant for a while in relation with the dewetting dynamics of the surrounding film (see later). The main qualitative difference observed on the central cap for the successive pulsations is, for P3 and P4 (Fig. 5.2 (b) and Fig. 5.4), the formation of convective cells that appear as stripes at the edge of the drop during the expanding phase (inset in Fig. 5.2 (b)) . For P3 these stripes are confined in the drop reservoir with apparently no further effect. They are more visible for P4 and this time they develop through the growing film that clearly shows thicker regular radial wrinkles accounting for the deformation of the film (Fig. 5.5). The film corrugations play an important part in the highly ordered pattern observed during film retraction for P4 and following pulsations. However, in the present case, they have no effect on the ejection process. The number of ejected droplets is related to the rim size and not to the number of wrinkles.

The dewetting stages are more difficult to grasp since the retracting film is not really visible for P1, P2 and P3. For the first three pulsations, after ejection of the droplets, the attached film appears as a fuzzy shadow. The edges deform while shrinking and slowly fade. The dewetting pattern shown by P4 is completely different. This difference finds its origin in a thicker expanding film (bigger droplets are ejected) but, most of all, in the surface corrugations of the growing film. These film thickness variations appear as spikes with sharp ends. When the ring of droplets detaches from the edge of the film, this one starts to recedes. The thinner parts of the film (between two spikes) move faster than the thicker zones which give rise to tips from which smaller droplets are ejected forming lines in the radial direction (Fig. 5.5).
During the first pulsation, the zig-zag pattern at the edge of the receding film shows 32 tips, the angle formed are around 70 ± 10 degrees. Droplets are emitted from these tips in a very original and ordered way (Fig. 5.6). Very small droplets are formed at the edge of the film in the valleys between

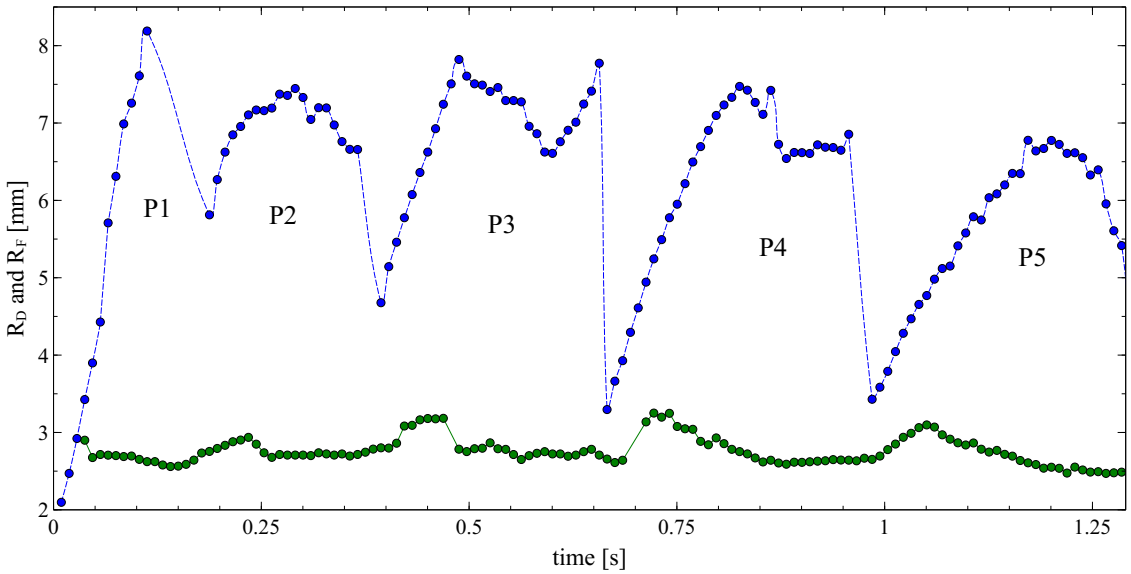

Figure 5.4: *Evolution of R_D (lower curve) and R_F (upper curve) for pulsations P1 to P4.*

two tips, they slide and grow along the film to reach the tips. Droplets sliding on the opposite faces of one tip meet at the sharp end and collide. When three to four have met, the resulting drop (about 90 um in diameter) is ejected from the tip (insert in Fig. 5.6) The ejection frequency is about 150 Hz while the velocity of the ejected droplets is around 40 $mm \cdot s^{-1}$.

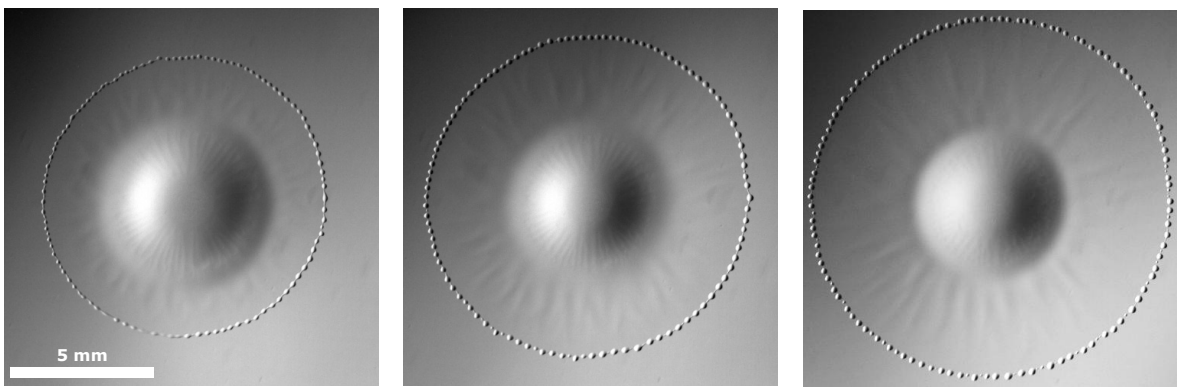

Figure 5.5: *Expanding phase of pulsation P4. Δt = 28.3 ms*

While the tips retract, dewetting holes arise at the back of the receding film, making the next expanding film appear as a new ring of droplets formed in the neighborhood of the central reservoir.

Since the spiky zones are detached from the reservoir drop, the remaining film quickly dewets in the transverse direction, leaving radial lines of droplets that disappear soon (see Fig. 5.7).

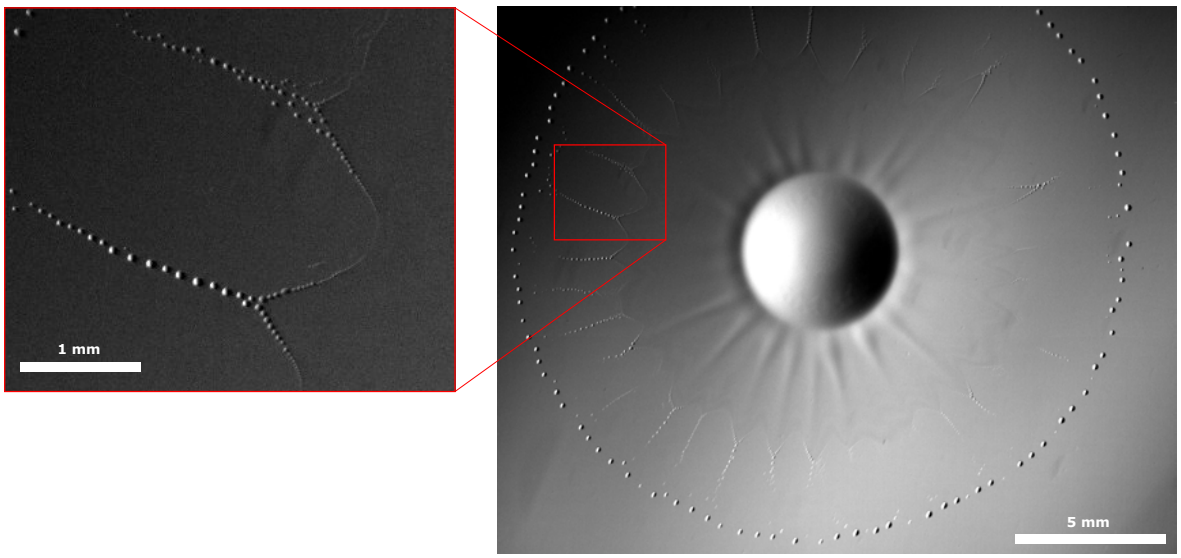

Figure 5.6: *Flower-like dewetting pattern observed during film retraction of pulsation P4. Insert: magnification of the framed area.*

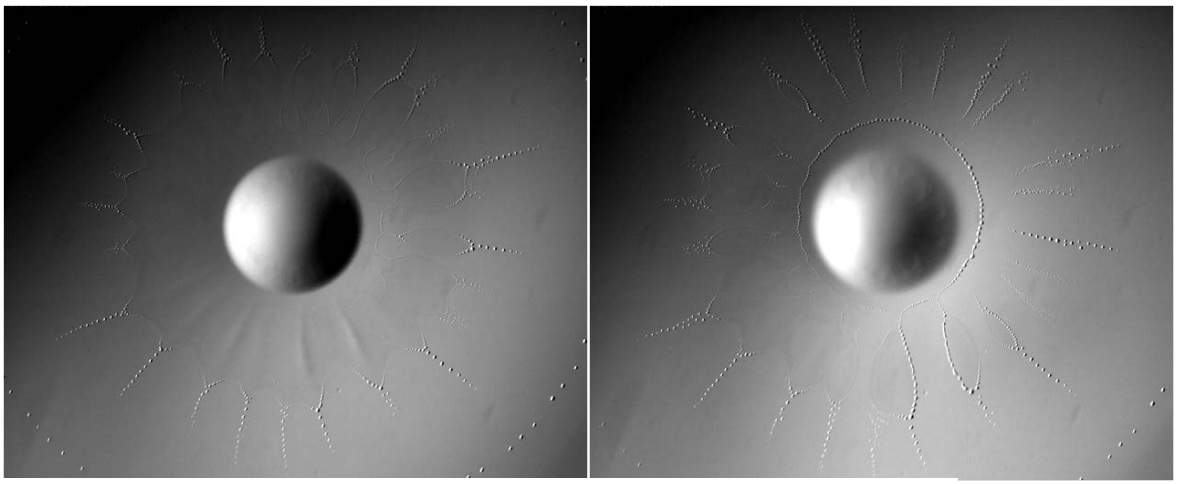

Figure 5.7: *Formation of holes at the back of the film, close to the drop reservoir*

5.3. Interpretation

The spreading coefficient, $S = \gamma_{w/a} - (\gamma_{o/a} + \gamma_{o/w})$, gives an indication on the initial behavior of a drop deposited on a surface. The determination of equilibrium values of interfacial tensions with the pendant drop technique provides the following values:

- 0.5 mmol/L CTAB aqueous solution: $\gamma_{w/a}$= 47 mN/m.
- DCM at the oil/air interface: $\gamma_{o/a}$ = 28 mN/m.
- Water/oil interfacial tension at partition equilibrium (0.5 mmol/L CTAB in the aqueous phase): $\gamma_{o/w}$ = 2.5 mN/m.

The spreading coefficient is then S = 47 – (28 + 2.5) = 17 mN/m > 0. This value is certainly overestimated, since the above value of $\gamma_{w/a}$ does not account for the effect of the primary film (see beelow) which tends to decrease it. Moreover, the effective value of $\gamma_{o/w}$ under present non-equilibrium conditions due to DCM dissolution and film expansion is expected to be higher than the above equilibrium value. However, S keeps a positive value in agreement with the expanding initial phase. The growing rim at the film leading edge of P1 is reminiscent of the Marangoni ridge observed for the deposition of surfactants on liquid pools [4]. The Marangoni effect arises in this case along the above mentioned primary film. The presence of such film is revealed, just before the drop release, by any dust present on the surface being swept away at a very high velocity [5]. This primary film accommodates the surface tension difference between the "clean" surface (only CTAB adsorption at the water/air interface) and the drop. Surface tension gradients created along the primary film induce shear stresses at the interface resulting in motion of the film and water subphase in the direction of high surface tension. Coupled to viscous retardation, the Marangoni flow gives rise to the formation of the advancing rim [6]. Up to that point, the described evolution corresponds to the one observed for volatiles films spreading on a deep fluid layer [7], with complete wetting as the expected final state. However, for surfactant-containing systems the initial expanding phase is sometimes followed by retraction [8]. The deposited drop modifies its own surroundings and the resulting spreading properties. The positive initial spreading coefficient switches to a negative value. In the present case, as $\gamma_{o/a}$ is not expected to vary significantly, a negative value can be reached if $\gamma_{w/a}$ decreases or $\gamma_{o/w}$ increases. The first effect can be achieved by considering the DCM surface activity at the water/air interface. A Wilhelmy plate placed 3 cm away from the release point of a DCM drop shows a decrease of $\gamma_{w/a}$ reaching up to 6 mN/m during the life time of the drop. When the maximum is reached, the drop has faded away and the initial surface tension is recovered (see Fig. 5.8)). Hence the DCM dispersed on the surface by the ejected droplets at the end of the expanding phase strongly modifies $\gamma_{w/a}$ at the vicinity of the now recoiling film.

For $\gamma_{o/w}$, as no molecular exchange is expected at the interface of a spreading film and accounting that the film surface is multiplied by a factor 6, the CTAB interfacial concentration will be decreased

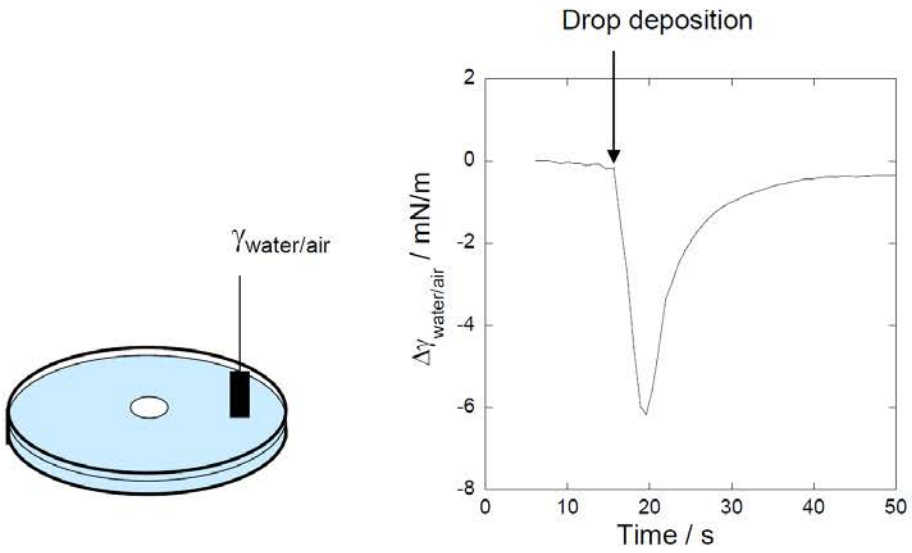

Figure 5.8: *a) Sketch of the experimental set-up for measuring the surface tension with the Wilhelmy plate method ; b) water/air surface tension variation after deposition of a 25* µ*L DCM drop.*

by the same amount leading to an increased $\gamma_{o/w}$ [9]. The contribution of these two effects is likely to represent the main causes of the dewetting stage. For such sequence to repeat and give rise to successive pulsations, recovery processes are compulsory to bring the system back to its initial spreading state. Film recoiling restores $\gamma_{o/w}$ but several processes may contribute at the water/air surface. Evaporation may play a part while direct dissolution seems to be too slow. However, at the required time scale, CTAB-assisted solubilization may also play an important part. Such an effect has been recently reported to be at the origin of the driving force for the reciprocation regime of an oil drop on a sodium dodecyl sulfate aqueous solution [10]. The explanation resides in an effect that was also observed for the present system [11]. The critical micellar concentration (CMC) of CTAB in pure water is 0.9 mmol/L (at CMC, $\gamma_{w/a}$ = 42 mN/m). When contacting DCM with aqueous solution of CTAB, an oil-in-water micro-emulsion is formed and the critical aggregation concentration (CAC) is decreased to 0.12 mmol/L (at CAC, $\gamma_{w/a}$ = 62 mN/m). The two curves plotted in Fig. 5.9 show that saturation with DCM induces an increase of the water/air surface tension from 47 mN/m up to 62 mN/m for a 0.5 mmol/L CTAB solution in water. Transfer occurs thanks to buds of oil surrounded by surfactants that detach from the interface. The surface tension of pure CTAB in water can be restored by air bubbling of the DCM saturated solution. These properties confer to the system its capacity to restore the water/air surface tension after each "contamination" of the surface by the CTAB-containing DCM film, creating the conditions for a new wave to develop.

This description gives a general explanation for the pulsating behavior. Compared to the scarces

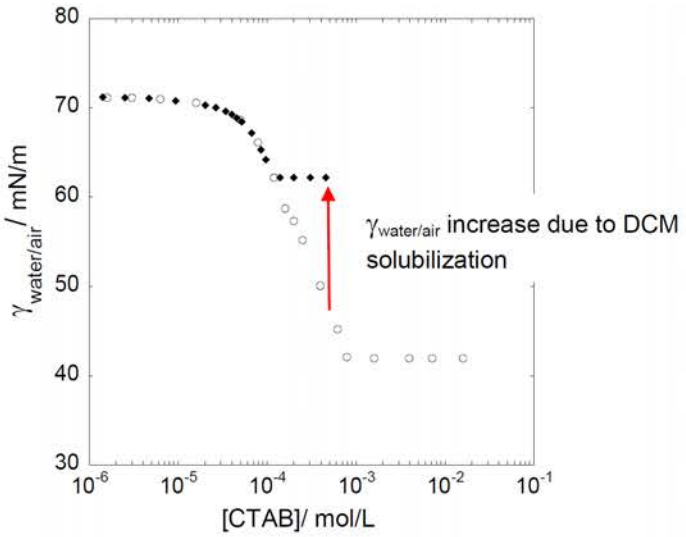

Figure 5.9: *Plot of $\gamma_{w/a}$ as a function of the CTAB concentration. Open circles: in pure water; filled diamonds: in DCM-saturated water. The arrow indicates the surface tension variation induced by saturation of a 0.5 mM CTAB solution with DCM.*

examples of the literature [12, 13, 14] (see chapter 1 (1.7)) the present system is unique if we consider the amplitude, regularity and symmetry of the repeated waves. However, its specificities go beyond the observed pulsations and several features contribute to enrich the complexity and organization.
The detachment of the rim forming a perfect ring of droplets is induced by film breakage of the thin region located just behind the rim. Induced by long-range intermolecular forces, it takes place when the film has reached a critical thickness in agreement with the calculated positive Hamaker constant [15] (see chapter 1 (1.1.5)). In this case, the film tends to thin because of attractive interactions leading to rupture and the liberation of the droplets. The formation of satellites is another manifestation of the Marangoni instability [16]. The amplification of an initial disturbance drives the fluid towards the swollen part of the expanding torus due to the higher capillary pressure in the thinning region. This flow drags the surfactant away from the thinning regions, forming surface tension gradients. Marangoni stresses impel the fluid back to the neck formed in between two droplets leading to smaller bulges that will transform into satellites at breakage.
Concerning the central reservoir, the stripes observed at the edge of the drop during the expanding phase for P3 and P4 are reminiscent of Benard-Marangoni convective rolls induced by evaporation and leading to thermal induced surface tension gradients [17]. These surface modulations form wrinkles in the growing film (see discussion in chapter 4 (4.7.1)) which are similar to the ones produced by an evaporating film climbing on a slightly incline plane [18]. The incline plane is here provided by the deformation of the water/air interface supporting the denser deposited drop (see discussion in

chapter 4 (4.7.1)). The film is hence the location of radial Marangoni driven spreading together with capillary driven transversal flow that maintain the surface corrugation of the growing film. These radial deformations play an important part during film retraction. S has turned negative and the film is metastable, which means that it is stable at larger thickness and unstable below a critical value. This property is at the origin of the zig-zag pattern at the edge of the receding film. Thinner regions tend to dewet while the thicker wrinkles resist back motion. The resulting spikes are the location of the directional droplet ejection. In the meanwhile, holes are created at the back of the existing film near the drop edge. These holes grow while the liquid moves and accumulates in the thicker regions. Not fed anymore by the central reservoir the wrinkles undergo a Rayleigh-Plateau like transition to smaller droplets that vanish mainly by solubilization. The surface is at that point regenerated; CTAB molecules adsorbed on the surface are dragged along with the oil in the subphase creating the conditions for a new wave to develop.

5.4. Comparison of the two Pulsating Regimes (with and without CTAB in the Drop)

The concentration of CTAB in the aqueous phase is here the essential parameter to observe pulsations. This regime is extremely stable and reproducible when the aqueous concentration is of 0.5 mM. The addition of CTAB in the drop does not change the nature of the instability but some (spectacular) modifications arise. The behavior at deposition is completely different. A lens shaped drop is initially observed for the pure DCM drop that survives during the induction period discussed in chapter 3. The spreading coefficient is negative but it increases with the progressive adsorption of CTAB at the water/oil interface.

In the presence of CTAB in the drop the initial spreading coefficient is positive, $\gamma_{w/o}$ is lowered more rapidly, CTAB being now in the dissolving phase. This leads to the immediate spreading of the drop at deposition. The period of oscillations is highly decreased by the addition of CTAB in the drop (by a factor of 3). In that case, the drop always appears like a reservoir (with radius R_D) surrounded by a film (with radius R_F) (see Fig. 5.10 (a)). The drop is more largely expanded on the surface (R_F reaches 7 mm for a 5.6 µL drop) compared to a 25 µL drop of pure DCM (R_F reaches 5.5 mm). In the case of a pure DCM drop the film appears only transiently. The film dewets completely and the drop shape is recovered at each pulsation (see Fig. 5.10 (b)). During the receding stage the spreading parameter reaches a more negative value that lasts longer. The recovery processes are more efficient in the presence of CTAB in the drop and the spreading parameter immediately switches back to a positive value. Evaporation may be more efficient as thinner films are involved and/or the surfactant mediated transfer could be favored by the presence of the "carrier" already in the transferred phase. Fig. 5.11 shows the comparison of R_F and R_D as a function of time for the two pulsating regimes.

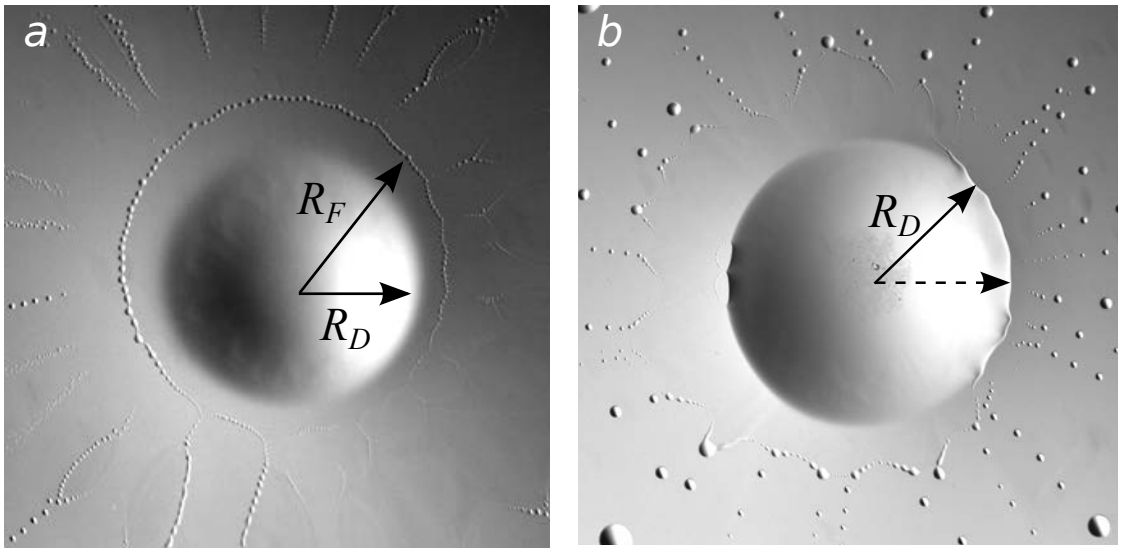

Figure 5.10: *Film surrounding the drop. a: Film does not vanish for a CTAB containing DCM drop (moment of minimal film expansion is shown). b: Film vanishes at the end of the pulsation and the drop shape is recovered for a pure DCM drop.*

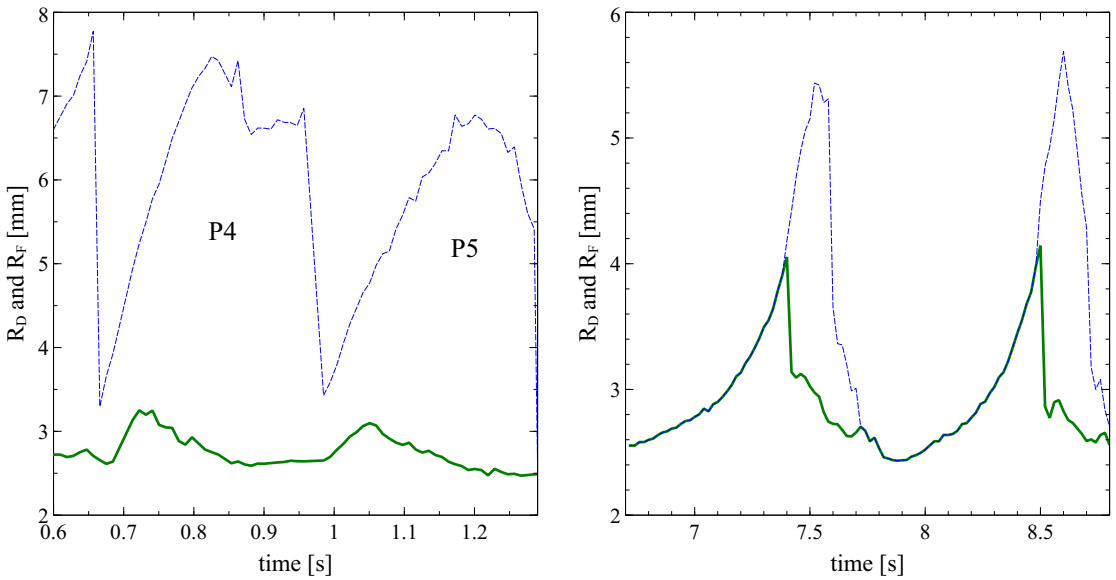

Figure 5.11: *Comparison of the two pulsating regimes (solid green line: R_D; dotted blue line: R_F). a: Pulsations of the DCM drop containing 0.5 mM CTAB.b: Pulsations of a pure DCM drop.*

The general explanation for the two regimes are finally very similar. The reasons for expansion (Maragoni-driven spreading and surfactant adsorption at the water/oil interface), the reason for

recession ($\gamma_{w/a}$ decreases by DCM) and the recovery process (evaporation and solubilization) are certainly the same in both regimes. The values of the related parameters are however slightly shifted giving rise to the characteristic features in each case.

5.5. Conclusion

The patterns revealed by the new experimental conditions explored here could be observed thanks to a high speed camera (see appendix). The pulsating regime is globally accelerated by the addition of CTAB to in the drop. Although faster, the organization culminates during the receding stage with a highly symmetric and complex dewetting pattern. The zig-zag patterns at the edge of the receding film is at the origin of a sophisticated droplet generator.
The enhanced complexity obtained in the presence of CTAB in the drop appears however as the optimization of properties already existing in the pure DCM case. The processes at play in both cases are the same, they are shifted by different initial conditions.

Bibliography

1. R. Xie, A. Karim, J. F. Douglas, C. C. Han, and R. A. Weiss, "Spinodal dewetting of thin polymer films," *Phys. Rev. Lett.*, vol. 81, pp. 1251–1254, Aug 1998.

2. D. Yamamoto, C. Nakajima, A. Shioi, M. P. Krafft, and K. Yoshikawa, "The evolution of spatial ordering of oil drops fast spreading on a water surface," *Nature Communications*, vol. 6, pp. 7189 EP –, May 2015. Article.

3. L. Keiser, H. Bense, P. Colinet, J. Bico, and E. Reyssat, "Marangoni bursting: Evaporation-induced emulsification of binary mixtures on a liquid layer," *Phys. Rev. Lett.*, vol. 118, p. 074504, Feb 2017.

4. X. Wang, E. Bonaccurso, J. Venzmer, and S. Garoff, "Deposition of drops containing surfactants on liquid pools: Movement of the contact line, marangoni ridge, capillary waves and interfacial particles," *Colloids and Surfaces A: Physicochemical and Engineering Aspects*, vol. 486, pp. 53 – 59, 2015.

5. C. Antoine, J. Irvoas, K. Schwarzenberger, K. Eckert, F. Wodlei, and V. Pimienta, "Self-pinning on a liquid surface," *The Journal of Physical Chemistry Letters*, vol. 7, no. 3, pp. 520–524, 2016.

6. G. Karapetsas, R. V. Craster, and O. K. Matar, "Surfactant-driven dynamics of liquid lenses," *Physics of Fluids*, vol. 23, no. 12, p. 122106, 2011.

7. A. D. Dussaud and S. M. Troian, "Dynamics of spontaneous spreading with evaporation on a deep fluid layer," *Physics of Fluids*, vol. 10, no. 1, pp. 23–38, 1998.

8. E. A. van Nierop, A. Ajdari, and H. A. Stone, "Reactive spreading and recoil of oil on water," *Physics of Fluids*, vol. 18, no. 3, p. 038105, 2006.

9. M. Santiago-Rosanne, M. Vignes-Adler, and M. Velarde, "Dissolution of a drop on a liquid surface leading to surface waves and interfacial turbulence," *J Colloid Interface Sci.*, 1997.

10. Y. Satoh, Y. Sogabe, K. Kayahara, S. Tanaka, M. Nagayama, and S. Nakata, "Self-inverted reciprocation of an oil droplet on a surfactant solution," *Soft Matter*, vol. 13, pp. 3422–3430, 2017.

11. R. Tadmouri, C. Zedde, C. Routaboul, J.-C. Micheau, and V. Pimienta, "Partition and water/oil adsorption of some surfactants," *The Journal of Physical Chemistry B*, vol. 112, no. 39, pp. 12318–12325, 2008.

12. R. Stocker and J. W. M. Bush, "Spontaneous oscillations of a sessile lens," *Journal of Fluid Mechanics*, vol. 583, pp. 465–475, 2007.

13. C. M. Bates, F. Stevens, S. C. Langford, and J. T. Dickinson, "Motion and dissolution of drops of sparingly soluble alcohols on water," *Langmuir*, vol. 24, no. 14, pp. 7193–7199, 2008.

14. D. K. Sinz, M. Hanyak, and A. A. Darhuber, "Immiscible surfactant droplets on thin liquid films: Spreading dynamics, subphase expulsion and oscillatory instabilities," *Journal of Colloid and Interface Science*, vol. 364, no. 2, pp. 519 – 529, 2011.

15. C. Antoine and V. Pimienta, "Mass-spring model of a self-pulsating drop," *Langmuir*, vol. 29, pp. 14935–14946, Dec. 2013.

16. V. Dravid, S. Songsermpong, Z. Xue, C. M. Corvalan, and P. E. Sojka, "Two-dimensional modeling of the effects of insoluble surfactant on the breakup of a liquid filament," *Chemical Engineering Science*, vol. 61, pp. 3577–3585, 2006.

17. F. H. Busse, "Non-linear properties of thermal convection," *Reports on Progress in Physics*, vol. 41, no. 12, p. 1929, 1978.

18. A. E. Hosoi and J. W. M. Bush, "Evaporative instabilities in climbing films," *Journal of Fluid Mechanics*, vol. 442, pp. 217–239, 2001.

RESUMÉE EN FRANÇAIS

Le régime de pulsation décrit dans ce chapitre a été obtenu en mettant cette fois du CTAB dans les deux phases : 0.5 mM dans la phase aqueuse comme précédemment et 0.5 mM dans la phase organique (la goutte). le régime de pulsation est maintenu mais il présente des propriétés différentes:

- La phase d'induction n'est plus observée.
- La vitesse du phénomène est modifiée, la période de pulsation passe de 1 s à 0.2 s.
- La phase de démouillage qui suit l'éjection du bourrelet montre une structure régulière tout à fait remarquable en forme de fleur.
- De nouveaux phénomènes d'éjection de gouttelettes sont observés.

La possibilité d'utiliser la caméra rapide nous a permis de mettre en évidence ce phénomène et de montrer sa reproductibilité au cours de deux campagnes de mesures. Nous avons commencé à caractériser les propriétés de ce régime en suivant l'évolution relative du rayon de la goutte centrale (RD) et du film (RF). La figure 5.12 b) montre que les pulsations démarrent en même temps pour le film (R_F) et le réservoir central (R_D). Par contre, le réservoir se rétracte alors que le film est toujours en expansion. Ceci s'explique peut être par le fait que la goutte alimente le film. En effet, cette diminution s'arrête et la courbe devient plate lorsque le film commence à démouiller. Il est également intéressant de noter que la pulsation suivante démarre alors que la précédente n'as pas encore disparu, contrairement à ce que l'on observe lorsqu'il n'y a pas de CTAB dans la goutte.
Comme dans le cas précédent on observe des rides radiales dans le film en expansion mais elles ne sont pas ici corrélées au nombre de gouttelettes éjectées mais jouent un rôle très important dans la formation de la structure de démouillage (Figure 5.13).

Une interpretation du phenomène du pulsation pourrait etre la suivante: Le calcul du coefficient d'étalement positif prévoit l'étalement de la goutte. C'est en effet ce qui est observé lors du dépôt

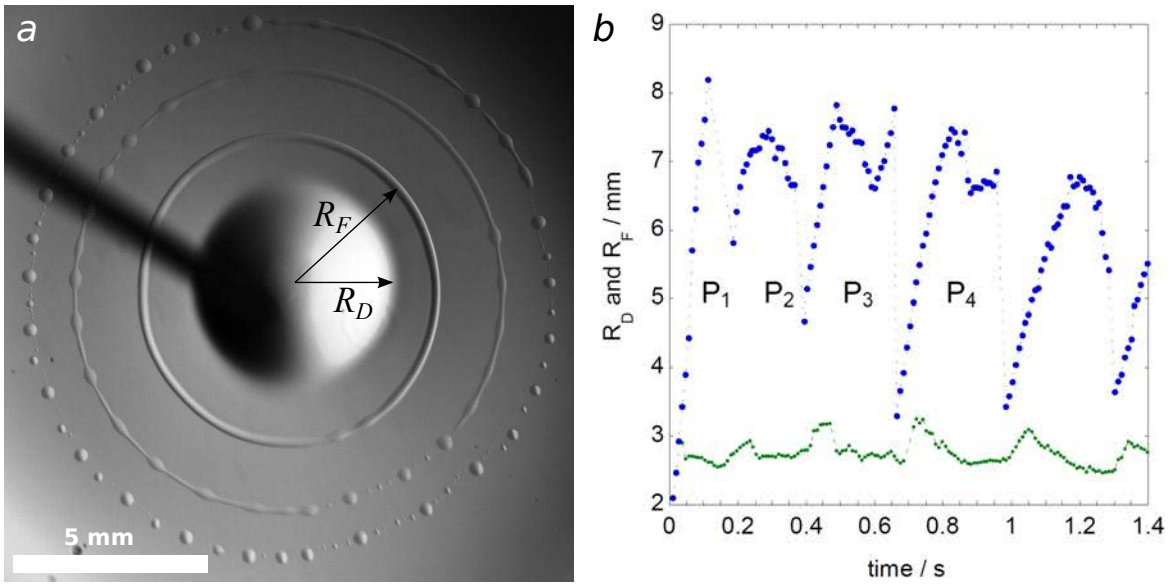

Figure 5.12: *Phase d'expansion de la pulsation. a: superposition de 3 images obtenues au cours d'une pulsation Δt = 28.3 ms; définition de R_D et R_F. b) évolution de R_D et R_F au cours du temps.*

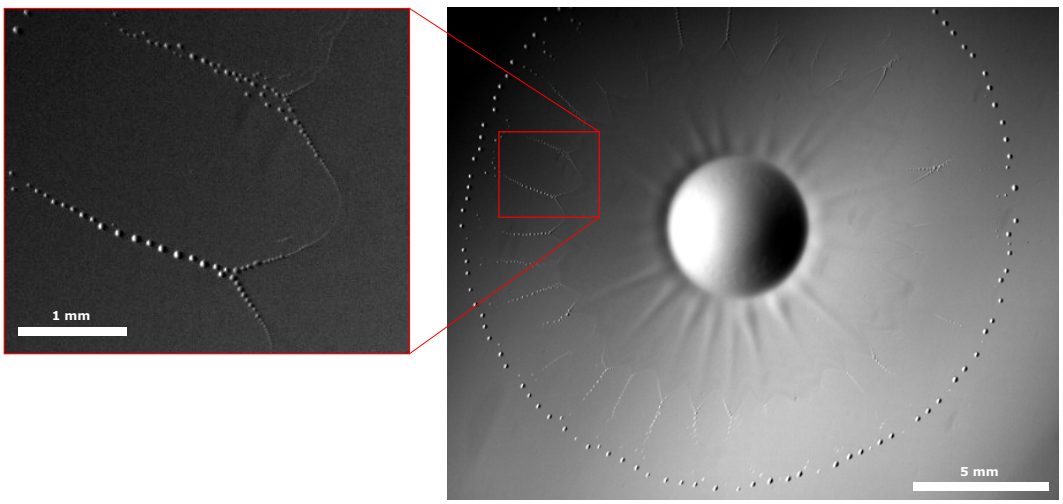

Figure 5.13: *la structure de démouillage de la pulsation P4.*

de la goutte; l'expansion donnant lieu également à la formation d'un bourrelet à l'extrémité du film, signe de la contribution de l'effet Marangoni.
Cependant lors de cette phase d'expansion les propriétés de la surface autour de la goutte sont modifiées (le DCM étant lui-même tensioactif) induisant une transition du système vers un coefficient

d'étalement négatif qui entraine le recul du film. Ce film dont l'épaisseur n'est pas homogène, ne démouille pas de façon homogène donnant lieu à un contour en zig-zag du film. Des gouttelettes sont ejectées par les pointes formées au cours de ce phénomène de démouillage selon un mécanisme tout à fait étonnant. Les gouttelettes sont initiées dans les creux, elles glissent le long du film sur les faces opposées de la structure en zig-zag et sont éjectées après coalescence de deux ou trois d'entre elles. Le film fini cependant par se contracter suffisamment. Les processus de restauration de la surface peuvent alors intervenir (évaporation, dissolution), le système retrouve ses propriétés initiales et peut donner lieu à une nouvelle pulsation.

General Conclusion

In this work we have deepened our understanding of the behavior of a dichloromethane (DCM) drop on the surface of a aqueous solution containing surfactants (CTAB). The main focus was on the pulsating regime that arises for a 0.5 mM CTAB concentration in the aqueous phase. The investigations presented in this work cover the induction period, the pulsating regime for pure DCM drops and DCM drops containing CTAB.

Studying the induction phase we have found an interesting behavior of the drop so far not seen in other systems. With the help of PIV measurement and side-view analysis we observed "self-pinning" (diameter stays constant while the height and the contact angle decreases) of the drop during the evolution towards the instabilities. This is the result of two antagonistic effects: the mass loss, due to evaporation and solubilization of the DCM, tends to decrease the diameter while the reduction of the water/oil interfacial tension, which is induced by the CTAB adsorption, tends to increase the diameter. When the dissolution flow that prevents surfactant adsorption at the water/oil interface is decreasing the diameter increases again leading to an increase in the spreading parameter and, after a peak in the diameter, the instability starts.

In the study of the pulsating regime we were specially interested in the rim break-up dynamics, which follows a Rayleigh-Plateau-like instability. Nevertheless we found a characteristic wavelength of a factor of 2 too small compared to a classic Rayleigh-Plateau instability. This discrepancy is surely comes from the fact that our system is more complex than a classic Rayleigh-Plateau instability where a static liquid column is breaking-up. First of all, the system shows a toroidal geometry, and more importantly to its dynamics, it is generated from a drop to which it is connected *via* a thin film throughout the whole expansion. The dynamic flows in the film eventually lead to the characteristic wavelength observed here, which are manifested by different structurations observed in the film as radial wrinkles. These wrinkles lead to an already pre-corrugated rim when the instability starts. The formation of the wrinkles is supposed to be due to a Benard-Marangoni instability induced by the evaporation of DCM.
Roisman et al. proposed a theory in which a rim connected to a liquid sheet under certain conditions can break-up with such a characteristic wavelength. We adapted this model to our situation and also in our case it theoretically predicts a characteristic wavelength within the range observed here.
Even though this model is able to predict the experimentally observed characteristic wavelength it does not give enough insight into the actual mechanism leading to the rim break-up. Further investigation regarding the flows in the film and the wrinkles formation are necessary to fully understand the underlying mechanism.

Investigating the pulsating regime that arises when DCM drops containing CTAB are placed on a 0.5 mM CTAB solution led us to the discovery of a remarkable flower-like dewetting pattern. The dynamics in this case is a factor of around 3 times faster than in the normal pulsating regime. One main difference between the two pulsating regimes is that the DCM drop containing CTAB spreads immediately on the surface and starts to pulsate while for a pure DCM an induction period exists. This is understood in terms of the spreading parameter, which is already positive for the DCM drop containing CTAB, while it is not in the case of the pure DCM drop. There, it starts with a negative value that increases due to the adsorption of surfactants at the oil/water interface, which leads to the appearance of an induction phase.
Another main difference is found in the dewetting part of the pulsations. We observe that the DCM drop containing CTAB is always surrounded by a film acting itself as a reservoir to this film while for the pure DCM drop the film completely recedes restoring the drop-shape at the end of each pulsation. This again might be understood in terms of the spreading parameter. The recovery processes are more efficient in the presence of CTAB in the drop and the spreading parameter immediately switches back to a positive value (even before the film completely dewets). Evaporation may be more efficient as thinner films are involved and/or the surfactant mediated transfer could be favored by the presence of the "carrier" already in the drop.
Nevertheless both pulsating regimes are different, the high complexity observed in the presence of CTAB in the drop appears as the optimization of properties already existing in the pure DCM case. In both cases the processes at play are the same but the initial conditions are different.

With this work we have increased our understanding of this rich and complex system but also new questions have arisen and still more dynamic regimes need to be studied. There is the rotating regime and the polygonal regime for instance, that appear for higher surfactant concentrations of 10 and 30 mM CTAB, that was briefly discussed in section 2, and there are also a whole range of regimes with CTAB in the organic phase on which we did some preliminary experiments that showed also interesting and not expected behavior.

Conclusion générale

Conclusion générale

Ce travail nous a permis d'approfondir notre compréhension du comportement d'une goutte de dichlorométhane (DCM) à la surface d'une solution aqueuse contenant du CTAB. Nous nous somme particulièrement intéressés au régime de pulsation observé lorsque la concentration en phase aqueuse est de 0.5 mM. Les travaux présentés dans ce travail couvrent la période d'induction, le régime de pulsation pour des gouttes de DCM pur et pour des gouttes de DCM contenant du CTAB. L'étude de la phase d'induction nous a permis de mettre en évidence un comportement non décrit dans la littérature. En effet, on observe une phase d'encrage (diamètre reste constant alors que la hauteur et l'angle de contact diminuent). L'observation en vue de côté couplée aux mesures de PIV nous ont permis de proposer une interprétation de ce phénomène. Il est le résultat de deux effets antagonistes : la perte de masse due à l'évaporation et à la solubilisation tend à diminuer le diamètre alors que l'adsorption du tensioactif à l'interface eau/huile tend à le faire augmenter. Lorsque le flux convectif induit par la dissolution du DCM diminue, l'adsorption du CTAB devient plus importante et la résultante de ces deux effets donne lieu à la phase d'encrage. Pendant cette phase le coefficient d'étalement augmente, une brusque augmentation du diamètre est observée juste avant le démarrage de l'instabilité.

Lors de l'étude du régime de pulsation, nous nous somme particulièrement intéressés à la dynamique de rupture du bourrelet dont le comportement est similaire à celui observé pour l'instabilité de Rayleigh-Plateau. Cependant, nous avons trouvé une longueur d'onde caractéristique deux fois plus faible qu'attendue. Cette différence provient certainement du fait que notre système est plus complexe que le cas classiquement étudié d'une colonne liquide et statique. Premièrement, le système est ici un tore et, plus important, il est généré par la goutte à laquelle il est connecté par un film mince pendant toute la phase d'expansion. Les flux générés dans le film sont sans doute à l'origine de cette différence et se manifestent par la formation d'ondulations en direction radiale. Ces variations d'épaisseur du film mènent à la formation d'un bourrelet qui montre des déformations avant le début de l'instabilité. Ces ondulations du film pourraient être dues à une instabilité de Bénard-Marangoni induite par l'évaporation du DCM. Roisman et al. ont proposé une théorie pour un bourrelet connecté à un film liquide montrant que sous certaines conditions la rupture peut avoir lieu avec une longueur d'onde équivalente à la notre. Nous avons adapté ce modèle à notre géométrie et montré que le modèle prévoit la longueur d'onde caractéristique dans la gamme mesurée expérimentalement. Cependant ce modèle ne permet pas d'expliquer entièrement le phénomène de rupture pour lequel nous devrions prendre en compte les flux dans le film et la formation des ondulations dans celui-ci.

Le régime de pulsations observé lorsque la goutte contenant du CTAB est placée sur une solution à 0.5 mM de CTAB nous a permis de mettre en évidence une structuration remarquable du film de

démouillage rappelant une fleur. La dynamique est à peut près 3 fois plus rapide que pour le régime obtenu en l'absence de tensioactif dans la goutte. L'une des principales différences entre ces deux régimes est, qu'en présence de tensioactif dans la goutte, celle-ci s'étalement dès le dépôt de la goutte à la surface alors qu'une phase d'induction est observée lorsque la goutte est constituée de DCM pur. Ceci s'explique par un coefficient d'étalement qui est initialement positif en présence de CTAB dans la goutte alors qu'il est négatif lorsque le DCM est utilisé pur. Une deuxième différence est observée lors de la phase de démouillage du film. En effet, en présence de tensioactif le réservoir central est toujours entouré d'un film alors qu'en l'absence de tensioactif le film disparait complètement pendant la phase de démouillage, la goutte retrouve sa forme initiale après chaque pulsation. Ceci peut également être interprété en termes de coefficient d'étalement, les processus de régénération de la surface autour de la goutte seraient plus rapides en présence de CTAB, le coefficient d'étalement commute très rapidement vers une valeur positive (avant que le film n'ait eu le temps de démouiller complètement). L'évaporation pourrait être plus rapide pour des films plus minces et/ou le transfert assisté par le tensioactif pourrait être plus rapide lorsque le « transporteur » est initialement dans la phase organique. Finalement dans les deux cas les processus à l'œuvre seraient similaires mais les conditions initiales sont différentes.

Ce travail nous a permis d'approfondir notre compréhension de ce système complexe mais a également soulevé de nouvelles questions. Il reste évidemment à étudier les régimes obtenus pour des concentrations en tensioactifs plus élevées (rotation, régime polygonal) mais également de nombreux régimes observés en présence de CTAB dans la goutte pour lesquels nous avons fait quelques expériences préliminaires qui montrent des comportements intéressants et inattendus.

APPENDIX

A

Materials and Methods

A.1. Reagents

All chemical reagents used are of analytical grade. Cetyltrimethylammonium bromide (CTAB) (Aldrich, $\geq 99\%$), Dichloromethane (DCM) (Aldrich, HPLC grade). Water is ultra-pure (resistivity > 17 M$\Omega \cdot cm$). All experiments are carried out at room temperature.

A.2. Physico-chemical Properties

The density of DCM (1.33 g/mL) is larger than that of water. The solubility of water in DCM is 2 g/L at 25 °C. The solubility of dichloromethane in pure water is 13 g/L, which corresponds to a volume of 250 µL in 25 mL. The solubility of CTAB in water is 15 g/L (41 mmol/L). The boiling point of DCM is 39.6 °C

A.3. Method of Placing the Drop

The DCM is placed on the surface of the aqueous solution with the help of a gastight HPLC syringe of 100 µL. Deposition of the DCM is done by emptying the syringe from around 5 mm away from the water surface. The maximal drop volume that can be deposited at once on the surface is 5.6 µL $\pm$ 0.1 µL. For bigger final drop volumes several smaller droplets are added together by emptying the syringe.

A.4. Optical Setup

An optical setup using the Schlieren technique[1] was constructed to visualize the DCM drop on the surface (see Fig. A.1). A LED backlight was used as a light source, the sharp edge of a metal ruler as the Schlieren source and a focusing lens of 12 cm focal lengths.

A.4.1. Used Cameras and Objectifs

Three cameras were used to record the images. The Stingray F080C with an acquisition rate of 24fps and the Canon EOS 600D with an acquisition rate of 24fps and a 100 mm macro objective which was used for the normal pulsating regime and the high-speed PCO Dimax camera with a maximal acquisition rate of 1279.348 fps and a 200 mm macro objective (AF Micro-Nikkor 200mm f/4D), which was provided by the Institut de Mécanique des Fluides de Toulouse (IMFT), was used for both the normal and the very fast pulsating regime.

[1] see e.g. G.S. Settles: *Schlieren and Shadowgraph Techniques*, Springer Verlag, 2001

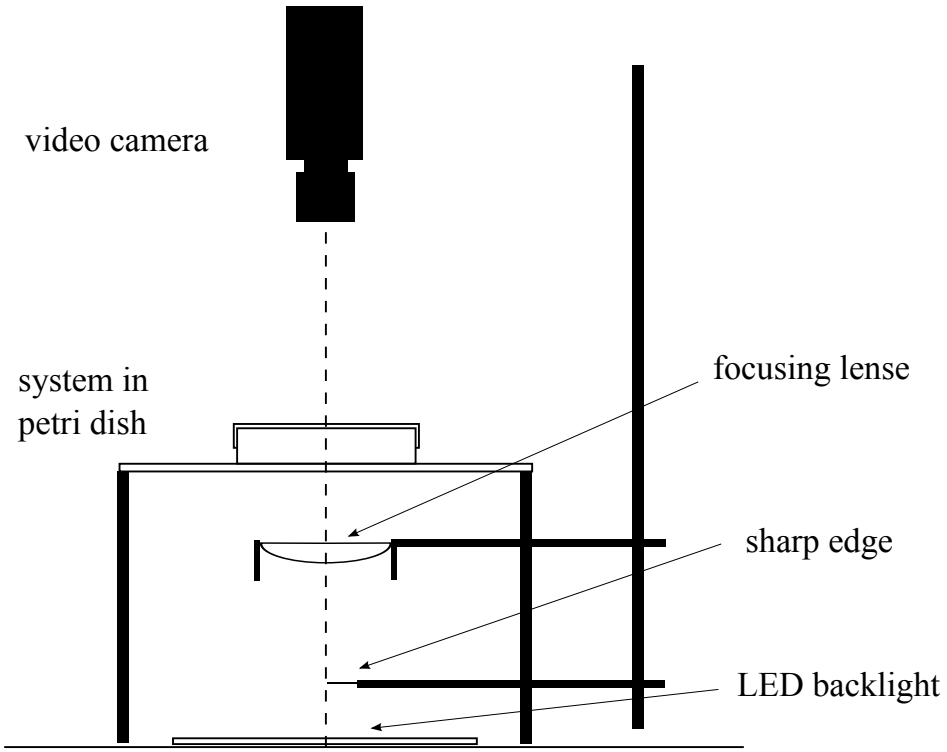

Figure A.1: *Optical Setup used to visualize the DCM drop. Distance between the sharp edge and the lens is 12 cm.*

B

Stability of the Drop on the Surface

In this appendix the stability of the drop on the liquid surface is investigated and the observations are qualitatively confirmed by a simple model based on the spherical cap approximation of the drop.

B.1. Observations

An interesting observation can be made if the air volume above the aqueous phase is small. In this case the drops are likely to drop down soon after covering. This effect is always accompanied by an increase in the contact angle and an elongation of the drop along the z axis until its finally drop down, while always a small part remains on the surface (see sequence of images in figure B.1).
This fact together with the fact that the oil/water interfacial tension does not change significantly during the first 100 seconds (see chapter 3 (3.2.)) and the assumption that the oil/air interfacial tension does not vary significantly during the whole process allows us to conclude that the rate of the decrease of the air/water interfacial tension is higher if the air volume above the drop is small.
In other words if the air volume is smaller its gets saturated faster with DCM gas and the evaporation rate of the DCM film is decreasing which increases its thickness and therefore decreases the air/water interfacial tension.

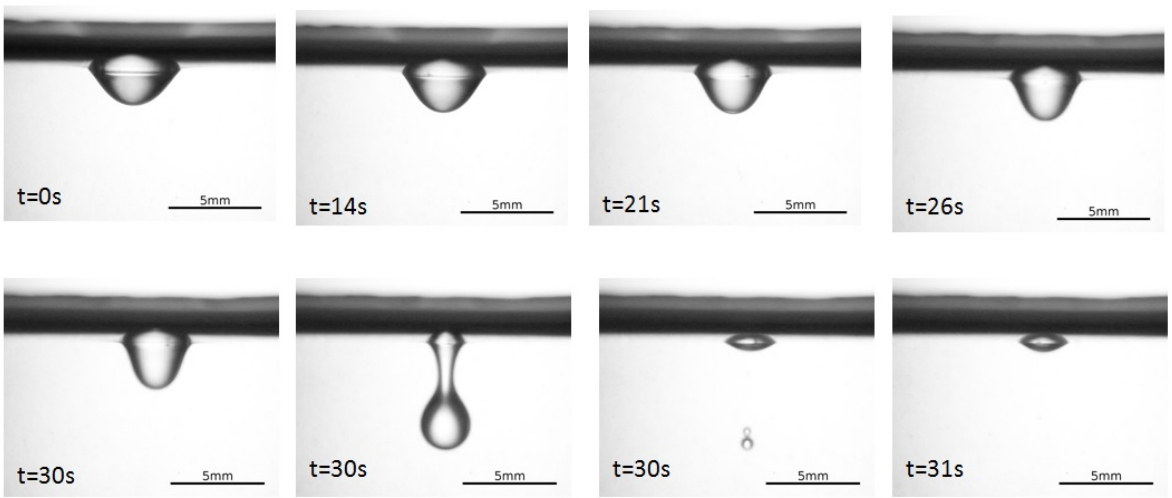

Figure B.1: *Sequence of a drop that is falling down shortly after adding (25µL on top of 10mM CTAB solution in a 3x3x3cm cuvette (13.5mL)).*

The increase in the contact angle is such that the shape of a 25µL drop on a 0.5mM CTAB solution in a 3x3x3cm cuvette with the same volume of air and aqueous solution (13.5mL) is changing after 90 s to a shape that is observed for a 25µL drop on a 10mM CTAB solution from the very beginning (see figure B.2). That means that in 90 s the water/air interfacial tension has decreased to the value of a 10mM CTAB solution.

From this observation it seems that the origin of the decrease of the air/water interfacial tension

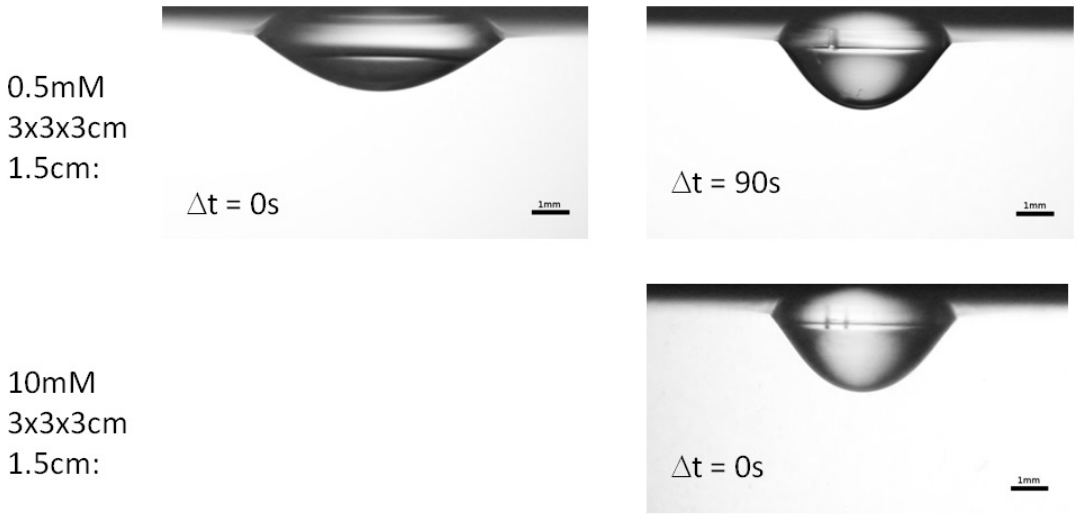

Figure B.2: *Apparent similarity between shape of a droplet on a 0.5mM CTAB solution after 90 seconds and a droplet on a 10mM CTAB solution right after adding (experiments carried out in a 3x3x3cm cuvette with 13.5mL air above). In the upper panel the side view of a droplet on a 0.5mM CTAB solution is shown right after adding and 90 seconds later. In the lower panel the side view of a droplet on a 10mM CTAB solution right after adding is shown.*

arises due to the presence of DCM gas in the air volume above the drop. The process of dropping down on the other hand can be related to buoyant forces.
Bigger (and therefore heavier) drops deform more the surrounding interface (see Fig. 4.16), which eventually leads to a bigger contact angle and a higher relative importance of buoyant forces. Too big drops (depending also on the concentration of the CTAB solution) can even drop down during the time while the drop is deposited on the surface.

The dropping down of a drop happens when the buoyant forces overcome the cohesive forces inside the DCM since then drop fission takes place. This buoyant forces are getting more important with the drop elongation which itself increases when the air/water interfacial tension decreases. In other words the decrease in the air/water interfacial tension leads to an increase in the importance of the buoyant forces, that can lead to a drop down of the drop.

An overview of the stability of drops for changing volume and changing CTAB concentration is shown in Fig. B.3. In the following we will discuss an analytical model, which will help us to verify our interpretations.

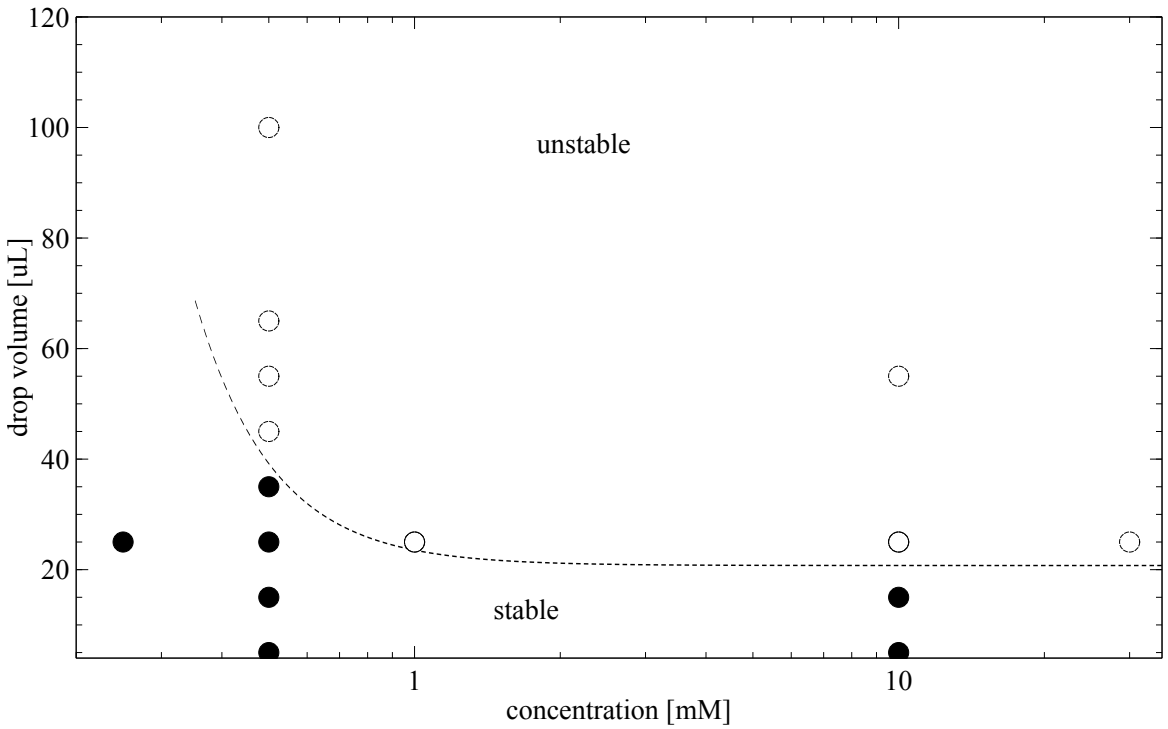

Figure B.3: *Stability of a DCM droplet on the surface of a 13.5mL (1.5cm height) CTAB solution in a 3x3x3cm cuvette with 13.5mL air volume above. "Stable" means that the drops are not falling down and "unstable" means that they are falling down shortly after deposition (sequence shown in Fig. B.1) (densely shaded points) or during deposition (white points). The line separating the different regimes serves as a guide for the eye.*

B.2. Modeling

For simplicity the drop was modeled as a spherical cap[1]. Even though simple it represents quite well the geometry of the drop (specially for very small drops). A comparison between the actual shape of the drop and a spherical cap approximation shows that the approximation is quite good in describing the dynamics of the drop in the induction phase. Even though the calculated contact angle in this approximation is around 14º to big compared to the measured ones. (see Fig. B.4).

This model shows indeed qualitatively that the decrease in the air/water interfacial tension increases the contact angle as well as that the buoyancy is affecting the contact angle. In this model we take the oil/water interfacial tension and the air/oil interfacial tension as constants according to the observations discussed above.

[1] adaptation of the model used in the diploma thesis F. Wodlei: *A Biophysical Model for the Biogenesis of Lipid Droplets* (Institute of Chemistry, Computational Physical Chemistry group. University of Graz, Austria.), 2010

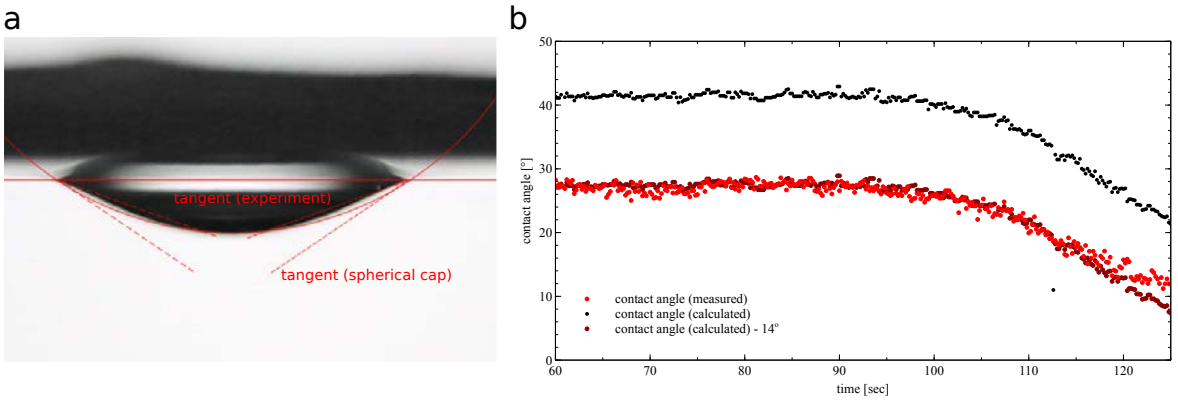

Figure B.4: *Spherical cap approximation. a: Comparison of the actual shape of a 20* µL *drop with a spherical cap shape (14° difference in the contact angle). b: Calculated contact angle in comparison to the measured one (black: Calculated contact angle by taking the measured height and diameter, red: measured contact angle, dark red: calculated contact angle -14°). Contact angle is calculated using measured height and diameter.*

We start with the surface energy of the system , which is given by

$$E_{\text{surface}} = \gamma_{\text{air/oil}} A_{\text{air/oil}} + \gamma_{\text{air/water}} A_{\text{air/water}} + \gamma_{\text{oil/water}} A_{\text{oil/water}}, \tag{B.1}$$

where $A_{\text{air/oil}}$, $A_{\text{air/water}}$ and $A_{\text{oil/water}}$ are the air/oil, air/water and oil/water interfacial areas. This energy has to be completed by a term taking into account the buoyancy of the drop. We obtain the total energy of the system by

$$E_{\text{tot}} = E_{\text{surface}} + E_{\text{pot}} = \gamma_{\text{air/oil}} A_{\text{air/oil}} + \gamma_{\text{air/water}} A_{\text{air/water}} + \gamma_{\text{oil/water}} A_{\text{oil/water}} + \Delta\rho\, V\, g\, (h_o - \bar{z}) \tag{B.2}$$

where $\bar{z}$ is the gravity center of the drop and h_o is the height of the aqueous phase. Now we need to find a minimum of the total energy E_{tot} with respect to the surface area. By noting $\gamma_{\text{air/oil}} = \gamma_1$, $\gamma_{\text{air/water}} = \gamma_2$ and $\gamma_{\text{oil/water}} = \gamma_3$ we are left with the expression

$$E_{\text{tot}} = E_{\text{surface}} + E_{\text{pot}} = \gamma_1 A_{\text{air/oil}} + \gamma_2 A_{\text{air/water}} + \gamma_3 A_{\text{oil/water}} + \Delta\rho\, V\, g\, (h_o - \bar{z}) \tag{B.3}$$

while $A_{\text{air/water}} = A_{\text{tot}} - A_{\text{air/oil}}$ which leads to

$$E_{\text{tot}} = E_{\text{surface}} + E_{\text{pot}} = (\gamma_1 - \gamma_2) A_{\text{air/oil}} + \gamma_3 A_{\text{oil/water}} + \underbrace{\Delta\rho\, V\, g\, (h_o}_{\text{constant}} - \bar{z}) + \underbrace{\gamma_2 A_{\text{tot}}}_{\text{constant}} \tag{B.4}$$

Within the spherical cap approximation we have

$$A_{\text{oil/water}} = 2\pi R_c^2(1-\cos\theta_c) \tag{B.5}$$

$$A_{\text{air/oil}} = \pi R_c^2 \sin^2\theta_c \tag{B.6}$$

$$\bar{z} = \frac{4hR_c - h^2}{4(3R_c - h)} \qquad \text{with } h = R_c(1-\cos\theta_c) \tag{B.7}$$

where R_c is the radius of the cap and θ_c is the contact angle. With this expressions the total energy writes

$$E_{\text{tot}} = \Delta\gamma_{12}\pi R_c^2 \sin^2\theta_c + 2\pi\gamma_3 R_c^2(1-\cos\theta_c) - \Delta\rho V g R_c \frac{(3-2\cos\theta_c-\cos^2\theta_c)}{4(2+\cos\theta_c)} + \text{const.} \tag{B.8}$$

where $\Delta\gamma_{12} = \gamma_1 - \gamma_2$. To find the state with the minimal energy, this expression has to be minimized with respect to θ_c and R_c and the constraint of constant volume, which reads

$$V = \frac{4\pi R_c^3}{3}\left(\frac{1}{2} - \frac{3}{4}\cos\theta_c + \frac{1}{4}\cos^3\theta_c\right) = V_o = \text{const.}. \tag{B.9}$$

This equations gives us a connection between R_c and θ_c. Using new variables $x := R/R_c$, where R is the theoretical radius of a sphere corresponding to the initial volume V_o and $y = \sin^2\frac{\theta_c}{2}$, the energy can be written as

$$E_{\text{tot}}(x) = 4\pi\left[a\frac{y}{x^2} + b\frac{y^2}{x^2} - \delta\frac{2y-y^2}{3x(3-2y)}\right] + \text{const.} \tag{B.10}$$

where y is a function of x, i.e. $y = y(x)$ which can be calculated from equation (B.9). The coefficients a, b and δ are given by

$$\begin{aligned} a &= (\gamma_1 - \gamma_2 + \gamma_3)R^2 \\ b &= (\gamma_2 - \gamma_1)R^2 \\ \delta &= \Delta\rho g R^4 \end{aligned} \tag{B.11}$$

Numerically finding the minimum in $E_{\text{tot}}(x)$ with regard to x gives us the contact angle θ_c and the diameter $D = 2R_c$ of the spherical cap. The mathematica program used for this purpose is given in appendix C.2

B.2.1. Discussion

This model, despite its simplicity, is able to describe quite well the behavior we observed experimentally. The increase in the contact angle due to an decrease in the air/water interfacial tension is quite well described by the model regarding a the systematic error of 14° between theory and experiment discussed above.

The model predicts a contact angle of 48.5° and a diameter of 8.6 mm compared to the experimental

ones of 33° and 6.5 mm for a 25µL drop on a 0.5mM CTAB solution. Subtracting the systematic 14° we obtain a value of 35.5°, which is almost the one observed experimentally.

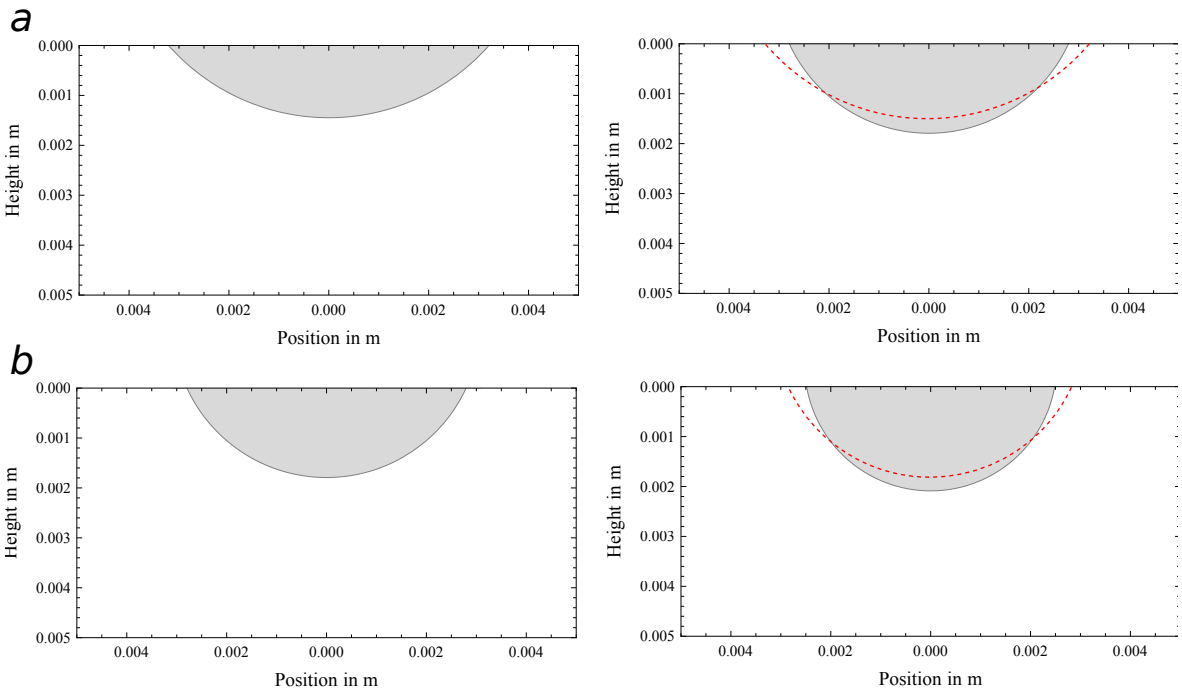

Figure B.5: *Predictions of the spherical cap model. a: Increase in the contact angle due to an decrease of the air/water interfacial tension from 48 mN/m to 42 mN/m due to the presence of DCM gas for a 25µL drop on a 0.5mM CTAB solution (evolution form left to right). a: Increase in the contact angle due to an decrease of the air/water interfacial tension from 42 mN/m to 36 mN/m due to the presence of DCM gas for a 25µL drop on a 10mM CTAB solution (evolution form left to right).*

The effect shown in Fig. B.2, namely that a 25µL drop on a 0.5mM solution increases its contact angle and reduces its diameter due to the presence of DCM gas such that it looks like a drop on a 10mM CTAB solution is also predicted by the model assuming a decrease of the air/water interfacial tension to the value of a 10mM CTAB solution (which corresponds to a decrease of 6mN/m). The model predicts here a contact angle of 65° and a diameter of 6.1 mm compared to the experimental ones of 50° and 4.6 mm. Subtracting the systematic 14° we obtain a value of 51°, which again is almost the one observed experimentally. Nevertheless the absolute values are not predicted correctly. Looking instead at the relative change in the diameter, we obtain the same ratio ($(D/D')_{\text{theory}} = 0.7$ compared to $(D/D')_{\text{exp}} = 0.7$) and if we take the increase in the contact angle we obtain again almost the same increase ($\Delta\theta_c^{\text{theory}} = 16°$ compared to $\Delta\theta_c^{\text{exp}} = 15°$).

The effect of dropping down of an initially stable drop is also rather well captured. For the drop down of a 25µL drop on a 10mM CTAB solution shown in Fig. B.1 a critical contact angle between 60-70° is observed. Assuming a decrease in the air/water interfacial tension of 6 mN/m due to the presence of DCM gas as in the other case discussed above leads to a model prediction of an increase in the contact angle to a value of 80°. Subtracting again the systematic 14° we obtain a theoretical drop-down value of 66°, which is in the range of the observed critical drop down contact angle.

The dropping down of a drop during the adding process is not so easy to capture by the model. As described in appendix A, the deposition process of the droplet is a multistep process which means that several subsequent droplets are added to the surface to form a drop of 25 µL. Since during the deposition the droplets are falling from a height of around 5mm the contact angle can be shortly bigger then the "equilibrium" one obtained after stabilization of the final drop.
If we assume that a critical contact angle has to be reached to obtain the dropping down, it might be already reached during the adding process.

As expected the model does not predict correctly the volumes for dropping down of the drop. It predicts a critical volume of $V_{crit.theory} = 330$ µL for 0.5mM compared to the much smaller experimentally value of 65 µL. For 1 mM it predicts a critical volume of $V_{crit.theory} = 110$ µL compared to an again much smaller experimentally observed value of 25 µL.
Nevertheless the relative decrease in the critical dropping volume with increasing CTAB concentration is predicted in good agreement with the experimental value ($(V_{0.5mM}/V_{1mM})_{\text{theory}} = 3$ and $(V_{0.5mM}/V_{1mM})_{\text{exp}} = 2.6$).

C

Programs and Macros

C.1. Side View Extractor

The side view of the drop allows to measure the contact angle, the height and the diameter from the pictures we obtain with the camera. To save time and have a good time resolution of the parameters I developed a small program in C++ to extract them from the images which was usually done before by hand.

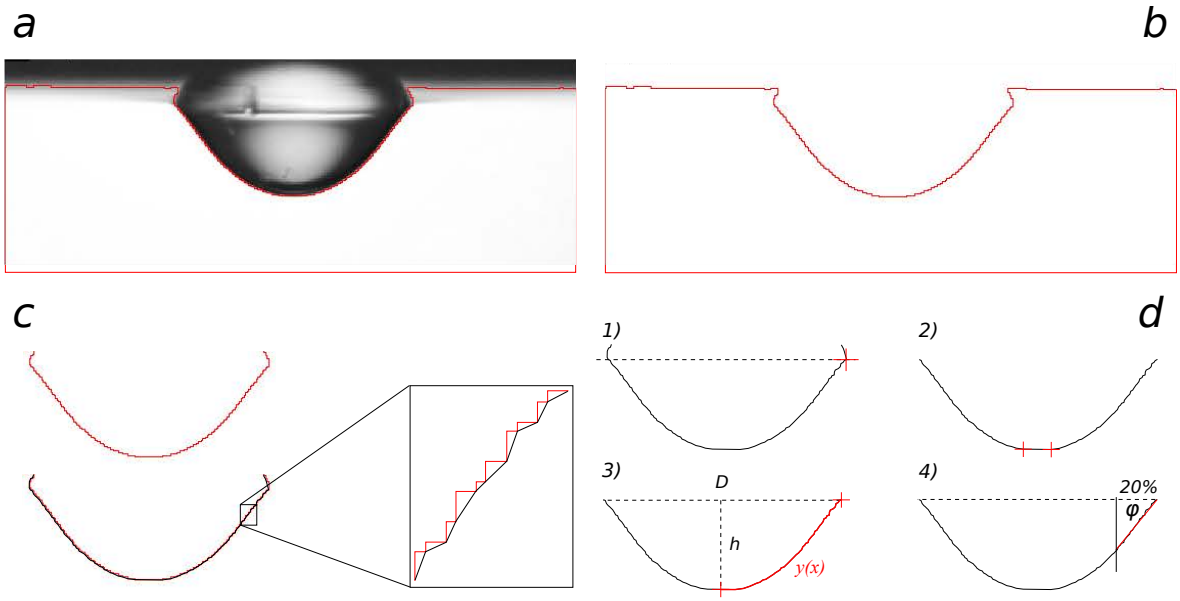

Figure C.1: *Details on the how the program extracts the height, the diameter, the contact angle and the volume from a sideview image. a: Side view image with selection of the white background.*

The optical setup was adjusted in such a way that the drop appears dark on an almost white background (see Fig. C.1 (a)). First the image treatment program "ImageJ/Fiji" was used to select the white part in the image with a tool called "Wand (tracing) tool", where a tolerance value between 40 and 90 was selected (depending on the contrast of the image). The selection of the white background includes already the profile information of the drop (see Fig. C.1 (b)). To automatize this work I wrote also a small ImageJ macro (see below).
This macro simply saves the selection in form of a text file containing the coordinates of the pixels forming the boundary (red line in Fig. C.1 (b)). As input the macro needs the coordinates where to do the "Wand (tracing) tool", typically a point of the white background and the tolerance value. Additionally it rotates the images if necessary.

```
inputFolder = getDirectory("Profile extractor - Choose the input folder!");
addpath = getString("Subfolder for saving the coordinate files (no points in name):", "");

d = getNumber("Rotation angle ([U+FFFD]):",-0.8);
runarg = "\"angle="+d+" grid=1 interpolation=Bilinear slice\" ";

a = getNumber("Give coordinates for Magic Stick (x):",63);
b = getNumber("Give coordinates for Magic Stick (y):",300);
c = getNumber("Give Tolerance level for Magic Stick:",80);

setBatchMode(true);

File.makeDirectory(inputFolder+"/"+addpath+"/");
images = getFileList(inputFolder);
notice = "coordinates extracted: \n";
for (i=0; i<images.length; i++) {
   inputPath = inputFolder + images[i];
       if(File.isDirectory(inputPath) == 1){
       i++;}
       else{
       open(inputPath);
       run("Rotate... ", runarg);
       doWand(a, b, c, "Legacy");
       run("Interpolate", "interval=1");
       name=images[i];
       path = inputFolder+addpath+"/"+name+"_xy.txt";
       saveAs("XY Coordinates", path);
       close();
       notice = notice + path + "\n";
       }
}
setBatchMode(false);
print(notice);
exit();
```

Code 1: *ImageJ macro to extract the coordinates of the profile*

This macro can be run in batch mode such that it processes all the files of one folder, which in our case corresponds to the images of the evolution of the drop taken from a standard film with 25fps. This leads to around 5000 to 10000 images per experiment. With this macro this is done in 5 minutes

on a standard PC. Normally its not necessary to treat all the images, in general it is sufficient to treat every tenths image to still get a smooth evolution of the parameters.

The macro is creating, for each image, a text file containing the coordinates of the pixels of the boundary shown in Fig. C.1 (b). Starting from this files the c++ program extracts the information to calculate the height, diameter, contact angle and volume of the drop.

The first step consists in importing the coordinates into the program, i.e. to read the text files produced by the ImageJ macro (line 23-54 of the code). Then the coordinates of the boundary pixels are cut of (line 64-76 of the code) and the remaining coordinates are just the profile of the drop with some more pixels on the top that correspond to the reflection of the drop on the meniscus (Fig. C.1 (c)). To get rid of these coordinates the maximum value among the x-coordinates was calculated (Fig. C.1 (d) 1)). By taking the corresponding y-coordinate all the pixels above are cut off and we are left with the actual profile of the drop (Fig. C.1 (d) 2)).
For further mathematical manipulations of the data the coordinates have to transformed into a function. Due to its origin (coordinates of pixels of an image) the coordinates does not represent a function since two y values correspond to one x value (Fig. C.1 (c); zoom-in, red curve). To transform the coordinates into a function we have to remove always one of these two y values, which can be done by selecting always the bigger one for example (Fig. C.1 (c); zoom-in, black curve). This transformation into a function is done in line 113-153.
Now all the parameters can be calculated from this function. The first step is to find the minimum of the profile which is done in practice by calculating the left and the right minimum of the y-coordinates and then taking the average of them (Fig. C.1 (d) 2)) (line 168-203 of the code). With this information at hand we can calculate the height (line 248 of the code) while the information of the diameter is simply calculated by computing the difference between the x-coordinates of the last and the first point of the profile (line 240 of the code). For calculating the contact angle the slope of neighboring pixels is calculated for 20% of the profile (see Fig. C.1 (d) 4)) and then averaged (line 206-236 of the code).
For calculating the volume I used the formula for calculating the volume of a solid of revolution by taking $y(x)$ shown on Fig. C.1 (d) 3)), i.e. the right (or left) side of the profile. The volume writes

$$V = \pi \int_{y_o}^{y_{max}} x(y)^2 dy. \tag{C.1}$$

We still have to shift the x values by the center of the drop, i.e. $x \mapsto x - x_o$, where $x_o = x(y_o)$ is the position of the minimum. This leads to

$$V = \pi \int_{y_o}^{y_{max}} (x(y) - x(y_o))^2 dy, \tag{C.2}$$

which is calculated in line 257. In the end all the parameters are printed and also saved in a text file. The full program is given below.

```
1
2  #include <iostream>
3  #include <fstream>
4  #include <stdbool.h>
5  #include <math.h>
6  #include <stdio.h>
7  #include <stdlib.h>
8  #include <iomanip>
9
10
11 using namespace std;
12
13 struct vector {
14    float x, y;
15 };
16
17 int main(int argc, char *argv[]){
18
19
20
21 int results = atoi(argv[9]);
22
23 // Extraction process
24
25 char filename[5000];
26
27 sprintf(filename,"%s/%s",argv[1],argv[2]);
28
29     // Open the ifile
30     //cout << filename << endl;
31     ifstream fin;
32     fin.open(filename);
33     if (fin.fail()){
34       cout << " " << endl;
35       cout << "Extractor : Error opening file (wrong directory ?) !!!" << endl;
36       cout << " " << endl;
```

```
37    exit(1);
38    }
39
40
41  // Read from the file content
42
43  vector input[10000];  //number of input coordinates
44  vector v[10000];
45  vector vv[10000];
46  int sizei=1;
47  while(!fin.eof()){
48
49         fin >> input[sizei].x >> input[sizei].y;
50
51         sizei++;
52  }
53
54     fin.close();
55
56
57  //input by argument
58
59  int x_min = atoi(argv[5]);
60  int x_max = atoi(argv[6]);
61  int y_min = atoi(argv[7]);
62  int y_max = atoi(argv[8]);
63
64  //cut off the boundaries
65
66
67  int size=1;
68  for(int i=1; i <= sizei;i++){
69       if(input[i].y > y_min && input[i].y < y_max && input[i].x > x_min && input[i].x <
           x_max){
70          vv[size].x = input[i].x;
71          vv[size].y = input[i].y;
72          //cout << vv[size].x << " " << vv[size].y << endl; //output without boundaries
73          size++;
74       }
75    }
76  size=size-1;
```

```
77
78
79  //find cut off value for interface
80
81  int mx = -500;
82  int my = 0;
83  for(int j=1; j <= size;j++){
84              if(vv[j].x > mx){
85                 mx = vv[j].x;
86             my = vv[j].y;
87             }
88  }
89
90  if(results == 1){
91  cout << " " << endl;
92  cout << "========================================================================" << endl;
93  cout << "Summary of " << argv[2] << endl;
94  cout << "========================================================================" << endl;
95  cout << " " << endl;
96  cout << "cut off value/(position of the interface): " << my << endl;
97  }
98  //cut off the interface
99
100 int sizeii=1;
101 for(int i=1; i <= size;i++){
102       if(vv[i].y > my){
103          v[sizeii].x = vv[i].x;
104          v[sizeii].y = vv[i].y;
105          //out << v[sizeii].x << " " << v[sizeii].y << endl; //output of the real shape
106          sizeii++;
107       }
108    }
109 sizeii=sizeii-1;
110
111
112
113 //convert to a function
114
115 vector w[10000];
116
117  int j=2;
```

```
 int k=0;
 int l=0;
 int sizemax;

w[1].x = v[1].x;
w[1].y = v[1].y;

for(int i=2; i <= sizeii;i++){
if(v[i].x == v[i-1].x || v[i].x == v[i+1].x ){
for(k; v[i].x == v[i+k].x;k++){
}
w[j].x = v[i+k].x;
w[j].y = v[i+k].y;
j=j+1;
i=i+k;
//cout << "k:" << k << endl; //output the step jump
k = 0;
}
if(v[i].x > v[i+1].x){
for(l; v[i].x > v[i+l].x;l++){
}
w[j].x = v[i+l].x;
w[j].y = v[i+l].y;
j++;
i=i+l;
l=0;
//cout << "l:" << l << endl; //output the step jump
}
if(v[i].x != v[i-1].x || v[i].x != v[i-1].x){
w[j].x = v[i].x;
w[j].y = v[i].y;
j++;
}


}
sizemax =j-3;



// Calculate Height, Diameter and Contact Angle(s) of the Droplet
```

```
159
160 float h;
161 float diam;
162 float c1angle;
163 float c2angle;
164 float vol = 0.0;
165 float intvol;
166
167
168 //find max of the function
169
170 //from left
171 int m1x = 0;
172 int m1y = -500;
173 int i1value;
174 for(int j=1; j <= size;j++){
175             if(w[j].y > m1y){
176                m1x = w[j].x;
177            m1y = w[j].y;
178            i1value=j;
179            }
180 }
181
182 //from right
183 int m2x = 0;
184 int m2y = -500;
185 int i2value;
186 for(int j=size; j >= 1;j--){
187             if(w[j].y > m2y){
188                m2x = w[j].x;
189            m2y = w[j].y;
190            i2value=j;
191            }
192 }
193
194
195 int maxx = (m1x + m2x )/2;
196 int maxy = (m1y + m2y )/2;
197 int ivalue = (i1value+i2value)/2;
198
199 if(results == 1){
```

```
cout << "position of max: " << m1x <<endl;
cout << "position of max: " << m2x <<endl;
cout << "position of max (middle): " << maxx <<endl;
}


//improved contact angle calculations

vector C[10000];

int maxii = 0.2*sizemax;

//calculating the slope

//cout << "" << endl;
//cout << "Contact Angle(s):" << endl;
//cout << "" << endl;

for(int ii=10; ii < maxii;ii++){
C[ii].y = (w[ii+1].y - w[ii-1].y)/(w[ii+1].x - w[ii-1].x);
C[ii].x = w[ii].x;
//cout << "c.A.: " << atan(C[ii].y)*180/3.141592 << endl;
}

//averaging

float cAav;

for(int ii=2; ii < maxii;ii++){
cAav = cAav + C[ii].y;
}

cAav = cAav/maxii;

if(results == 1){
cout << "c.A.av: " << atan(cAav)*180/3.141592 <<"[U+FFFD]"<< endl;
}

//calculate diameter

diam = w[sizemax-1].x - w[1].x;
```

```
241
242 if(results == 1){
243 cout << "Diameter: " << diam <<endl;
244 }
245
246 //calculate height
247
248 h = maxy - w[1].y;
249
250 if(results == 1){
251 cout << "Height: " << h <<endl;
252 }
253
254 //calculate the volume
255
256 for(int ii=1; ii < sizemax/2;ii++){
257 vol = vol + (w[ii].x - w[sizemax/2].x)*(w[ii].x - w[sizemax/2].x)*abs(w[ii].y - w[ii+1].y);
258 }
259
260 intvol = 3.141592*vol;
261
262 if(results == 1){
263 cout << "Volume: " << intvol <<endl;
264 cout << " " << endl;
265 cout << "========================================================================" << endl;
266 cout << " " << endl;
267 }
268
269
270 //write function to file
271
272 sprintf(filename,"%s/%s_profile_functions/%s_%s_function.txt",argv[1],argv[3],argv[3],argv[4]);
273
274    ofstream foutFUNC;
275     foutFUNC.open(filename);
276
277
278   for(int i=1; i < sizemax+1;i++){
279       foutFUNC << w[i].x << " " << w[i].y << endl;
280   }
281
```

```
282
283     foutFUNC.close();
284
285
286 //Write (append) values to file
287
288    sprintf(filename,"%s/%s_values/%s_extracted_values.txt",argv[1],argv[3],argv[3]);
289
290     ofstream fout3;
291     fout3.open(filename, ios::out | ios::app | ios::binary);
292
293  // height | diameter | contact angle | volume | lateral displacement | position of the
       interface | filename (framenumber)
294
295
296    fout3 << std::setprecision(9) << h << " " << diam << " " << atan(cAav)*180/3.141592 << "
         " << intvol << " " << maxx << " " << my << " " << argv[4] << endl;
297
298    fout3.close();
299
300
301 }
```

Code 2: *C++ program to extract the height, the diameter, the contact angle and the volume starting from the profile contour obtained with ImageJ.*

The usage of the program, i.e. the way to specify the arguments is given below.

```
========================================================================

            Program to extract the side-view parameters

This program takes a xy-coordinate file originated from a ImageJ picture
it cuts out only the necesarry part (by giving the boundaries) and conv-
erts the xy-coordinates in a function which is saved in :

FULL_PATH/PREFIX_profile_functions/PREFIX_FILENUMBER_function.txt

(if the folders exists !)
```

```
From the function it calculates the diameter, the height, the contact
angle and the volume (by numerical integration of the profile). The ex-
traced values are saved in :

FULL_PATH/PREFIX_values/PREFIX_extracted_values.txt

(if the file exists !)

This program should be used TOGETHER with extractionL (source file :
extraction_loop.cpp)

=========================================================================

-------------------------------------------------------------------------
         I M P O R T A N T : Please give input in the form :
-------------------------------------------------------------------------

./extractV FULL_PATH FILENAME PREFIX FILENUMBER X_MIN X_MAX Y_MIN Y_MAX R


Description of the arguments :
-------------------------------------------------------------------------

FULL_PATH = full path of the directory where the profiles are situated

FILENAME = filename of the file to be analyzed

PREFIX = filename-prefix declaring the experimental conditions (part of
        the filename)

FILENUMBER = number corresponding to the frame (part of the filename)

X_MIN X_MAX Y_MIN Y_MAX = coordinates of the boundary box

R = shows results if 1 and doesn't show them if 0
```

Code 3: *usage of the program shown in Code 2.*

What is shown in Code 2 is a program to extract the parameters from one profile. To automatize the procedure I also wrote a program that runs all the files in a folder by specifying the start and the

end profile. This program calls the above mentioned program (Code 2) and loops it over the profiles indicated. The code is shown below.

```
 #include <iostream>
#include <fstream>
#include <stdbool.h>
#include <math.h>
#include <stdio.h>
#include <stdlib.h>

// This program extracts the values of the contact angle(s), the diameter and the height of
    the droples aswell as the volume of the droplet from a series of images files.

using namespace std;

struct vector {
   float x, y;
   };



int main(int argc, char *argv[]){


//creation of a folder for the result file

char SYS[1000];

   sprintf(SYS,"mkdir %s/%s_values",argv[1],argv[2]);
   system (SYS);

      sprintf(SYS,"mkdir %s/%s_profile_functions",argv[1],argv[2]);
   system (SYS);

float scale;
scale = 1;


// Open the file for the results
```

```
36
37
38  char ofile[1000];
39
40     sprintf(ofile,"%s/%s_values/%s_extracted_values.txt",argv[1],argv[2],argv[2]);
41     cout << ofile << endl;
42     ofstream fout3;
43        fout3.open(ofile);
44        if (fout3.fail()){
45        cout << " " << endl;
46        cout << "Extracting loop : Error opening file (wrong directory ?) !!!" << endl;
47        cout << " " << endl;
48     exit(1);
49     }
50  fout3 <<"#height | diameter | contact angle | volume | lateral displacement | position of
       the interface | filename (framenumber)" << endl;
51  fout3.close();
52
53
54  // call the programm that extract the values of the contact angle(s), the diameter and the
       height of the droples
55
56  int minindex=atoi(argv[3]);
57  int maxindex=atoi(argv[4]);
58
59  for(int ii=minindex;ii<maxindex+1;ii++){
60
61        cout << ii << " (" << 100*(ii-minindex)/(maxindex-minindex) << "%)" << endl;
62        // ./extractionL FULL_PATH PREFIX starting_frame final_frame x_min x_max y_min y_max
             show results
63
64        // ./extractV FULL_PATH FILENAME PREFIX FILENUMBER x_min x_max y_min y_max show_results
65
66        sprintf(SYS,"./extractV %s %s_%i.jpg_xy.txt %s %i %s %s %s %s
             0",argv[1],argv[2],ii,argv[2],ii,argv[5],argv[6],argv[7],argv[8]);
67        system (SYS);
68        //cout << SYS;
69    }
70
71  cout << "values are extracted!" << endl;
72
```

```
73
74 }
```

Code 3: *C++ program to loop the program given in Code 2.*

The usage of the loop program, i.e. the way to specify the arguments is given below.

```
==========================================================================

          Looping Program for the side-view extraction

This program loops the extraction program \"extractV\" (with source file
extractor.cpp) between two given framenumbers and saves the profile
functions in :

FULL_PATH/PREFIX_profile_functions/PREFIX_i_function.txt

(where i is the running frame)

and the extracted parameters (each line in the following file corresponds
to a frame) in :

FULL_PATH/PREFIX_values/PREFIX_extracted_values.txt

In fact it creates the folders and the parameter file from the given
arguments and passes the arguments to the extraction program which then
saves the data accordingly.

==========================================================================

--------------------------------------------------------------------------
I M P O R T A N T : Please give input in the form :
--------------------------------------------------------------------------

./extractionL FULL_PATH PREFIX ST_FRAME FI_FRAME X_MIN X_MAX Y_MIN Y_MAX


Description of the arguments :
--------------------------------------------------------------------------
```

```
FULL_PATH = full path of the directory where the profiles are situated

PREFIX = filename-prefix declaring the experimental conditions (part of
        the filename)

ST_FRAME = starting frame

FI_FRAME = final frame

X_MIN X_MAX Y_MIN Y_MAX = coordinates of the boundary box
```

Code 3: *usage of the loop program shown in Code 3.*

After having extracted the parameters for all the time points of interest, we are able to plot the parameters as a function of time. This is shown below for the diameter $D(t)$, the height $h(t)$ and the contact angle $\varphi(t)$ (Fig. C.2).

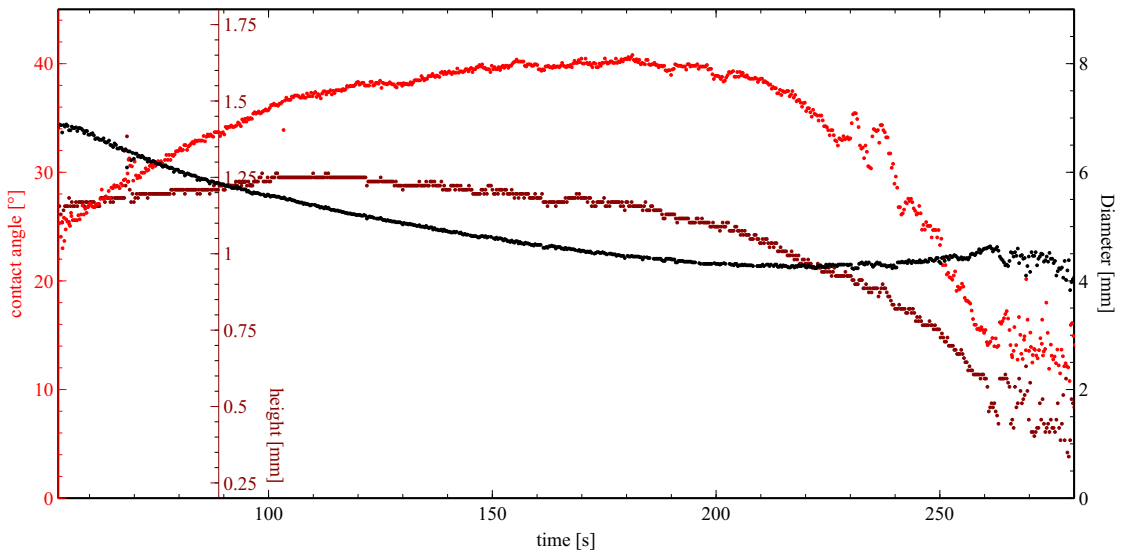

Figure C.2: *Evolution of height, diameter and contact angle of a 30µL drop on the surface of a 0.5mM CTAB solution in a 3x3x3cm cuvette with the same volume of air and aqueous solution (13.5mL).*

C.2. Spherical Cap Approximation - Mathematica Program

The program described here is used to numerically minimize the energy of the drop within the spherical cap approximation. The equation of the energy in the non-dimensional variable x is given by

$$E_{\text{tot}}(x) = 4\pi \left[a\frac{y}{x^2} + b\frac{y^2}{x^2} - \delta\frac{2y - y^2}{3x(3-2y)} \right] + \text{const.} \tag{C.3}$$

where y is a function of x, i.e. $y = y(x)$ which can be calculated from equation

$$x^3 = 3y^2 - 2y^3. \tag{C.4}$$

The coefficients a, b and δ are given by

$$\begin{aligned} a &= (\gamma_1 - \gamma_2 + \gamma_3)R^2 \\ b &= (\gamma_2 - \gamma_1)R^2 \\ \delta &= \Delta\rho g R^4 \end{aligned} \tag{C.5}$$

Numerically finding the minimum in $E_{\text{tot}}(x)$ with regard to x gives us the contact angle $\theta_c = (1 - 2y(x_{min}))$ and the diameter $D = 2R_c = 2R/x_{min}$ of the spherical cap. The *mathematica* program used is given below.

```
y0[x_] = y /. Solve[x^3 == 3*y^2 - 2*y^3, y][[3]]
Plot[y0[x], {x, 0, 1}]

gamma1 = 29*10^-3; (*Air/Oil*)
gamma2 = 42*10^-3; (*Air/Water*)
gamma3 = 27*10^-3; (*Oil/Water*)
drho = 0.33*10^3;
V0 = 25*10^-9;

R = N[(3*V0/(4*Pi))^(1/3)];
g1 = Sqrt[gamma1]*R;
g2 = Sqrt[gamma2]*R;
g3 = Sqrt[gamma3]*R;
a = (g1^2 - g2^2 + g3^2);
b = g3^2 - a;
delta = drho*9.81*R^4;

Etot[x_] := 4*Pi*(a*y0[x]/x^2 + b*(y0[x]/x)^2 - delta*(2*y0[x] - y0[x]^2)/((3 -
    2*y0[x])*x*3));
```

```
xmin = x /. FindMinimum[Re[Etot[x]], {x, 10^-10, 1 - 10^-20}, AccuracyGoal -> 10,
    PrecisionGoal -> 10][[2]];

Rc = R/xmin;
D0 = R/xmin*2;
Thetac = ArcCos[1 - 2*Re[y0[xmin]]];
ThetacAngle = 180*Thetac/Pi;
ThetacAngleCorr = ThetacAngle - 14;
h0 = Rc*(1 - 2*Re[y0[xmin]]);

Plot[Etot[x], {x, 0, 1}];
Plot[{h0 + Sqrt[Rc^2 - x^2], h0 - Sqrt[Rc^2 - x^2]}, {x, -0.01, 0.01}, PlotRange -> {{-0.01,
    0.01}, {-0.01, 0}}, AspectRatio -> 0.5, Filling -> {1 -> {h0, LightGray}, 2 -> {h0,
    LightGray}}, PlotStyle -> {Gray, Gray}, Frame -> True, Axes -> False, FrameLabel ->
    {Style["Position in m", 10], Style["Height in m",10]}, BaseStyle -> {FontWeight ->
    "Plain", FontSize -> 8}]
```

Self-Pulsations of a Dichloromethane Drop on a Surfactant Solution

Supervisor: Véronique PIMIENTA

Far-from-equilibrium systems exhibit a wide variety of spatial and temporal patterns known as dissipative structures. The interplay between physico-chemical processes and mass or heat transfer can give rise to spatio-temporal structures induced by convective flows. These flows may result from density or surface tension gradients. They are the expression of the conversion from chemical into mechanical energy. When surface tension is the driving force, the corresponding effects are known as Marangoni effects. They are at play in numerous applications as extraction processes, oil recovery, and chemical reactors at all scales and noticeably modify transfer rates. The complexity of real systems deserves the development of model systems, essentials to settle, on a fundamental level, the theory governing the related dynamics.

A succession of dynamical regimes is observed during the dissolution of a dichloromethane drop deposited on aqueous solutions of a cationic surfactant (cetyltrimethylammonium bromide, CTAB). The remarkable range of shapes and motion patterns that emerges is related to the surfactant concentration, which is used as a control parameter. For low surfactant concentrations, we observe translational motion and pulsations of the drop. At intermediate concentrations the drop transforms and starts to rotate. At higher concentrations polygonal shapes are observed.

Although chemically simple and of easy implementation, the system is relatively complex and involves several processes: evaporation, solubilization, surfactant mass transfer, interfacial adsorption and self-aggregation. Thermal and transport effects induced are at the origin of local variations of interfacial tension leading to the Marangoni flows.

In this thesis, we focused on the behavior of the dichloromethane drop when the aqueous surfactant concentration (0.5 mM) leads to the pulsating regime. At this concentration, we have first analyzed the behavior of the drop during the induction period that precedes the instable regime. Drop shape analysis, correlated to Particle Image Velocimetry (PIV) measurements, showed that dissolution flows initially hinder adsorption of CTAB at the water/oil interface. The instability is only triggered when dissolution is reduced and water/oil adsorption becomes effective. The induction period appears as a slow transition from an initial negative spreading coefficient (a lens shape drop) towards a positive spreading coefficient that triggers film expansion and following pulsations.

These pulsations are accompanied by the ejection of smaller droplets which are formed from a toroidal rim that is created during the expanding phase of the drop. The break-up of this toroidal rim, resembles to what is known as the Rayleigh-Plateau (RP) instability. Nevertheless, the observed characteristic wavelength is a factor of 2 too small in respect to the classical RP instability. We have found the origin of this discrepancy in the fact that modulations that appear on the rim before it transforms into droplets are settled by deformations arising at the surface of the expanding film. They appear as wrinkles that form in the film and may be related to thermal Marangoni effects known as Benard-Marangoni instability. These wrinkles play an important part in the highly organized dewetting structure described in the last chapter of the thesis. The addition of CTAB also in the organic (drop) phase leads to faster pulsations which, after a very high amplitude expanding stage and the ejection of a perfect crown of droplets, result during the film receding stage in the formation of a pattern which symmetry is reminiscent of a flower. A qualitative interpretation aimed at identifying the main processes at play and based on independent surface tension data gives a consistent explanation of the observed pulsations and related self-organized patterns.

Keywords: Marangoni effect, hydrodynamic instability, surfactants, drop, self-organization

Laboratoire des Interactions Moléculaires et Réactivité Chimique et Photochimique, UMR 5623 Université Paul Sabatier, Bât 2R1, 118 Route de Narbonne, 31062 Toulouse

Pulsations d'une goutte de dichloromethane sur une solution de tensioactifs

Directeur de thèse: Véronique PIMIENTA

Le couplage entre processus physico-chimiques et le transfert de matière ou de chaleur peuvent donner lieu à des structures spatio-temporelles induites par des flux convectifs. Ces flux peuvent résulter de gradients de densité ou de tension superficielle et sont l'expression de la conversion d'énergie chimique en énergie mécanique. Quand la tension superficielle est à l'origine de ces mouvements, les effets correspondants sont connus sous le nom d'effet Marangoni. Ils jouent un rôle dans de nombreuses applications comme les procédés industriels d'extraction en amplifiant notablement la vitesse des processus de transfert. Les systèmes réels, trop complexes, doit être simplifiés par le développement de systèmes modèles afin d'établir au niveau fondamental la théorie sous-jacente à de telles dynamiques.
Une succession de régimes dynamiques est observée lors de la dissolution d'une goutte de dichlorométhane (DCM) déposée sur une solution aqueuse de tensioactif (bromure de céthytriméthylammonium, CTAB). La succession remarquable de formes et de mouvements induits est déterminée par la concentration du tensioactif qui joue le rôle de paramètre de contrôle. A faible concentration en CTAB, un mouvement de translation ou des pulsations. Aux concentrations plus élevées, la goutte entre en rotation ou forme des structures polygonales.
Bien que chimiquement simple, le système est complexe et implique plusieurs processus physico - chimiques : évaporation, solubilisation, transfert de tensioactifs, adsorption aux interfaces et agrégation. Les effets thermiques et de transport qui en résultent sont à l'origine des variations locales de tension interfaciale donnant lieu aux effets Marangoni.
Nous nous sommes concentrés sur le comportement de la goutte quand la concentration en tensioactif conduit au régime de pulsation. Nous avons tout d'abord analysé le comportement de la goutte pendant la période d'induction qui précède le régime instable. L'analyse de la forme de la goutte corrélée à des mesures d'Imagerie par Vélocimétrie de Particules (PIV), ont montré que les flux créés par la dissolution du DCM limitent dans un premier temps l'adsorption du CTAB à l'interface eau/huile. L'instabilité ne démarre que lorsque la dissolution est réduite et que l'adsorption devient effective. La phase d'induction apparait comme une transition lente entre un coefficient d'étalement négatif (goutte ayant la forme d'une lentille) vers un coefficient d'étalement positif qui entraine l'expansion du film et les pulsations suivantes.
Ces pulsations sont accompagnées par l'éjection de gouttelettes qui se forment à partir d'un bourrelet apparaissant au bord du film pendant la phase d'expansion. La rupture de ce bourrelet ressemble au phénomène connu sous le nom d'instabilité de Rayleigh-Plateau (RP). Cependant, la longueur d'onde caractéristique de formation des gouttelettes est deux fois plus faible que celle attendue dans le cas d'une instabilité de RP classique. L'origine de cet écart réside dans la modulation du bourrelet avant sa rupture. Cette modulation est en fait déterminée par des ondulations apparaissant à la surface du film et formant des rides en direction radiale. Ces rides pourraient être attribuées à un effet Marangoni thermique connu sous le nom d'instabilité de Bénard-Marangoni. Elles jouent également un rôle important dans la formation de la structure de démouillage hautement organisée décrite dans le dernier chapitre. L'ajout de CTAB dans la phase organique (goutte) donne lieu à des oscillations plus rapides qui, après une phase d'expansion de grande amplitude et l'éjection d'une couronne parfaite de gouttelettes, résultent lors de la phase de démouillage en une structure dont la forme rappelle une fleur. Une interprétation qualitative permettant d'identifier les principaux processus à l'œuvre et basée sur des mesures indépendantes de tension interfaciale apporte une explication des pulsations observées et de l'auto-organisation induite.

Mots-clés: effet Marangoni, instabilité hydrodynamique, tensioactifs, goutte, auto-organisation

Laboratoire des Interactions Moléculaires et Réactivité Chimique et Photochimique, UMR 5623 Université Paul Sabatier, Bât 2R1, 118 Route de Narbonne, 31062 Toulouse